NUMERICAL STUDY OF THE PIEZOELECTRIC AND DIELECTRIC PROPERTIES OF PZT-EPOXY COMPOSITES AS A FUNCTION OF CURING PROCESS

by

RUI WANG

A dissertation submitted to the

School of Graduate Studies

Rutgers, The State University of New Jersey

In partial fulfillment of the requirements

For the degree of

Doctor of Philosophy

Graduate Program in Mechanical & Aerospace Engineering

Written under the direction of

Kimberly Cook-Chennault

And approved by

_____

_____

_____

_____

New Brunswick, New Jersey

May, 2019

ABSTRACT OF THE DISSERTATION

Numerical Study of the Piezoelectric and Dielectric Properties of PZT-EPOXY Composites as a function of Curing Process
BY RUI WANG

Dissertation Director:
Professor Kimberly Cook-Chennault

In this study, simulation of the piezoelectric and dielectric properties of the PZT-5A and epoxy DGEBA piezoelectric composites is interested. The deformation of the samples will be caused by the thermal expansion and the shrinkage of the geometry by curing process when heat transfer happened in the samples during the time. Thus, the electric charges will be generated by the composites due to the material properties of piezoelectric materials. Comsol Multiphysics 5.3a and Matlab Live Link 2016a are used to do the simulation of temperature distribution in the two-phase (Epoxy (DGEBA)-lead zirconate titanate $(Pb[Zr_x Ti_{1-x}]O_3 (0 \leq x \leq 1)$ composites structures. Thermal stress (including Solid mechanics and Heat transfer in solid), electrostatics physics were used to generate the models. Curing process of the epoxy matrix will be shown in the simulation at 75C. Non-cured epoxy was used for the epoxy with epoxy hardener as the curing agent and PZT-5A was chosen for piezoelectric materials. The

dimension for PZT-5A is 5μm to 8 μm for diameters. Three kinds of the geometry of samples were considered in the simulation models, bulk models, planar models, and dome shape models. The dimensions for bulk samples are 1.4cm in thickness and 0.6cm in width. Dimension for planar models is 0.02cm for the thickness and 2.54cm for the width. Dimension for dome-shape models is 2.54cm for the length and 0.508cm in height and 0.02cm in thickness. The models were made as 2D models. Pure epoxy resin models and pure PZT-5A models were generated. For the composites, the volume fraction of PZT is from 10%,20%,30% to 70%. Rest of the material is epoxy. Boundary conditions for heat transfer in solid were considered as heat convection and surface radiation. And there is fixed temperature 75C applied at the bottom of the models. Since the PZT particles are very small, it is impossible to generate huge amounts of particles for the volume fractions need in the model because the computer cannot run this. In order to solve this problem, the unit cell method and the scaled method were used. The results for temperature, stress-strain, displacement, voltage, and capacitance were generated by the models. The curing process of epoxy was shown as well. Piezoelectric strain coefficient d_{33} and dielectric constant were calculated and compared to the experimental results. PZT particle floating during the curing process was compared with the scanning electron microscopy (SEM) images.

Acknowledgement

Table of Contents

List of Tables

List of illustrations

Chapter 1

Introduction

1.1 Background

The piezoelectric effect is a molecular phenomenon that can be observed at the macroscopic level as a change in electric potential that is created when a piezoelectric substance is deformed[1]. Piezoelectric material is a class of dielectric material generates electric charges when a mechanical stress is applied. Certain materials such as quartz, salt, and even sugar generate a voltage when subjected to mechanical stress[1]. In addition, piezoelectric materials can be polarized (polarization is the phenomenon that the dipoles inside the composite will be reoriented) not only by the application of a mechanical stress but also by an electric field. This unusual property exhibited by a certain class of dielectric materials is called piezoelectricity, where the polarization is proportional to the strain and charges associated with it[1]. Piezoelectric materials exhibit a non-centrosymmetric structure in the tetragonal phase so that they have a linear relationship between mechanical and electrical energy of the materials[2].

All these materials have characteristic crystal structures formed from lattice of molecules with asymmetric dipole moments that would respond to mechanical pressure. This effect was first observed by Carl Linaeus and Franz Aepinus in the mid-1800s. In the early 1900s, scientists found that the crystals would vibrate when a current was

passed through them, which showed that piezoelectric materials could be polarized when they were subjected to an electric field due to the wave form of voltage, sound was generated. Because of this material property, quartz crystals were created as piezoelectric transducers, that were used as submarine sonars. Later, piezoelectric materials were incorporated into radios, televisions, and other electronics, such as audio filters and buzzers. Among those piezoelectric materials, the most commonly used in industry was quartz both because they were inexpensive. In modern times, the most common use for piezoelectric materials has remained in audio equipment, such as guitar pickups and barbeque grill igniters. Other applications in modern times are in watches, piezoelectric motors, vibrational dampeners, and inkjet ejectors.

Presently, piezoelectric materials are commonly used as transducers due to their property to convert mechanical energy into electrical energy, or vice versa[2]. This is because homogenous piezoelectric ceramic actuators are very simple in structure and design, e.g. plates, disks, rings and cylinders) [3]. Homogenous piezoelectric ceramics (this type of ceramics have uniform composition and properties throughout) have some other advantages. For example, they are highly reliable with cycle lives with range from 10^3 to 10^6 [4, 5]. They can provide large actuation forces (dynamic force = 128 N at 120 Volts and static forces from 275 N to 375 N at 100 Volts)[6]. They have high sensitivity with rapid response of time (response time can range from 5 μsec to 50 μsec)[7] and consume lower power during operation which ranges from 100 μw to 500 μw[8]. Many piezoelectric materials, such as quartz, ceramics (like Pb(Zr_xTi$_{1-x}$)O_3, BaTi O_3) have high piezoelectric strain coefficient. For example, piezoelectric

coefficient d_{33} of PZT (lead-zirconate titantate) is ~630 pC/N and barium titanate (BaTiO_3) for 191 pC/N[9]. Polymers such as poly (vinylidene difluride) (PVDF) are sometimes used instead of ceramics because of their large g_{33} voltage coefficient, which ranges from 0.14 to 0.22 V.m/N. It is also used because it is more flexible, and has low acoustic and mechanical impedance[3]. The higher g_{33} value the material has, the more sensitive the material is. To this point, sensitive piezoelectric materials need less mechanical force to generate a piezoelectric response. However, even though that PVDF has high g_{33} value, it has a much lower piezoelectric strain coefficient d_{33} compared with other piezoelectric ceramic materials[10].

Despite that homogenous ceramic piezoelectric materials have so many advantages, they are still limited in the application in industry because that they have high stiffness (51-59 GPa for PZT) [11], poor mechanical strength, brittle nature (ultimate strength < 100 MPa), little displacement, low fracture toughness (0.5~2.0 MPa.$\sqrt{m}$) and high processing temperature[10]. Many applications such as sensors, actuators, hydrophones, static and vibration-based energy harvesting devices require compliant and flexible materials impedance. So, the poor mechanical properties mentioned before will limit their effective and efficient application. Hence, researchers thus explore polymer-ceramic composites to take advantage of each individual material in the composite to alleviate some of the challenges in the application[3].

Composite piezoelectric materials can provide improved mechanical strength and toughness; they are much easier to fabricate than single phase materials and are compatible to mass production techniques; they have better electromechanical coupling

properties with host structure. There are many types of piezoelectric composites. They are able to form many types of connectivity of composites. For example, there are total 10 types of connectivity for two-phase composites, such as (0-0), (0-1), (0-2), (0-3), (1-1), (1-2), (2-2), (1-3), (2-3), and (3-3). Among these types, 0-3 connectivity piezoelectric materials are easy to fabricate and commonly used. For this type of composite, piezoelectric filler particles are embedded within a matrix such as epoxy. Piezoelectric filler particles are uniformly distributed in the matrix but they are not self-connected throughout the material. However, the matrix itself is self-connected throughout the material.

There are several challenges exist for fabricating 0-3 piezoelectric composites. First, piezoelectric filler particles are difficult to be uniformly distributed in the matrix, especially when the volume fraction of filler particles are high. Second, dielectric properties of the composite decrease even though the flexibility and compliance increase. Third, it is very easy to form air bubbles and porosity within the composite. Some of these factors lead to premature dielectric breakdown and ineffective polarization. So in order to overcome all these problems, researchers have tried to solve them by adding another phase material into composites which is an electrically conductive filler, such as carbon black, aluminum and MWCNT[1, 12-15]. In this case, the composite that is formed has 0-3-0 connectivity. Inclusion of electrically conductive fillers increase the electrical and thermal conductivity of the matrix. However, since it does not quite know about how the electrically conductive particle and piezoelectric composites themselves will affect their piezoelectric and dielectric

properties.

In this thesis, the materials of interest are PZT and epoxy DGEBA. Experimental results of previous works of S.Banerjee[13] and Wanlin Du[14] et al will be compared to the predictions of the numerical models.

1.2 Research Goals and Hypotheses

In this thesis, 0-3 connectivity piezoelectric composites were modeled and compared to empirical results. These composites consisted of lead-zirconate titanate $(Pb(Zr_x Ti_{1-x})O_3)$ and an epoxy polymer matrix (DGEBA). The composites are modeled were in different shapes: bulk-discs, planar-discs and dome shapes, which were fabricated by the Cook-Chennault group using a cast-mixed method as well as spin coat method.[13,14]The reasons why the dome and curved shape piezoelectric devices were interested are because that these structures are proved have higher deformation (PZT~25.3% AT 2.54 KV/cm [14]) and better electromechanical conversion accuracy (mechanical coupling factor, PZT-5A, K_{eff} ~38% [14]) in comparison to planar actuators. However, during the fabrications, these composites suffered from the high agglomeration of PZT particles, ununiformed surface morphology and formation of air bubbles which will lead to low piezoelectric coefficients and dielectric properties[14, 16, 17]. So, in this work, how temperature gradients in these composites due to heat transfer affects the piezoelectric and dielectric properties of such devices were explored, including the viscosity change with the epoxy gel form and the curing condition will affect the piezoelectric, dielectric properties and displacement. In this work, only numerical part will be studied and all the challenges

mentioned before in the experimental work can be neglected because the models were simulated as ideal model. The numerical data will be compared with the experimental data so as to see how greatly those challenges affected the results in the experimental work. Three hypotheses were developed to deal with some of the challenges previously mentioned.

Hypothesis I: Due to difference in stiffness of two materials, the largest displacement may not occur at the highest concentration of the piezoelectric material. From literatures, composite materials with higher volume fraction of the ceramic powders will be more stiffness because of its high value of Young's Modulus. This is because Young's Modulus of the ceramic powders are much larger than polymer matrix. Thus, if same amount of force is applied on two different volume fraction composites, the stiffer composite will produce less strain, this suggest that smaller amount of strain will be observed in higher ceramic volume fraction composites; but on the other hand, our ceramic powder here is PZT, and is our active material, which provide the activation force, so the higher concentration of the active ingredient will provide larger activation forces, this suggests that the higher concentration of PZT might result in larger displacement. In this study the displacement will be modeled to see where the largest displacement could be achieved.

Hypothesis II: Curing conditions will have influences on piezoelectric, dielectric properties and displacement.

Hypothesis III: The rate of crosslinking of the epoxy influences the distribution of the PZT within the piezoelectric composite, which ultimately influences the

macroscopic piezoelectric strain coefficients and dielectric properties. It is hypothesized large thermal gradients within the composite reduce the distribution of the PZT within the composite, thereby sequestering the PZT particles to the cooler portion of the samples.

1.3 Research Materials and Methodology

The materials of interest in this work are PZT-epoxy composites. The volume fraction of PZT was varied from 0.1 to 0.7, for which the increment is 10% for each volume fraction. The "lead-zirconate titanate" (also called PZT) that was used experimentally and in numerical models is PZT-855 and the two-part epoxy is DGEBA, the epoxy hardener EpofixTM Cold-setting embedding Resin (purchased from APC International and Electron Microscopy Sciences, respectively). The processes for fabrication and characterization of the samples for the empirical results may be found in references[18, 19]. Piezoelectric strain coefficients (also called d_{33} and d_{31}) were measured using a Piezo-meter at 110HZ. The electrically induced displacement was measured by KEYENCE LG-10 interferometer. The dielectric impedance, capacitance, resistance, conductance, phase angle and dielectric loss (tanδ) were measured as a function of frequency, where the frequency was from 2 KHz to 20 MHz. Aluminum tape was used as the electrode on the top of the sample and stainless steel was used as the bottom electrode. The dielectric constant, conductivity and resistivity are calculated from the measured parameters, such as capacitance, conductance, resistance and the geometry of the samples. The surface morphology and particle distribution were

investigated with the aid of Zeiss Sigma Emission Scanning Electron Microscope (SEM) and Energy Dispersive X-Ray Spectroscopy (EDS) methods. The thermal gradients, conduction, convection and radiation of heat transfer is be considered here to see how the temperature affect the piezoelectric and dielectric properties of the samples.

1.4 Research Motivations and Applications

Piezoelectric ceramics are widely employed as sensors and actuators because of their ideal electromechanical properties. Homogenous ceramic piezoelectric actuators are typically simple in structure and design (disks, rings, plates and cylinders)[14]. A piezoelectric/electrostrictive sensor converts a mechanical variable, such as displacement or force) into a measurable electrical quantity by means of piezoelectric/electrostrictive effect. These smart materials are used in many fields. For example, piezoelectric and dielectric sensors/actuators were embedded in a technological demonstrator for space structures. The sensors and actuators were embedded with a sensing/actuating pack, i.e. robust and easy to handle sensor/actuator unit, in the demonstrator structure[4]. Piezoelectric ceramic-polymer composites have been conceptualized, prototyped, fabricated, and implemented in applications encompassing medical imaging and military missions and so on[6]. Piezoelectric composites are also commonly used in transducers to improve acoustic, mechanical and electrical performance of piezoelectric devices. Functional composite transducers for sensors and actuators generally consist of an active ceramic phase incorporated with a passive polymer phase. Some of the polymer-piezoelectric ceramic composite

transducers were designed for sensing hydrostatic waves[7]. Some researchers used the piezoelectric fiber composite transducers to evaluate them as an effective embedded sensor inside the composite structures to monitor the stress/strain concentration levels at the critical location. For example, to detect all loading conditions acting on to the structure, to predict the occurrence of damage while in-service under dynamic loads, and to monitor the pre-existing damages in the composite structures so that the severity can be ascertained to avoid eventual catastrophic or brittle failures[8]. High-temperature ultrasonic transducer were used for high-temperature non-destructive testing (NDT), and well logging for oil, gas and geothermal industries. The epoxy filler was modified with glass spheres in order to improve the thermal reliability of the composites at elevated temperatures[5]. In this study, three different types of composite samples were fabricated by the formal Ph.D. students in our lab. These composites can be used as sensors and actuators in structures in civil engineering.

In previous work (reference work of Udhay Sundar and Wanlin Du) performed in the HESML, it was observed that the cross-section of the thin film composites contains three part. The bottom part is stainless steel substrate. Above the substrate, there is layer consists of epoxy polymer without ceramics. At the top part of the composites, PZT ceramics and epoxy polymer are bonded together, they are mixed with each other. As from the SEM images, it was found that the ceramic particles were not uniformly distributed inside the composites. Such phenomenon makes us curious about what makes this happen. It is possible that the different temperature gradient inside the composite leads to this phenomenon. This is because the temperature at the bottom side

of the composite is higher than the temperature at the top side of the composites at the beginning of the curing process, which will make the crosslinking rate of the epoxy at the bottom part faster than the crosslinking rate of epoxy at the top part of the composites. It might be the force of the bond of the crosslinking of the epoxy will push the ceramic particles to the top side of the composites. The motivation for this study is to find out the factors which lead to this phenomenon. The way to do this is to build the simulation models to get the simulation data of the mechanical properties and piezoelectric and dielectric properties of the composites of three different types of samples under the curing temperature at 75C so as to compare the simulation data with the experimental data to see if the experimental work did before is good or not. If the simulation work is approximately matched with the experimental work. Then, it means that the samples made in our group can be applied as sensors and actuators in civil engineering or some other industry fields.

1.5 Overview of the organization of the thesis

The chapters in this thesis are organized as follows: In Chapter 1, the background, research goals and some hypotheses are introduced, as well as the research materials used and some methodology; In Chapter 2, basic concepts for dielectric, piezoelectric and ferroelectric materials will be introduced, in addition to connectivity patterns of composites. In Chapter 3, the literature review of PZT-epoxy composites with both two-phase bulk and thin films will be provided. And, the experimental procedures for fabrication of the samples and analyses will be provided. In Chapter 4,5 and 6, the

results of the studies will be presented, including the results of analytical models and

simulation models. In Chapter 7, the conclusions of this work and the future work will

be provided.

Chapter 2

Definitions, Fundamental Concepts and Literature Review

In this chapter, the definition and history of dielectric, piezoelectric and ferroelectric materials will be introduced in Sections 2.1- 2.7. Polarization processes are introduced in Section 2.8. Also, the definition and description of epoxy materials and connectivity of composite piezoelectric materials are introduced in Section 2.10- 2.11. Heat transfer topics pertaining to the analysis of the devices and materials are described in Section 2.12, along with the literature review of composite piezoelectric materials and the research hypotheses are given at the end of this chapter in Section 2.13.

2.1 Dielectric Materials

Dielectric materials are a type of electrical insulator that inherently possess or may be processed to exhibit an electric dipole structure[14], where the positive and negative charged particles can be separated on a molecular or atomic level when an external electric field is applied. In this scenario, the positive charges are attracted to the surface with lower electric potential while the negative charges go to the opposite surface which has higher electric potential. In certain types of amorphous materials, the dipoles of dielectric materials are randomly distributed in the material without an external electric

field except some types of single crystalline structures. By applying an external electric field, the electric charges will accumulate on the surfaces of the dielectric materials so that the dipoles be in the alignment direction of the applied electric field. Figure 2.1 will show this phenomenon.

(A)   **(B)**
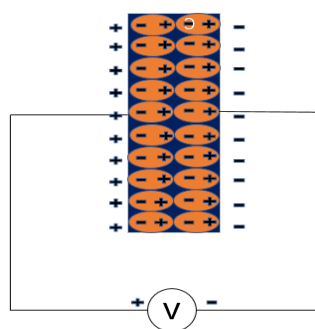
Figure 2. 1. (A) The dipoles are randomly oriented in the dielectric material in the natural state. (B) All the dipoles aligned in the same direction under the influence of an external electric field.

Dielectric materials can be divided into two groups, polar and non-polar dielectrics[14]. Polar dielectric materials are those materials comprising two or more atoms that have separated positive and negative charge centers. Two examples of these are chlorine hydride (HCl) and water (H_2O). In the natural state, the dipoles are randomly distributed in the material. The total polarization of the material is equal to zero even though these materials have permanent dipole moments. Dipoles in this type of dielectric material can be reoriented into a specific direction by applying an external electric field. Non-polar dielectric materials are those materials that only have one type of atoms or they have coincidental positive and negative charge centers. In this case, there is no permanent dipole moment in these materials, i.e. H_2 and O_2. However,

dipole moments may be induced in this group of dielectrics also by applying an external electric field. Figure 2.2 depicts the polar and non-polar atomic structures of dielectric materials, H_2O and H_2.
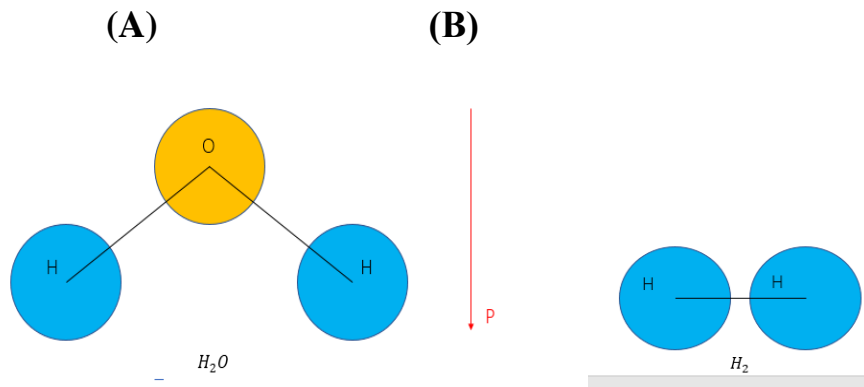
Figure 2. 2. (A) Example of polar dielectric material, centers of positive and negative are separated, permanent dipole moment possessed. (B) Example for non-polar dielectric material, no negative charge center exists and no permanent dipole moment possessed.

2.2 Polarization

Polarization is the process of dipole formation, or alignment of already existing permanent or induced dipoles under the influence of an electric field. This property is important because only dielectrics that are a type of electric insulator can be polarization by an external electric field. Polarization describes the density of permanent or induced electric dipole moments in dielectric materials. These dipole moments are expressed as vectors which point to the direction of the alignment of the dipoles in the materials. Polarization is the summation of dipole moments per unit volume of the materials. Figure 2.3 shows a dipole pair that possess a permanent dipole moment[20].
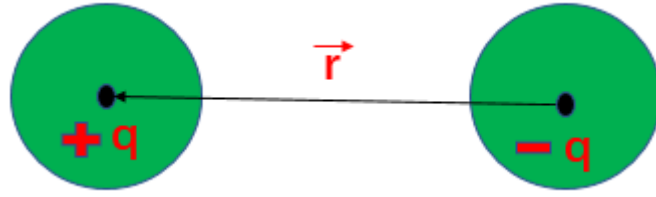
Figure 2. 3. An example shown the dipole pair which consist of both positive and negative charge centers with the displacement r, which exhibit a permanent dipole moment.

The dipole moment of a single dipole pair in shown in Figure 2.3. The dipole moment can be calculated by vector equation 2.1:

$$\vec{p} = q.\vec{r}, \qquad (2.1)[20]$$

where $\vec{p}$ is the dipole moment and $\vec{r}$ is the distance between positive and negative charge centers, and q is the electric charges, the total polarization can be calculated by equation 2.2:

$$\vec{P} = \frac{\sum \vec{p_i}}{V}, \qquad (2.2) [20]$$

where $\vec{P}$ is the polarization of the dielectric materials, $\vec{p_i}$ is dipole moment of the ith pair of charges per unit volume V.

There are four types of polarization: electronic, ionic, dipolar and orientation. Dielectric materials exhibit one or more of these forms. In addition, dielectric materials can exhibit interface and space, which is the fourth type of polarization. The first type of polarization is electric polarization. Electronic polarization occurs when the electrons displace relative to their nuclei when an external electric field is applied. When this occurs, the center of the electron clouds displace in the direction of lower electric potential and a dipole moment is induced. Figure 2.4 shows two examples of electronic polarization.
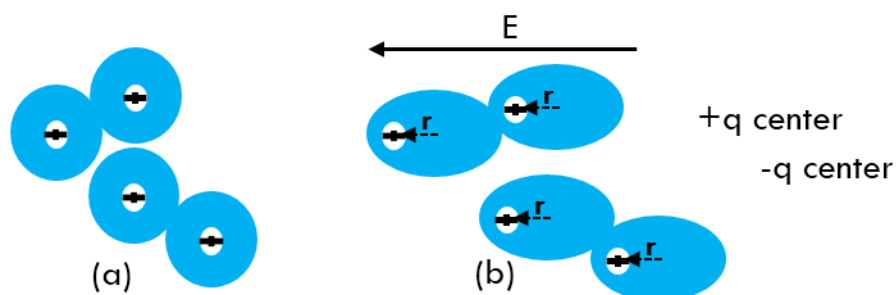
Figure 2. 4. H_2 is an example of electronic polarization. (a) has a positive charge nucleus surrounded by negative electron cloud. (b) The external electric field E induce the dipole moment.

The second type of polarization is ionic polarization. This form of polarization occurs when an external electric field is applied and the positive and negative centers of the molecules are reoriented. Figure 2.5 shows an example of common salt for ionic polarization.
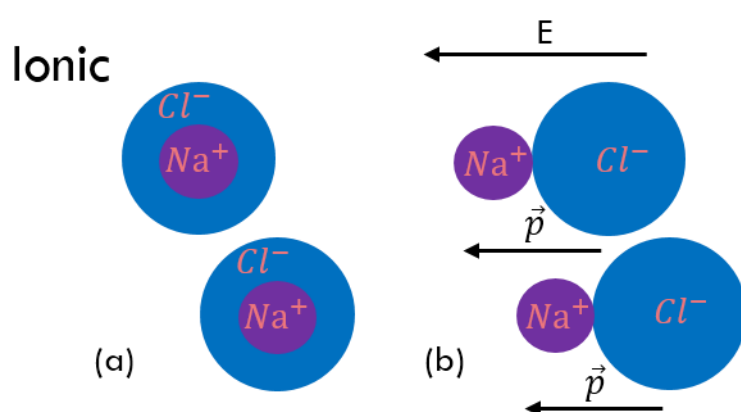
Figure 2. 5. Represents the ionic polarization mechanism.

The third type of polarization is orientation polarization. This occurs when the molecules themselves possess a permanent dipole moment. When an external electric field is applied, the molecules will be re-oriented and the permanent dipole moment will be aligned to the opposite direction of the external electric field. Figure 2.7 gives

an example for orientation polarization.
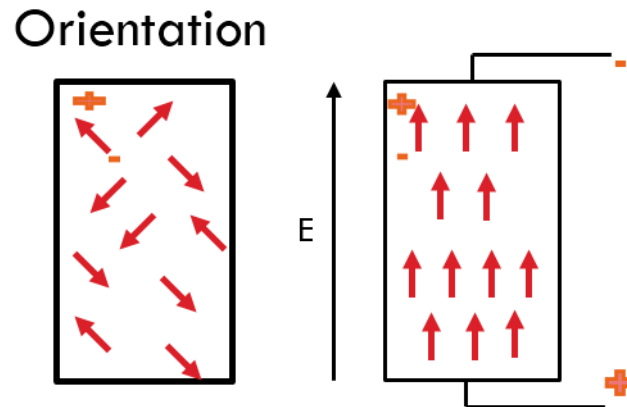
Figure 2. 6. Represents the orientation polarization.

The last type of polarization is space charge polarization. This type of polarization involves the limited movement of charges resulting in the alignment of charge dipoles under an applied electric field. This usually happens at the grain boundaries or any other interface such as an electrode-material interface. It happens when charges are accumulated at an interface between two different types of materials or two regions within a material when under an external electric filed. This type of polarization is different from previous three types of polarization mentioned before because it not only affects the positive and negative charges, but also affects the free charges as well. This is important to not because free charges are bunded by molecular forces, an external electric field that is applied to a dielectric material causes a displacement of bound charged elements. Figure 2.7 shows an example for space charge polarization.

Space charge
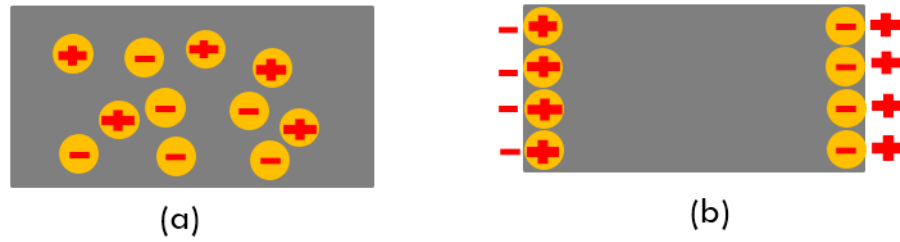
Figure 2. 7. Represents the space charge mechanism. (a) ions are mixed together in the normal state. (b) ions travel large distance to the surface of the material when apply an external electric field.

Dielectric materials can store energy through the polarization process. One way of quantifying a material's ability to store energy is through the measurement of its relative complex permittivity (ε_r), which is a dimensionless quantity. It can represent the effectiveness in storing energy of dielectric materials. The relative complex permittivity is compared to the complex permittivity of a material (ε_0) to the permittivity of the free space, where $\varepsilon_0 = 8.854 \times 10^{-12}$ Farads / meter (F/m). The relationship between the overall complex permittivity of the occupied space and relative permittivity is expressed in equation 2.3:

$$\varepsilon_r = \frac{\varepsilon}{\varepsilon_0} \qquad (2.3)$$

In equation 2.3 ε_r is relative complex permittivity, ε_0 is the dielectric constant of vacuum and ε is the overall complex permittivity of the occupied space, which is the measure capacitance that is encountered when forming an electric field in a particular medium. More specifically, permittivity describes the amount of charge needed to generate one unit of electric flux in a particular medium.

The relative complex permittivity describes the interaction of a dielectric material related to the applied electric field. It consists of two parts, real part ε_r' and imaginary

part ε_r'' .The real part of the permittivity at a constant frequency is called the dielectric

constant. The imaginary part of permittivity represents the dissipation and loss of a

material, which is called loss factor[21]. The relation of dissipation and dielectric loss

is shown in equation 2.5. Figure 2.8 shows the vector diagram of relative permittivity.

The real and imaginary components are 90° out of phase and the vector sum (ε_r) forms

an angle δ with the real axis $\varepsilon_r{}'$.
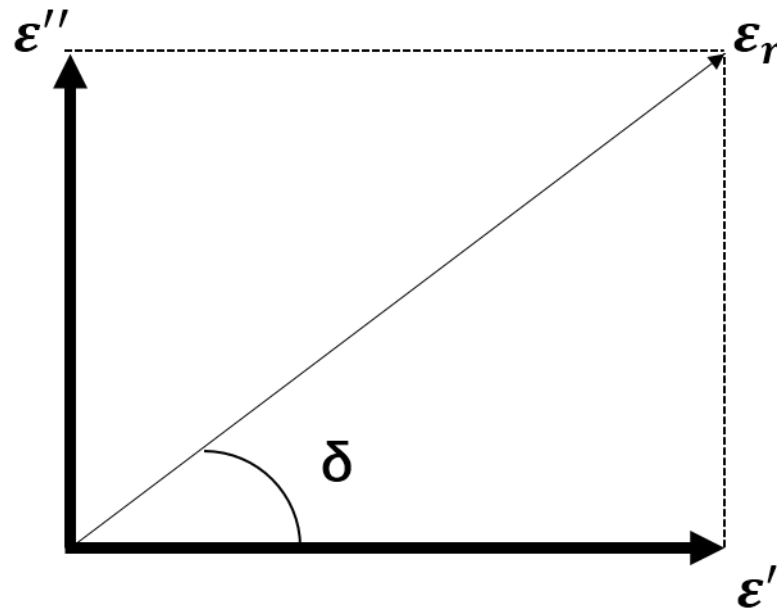
Figure 2. 8. Shows the vector diagram of relative permittivity. real part $\varepsilon_r{}'$ and imaginary part $\varepsilon_r{}''$ are 90° out of phase. The vector sum forms an angle δ with the real axis.

The dielectric loss, *tanδ*, represents the damping capacity of the material and it

represents the ability that the material can convert mechanical energy into electric and

heat energy when an external load or thermal load caused by thermal expansion is

applied. The dielectric loss is the tangent of the dielectric loss angle δ for the ceramic

materials[14]. It can be calculated by equation 2.4:

$$\tan\delta = \frac{\varepsilon_r{''}}{\varepsilon_r{'}}, \qquad (2.4)$$

where δ is the phase angle between stress and strain of a material, $\varepsilon_r{'}$ and $\varepsilon_r{''}$ can also be called as the elastic storage modulus and elastic loss modulus.

The dielectric constant indicates how effective the material behaves as a capacitor. However, the dielectric constant cannot be measured directly. Instead, the capacitance is measured and the dielectric constant is a function of the capacitance, and can be calculated by equation 2.5:

$$\varepsilon_r = \frac{Cd}{\varepsilon_0 A}, \qquad (2.5)$$

where C is the capacitance of the material, d is the thickness of the material, ε_0 is the dielectric constant of vacuum and A is the area of the material.

2.3 Piezoelectric Materials

Piezoelectric materials have the special property of producing an electrical voltage in response to an applied force. Piezoelectric materials have a variety of uses including sonar, sound detection and high-voltage generation in addition to everyday uses, such as cigarette lighter ignition sources and barbecue-grill igniters. They are a class of dielectric materials. They cannot only be polarized by external electric field but also by applying mechanical stress and/strain and thermal expansion. This means voltage will be generated when a mechanical stress or strain via mechanical or thermal loading is applied. Due to the natural non-centrosymmetric crystalline structure of piezoelectric materials, the distortion caused by mechanical stress will further separate the positive and negative charges centers. Figure 2.9 shows quartz as an example for this

phenomenon.
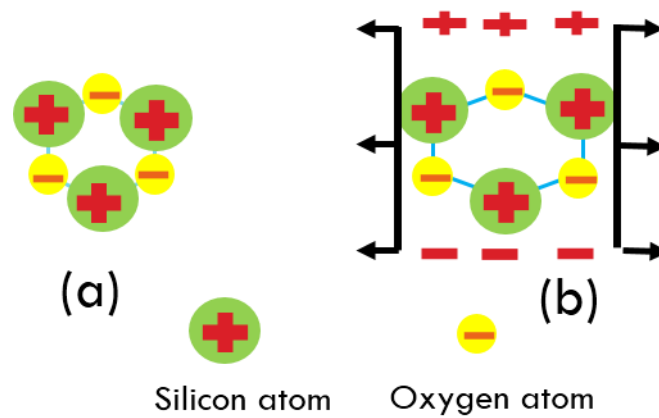
Figure 2. 9. Represents the piezoelectric effect in quartz. (a) shows the non-centrosymmetric of positive charges and negative charges in normal state. (b) generate voltage when apply tension on the material

2.4 Piezoelectricity

Materials demonstrating the piezoelectric effect also show the opposite effect called converse piezoelectric effect. This means a piezoelectric material becomes deformed, as if undergoing stress, when being exposed to an electrical field. There are many types of materials that possess piezoelectricity, such as quartz, zincblende and tourmaline[22]. The piezoelectric effect and converse piezoelectric effect are shown in Figure 2.10. (a) The piezoelectric material after polarization. (b) and (c) represents direct piezoelectric effect, the material generate voltage when applied the tension and compression because of the deformation of the material. (d) and (e) represent converse piezoelectric effect, when apply an external electric field on the polarized material, it will induce strains.
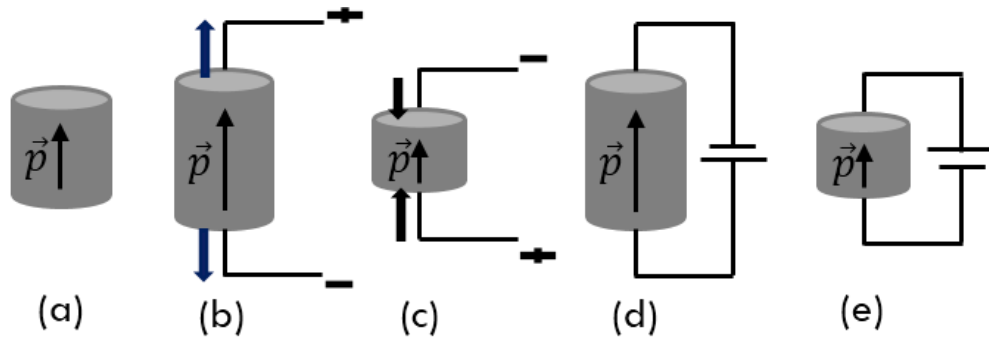
Figure 2. 10. Represents both piezoelectric effect and converse piezoelectric effect.

Figure 2.11 shows the piezoelectric effect by heat transfer under a certain temperature: The material properties such as Young's modulus increases with increasing the temperature in some materials, and the Curie temperature is very important for this process. If the temperature is below the curie temperature, the structure is deformed and it will generate voltage. To the contrary, if the temperature is above the Curie temperature, the structure will have a phase change so that some material properties will be changed. This phenomenon will be discussed in the Perovskite structure later in this chapter.
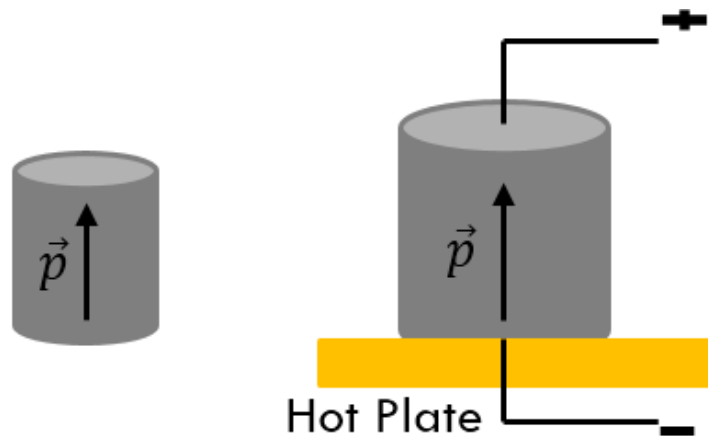
Figure 2. 11. Represents the polarization by heat transfer. (a) the piezoelectric material after polarization. (b) The material generates the voltage because of the deformation of the material caused by thermal expansion.

There are 7 crystal systems for piezoelectric materials. Among these systems, there are 32 point groups that have the possible combinations of symmetries[14]. 11 of them are centrosymmetric point groups, 21 of them are non-centrosymmetric groups[14]. For those 21 non-centrosymmetric groups, 20 of them are potentially piezoelectric. One special point group 432 is not piezoelectric because the dipole moments generated along axis (111) cancels each other, which make this point group similar to centrosymmetric group. Of those 20 potential piezoelectric materials, 10 of them are polar dielectrics, which possess a permanent dipole moment. Such materials have a spontaneous polarization. Thus, these materials are also pyroelectric. Non-centrosymmetric crystals of piezoelectric materials do not have a center for symmetry, which is a very important factor for representing piezoelectricity. This occurs because the application of mechanical stress on these crystals induces the displacement of positive and negative ions[23]. Figure 2.12 shows the classified crystal systems for piezoelectric materials:
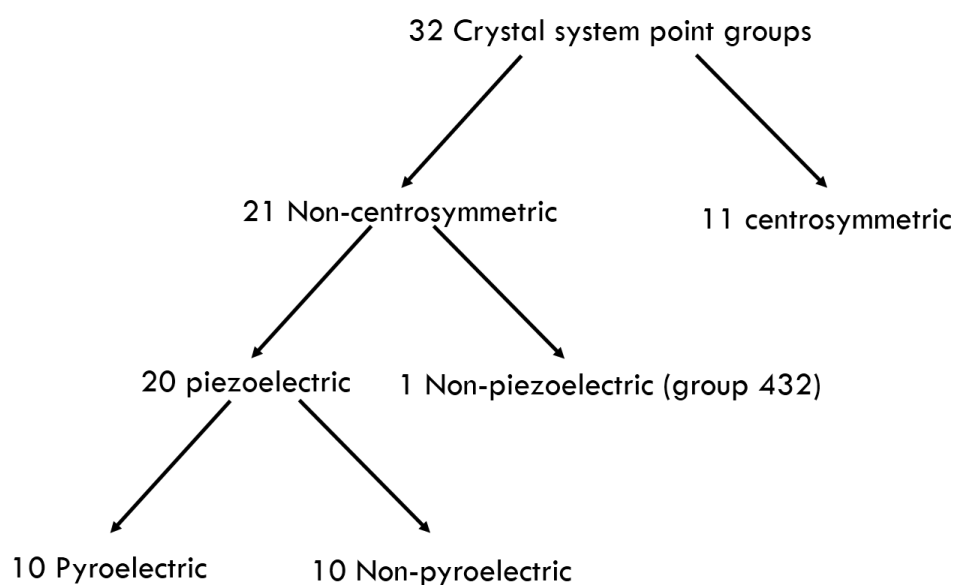
Figure 2. 12. Represents the classified crystal systems for piezoelectric materials.

The main variables that describe piezoelectricity are piezoelectric charge coefficients and piezoelectric strain coefficients that are related to the direct piezoelectric and converse piezoelectric effects. The direct piezoelectric effect states that voltage will be generated when a mechanical stress is applied. This phenomenon can be applied to use as sensors. While the converse piezoelectric effect occurs when strain is generated due to the application of an external voltage potential. This phenomenon can be used as actuators in industry[23].

The constitutive equations for the direct and converse piezoelectric effect of linear piezoelectric materials are given by equations 2.6 and 2.7:

$$D_k = d_{kij}.\delta_{ij} \text{(direct piezoelectric effect)} \quad (2.6)$$

and

$$S_{ij} = d_{kij}.E_k \text{(converse piezoelectric effect)} \quad (2.7)$$

where D_k is the applied electric displacement and E_k is the electric field, both, D_k and E_k are both first order tensors. δ_{ij} is the stress tensor and S_{ij} is the corresponding strain tensor. The relation for stress and strain is that stress is equal to product of Young's Modulus and strain. d_{kij} is piezoelectric charge coefficient tensor, which is a third order tensor, where i , j=1,2,3. This third order tensor has 3^3=27 elements in total. Due to the symmetric properties of stress and strain($\delta_{ij} = \delta_{ji}$, $S_{ij} = S_{ji}$), the total number of piezoelectric coefficients of d_{kij} reduce to 18[24].

Point 1 group has the lowest symmetry for all 32 points groups. The crystals in this

point group will not reduce further in the number of piezoelectric charge coefficients like other point groups who have more symmetry elements because of the triclinic crystal system, which only has 1fold of rotation. The expressions of the piezoelectric charge tensors for this point group are given in equations 2.8, 2.9, and 2.10:

$$d_{1jk} = \begin{matrix} d_{111} & d_{112} & d_{113} \\ d_{112} & d_{122} & d_{123} \\ d_{113} & d_{123} & d_{133} \end{matrix} \quad (2.8)$$

$$d_{2jk} = \begin{matrix} d_{211} & d_{212} & d_{213} \\ d_{212} & d_{222} & d_{223} \\ d_{213} & d_{223} & d_{233} \end{matrix} \quad (2.9)$$

$$d_{3jk} = \begin{matrix} d_{311} & d_{312} & d_{313} \\ d_{312} & d_{322} & d_{323} \\ d_{313} & d_{323} & d_{333} \end{matrix} \quad (2.10)$$

From the equations above, it can be seen that all three tensors are symmetric. So, the index can be rearranged for the last two index and rewrite the piezoelectric charge coefficient tensor. The rearranged indexes are given in Table 2.1:

Table 2. 1: rewrite the index for piezoelectric charge coefficient tensor in a simple way.

11	1
22	2
33	3
23/32	4
13/31	5
12/21	6

The piezoelectric charge tensor can be rewritten as:

$$d = \begin{matrix} d_{11} & d_{12} & d_{13} & d_{14} & d_{15} & d_{16} \\ d_{21} & d_{22} & d_{23} & d_{24} & d_{25} & d_{26} \\ d_{31} & d_{32} & d_{33} & d_{34} & d_{35} & d_{36} \end{matrix} \quad (2.11)$$

Since the crystal structures are centrosymmetric, if multiply a transformation

matrix $\begin{pmatrix} -1 & 0 & 0 \\ 0 & -1 & 0 \\ 0 & 0 & -1 \end{pmatrix}$ on the left of equation 2.11, the piezoelectric charge tensor will

be -d. And according to Neumann's Principle, d should equal to $-d$. Thus, all elements

in tensor will be cancelled with each other, which means non-centrosymmetric is

necessary for piezoelectricity. For other point groups of piezoelectric materials, they

possess more symmetry, which will reduce the remaining piezoelectric charge

coefficient elements in the tensors. Among these coefficient elements, d_{31} and d_{33} are

commonly measured. The piezoelectric strain coefficient d_{31} and d_{33} indicate the

polarization in the perpendicular direction in Z-direction and the strain are developed

in the lateral direction, like in X-direction and Z-direction. The equations to calculate

d_{33} for both direct piezoelectric effect and converse piezoelectric effect are given as

follows:

$$D_3 = d_{33}.T_3 \qquad (2.12)$$

$$S_{33} = d_{33}.E_3 \qquad (2.13)$$

Piezoelectric materials have great ability to withstand large amounts of strain and

large strains can potentially lead to large mechanical energy, which can be converted to

electrical energy. Thus, in order to get more energy, it is necessary to choose effective

coupling mode. And -31 mode and -33 coupling mode are most commonly used mode

presently. This is the reason that d_{31} and d_{33} are common measured for piezoelectric

strain coefficient where the first index means the poling direction of the materials. The

second index means the direction of the applied force. In -31 mode, it means the applied

force is perpendicular to the poling direction and in -33 mode, it means the applied

force is with the same direction of the poling direction. The difference for -31 mode

and -33 mode is that -33 mode has a higher coupling coefficient and yields a higher

overall power output[25]. These two coupling modes are shown in Figure 2.13.
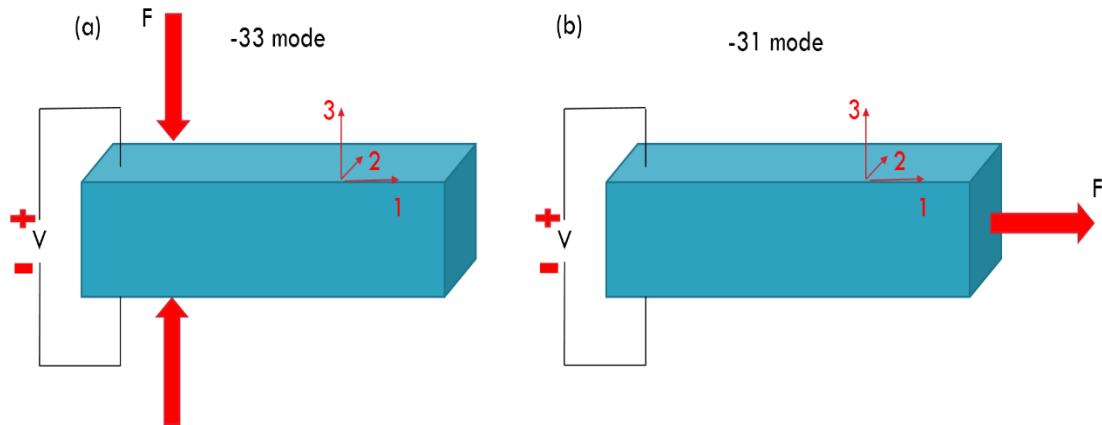
Figure 2. 13. Shows two coupling molds. (a) is -33 mode, the applied force is with the same direction of poling direction. (b) is -31 mode, which the applied force is perpendicular with the direction of poling direction.

2.5 Ferroelectric Materials

Ferroelectric materials are a class of dielectric materials, which can exhibit

spontaneous polarization. All ferroelectric materials are piezoelectric materials.

However, they are different from normal piezoelectric materials. All ferroelectric

materials with spontaneous polarization can be switched or reversed by applying an

electric field in the opposite direction, which is called ferroelectric switching.

Moreover, phase transition will affect the spontaneous polarization. As temperature

increases, the structure of ferroelectrics which have perovskite structure will

transform to a crystal cubic. If the temperature goes above the Curie temperature, the

structure will become a centrosymmetric cubic. In this case, ferroelectric materials

will lose their spontaneous polarization[23]. The Curie temperature is the temperature

at which ferroelectrics start to have a phase change. Beyond the Curie temperature,

ferroelectrics will not have spontaneous polarization. The non-polar phase

encountered above the Curie Temperature is known as the paraelectric phase. Below

the Curie temperature, they will possess spontaneous polarization.

The direction of the spontaneous polarization conforms to the crystal symmetry

of the material. While the reorientation of the spontaneous polarization is a result of

atomic displacements, the magnitude of the spontaneous polarization is greatest at

temperatures well below the Curie temperature and approaches zero as the Curie

temperature is neared[26].

The most important property for ferroelectric materials is that they exhibit

Polarization-Electric (P-E) hysteresis loops because they have reversible spontaneous

polarization. The P-E hysteresis loop is used to measure the polarization accumulated

versus the increasing strength of externally applied electric field. For common

dielectric materials except ferroelectric materials have a linear P-E hysteresis loop,

which is shown in Figure 2.14:
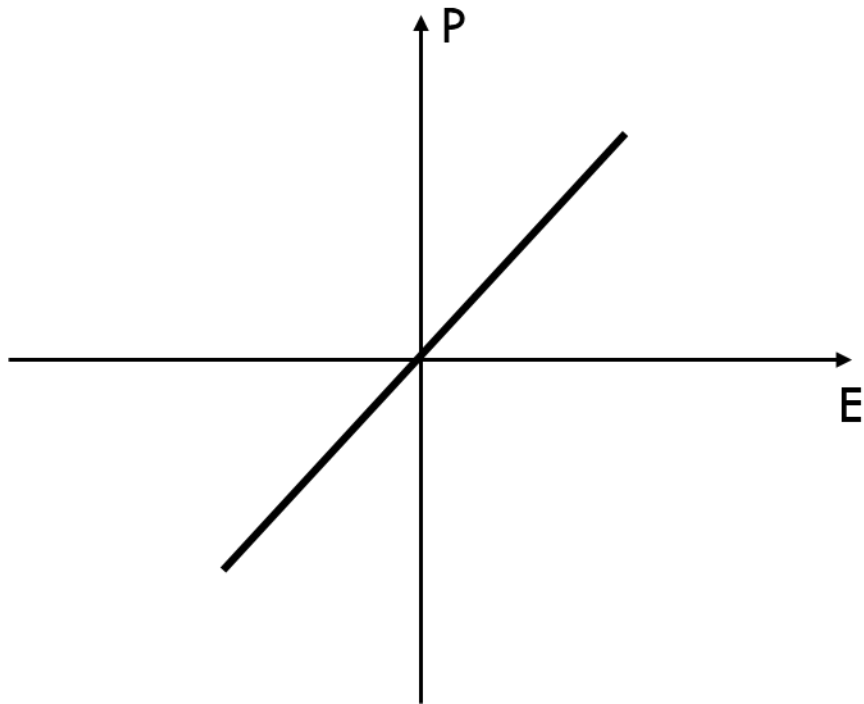
Figure 2. 14. Represents the linear P-E hysteresis loop for dielectric materials.

The P-E hysteresis loop for ferroelectric materials is illustrated in Figure 2.15.
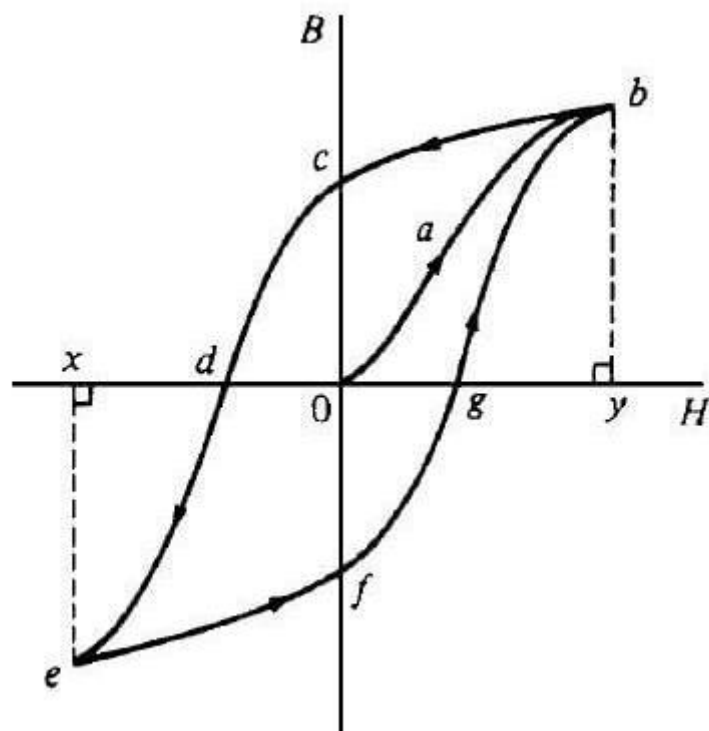
Figure 2. 15. Shows the P-E hysteresis loop for ferroelectric materials[26].

At point b, if the field intensity (H) is increased further, the flux density(B) will not increase any more. This is called saturation (the material is said to be saturated). In this figure b-y is called as saturation flux density. If the field intensity (H) is decreased, the flux density (B) will follow the curve b-c. When field intensity (H) is reduced to zero, which is called as remnant flux density or remanence. It is shown in the figure as o-c. If the H is increased in the opposite direction, the flux density decreases as well. It will decrease until the point d. Here the flux density (B) is zero. The magnetic field strength (points between 0 and d) required to remove the residual magnetism, i.e. reduce B to zero is called the coercive force. If H is increased further in the reverse direction, the flux density increases in the reverse direction until the saturation point (point-e) is reached. If H is varied backwards from 0x to 0y, the flux density(B) follows the curve e-f-g-b, similar to curve b-c-d-e. The flux density changes lag behind the changes in the magnetic field strength. This effect is called Hysteresis. The closed figure b-c-d-e-f-g-b is called the Hysteresis Loop (or the B/H Loop) [26].

2.6 Perovskite Structure

A Perovskite is any material with the same crystalline structure as calcium titanium oxide ($CaTiO_3$), with the oxygen in the edge centers[27]. It was first discovered in the Ural Mountains of Russia by Gustav Rose in 1839 and is named after Russian mineralogist L.A. Perovski. The general chemical formula for perovskite compounds is ABO_3, where 'A' and 'B' are two cations of very different sizes, and O is an anion that

bonds to both. The 'A' atoms are larger than the 'B' atoms. The ideal cubic structure has the B cation in 6-fold coordinate and is surrounded by an octahedron of anions and the A cation in 12-fold coordinated with respect to oxygen. The relative ion size requirements for stability of the cubic structure are quite stringent, so slight buckling and distortion can produce several lower-symmetry distorted versions, in which the coordination numbers of A cations, B cations or both are reduced.

Perovskite electro-ceramics are primarily used in bulk capacitors, piezoelectric transducers and are increasingly being used in thin film applications. The perovskite structure is adopted by many oxides that have the chemical formula ABO_3, depending on the size of A atom and B atoms. This is because there are many types of B atoms. This kind of structure could be tetragonal, orthorhombic, rhombohedral and cubic crystal systems. A perovskite structure will show high symmetry with increasing the temperature until reach a cubic shape, in which the temperature is beyond the Curie temperature. The most commonly used piezoelectric materials is Lead-zirconate titanate, $PbZr_{1-x}Ti_xO_3$ or PZT. This is because it boasts very high relative permittivity values and possesses strong piezoelectric coefficients[28-31]. PZT is formed by the solid solution of PbTiO3, which is anti-ferroelectric and PbZrO3, which shows limited piezoelectric characteristics. If take PZT as an example, figure 2.16 is the perovskite structure of PZT. The blue atoms will be Pb^{2+}, the red big atoms will be O^{2-} and the smallest black atom will be Zr^{4+}. From figure 2.16, it shows that the structure is centrosymmetric when the temperature is above the Curie temperature and non-centrosymmetric when the temperature is below the Curie temperature. This is because

when the temperature is above the Curie temperature, the materials have a phase change that the positive and negative charge centers are in coincidence, which does not possess permanent dipole moment. However, when the temperature is below the Curie temperature, the increasing temperature will lead to further distortion of the structure that further separate the positive and negative charge centers, which make the materials have the spontaneous polarization and possess a permanent dipole moment. In Figure 2.17 a phase change diagram of PZT during the change of the temperature is depicted. When the temperature is above the curie temperature, the structure is cubic, but the structure is non-centrosymmetric when the temperature is below the curie temperature.
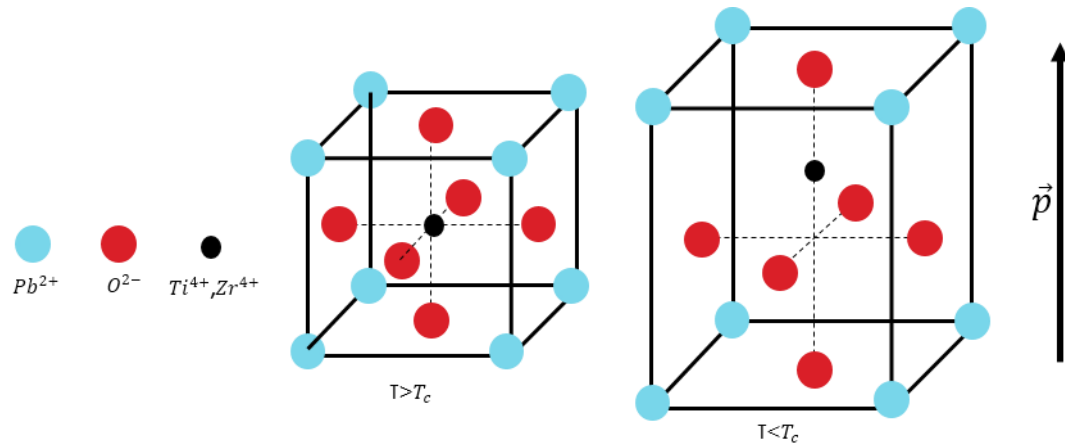
Figure 2. 16. Represents the perovskite structures of PZT for both temperatures above the Curie temperature and below the curie temperature.
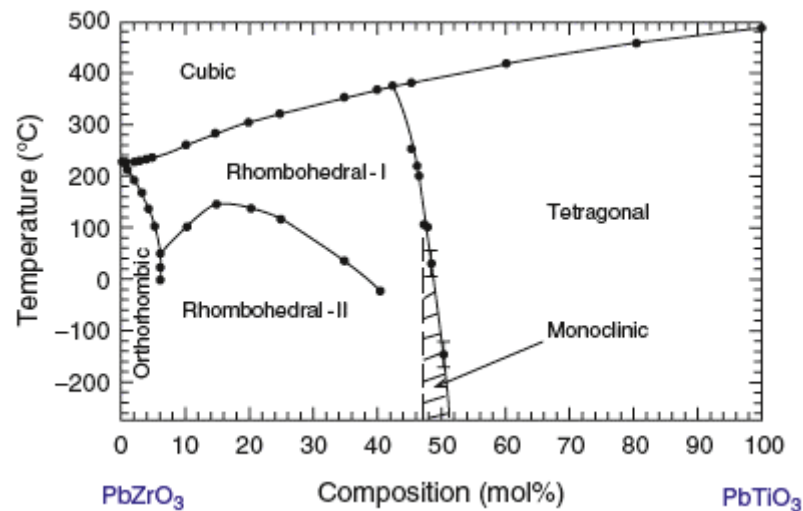
Figure 2. 17. Shows the phase change of PZT material during the temperature change[32, 33].

From figure 2.17, it shows that PZT possesses a rhombohedral structure at high temperatures, but it takes up a tetragonal structure once it begins to cool below the Curie temperature. A Venn diagram that summarizes the interrelationship between these materials is provided in Figure 2.18.
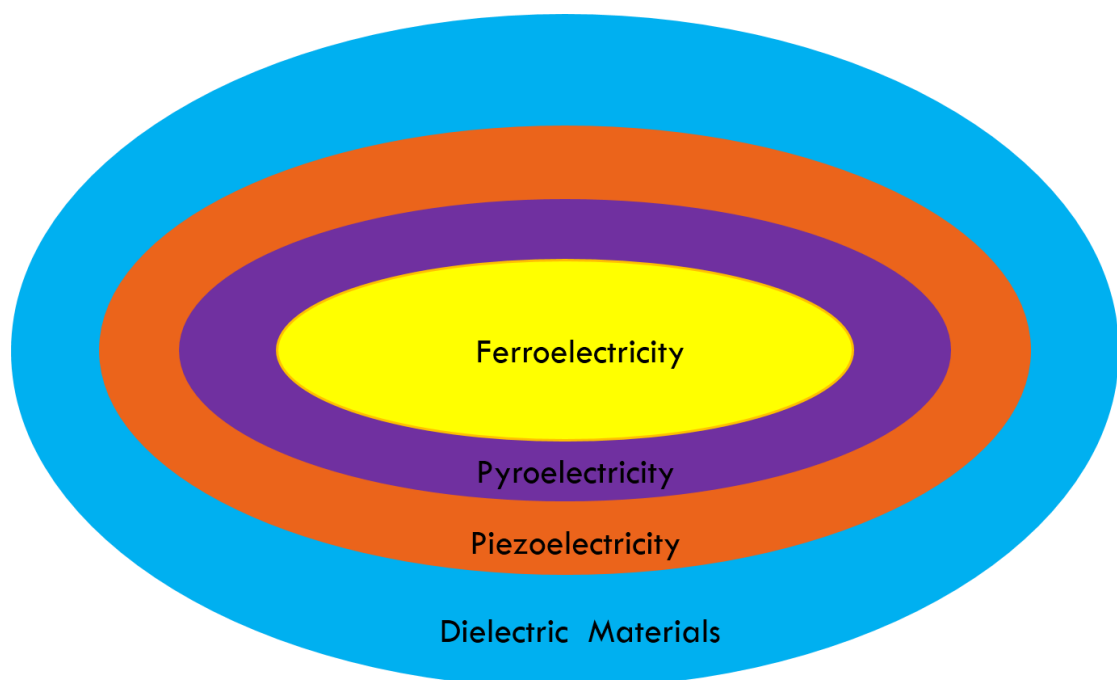
Figure 2. 18. Shows the Venn diagram to describe the interrelationship between these materials.

From Figure 2.18, it shows that all ferroelectric materials are pyroelectric materials and all pyroelectric materials are piezoelectric materials and all piezoelectric materials are dielectric materials.

2.7 History of dielectric, piezoelectric and ferroelectric materials

Traditionally dielectric materials are made from inorganic substances, e.g. mica and silicon dioxide. However, polymers are gaining wider use as dielectric materials. This is due to the easier processing, flexibility of these materials. Also, it is easier to these types of materials for specific uses. These materials in some cases can provide better resistance to chemical attack. As early as mid-60's polymers, e.g. polyvinyl fluoride and aromatic-containing polymers were used as dielectric materials in capacitors. Further improvement in organic film fabrication was established as revealed in US Patent 4153925. P[34].

Ferroelectric ceramics were born in the early 1940s with the discovery of the phenomenon of ferroelectricity as the source of the unusually high dielectric constant in ceramic barium titanate capacitors. Materials based on two compositional systems, barium titanate and lead zirconate titanate, have dominated the field throughout their history. The more recent developments in the field of ferroelectric ceramics, such as medical ultrasonic composites, high-displacement piezoelectric actuators (Moonies, RAINBOWS), photostrictors, and thin and thick films for piezoelectric and integrated-circuit applications have served to keep the industry young amidst its growing

maturity.[23]

2.8 Polarization process

Polarization is a process used to align the domains within a grain by applying an external electric field. It is first discovered by Gray *et al*[20]. It is a very important process because it provides a mechanism for the conversion of inert ceramics into electromechanically active materials[35]. In composite materials, poling takes place under the material's glass transition temperature, by gradually heating it and placing it in a strong static external electric field[36, 37]. The poling temperature and the strength of the applied external electric field will greatly affect the electromechanical properties of the poled materials.

There are two types of polarization method: contact polarization and corona polarization. The contact poling method are suitable for most multiphasic composites. The charge from the corona point is sprayed onto the surface of a material that does not possess an electrode, therefore, creating an electric field between the sample surfaces. In order to uniformly heat the samples, this type of poling process was carried out in the silicon bath oil. The reason researchers use silicon oil is because it was often used for the preparation of oil baths having a temperature in the range of -50C to +200C. In addition, it can protect carbon steel alloyed samples. Despite that this poling method has some advantages, it has some disadvantages. During the fabrication, deficient points and voids would commonly occur on samples, when poled by conventional contact poling. Once the charges find one pathway to go

through, not only the electric field over that deficient point will be lost but the whole electric field vanishes. Thus, the sample will not be properly poled, this is called dielectric breakdown in poling process. In order to overcome the disadvantages of contact poling method, researcher often employ the corona poling method. This type of poling method is non-contact to the samples. It applies a high poling voltage to the air molecules above the samples. In this type of poling method, researchers found that it can achieve much higher poling voltages than the contact poling method.

2.8.1 Contact poling method

Contact poling method as mentioned before is suitable for piezoelectric ceramic composites. It is poled by applying a large voltage. The samples are sandwiched between the two metal electrodes and the metal electrodes are connected to a high external electric field. The electrodes are in direct contact with the samples and the whole set up are put into heated silicon bath oil under a certain temperature. Figure 2.19 shows the diagram of contact poling process.
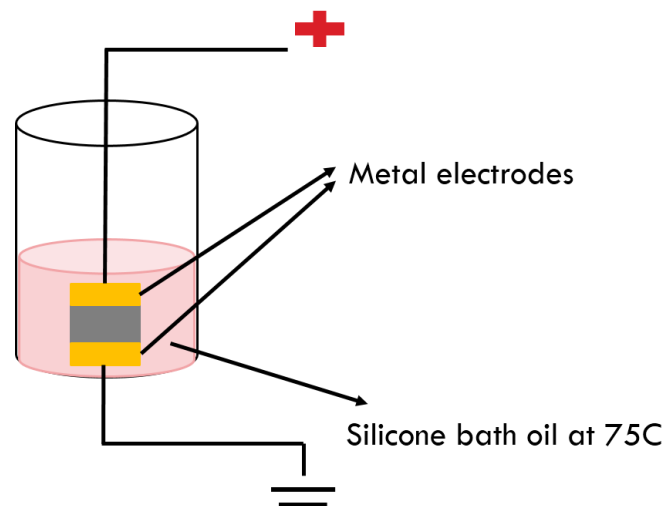
Figure 2. 19. Represents the process for contact poling method. Samples are uniformly heated in silicone bath oil and they are directly contacted with two metal electrodes with both top and bottom surfaces.

2.8.2 Corona poling

For the corona poling method, charges come from the corona point /needles. Samples are heated on a hot plate with a certain temperature. Only the bottom surface is in contact with the ground. The corona needle is connected with a high voltage. The charges from the corona needle ionize the surrounding air and the ionized air creates an external electric field between the corona needle and the top surface of the samples, which aligns the dipoles in the samples. In corona poling method, there are several advantages. For example, it can achieve much higher poling voltage than contact poling method. This is because the deficient points where charges could leak through, will not affect the overall electric field except the deficient point itself since the 'top electrodes' are ionized air. Figure 2.20 shows the process for corona poling.
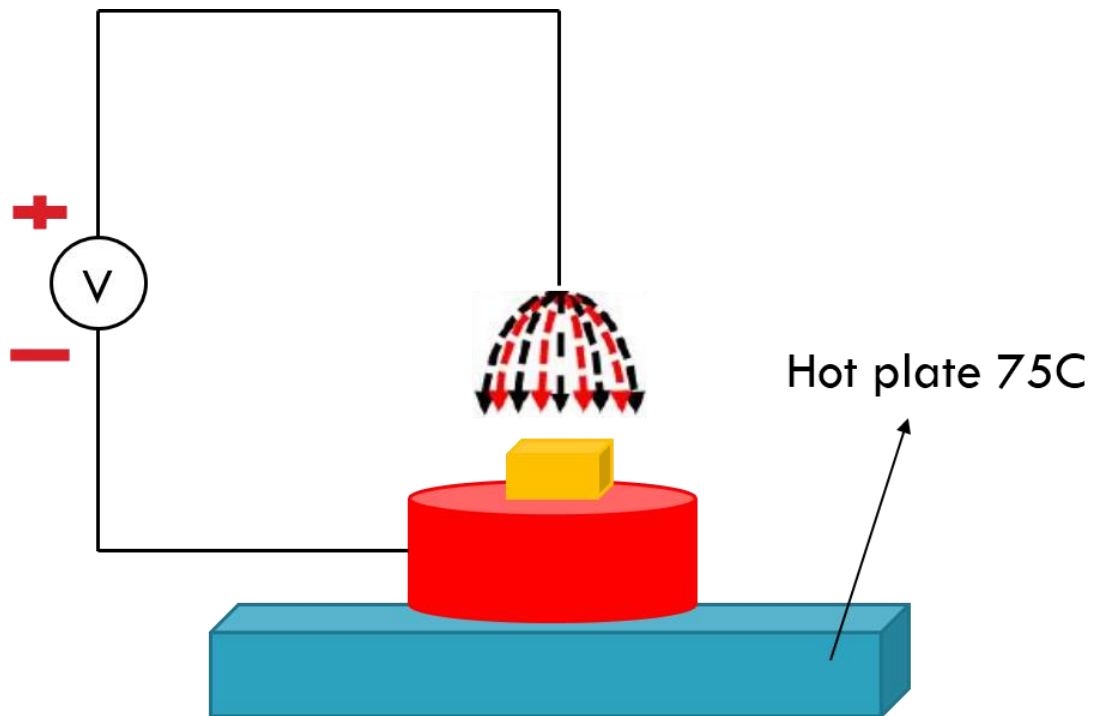
Figure 2. 20. Represents the corona poling process. Samples are put on a hot plate at a fixed temperature 75C. Charges are from the corona needle, which is connected to a high voltage and ionized the air. The ionized air will create an external electric field which will align the dipoles in the samples.

2.9 How will the piezoelectric materials behave with temperature

For the piezo actuator, below the Curie temperature, the temperature dependence of the remnant strain and the coercive field strength decide how will the temperature behave. Both the attainable displacement with electric operation and the dimensions of the piezoceramic element change depending on the temperature[38].
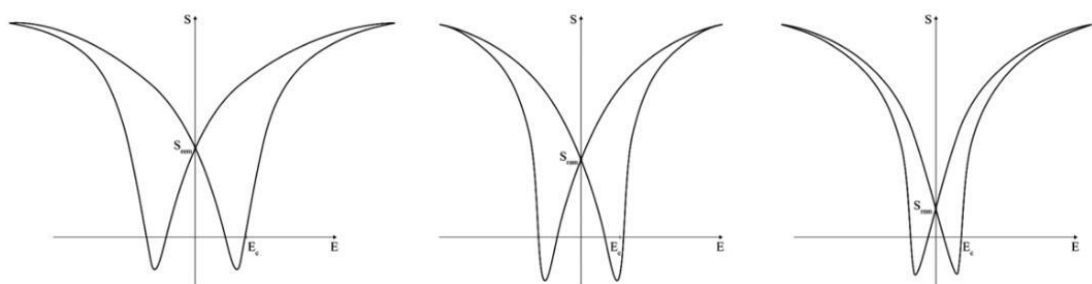
Figure 2. 21. Shows the bipolar electromechanical large-signal curve of piezo actuators at different

temperatures. From left: Behavior at low temperatures, at room temperature, at high temperatures[38]

Figure 2.21 shows the relationship of remnant strain S_{rem} and the coercive field strength, E_{rem}, with different temperatures. It shows that the cooler the piezo actuator, the greater the remnant strain S_{rem} and the coercive field strength E_{rem}. The curves become increasingly flatter with decreasing temperatures. This causes the strain induced by a unipolar control to become smaller and smaller even though the total amplitude of the bipolar strain curve hardly changes over wide temperature ranges. The lower the temperature, the greater the remnant strain. Hence, the piezo ceramic has a negative thermal expansion coefficient, i.e., the piezo ceramic becomes longer when it cools down. In comparison: a technical-ceramic-contracts with a relatively low thermal expansion coefficient upon cooling. This surprising effect is stronger, the more completely the piezo ceramic is polarized.
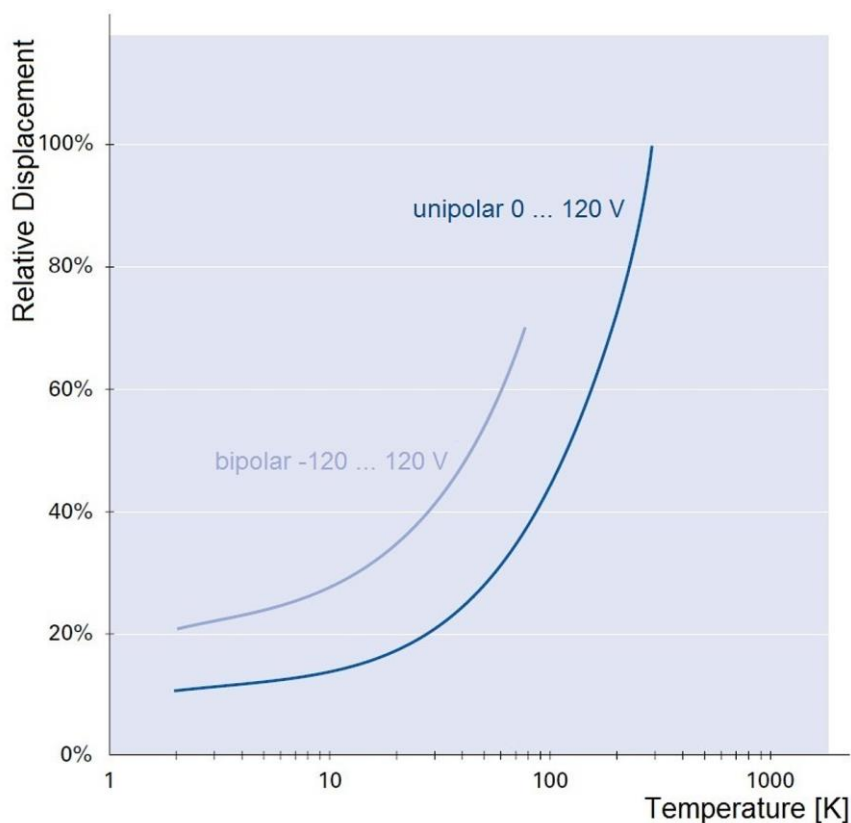
Figure 2. 22. Shows the displacement change with temperature using the example of a PICMA stack actuator in the cryogenic temperature range with different piezo voltages, in relation to nominal displacement at room temperature[38].

Highly Reliable Multilayer Piezo Actuators have a relatively high Curie temperature of 350 °C. From figure 2.22, it shows that, at high operating temperatures, their displacement only changes by a factor of 0.05 %/K. At cryogenic temperatures, the displacement decreases. When driven unipolarly in the liquid-helium temperature range, piezo actuators only achieve 10 to 15 % of the displacement at room temperature. Considerably higher displacement at lower temperatures can be achieved with a bipolar drive. Since the coercive field strength increases with cooling, it is possible to operate the actuator at higher voltages, even against its polarization direction.
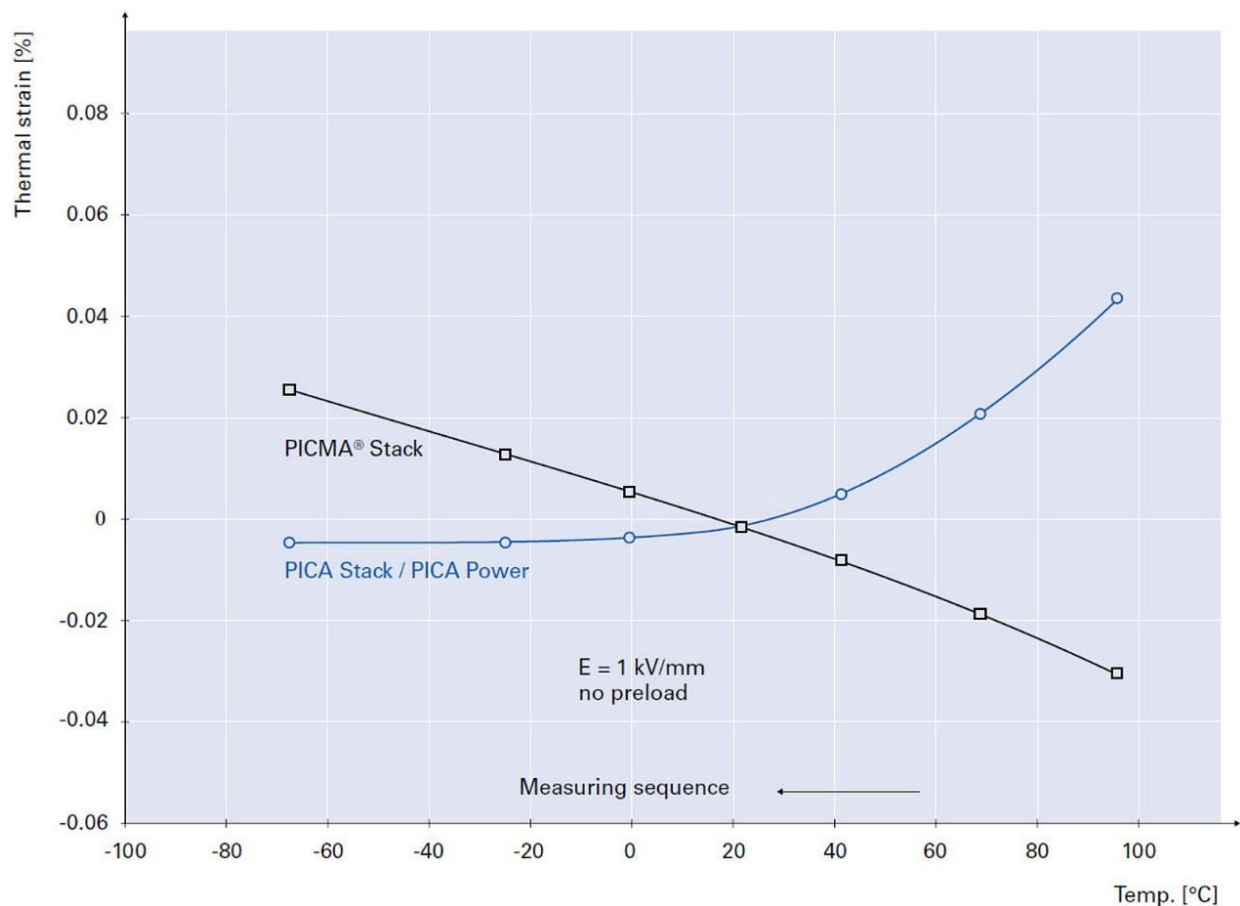
Figure 2. 23. Shows the temperature expansion behavior of PICMA and PICA actuators with electric large-signal control[38].

The temperature expansion coefficient of an all-ceramic Highly Reliable Multilayer Piezo Actuators is approximately -2.5 ppm/K. In contrast, the additional metal contact plates and the adhesive layers in a Preloaded High-Load Piezo Actuators lead to a nonlinear characteristic with a positive total coefficient. When a nano-positioning system is operated in a closed servo loop, it will eliminate the temperature drift in addition to nonlinearity, hysteresis, and creep. If the controlled reserve is kept for this purpose, it will reduce the usable displacement. In this case, the temperature drift is often passively compensated for by selecting suitable involved materials, the actuator types, and the system design. For instance, all-ceramic Highly Reliable Multilayer Piezo bender actuators

show only a minimal temperature drift in the displacement direction because of their symmetrical structure[38].

2.10 Epoxy Materials

2.10.1 Thermoplastic and thermoset materials

Thermoplastic and thermoset are terms used when characterizing polymers depending on their behavior when subjected to heat, hence the prefix, 'thermo'. Polymers are large molecules made of repeating subunits, and these subunits are called monomers[39, 40]. Thermoplastic polymers are also called "Thermo-softening Plastics". This type of polymers can be melted under the high temperature and cooled to gain back to solid form when it is cool down. This type of polymer has high molecular weight and the polymer chains are associated together and subject to intermolecular forces. However, the intermolecular forces are very easy to be broken when energy is supplied. This is the reason why thermoplastic polymers will melt under a certain heat. When enough heat energy is supplied to get rid of the intermolecular forces that hold the polymer as a solid, it will melt. When it is being cooled, the polymer gives off heat and re-forms the intermolecular forces making it a solid. Therefore, the process is reversible. This type of polymers can be modeled into different shapes. Thermoplastics also possess a characteristic feature by showing different physical properties between the melting point and the temperature where solid crystals are formed. It is observed that they possess a rubbery nature between those temperatures. Examples of thermoplastics are nylon, Teflon and polyethylene[39, 40].

Thermoset polymers are also called 'Thermosetting Plastics'. This type of polymers can endure high temperature without melting. This property will lead to hardening soft or viscous polymers through cross-links between polymer chains, such a process is active as chemical reaction. It is also referred to as 'curing' process and can be initiated by heat above 200˚C, UV radiation, high energy electron beams and additives[39, 40]. The cross-links are stable chemical bonds. Once the polymer is cross-liked, it gets a 3D structure which is very rigid and strong, that refuses to melt upon heating. Therefore, this process is irreversible converting the soft starting material into a thermally stable polymer network. The epoxy used in this study is one of this type of thermoset.

There are several differences between thermoplastics and thermosets. The main difference between the two is that a thermoset polymer doesn't melt upon heating and withstands high temperatures, whereas a thermoplastic-polymers melts beyond a certain temperature and thus have moldable properties and solidify upon cooling. Thermosets are more brittle in nature than thermoplastics. The second difference between these two polymers is that thermosets are usually much stronger than thermoplastics. This is because thermosets possess a 3D network of cross-linking bonds. The third difference is that thermosets have a permanent shape and cannot be recyclable into new forms of plastic, whereas thermoplastic can be melted into any shape and re-used.

2.10.2 Two-part of epoxy materials

There are many types of epoxy resin in nature, such as Bisphenol A epoxy resin, Bisphenol F epoxy resin, Novolac epoxy resin, Cycloaliphatic epoxy resin and Glycidylamine epoxy resin. Basically, there are generally three classes of epoxy: pure epoxy, polyester resins, and epoxy acrylates that can be categorized in terms of properties and performance[41]. Pure epoxy materials generally consist of two parts: a resin and a hardener. The curing process for pure epoxy is much slower than the other two classes epoxy. In this case, it offers less shrinkage, excellent adhesion, and high strength performance. However, with slow cure times, pure epoxy should not be specified for low-temperature applications (generally limited to a 4-C [40-F] minimum substrate temperature). But for the other two category epoxy, they can be specified for lower temperatures (down to as low as 2 C [35 F]) [41]. In this study, epoxy DGEBA was used for our samples. The reason the epoxy DGEBA was chosen is because this type of epoxy is widely for commercial used in industry. A lot of companies sell this type of epoxy, such as APC International Ltd, GLOBAL COMPOSITES PIEZOELECTRIC MATERIAL MARET, WEIFANG JUDE ELECTRONIC CO. LTD, IMASONIC Dynamic Structure & Materials, LLC,TRS Technologies and MSI TRANSDUCERS. It consists of two chemical groups, bis-phenol A group and epoxide group. During the kinetics of the curing process, the C-O bond of the epoxide group needs to be broken in order to form a reactive $-C\boldsymbol{H_2}$ site, capable to crosslink to the epoxy hardener molecule. This is called crosslinking process. Figure 2.24 represents the two parts of the epoxy DGEBA.

CH₃

CH_3

HO —〇— C —〇— OH

bis-phenol A CH_3

H_2C — CH_2Cl

epichlorohydrin
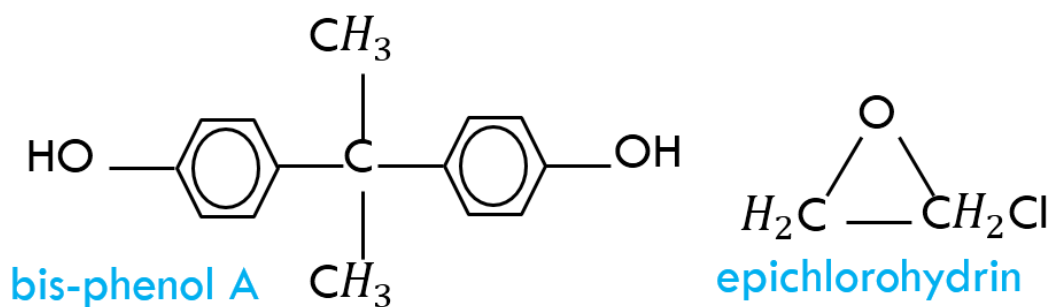
Figure 2. 24. Represents the two chemical parts of epoxy DGEBA. bis-phenol A group and epoxide group.

The curing process of epoxy DGEBA is usually mixed with curing agent. In this study, the curing agent is an epoxy hardener. The ratio of volume fraction of epoxy resin and epoxy hardener is 7.69. The curing process in under a certain temperature, which is at 75C. Figure 2.25 and 2.26 shows the curing process of epoxy 828 with DETA as the curing agent.
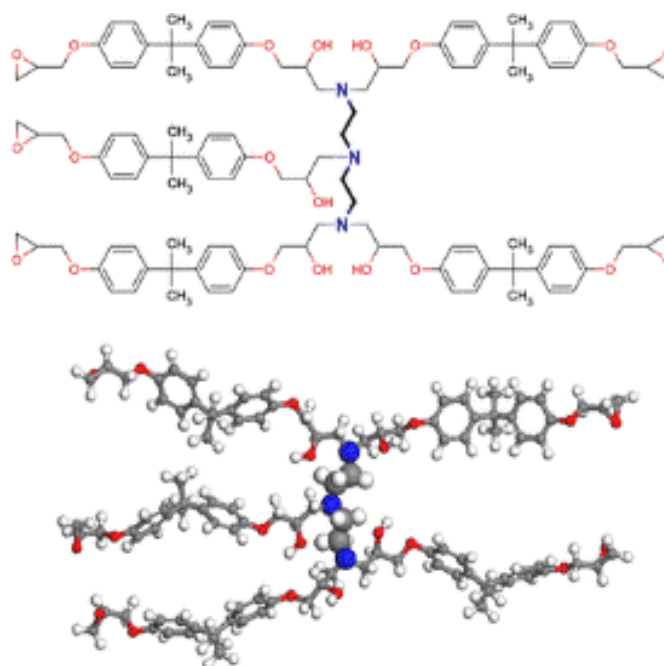
Figure 2. 25. Shows the schematic 2D (top) and 3D (bottom) representations of a fully cross-linked set of DETA and EPON 828 molecules[42].
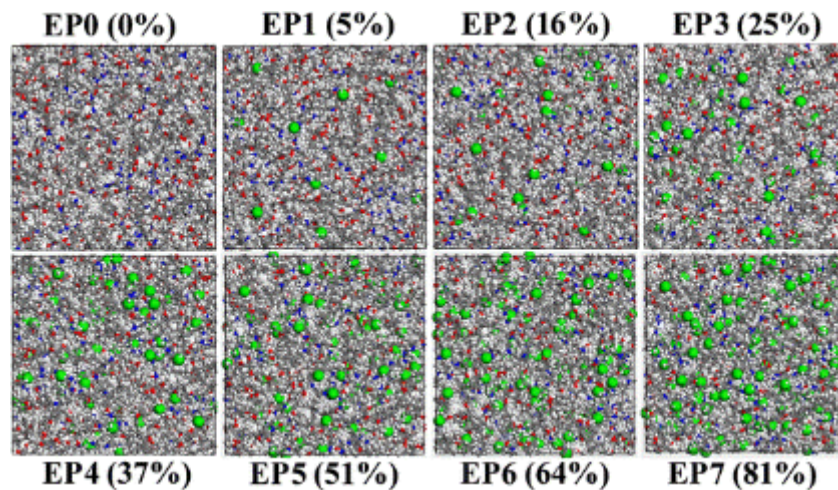
Figure 2. 26. Shows the snapshots of the simulated polymer at different cross-linking densities. The cross links are represented through the green-colored particles[42]

2.10.3 Material properties of epoxy DGEBA behave with temperature

In order to find out how will the material properties of epoxy DGEBA behave with the temperature, it needs to measure how will the mechanical properties, such as Young's Modulus, density, and thermal properties, such as thermal conductivity, heat capacity change during the curing process of epoxy. Epoxy resin may be reacted with itself or they may be cured with a wide range of co-reactants including polyfunctional amines, acids, phenols, alcohols and thiols (usually called mercaptans). These co-reactants are often referred to as hardeners or curatives, and the cross-linking reaction is commonly referred to as curing. Presently, researchers use different types of curing agent or curative mix with epoxy DGEBA to find out the curing process, such as DETA (diethylenetriamine), TETA (triethylenetetramine), DDS (diaminodiphenilsulfone) and DEA (diethanolamine) and so on. There are different approaches were used for the study, such as Multi-scale approach analytical method, like DSC (differential scanning calorimetry), DMTA (dynamic mechanical thermal

analysis), ss-NMR (solid-state NMR spectroscopy), PALS (positron annihilation

lifetime spectroscopy), which all these acronyms are the name of the instruments and

techniques to measure the material properties of epoxy during the curing process [3,

10, 11, 42, 43]. Such kinds of methods are used for find out the cross-linking rate of

epoxy with different curing time and temperature. For instance, researchers use

different curing time as 10 min,45min,90min,120min to find out the material

properties and cross-linking density rate with DGEBA/DDS[3]. They used 500ps for

equilibration step and 300ps for creation of covalent bonds step, 500ps for pos

equilibration and sampling step, and the temperature they used for pre-equilibration

step is 298K and the temperature for creation of covalent bonds step is 500K to find

out the material properties with change of cross-linking density and conversion rate of

curing process with DGEBA/DETA[44]. Another article used 30-350C at a heating

rate of 5,10,15 or 20C for dynamic curing reaction and at a heating rate of

200,210,220,230C for Isothermal curing to find out the activation energy with

DGEBA/MP[10]. Some researchers kept the temperature at 70C for 30min for

secondary amine hydrogen reacts quickly with the epoxide and they kept the same

temperature for 24h for the remaining epoxide reacts slowly(90%) with

DGEBA/DEA[43]. The material properties and cross-linking rate of epoxy DGEBA

depends on the curing temperature and curing time. Generally, the cross-linking

density is enhanced by increasing the curing temperature and curing time. The

material properties improved by increasing the cross-linking density. For example,

DSC shows cross-linking degree enhanced with the holding time. DMTA shows tanδ

increases with the increase of curing time. PALS (positron annihilation lifetime spectroscopy) is an important microanalytical probe for the direct measure the size of the free volume in polymers. It indicates no. of free volume of epoxy groups decreases when increasing the curing time[3]. Another article use EHBPES (epoxide-terminated hyperbranched polyether sulphone) as curing agent with epoxy DGEBA and it shows that Modulus (Young's Modulus and Shear Modulus) increase with the increasing EHBPES (curing agent) loading. Highest modulus achieved at 7wt% EHBPES loading, as well as crosslinking density and CED (cohesive energy density)[44]. Another article used MP (melamine phosphate) as curing agent and DSC technique to measure the activation energies during the curing process. It shows that the activation energies are 83.9 and 85.6 KJ/mol by two method and Isothermal-cure activation energy is 110.0 KJ/mol[10].

2.11 Composite piezoelectric materials

Piezoelectric ceramic materials have a lot of advantages and disadvantages. For example, piezoelectric ceramics have high electromechanical coupling coefficients (K), high piezoelectric strain coefficients d_{33} and very fast response times. However, they are dense, have high acoustic impedance and they are brittle in nature and difficult to machine. However, piezoelectric polymers have low acoustic impedance, are not brittle in nature, have good mechanical and thermal properties and outstanding adhesion to various substrates. Piezoelectric polymers have much lower piezoelectric coefficients and lower electromechanical coupling coefficient(K)in comparison to

their counterparts. Piezoelectric composites are of interest to researchers over the past

few decades. They consist of piezoelectric ceramics and polymer composites and are

called piezocomposites. These type of composites show great properties in

comparison to single-phase materials[45]. Piezocomposites combine high coupling,

low impedance, low mechanical quality factors and intermediate dielectric constants,

thereby proving to be excellent candidates for electromechanical transducers, in

addition to better flexibility[45]. The definition of composite is any material

consisting of two or more distinct phases[46]. The properties of the composites are

based on arrangement of the phases comprising the composites[6].

The connectivity of composites is the microstructural arrangement of the

individual components, which was first proposed by Skinner and Newnham[47, 48]

and later modified by Pilgrim[49]. The connectivity is based on how many directions

the material phase is self-connected. For example, if a composite has two-phase

materials and each phase material has two directions for self-connected, then this

composite is a 2-2 two-phase material. The connectivity is a critical parameter that

determines the electromechanical performance of the composite. As the piezoelectric

ceramic fillers are randomly distributed in polymer matrix, they are able to form many

types of connectivity of composites. For example, there are total 10 types of

connectivity for two-phase composites, such as (0-0), (0-1), (0-2), (0-3), (1-1), (1-2),

(2-2), (1-3), (2-3), and (3-3)[6]. In this representation, the first digit refers to the

dimension of the piezoelectric ceramic, also known as the active phase and the second

digit represents the dimension of the inactive phase. Figure 2.27 illustrates the types

of connectivity of two-phase composites. In this representation, the first digit refers to the dimension of the piezoelectric ceramic, also known as the active phase and the second digit represents the dimension of the polymer or inactive phase
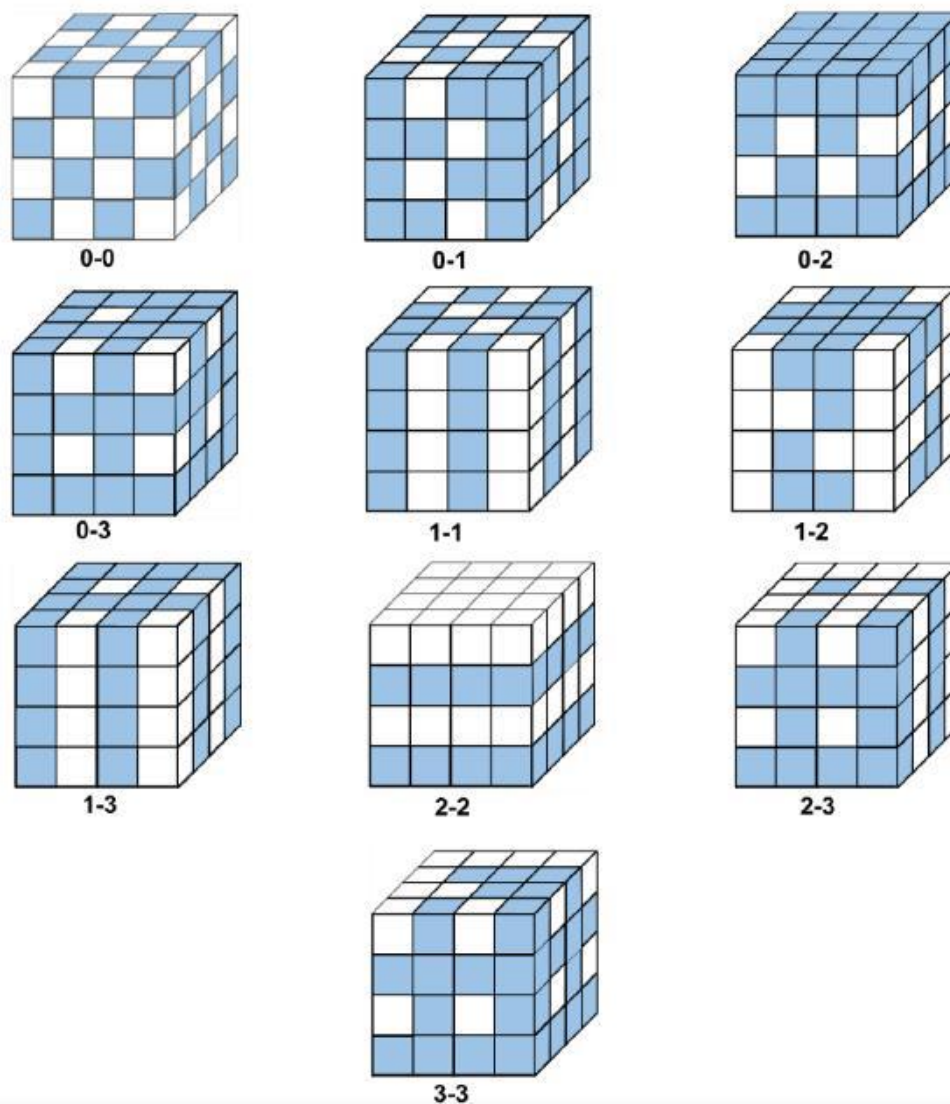
Figure 2. 27. Represents ten different connectivity patterns of diphasic-composites, the digits represent the number of dimensions in which the phase within the composite is self-connected. [48].

A polymer matrix with piezoelectric ceramic fillers generally represents a 0-3 connectivity pattern. For most research, researcher have studied the use 0-3 connectivity piezocomposites, which is consist of randomly distributed ceramic fillers

embedded in a 3-dimensional polymer matrix. The reason why this type of connectivity pattern is popular is because of their flexibility, ease of processing. This type of composites is widely used in passive devices embedded in concrete, such as sensors[50-52].

2.12 Heat Transfer

In this study, the work was focus on how will the temperature affect the piezoelectric and dielectric properties of the PZT composites. It is very important to understand how will the temperature change in the composites because these changes will affect the curing process of the epoxy and the material properties of the composites will be changed during this curing process. The change of the material properties of the composites will affect the piezoelectric and dielectric properties of the models. This is why it is important to understand the principals of the heat transfer process because it is the way to represent the transfer of the heat energy and the temperature difference from the applied heat source to the composite and the same process transferred in the composites. The definition of heat transfer is energy in transit due to a temperature difference[53]. Whenever there exists a temperature difference in a medium or between media, heat transfer occurs. There are three types of heat transfer in nature, heat conduction, heat convection and thermal radiation. Heat conduction occurs when a temperature gradient exists in a stationary medium, which may be a solid or a fluid. Conduction may be viewed as the transfer of energy from the more energetic to the less

energetic particles of a substance due to interactions between the particles[53]. On the other hand, heat convection occurs between a surface and a moving fluid or gas when they are at different temperatures. The last type of heat transfer, which is thermal radiation happens between two surfaces at different temperatures. All surfaces of finite temperature emit energy in the form of electromagnetic waves. Thus, it is a net heat transfer by thermal radiation. Figure 2.28 shows three different type of modes for heat transfer.
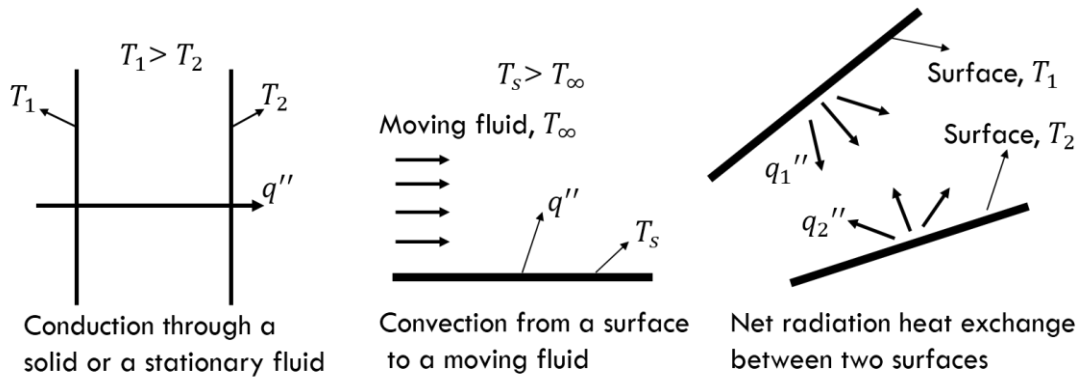
Figure 2. 28. Shows three type of modes for heat transfer. From left to right are with respect to heat conduction, heat convection and thermal radiation.

In order to describe the amount of the energy transfer during the heat transfer process. Equation 2.14 shows the rate equation of an example for one-dimensional plane wall for heat conduction.

$$q_x{}'' = -k\frac{dT}{dx} \qquad (2.14)$$

In equation 2.14, $q_x{}''$ is defined as heat flux, which is the heat transfer rate in the x direction per unit area perpendicular to the direction of transfer. The parameter, k is a transport property known as thermal conductivity with units (W/m.K), which depends on the materials.

For heat convection mode, the rate equation or the heat flux is given by equation

2.15:

$$q'' = h\,(T_s\text{-}T_\infty) \quad (2.15)$$

where h is the convection heat transfer coefficient with unit (W/m^2.K), which depends on the conductivity of the fluid and the motion of the fluid. T_s is surface temperature and T_∞ is the fluid or gas temperature.

For thermal radiation mode, the rate equation or the heat flux is given by equation 2.16:

$$q'' = \frac{q}{A} = \varepsilon\sigma\,(T_s{}^4\text{-}T_{sur}{}^4) \quad (2.16)$$

where A is the surface area and ε is the surface emissivity. T_s is surface temperature and T_{sur} is the temperature of the surroundings. σ is the Stefan-Boltzmann constant (σ =5.67X10^{-8} W/m^2.K^4). The equation of the energy for the conservation law over a time interval is given by equation 2.17:

$$E_{in}+E_g\text{-}E_{out} = \triangle E_{st} \quad (2.17)$$

where E_{in} is the inflow of the energy, E_g is the generation of the energy during the heat transfer process, E_{out} is the outflow of the energy and $\triangle E_{st}$ is the energy stored in the control volume after the heat transfer process. If considered equation 2.17 at an instant time, the equation then could be written as:

$$\dot{E}_{in}+\dot{E}_g\text{-}\dot{E}_{out} = \dot{E}_{st} \quad (2.18)$$

If write equation 2.18 as a heat flux rate equation, then it could be written as equation 2.19:

$$\frac{\partial}{\partial x}(k\frac{\partial T}{\partial x})+ \frac{\partial}{\partial y}(k\frac{\partial T}{\partial y})+ \frac{\partial}{\partial z}(k\frac{\partial T}{\partial z})+\dot{q} = \rho c_p \frac{\partial T}{\partial t} \quad (2.19)$$

where $\dot{q}$ is the rate at which energy is generated per unit volume of the medium with unit (W/m^3), $\rho c_p \frac{\partial T}{\partial t}$ and is the time rate of change of the internal (thermal) energy of the medium per unit time.

There are three common kinds of boundary conditions. If it assumes that the heat transfer is in the positive x direction, then the temperature distribution, which assumes time dependent, could be expressed as T(x,t). The first kind of boundary condition is called the 'Dirichlet condition', which corresponds to a situation where the surface is maintained at a fixed or constant temperature T_s. In this case, there is heat transfer from the surface, while the surface remains at the temperature of the phase change process. The equation of the first kind of boundary condition is expressed as equation 2.20:

$$T(0, t) = T_s \quad (2.20)$$

The second kind of boundary condition is called the 'Neumann condition', which corresponds to the existence of a fixed or constant heat flux $q_s{}''$ at the surface. This heat flux is related to the temperature gradient at the surface by Fourier's law and the expressions of this type of boundary condition are given by equations 2.21 and 2.22:

$$-k\frac{\partial T}{\partial x}|_{x=0} = q_s{}'' \quad (2.21)$$

$$\frac{\partial T}{\partial x}|_{x=0} = 0 \quad (2.22)$$

Equation 2.21 and 2.22 are both for constant surface heat flux. However, equation 2.22

is a special case of this condition corresponds to the perfectly insulated of the

boundaries, which means there is no heat flux or heat transfer happen at this boundary.

The third kind of boundary condition corresponds to the existence of convection

heating or cooling at the surface, which is expressed as equation 2.23:

$$-k\frac{\partial T}{\partial x}\big|_{x=0} = h\ [T_\infty\text{-T}\ (0,\ t)] \quad (2.23)$$

Figure 2.29 shows the three kinds of boundary conditions for the heat diffusion equation

at the surface (x=0) . The left one on the top is first kind boundary condition, which

is constant surface temperature. The right one on the top is constant surface heat flux

of finite heat flux and the left one at the bottom is a special case for second kind

boundary condition, which is perfectly insulated. The last one is the third kind boundary

condition, which is convection heating or cooling at the surface.
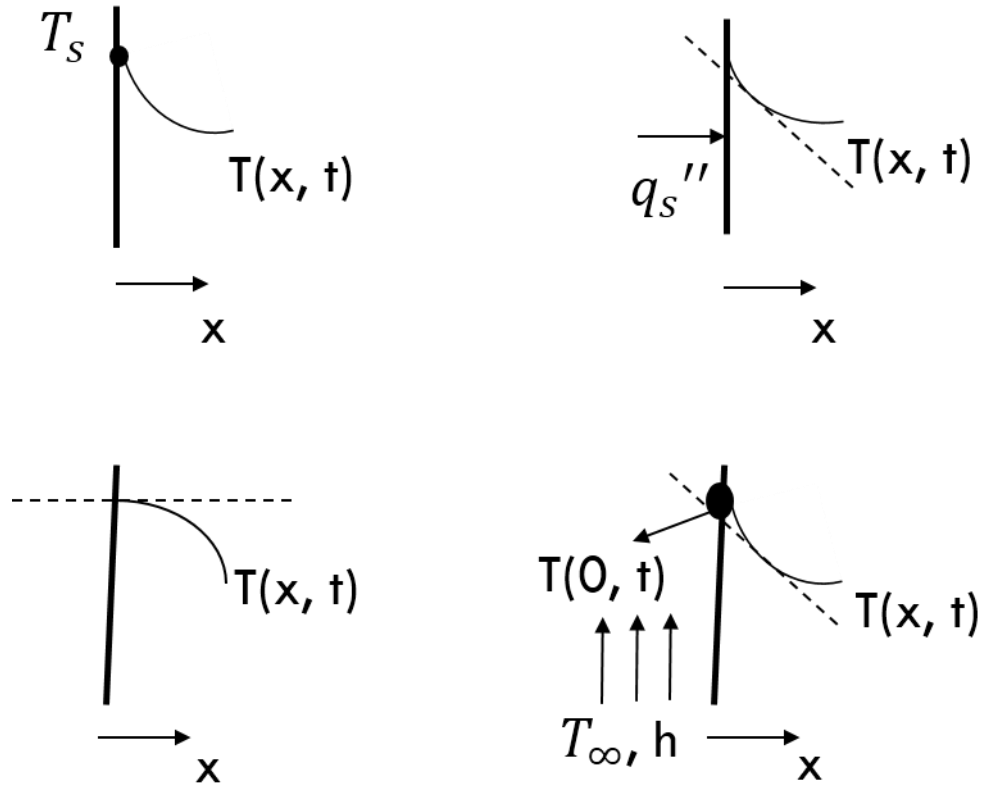
Figure 2. 29. Represents three kinds of boundary conditions for heat transfer.

2.13 Literature review

2.13.1 Composite piezoelectric material

0-3 piezoelectric composites are a category of composite piezoelectric materials that has been extensively studied. Table 2.2 is a summary of piezoelectric composite materials. As it indicated from Table 2.2, the composites are two-phase materials. Most of them are fabricated by mold cast method[54, 55]. For example, PZT CERAMIC trs203 and epoxy TEC were used by L. Li et al[54]. PZT-5A-AS4, 3501-6 carbon and epoxy were used by H. J. Lee et al[55]. SMA and piezoelectric laminated composites were used by M. Kang et al[56].Different temperatures and times were applied to find

out how they will affect the material properties of the composites, such as 120C and 4h

for curing the glass sphere epoxy[54], transition temperature around 70C[56]. DMTA

and DMA,Q800 TA instruments were used to observe nanosized level PZT particles[54].

Different approaches were used to solve these problems, such as numerical study to

determine the nonlinear effects of incorporating material properties by finite element

method [55, 57] and direct Joule heating for the working temperature in

experiments[56].Also, some applications and results are listed in Table 2.2 as well.

Table 2. 2: relation of piezoelectric composite materials with temperature

Type of composites	Volume fraction	Temperature	Time for ageing	Approach	Applications	Objectives and Results
[54] PZT ceramic (TRS203) and glass sphere modified epoxy (reduce TEC of epoxy)	0%,4%,12%,20% for glass spheres in epoxy 56% of PZT	120C for 4h for curing the glass sphere epoxy Aged at 230C for 16h for the glass sphere epoxy 30-275C for the measurement of thermal expansion 250C for ageing Max temperature	4h for curing the glass sphere epoxy 16h for the glass sphere epoxy 200h and 500h for ageing	DMTA (dynamic mechanical thermal analysis) to determine T_g by using a dynamic mechanical analyser (DMA Q800, TA instruments) $\alpha = \frac{1}{L_0} \times \frac{\Delta L}{\Delta T}$ where L_0 is the specimen length at room temperature	NDE type transducer High-temperature ultrasonic transducers NDT Well logging for oil, gas and geothermal industries	The reliability of the composites improved Thermal expansion decreases after ageing at 250C up to 500h Potential applications at elevated temperature.

		300C				
[55]PZT-5A-AS4/3501-6 carbon/epoxy composite plates		Fixed at 20C with the bottom surface Varying from 45C to 170C on the upper surface 100C for thermal shape control 150C to study thermal stress		Numerical study was conducted to determine the nonlinear effects of incorporating material properties by FEM Thermopiezoelectric constitutive equations were used	Sensors for study thermal deflection and the corresponding sensory voltages. Actuators used to study thermal shape control applications. Actuators to study thermal stress.	Coefficient of thermal expansion mismatch between the various composites were studied Pyroelectric effects on the piezoelectric material were studied
[56]SMA/piezoelectric laminated composite ($Ti_{50}Ni_{25}Cu_{25}$ ribbons as SMA layer		Transition temperature is around 70C The peak-to-peak temperature variation is estimated as $\Delta T = 10°C$	4s for voltage response as a function of time for different current modulation frequencies 600s for thermal energy harvesting tests from natural air room temperature fluctuations	Direct Joule heating for the working temperature in experiments Frequency dependence measurements	Energy harvesting devices	composites may offer much potential for low and medium frequency thermal energy harvesting
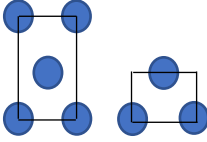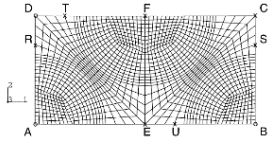
[57] Piezoelectric beams				Last energy norm method Galerkin methods AM method and finite element method	Use as sensors and actuators	To propose reliable methods to extract modal frequencies and mode shapes of beams. To comment on the errors to suggest possible improvements. To experimentally show that the modal properties of a beam can be estimated Euler-Bernoulli model.

In Table 2.3, there are some summaries about the numerical models to solve the composite piezoelectric materials, which is unit cell method. As it indicated from Table 2.3, there are four types unit cells generally used to simulate piezoelectric composites, such as rhombic, square, hexagonal and random[58]. All the unit cell method must obey the periodic boundary conditions, otherwise, the unit cell is not good enough to represent the whole domain of the material[58, 59]. Random sequential adsorption algorithm method[58, 60] and constitutive equations[59] are

often applied in the unit cell method to give the relation of the mechanical properties

of the composites. ANSYS is the software used to generate the numerical models for

this method[58, 59]. In this study, the square unit cell and hexagonal unit cell were

used for the bulk composite models and the planar sheet composite models. This is

because the representative volume element (RVE) was used and Random Sequential

adsorption algorithm (RSA) method was used to generate the RVE models of

randomly distributed particles. Both these two methods can be applied in square and

rectangle unit cells. In addition, since the geometries of the cross-section of the bulk

models and the planar sheet models are very close to square and rectangle, it is more

appropriate to use these two types of unit cells.

Table 2. 3: numerical method to simulate piezoelectric composites materials.

Type of composite	Software to do the simulation	Method for simulation	Type of unit cell	Algorithm for calculation	Periodic BCS	Conclusions
[58] PZT-5 fiber and epoxy	FE package ANSYS	Unit cell method	Rhombic Square Hexagonal Random	RSA (Random Sequential adsorption algorithm)	$u_i^{k^+}-u_i^{k^-}=\overline{S_{ij}}(x_j^{k^+}-x_j^{k^-})$ $\phi^{k^+}-\phi^{k^-}=\overline{E}_i(x_i^{k^+}-x_i^{k^-})$ $\overline{S_{ij}}=\frac{1}{V}\int S_{ij}dV$ $\overline{E}_i=\frac{1}{V}\int E_i dV$ $\overline{T_{ij}}=\frac{1}{V}\int T_{ij}dV$ $\overline{D}_i=\frac{1}{V}\int D_i dV$	Possible to calculate anisotropic material constants. Provide convenient possibilities fo practical use.
[59] PZT fibers or BaT_iO_3		Unit cell method for aligned fibers	Rectangle unit cell	Constitutive equations:	$u^R-u^A = u^S-u^B$ $u^S-u^B-u^R =0$ $u^T-u^P=u^U-u^E$ or	The comprehensive unit cell mode

					$$u^T - u^P - u^U + u^E = 0$$	is an extension of the widely used standard models.
					$\sigma_{ij} = C^E_{ijkl}\varepsilon_{kl} - e_{ijk}E_k$ $D_i = e_{ijk}\varepsilon_{kl} + K^\varepsilon_{ij}E_j$ σ_{ij}, ε_{kl} are stress and strain tensors. E_i is electric potential. C^E_{ijkl} is elasticity tensor K^ε_{ij} is electric permeabilities e_{ijk} is piezoelectric coupling tensor.	The model can be applied to simulate any loading mode and loading path in nonlinear composites.
[60] short fibers and spherical particles reinforced composite structures	FE package ANSYS	Unit cell method RVE (Representative volume element)	Random arrangement unit cell Min size of RVE is that the effective material properties were obtain for 30% volume fraction (with one size of particles) L/D≥10/3 L is the length of RVE D is the diameter of particles	RSA (Random Sequential adsorption algorithm)	$u_i = \overline{S_{ij}}x_j + v_i$ $u_i^{k+} = \overline{S_{ij}}x_j^{k+} + v_i^{k+}$ $u_i^{k-} = \overline{S_{ij}}x_j^{k-} + v_i^{k-}$ $\overline{S_{ij}} = \frac{1}{V}\int S_{ij}dV$ $\overline{T_{ij}} = \frac{1}{V}\int T_{ij}dV$ $\overline{S_{ij}}$: averaged strains v_i: periodic part of the displacement components on the boundary u_i^{k+}, u_i^{k-}: displacement on a pair of opposite boundary surface k^+, k^-: positive and negative x_i direction.	L/D≥10/3 is sufficient to predict the effective material properties with a small error (less 1%) The effect of material properties depends mainly on the volume fraction of particles No significant variations with

						respect to the change in the size of the particles

Table 2.4 gives some literature review for analytic models for composite piezoelectric materials. These references were used to compare the simulation data of piezoelectric and dielectric properties with the analytical models. From the table, it indicates that Kar-Gupta and Venkatesh method is used to calculate piezoelectric strain coefficient[61]. Lichtenecker's logarithmic mixture formula[62] and Maxwell Garnett approximation[63] are used to calculate the dielectric constant.

Table 2. 4: Analytic models for piezoelectric composite materials.

Type of composites	Method for analytic models	Algorithm for calculation		Calculation for dielectric constant	Calculation for piezoelec strain coefficient
[61] 1-3 piezoelectric composites TLZ-5 fiber and the matrix are VDF/TrFE copolymer	Kar-Gupta and Venkatesh method	Constitutive equations: $\sigma_{ij}=C^E_{ijkl}\varepsilon_{kl}-e_{ijk}E_k-\beta_{ij}\theta$ $D_i=e_{ikl}\varepsilon_{kl}+K^\varepsilon_{ij}E_j+P_i\theta$ where σ_{ij}; ε_{ij}, E_i and D_i are the stress tensor, stain tensor, electric field vector and electric displacement vector, respectively. C^E_{ijkl}; e_{ijk}; K^ε_{ij}; β_{ij}			$d_{33}=(\frac{(d^m_{33}-d^f_{33})V^m}{V^m S^f_{33}+Vf S^m_{33}})Vf S^f_{33}+$

		and P_i are the elastic stiffness tensor, piezoelectric tensor, permittivity tensor, thermal coefficient tensor and pyroelectric vector, respectively. θ is the change in temperature			
[62]Homogenized dielectric mixtures	Lichtenecker's logarithmic mixture formula	Start from Maxwell curl equation $\nabla \times H = \sigma E + j\omega\varepsilon E$ Where E is the electric field vector, ω is the angular velocity, σ is the electric conductivity, ε is complex permittivity.		$\varepsilon_{eff} = \varepsilon_2 \left(\frac{\varepsilon_1 + 2\varepsilon_2 + 2(1-\alpha)(\varepsilon_1 - \varepsilon_2)}{\varepsilon_1 + 2\varepsilon_2 - (1-\alpha)(\varepsilon_1 - \varepsilon_2)} \right)$ where ε_{eff} is the dielectric constant of the composite, ε_1 is the dielectric constant of the matrix medium and ε_2 is the dielectric constant of piezoelectric ceramics, α is the volume fraction of piezoelectric fillers.	
[63]Isotropic and anisotropic media. Multicomponent mixtures	Maxwell Garnett approximation	Lorentz local field correction Clausius-Mossotti relation		$\varepsilon = \frac{1 + \left(\frac{8\pi}{3}\right)\left(\frac{\alpha}{v}\right)}{1 - \left(\frac{4\pi}{3}\right)\left(\frac{\alpha}{v}\right)}$ This is Lorentz formula for the permittivity of a nonpolar molecular gas	

$$\varepsilon_{MG} = \varepsilon_h \frac{\varepsilon_h + \frac{1+2f}{3}(\varepsilon_i - \varepsilon_h)}{\varepsilon_h + \frac{1-f}{3}(\varepsilon_i - \varepsilon_h)}$$

This is Maxwell Garnett

Mixing Formula.

2.14 Research Goals and Hypotheses

The objective of this study is to understand how temperature gradients and heat transfer affects the piezoelectric effect and material properties of the composites. Another objective of the study is to understand how the curing process of the epoxy affects the distribution of PZT particles inside the composites. The numerical results will be compared with analytical models and the experimental data.

In this study, three types of models are simulated by Comsol 5.3a. They are bulk, planar and dome shape models. All models are of are two-phase piezoelectric composites. The composites consisted of two kinds of materials, one was lead-zirconate titanate (Pb $(Zr_x Ti_{1-x})O_3$ $(0 \leqslant x \leqslant 1)$), which is this piezoelectric ceramic and the other one is the epoxy DGEBA, which is the polymer used as matrix. The volume fraction of PZT-5A was varied from 0-70%.

Four hypotheses are developed in this PhD thesis. Hypothesis one is that due to difference in stiffness of two materials, the largest displacement may not occur at the highest concentration of the piezoelectric material. The displacement here is generated by thermal expansion not the electric displacement caused by piezoelectric effect. This is because that from some articles, higher volume fraction of ceramic powders will lead to stiffer composites and less strain will be produced by stiffer

composites under a same boundary conditions of the heat transfer process which indicates that smaller amount of strain will be observed in higher ceramic volume fraction composites. On the other hand, PZT as the active material will create activation force, which indicates that higher concentration of PZT will create larger activation force, which indicates higher concentration of PZT will result in larger displacement, which is the electrical displacement caused by direct piezoelectric effect not the strain generated by thermal expansion. This means higher volume fraction PZT models should have a better piezoelectric effect. In order to verify this hypothesis, in this study, volume fraction of PZT range from 10% to 70% composites models of three types will be modeled. The electrical displacement cannot be got directly from the Comsol models. However, instead of getting the electrical displacement, if a fixed electrical displacement was set up for all the composites models, then, the electric potential will be generated by the direct piezoelectric effect for all composite models. If the electric potential increases with increasing the volume fraction of PZT, it means that this hypothesis is verified.

The second hypothesis is that curing conditions will influence piezoelectric composite dielectric properties and displacement. Curing processes in an ambient environment and on a hot plate are modeled. The degree of cure, α, will be the parameter modeled for curing process. It might take much longer time to be fully cured in ambient environment. It is hypothesized that the final value for the degree of cure in the ambient condition will be less than the cure process that includes the hot plate. The curing temperature is very important for this study. If the curing

temperature is below the Curie temperature of the material, the epoxy will not have phase change and it will stay in gel form. If the curing temperature is above the Curie temperature, the epoxy will have phase change from gel form to solid form and the material properties of the composites will be changed. This phenomenon will affect the piezoelectric and dielectric properties of the composites. The Curie temperature of the epoxy DGEBA is 75C. In this study, the curing temperature will be fixed at 75C which the epoxy will start the phase change. The difference between these two curing conditions will be simulated in this study. Usually, higher temperature will lead to faster curing process.

The third hypothesis is that the rate of crosslinking of the epoxy influences the distribution of the PZT within the piezoelectric composite, which ultimately influences the macroscopic piezoelectric strain coefficients and dielectric properties. This is because that large thermal gradient within the composite reduces the distribution of the PZT within the composite and sequestering the PZT particles to the cooler portion of the samples. Figure 2.30 shows the PZT particles distributed in the composites before and after curing process. PZT particles will move to the upside of the composites. The crosslinking rate is faster in hot place than cool place. Samples with more distributed PZT might have less displacement and material properties will be improved with less distributed PZT models.

75C
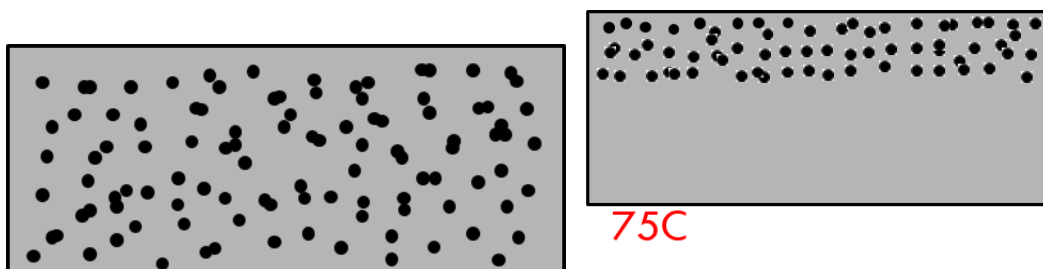
Figure 2. 30. shows the distribution of PZT particles in the composites before and after curing process of epoxy.

To test this hypothesis, I need to do the phase change material of epoxy from gel form to solid form in Comsol and to see if the PZT particles move to the upside of the composites.

The fourth hypothesis is about the boundary conditions of heat transfer. Heat conduction is considered as main heat transfer in composites, heat convection and surface radiation are considered as boundary conditions in heat transfer in solid physics. Heat conduction and heat convection might dominate the electric and dielectric properties. Surface radiation might slightly affect the properties of piezoelectric composites. This is because surface radiation happens mainly when there is temperature difference between two solid material surfaces. However, in this study, the samples are heated in the air. There is no other solid surface. Thus, in this study, I will do both the simulation by considering surface radiation and without considering surface radiation, then compare the results of the two cases to see if they have much difference or not.

Chapter 3

Methodology

This chapter will introduce the material properties of the two-phase composite materials used in this study. In addition, the detailed information of the simulation models made by Comsol 5.3a and Matlab Livelink 2016a will be introduced, including the geometry, material properties, physics, boundary conditions, mesh and study. Also, the curing process of the epoxy will be introduced as well.

3.1 Materials

In this study, two materials are used as piezoelectric composites. They are lead-zirconate titanate (Pb $(Zr_xTi_{1-x})O_3$ ($0 \leq x \leq 1$)) and the two-part epoxy - DGEBA, Epofix^{TM} Cold-setting embedding resin (purchased from APC International and Electron Microscopy Sciences, respectively). The physical, dielectric and piezoelectric and some thermal properties are presented in Table 3.1.

Table 3. 1: Thermal properties for epoxy DGEBA and PZT-5A

Property	PZT 855	DGEBA
Relative dielectric constant, ε_r	3300	3.7-3.9
Dielectric dissipation, *tanδ*	2.50%	~0.002-0.004
Yong's Modulus, Y_{11}^E/Y_{33}^E	5.9/5.1 GPa	0.827 GPa **Error! Reference source not found.**
Piezoelectric strain coefficient, d_{33}	630	

Piezoelectric strain coefficient, d_{31}	276	
Curie temperature, T_c	325°C	
Max. curing temperature, T		75°C

3.2 Geometry set up

In this study, there are three different types of the geometry of the samples. They are bulk samples, planar sheet samples, dome shape samples. The dimensions for the experimental samples for each type and the dimensions of the simulation models for each type are given by Table 3.2.

Table 3. 2: Dimensions for experimental samples and Comsol models for all three types of models

	Width(m)	Thickness(m)	Technique
Experimental samples			
Bulk	0.014m	0.006	Cast-mold
Planar sheet	0.0254	0.0002	Spin-coat
Dome shape	0.0254	0.0002	Spin-coat
Comsol models			
Bulk	0.00007	0.00007	Unit cell method
Planar sheet	0.00007	0.00003	Unit cell method
Dome shape	0.00254	0.00002	Scaled method

In Comsol 5.3a, this was done by 2D space dimension for bulk samples and planar sheet samples. The simulation is a cross section of bulk and planar sheet samples. This is because the heat transfer is from the bottom side to the upside of samples and the bulk and planar sheet samples are uniformly heated on a hot plate.

Thus, the biggest cross-section of the sample can represent the material properties related to the temperature. For dome shape models, this was done by the 2D axisymmetric space dimension. This is because the cross section of the dome shape model will rotate with the axis, which is the same geometry with the experimental samples fabricated. The dimensions of bulk samples are 0.014m in width and 0.006m in thickness. Figure 3.1 represents the geometry of the bulk samples and the simulation set up for corona poling.
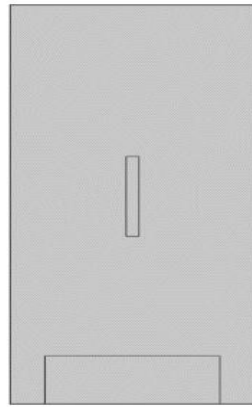
Figure 3. 1. Shows the geometry of the pure PZT bulk samples in Comsol 5.3a.

The small rectangle at the bottom of Figure 3.1 is the cross section of pure PZT bulk samples. The outside big rectangle represents the around air and the small rectangle in the middle represents the corona needle for corona poling. Since the polarization procedure is not automatically included in Comsol models, this procedure needs to be set up by ourselves. The dimension of the outside rectangle air is 0.02m in width and 0.05m in height and the dimension for corona needle is 0.001m in width and 0.01m in height. The distance between the corona needle and the bulk sample is 1.5cm, which is the same as the experimental procedure. The size of the corona needle

is similar to the real size in the experiment but not the exactly same. In the unit cell

method and scaled method used for the Comsol models, the ratio of the dimension of

the corona needle is the same with the geometry of the width of the model and the

width of the unit cell.

Figure 3.2 shows the geometry of planar sheet samples in Comsol 5.3a. The

dimension of the planar sheet model is 0.0254m in width and 0.0002m in thickness,

which is the very thin rectangle at the bottom side of the model.
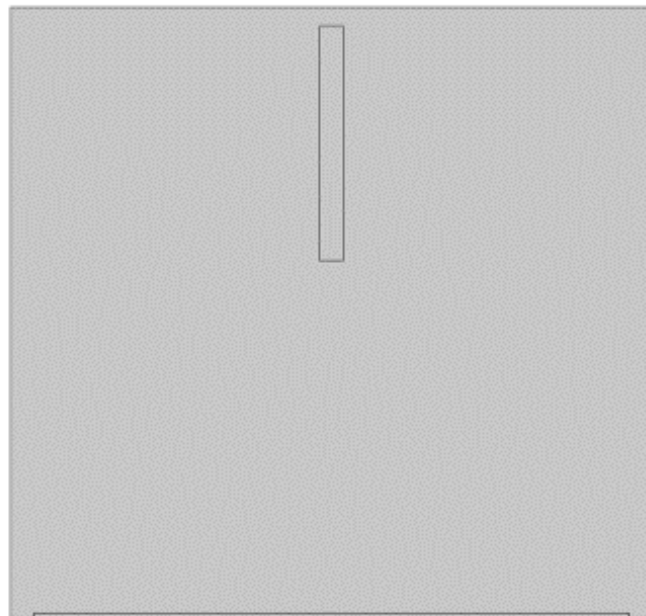
Figure 3. 2. The cross-section of the pure PZT planar samples. The dimensions of the cross-section are 2.54cm in width and 0.02cm in height

The dimension of the outside rectangle air is 0.0274m in width and 0.026m in

height and the dimension for corona needle is 0.001m in width and 0.01m in height.

The distance between the corona needle and the bulk sample is 1.5cm, which is the

same as the experimental procedure.

Figure 3.3 represents the geometry of pure PZT dome shape model. The

dimension of the dome shape model is 0.0254m in width and 0.0002m in thickness,

which is the curved thin sheet in the model.
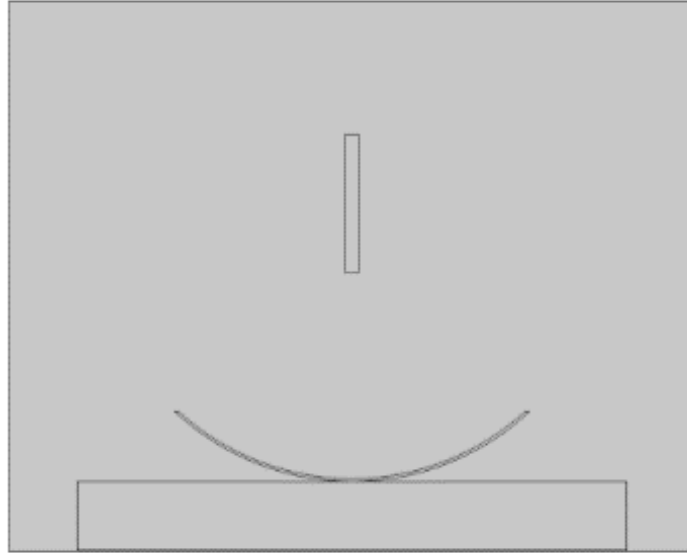
Figure 3. 3. The cross-section of the pure PZT planar samples. The dimensions of the cross-section are 2.54cm in width and 0.02cm in height

The dimension of the outside rectangle air is 50mm in width and 40mm in height

and the dimension for corona needle is 0.001m in width and 0.01m in height. The

distance between the corona needle and the bulk sample is 1.5cm, which is the same

as the experimental procedure. The rectangle at the bottom of the model represents the

hot plate, which has a fixed temperature at 75C. The dimension of this hot plate is

40mm in width and 5mm in thickness.

For the composite piezoelectric material, the models of geometry are generated

by Matlab 2016a of Comsol Matlab live link with writing a script to generate the

small PZT particles inside the epoxy DGEBA matrix. The dimension of the PZT

particles is 5μm-8μm in diameter. The volume fraction of composites is from 10% to

70%. Since the dimension of PZT particles is very tiny, it will generate millions of small circles to reach the volume fraction of PZT in Comsol models, which is impossible with regular computers. Thus, in order to generate the geometry for composite piezoelectric material models, the unit cell method was used to do the simulation and get the numerical results by using this method.

3.3 Unit cell method

As mentioned before, the diameter of PZT particles is very tiny. It is impossible for regular computers to generate millions of particles to reach the volume fraction of PZT. In this case, the unit cell method is introduced to solve this problem. The main idea of the method is to find a globally homogeneous medium equivalent to the original composite, where the strain energy stored in both systems is approximately the same[58]. The Unit Cell Method involves choosing a small unit area in the domain which can globally represent the material properties of the whole domain, and then hold the same volume fraction of the PZT in this unit cell[58]. In this way, the number of PZT particles which needs to be generated for the Comsol model is very small. However, in order to choose a good small area, some periodic boundary conditions and some steps need to be obeyed to generate the particles to make sure the unit cell has similar material properties as the original domain. The periodic boundary conditions are given through equation 3.1 to 3.6[58, 60].

$$u_i^{k^+} - u_i^{k^-} = \overline{S_{ij}}(x_j^{k^+} - x_j^{k^-}) \quad (3.1)$$

$$\phi^{k^+} - \phi^{k^-} = \overline{E_i}(x_i^{k^+} - x_i^{k^-}) \quad (3.2)$$

$$\overline{S_{ij}} = \frac{1}{V} \int S_{ij} dV \qquad (3.3)$$

$$\overline{E_i} = \frac{1}{V} \int E_i dV \qquad (3.4)$$

$$\overline{T_{ij}} = \frac{1}{V} \int T_{ij} dV \qquad (3.5)$$

$$\overline{D_i} = \frac{1}{V} \int D_i \ dV \qquad (3.6)$$

where $\overline{S_{ij}}$ is the averaged strains, $\overline{E_i}$ is averaged electric fields, $\overline{T_{ij}}$ is averaged stress, $\overline{D_i}$ is averaged electric displacements, $u_i^{k^+}$ and $u_i^{k^-}$ are displacements on a pair of the opposite boundary surface, ϕ^{k^+} and ϕ^{k^-} are electric potential generated on a pair of the opposite boundary surface, k^+, and k^- are positive and negative x_j direction.

Figure 3.4 shows the steps to generate PZT particles inside the unit cell.
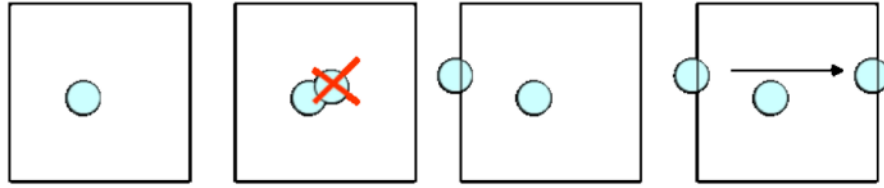
Figure 3. 4. Shows the step of RSA algorithm to generate the unit cell[58].

The RSA algorithm starts with random center coordinates of the first circle with a prescribed radius. Then a next circle is randomly generated. It is checked for non-overlapping with the previously deposited circle. If there is no overlap between the current circle and actual circle, then it is placed on the plane. Otherwise, it is rejected. A second check is made for intersection with the boundary of the cell. In case of intersection, it is copied to the opposite edge with the distance of the cell width to ensure periodicity. The size of the unit cell chosen for this study is 70μm. The condition to choose an effective unit cell is that the minimum size of the effective unit cell is that it can hold at least 30% volume fraction PZT particles with size fixed at 8μm in diameter. L/D≥10/3 is sufficient to predict the material properties for a unit

cell, where L is the length of RVE (unit cell) and D is diameter for PZT[58]. In the

script, the diameter of the PZT particles was defined in a range of 5µm to 8µm. For

example, if the volume fraction of PZT particles is fixed at 50%, in the process of

generating PZT particles in the unit cell, the particles will first be randomly generated

as 8µm in diameter until it reaches the maximum number of particles that the unit cell

can hold in this diameter without overlapping with each other. Then, smaller PZT

particles will be randomly generated in the space between the large particles within

the range of the diameter, which is from 5µm to 8µm until it reaches the volume

fraction set up, which is 50% in the example. Figure 3.5 shows an example of a unit

cell.
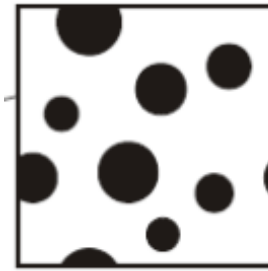
Figure 3. 5. Shows the random PZT particles generated in a unit cell[58].

3.4 Material properties set up in Comsol models

For Comsol models, once the geometry is set up, the next step is to set up the

material properties of each part of geometry. As for bulk and planar sheet models, five

types of materials were used for our models. For the corona needle, steel AISI 4340

was used as the material for this part and the material properties are listed in Table 3.3:

Table 3. 3: Material properties for corona needle

Property	Value	Unit
Heat capacity at constant	475	J/(kg·K)

pressure		
Density	7850	kg/m^3
Thermal conductivity	44.5	W/(m*K)
Relative permeability	1	1
Electrical conductivity	4.032e6	S/m
The coefficient of thermal expansion	12.3e-6	1/K
Relative permittivity	1	1
Young's modulus	205e9	Pa
Poisson's ratio	0.28	1

For the outside rectangle shown in Figure 3.3 which represents the air, the material properties were found out for air from the material library. Some of the material properties are as a function of time or temperature which is called by Comsol 5.3a itself. All the information about material properties for air are listed in Appendix 1. For PZT particles, PZT-5A was used from the material library and all the material properties are listed in Table Appendix 2.

For polymer matrix, two different types of epoxy were chosen from Comsol material library. These materials are generally used in real life and they can directly get the material properties in Comsol library. One is epoxy molding compound partially cured and the other one is epoxy molding compound fully cured. The reason why the two types of epoxy were used is to simulate the phase change of epoxy due to the curing process of epoxy with the temperature at 75 C. The difference of these two types of epoxy is that partially cured epoxy is in gel form and fully cured epoxy is in solid form. Only partially cured epoxy will have phase change during the heat transfer process. In

addition, some of the thermal properties of partially cured epoxy are the function with change of the temperature or time, however, some of the material properties of fully cured epoxy are kept at some constants. The material properties of partially cured and fully cured are listed in Appendix 3 and Appendix 4.

For dome shape models, which are the models with the same geometry with dome shape experimental samples, have total six types of materials used for the models. There is only one part of the model which has different material, which is the hot plate. The material is chosen as iron. The rest of the materials for each part are the same with bulk and planar sheet models. The material properties for iron are listed in Appendix 5.

3.5 Theoretical Models

In this study, five types of physics are used to set up the models. They are thermal stress model, Electrostatic model, Laminar flow model, and Level Set model. Thermal stress model is composed of two types of modles which include Solid Mechanics model and Heat Transfer in Solids model. These two types of models will give the relation between heat transfer in the composites and the deformation caused by thermal expansion. Thus, these two models will give the results for stress caused by thermal expansion during the heat transfer process. The governing equation of this model is given by equation 3.7:

$$\nabla \cdot S + Fv = 0 \qquad (3.7)$$

This equation is about the relationship between stress and strain, where S is strain and F is stress, v is the velocity.

For "Heat Transfer in Solid" model, the heat generation and conduction are from a nonlinear internal heat source in resin curing reaction during the curing process of the thermosetting resin composites. it has three original conditions, "Solid 1", "Initial Values 1" and "Thermal insulation 1". These three conditions represent that the heat transfer occurs in solid materials with the initial temperature of the whole domain at 293.15K. All of the boundaries are initially insulated with the boundary condition given by equation 3.8:

$$-n \cdot q = o \quad (3.8)$$

This equation satisfies the second type of boundary of heat transfer, which is the Neumann Boundary condition, where n is the normal direction and q is heat flux. In addition, three more boundary conditions and one condition were added for phase change material due to the curing process of epoxy. A fixed temperature 75C is added at the bottom side of the unit cell. The convection heat flux and surface radiation heat flux are added for the rest of three boundaries of the unit cell. The equations for heat convection and radiation are given by equation 3.9 to 3.11:

$$-n \cdot q = d_z q_0 \quad (3.9)$$

$$q_0 = h(T_{ext} - T) \quad (3.10)$$

$$-n \cdot q = d_z \varepsilon \sigma \left(T_{amb}^4 - T^4 \right) \quad (3.11)$$

where h is the heat convection coefficient which is 12.5 $W/(m^2.K)$ for the air, T_{ext}, and T_{amb} are the surrounding temperature which is 293.15K in this study, q_0 is the convective heat flux. d_z is the thickness which is 1m. ε and σ are surface emissivity and Stefen-Boltzmann coefficient which is mentioned in Chapter 2.

Since the epoxy is partially cured at the beginning, it will have a phase change from the gel form to the solid form during the curing process. Thus "Phase Change Material " is added to represent this procedure and the equations for this condition are given by equations 3.12 through 3.17:

$$d_z \rho C_p \frac{\partial T}{\partial t} + d_z \rho C_p u \cdot \nabla T + \nabla \cdot q = d_z Q + q_0 + d_z Q_p + d_z Q_{vd} \quad (3.12)$$

$$Q = -d_z k \nabla T \quad (3.13)$$

$$\rho = \theta \rho_{phase1} + (1-\theta) \rho_{phase2} \quad (3.14)$$

$$C_p = \frac{1}{\rho} \left(\theta \rho_{phase1} C_{\rho,phase1} + (1-\theta) \rho_{phase2} C_{\rho,phase2} \right) + L \frac{\partial \alpha_m}{\partial T} \quad (3.15)$$

$$k = \theta k_{phase1} + 1-\theta) k_{phase2} \quad (3.16)$$

$$\alpha_m = \frac{1}{2} \frac{(1-\theta)\rho_{phase2} - \theta \rho_{phase1}}{\theta \rho_{phase1} + (1-\theta) \rho_{phase2}} \quad (3.17)$$

where Q is heat source item, Q_{vd} is viscous dissipation heat, and Q_p is the heat generated by the pressure work

The governing equations for Heat transfer in solid model are given by equation 3.18 and 3.19:

$$d_z \rho C_p \frac{\partial T}{\partial t} + d_z \rho C_p u. \nabla T + \nabla .q = d_z Q + q_0 + d_z Q_{ted} \quad (3.18)$$

$$q = -d_z k \nabla T \quad (3.19)$$

The third type of model is "Electrostatics", which is used to represent the direct piezoelectric effect in this model. Since the composites are piezoelectric composite materials, they will generate voltages due to the deformation caused by thermal expansion. The governing equation of this model is given by equation 3.20 and 3.21:

$$\nabla \cdot D = \rho_v \quad (3.20)$$

$$E = -\nabla v \quad (3.21)$$

For this model, it has three original conditions. They are "Charge Conservation 1", "Zero Charge 1" and "Initial Values 1". For "Charge Conservation 1", the equations are given by 3.21 and 3.22:

$$\nabla \cdot (\varepsilon_0 \varepsilon_r E) = \rho_v \quad (3.22)$$

where ε_0 and ε_r are dielectric constant in a vacuum and dielectric constant for the materials, which is mentioned in Chapter 2. "Zero Charge 1" means that the outside boundaries of air are insulated that has no displacement generate for the air. The equation is given by 3.23:

$$n \cdot D = 0 \quad (3.23)$$

The initial value for the whole domain is zero electric potential at the beginning. Three other conditions are added to completely set up this physics. The first condition is "Charge Conservation, Piezoelectric 1", which is the relation between the applied outside electric field with the generated electric potential. The equations for this condition are given by equation 3.22, 3.21 and 3.24:

$$D = \varepsilon_0 \varepsilon_{rs} E + P_{pze} \quad (3.24)$$

where D is electric displacement, E is applied electric field and P_{pze} is the polarization of piezoelectric in solid

In addition, a constraint for "Ground" is set up at the bottom side of the unit cell, where the electric potential is zero. The "Terminal 1" is also added for the corona needle, which is set up for the poling process and the applied external electric field. The applied electric field is 0.2kV/mm for bulk models, planar sheet models and dome shape, which is the same with the experiment work.

The fourth model is "Laminar Flow", which is used to simulate the gel form of partially cured epoxy. The governing equations of this physics are given by 3.25 and 3.26:

$$\rho(u_3.\nabla)\,u_3 = \nabla\cdot[-\rho 2l + \mu(\nabla u_3 + (\nabla u_3)^T)] + F \quad (3.25)$$

$$\rho\nabla\cdot(u_3) = 0 \quad (3.26)$$

This equation is the conservation of mass equation for Laminar flow, where ρ is density, μ is dynamic viscosity, u is the velocity field and F is the volume force. There are three original conditions come with this physics. They are "Fluid Properties 1", "Initial Values 1" and "Wall 1". The first condition represents the relation between stress and strain. The equations for this condition are the same as the governing equations 3.25 and 3.26. The initial values for velocity and pressure for the composite are both zero at the beginning. The four boundaries of the unit cell are set up as a wall, which means there is no flow moving inside and outside of the composites. Another two conditions are added to make this physics completely set up. One is "Pressure Point Constraint 1" and "Volume Force 1". The point constraint is set up as left corner point on the top surface with value 0, which means there is no pressure added on the model and the volume force is the body force by the composite itself.

The last model is "Level Set". This physics is used to simulate the phase change of epoxy due to the heat transfer. The governing equation of this physics is given by equation 3.27 and 3.28:

$$\frac{\partial\Phi}{\partial t} + u\cdot\nabla\Phi = \gamma\nabla\cdot(\varepsilon_{ls}\nabla\Phi - \Phi(1-\Phi)\frac{\nabla\Phi}{|\nabla\Phi|} \quad (3.27)$$

$$\Phi = phils2 \quad (3.28)$$

where Φ is the specify level set function explicitly and phils2 is the level set variable, which does not have physic meaning but only the representation in Comsol models

There are three original conditions that come with this physics. They are "Level Set Model 1", "Initial Values 1" and "No Flow 1". The level set model has the same equations with 3.27 and 3.28. The unit cell was separated into two parts, one represents the gel form for epoxy and the other one is the solid form of epoxy. The bottom part is the solid form because the temperature at the bottom is higher than the temperature at the top side at the beginning of heat transfer. So, the phase change happens first at the bottom side. The initial value for the bottom part is Φ=1, which means the epoxy is in solid form and the initial value for the up part is Φ=0, which means the epoxy is in the gel form. A constraint of no flow is set up for the outside boundaries of the unit cell which means there is no liquid moving in the composites. In addition, an initial interface was added to start the phase change of the epoxy. This is because, in Comsol, you need to tell Comsol when and where to start the calculation. The interface is very close to the bottom side, which means the phase change will start from the bottom side and the same direction of heat transfer.

3.6 Multi-theoretical Models

Once the different types of models are set up, the next step is to combine these theoretical models together. This is because different type of theoretical models will give different results. For example, 'Solid mechanics model" will give the results for stress and strain, 'Heat transfer in solid model" will show the results for temperature

distribution and so on. The application for Multi-theoretical models is to combined different models and find out the relationship between them, such as the deformation caused by thermal expansion or piezoelectric effect caused by the structure deformation of the composites.

In this study, there are four types of Multi-theoretical models. They are "Thermal Expansion", "Temperature Coupling", "Piezoelectric Effect" and "Two-Phase Flow, Level Set". "Thermal Expansion" is used to relate two models which are "Heat transfer in solid" and "Solid Mechanics". This Multi-theoretical model will give us the results for stress and strain caused by thermal expansion. "Temperature coupling" relates two models which is the same with "Thermal Expansion". The coupled interfaces are "Heat Transfer in Solid" and "Solid Mechanics". "Piezoelectric Effect" relates two models for "Solid Mechanics" and "Electrostatics". This Multi-theoretical model gives us the results for direct piezoelectric effect, which is the electric potential generated by the deformation of the composites. The last one is the Multi-theoretical model relate two physics for "Laminar Flow" and "Level Set". This will give us the results for the phase change of epoxy and particle floating during this process.

3.7 Finite element process

For Comsol models, once the geometry, material properties, physics, and Multiphysics are set up, the next step is to set up the finite element method before calculating the results. This process in Comsol is called "Mesh". There are basically two ways to set up the mesh. One is to set up the element and shape by yourself, which

is called "user-controlled mesh". You can choose different types of shape to mesh the element, such as "Free Triangular", "Free Quad" and so on. Triangular elements, in general, will give us more accurate results because this type of elements will have more elements for the whole domain and the more elements will cause more calculations for the solution. However, the shape of the element chose for our models depends on the geometry of the models and some the boundary conditions. You can define the number of element and size of the element you choose for each part of the geometry for the model. Another way to set up the mesh is by auto-mesh Comsol has for itself, which is called "Physics-controlled mesh". They have nine types of element size to use for meshing. They are 'Extremely fine', 'Extra fine', 'Finer', 'Fine', 'Normal', 'Coarse', 'Coarser', 'Extra Coarse' and 'Extremely coarse''. The size of the element is from small to large. The smaller the element is, the better results will get. But it will take more time to run the models if the size of the element is too small.

In this study, auto-mesh was used for bulk and planar sheet models. The size of element chosen was 'Finer', which is enough to calculate my models. In our Comsol models, if the auto mesh was chosen to generate the finite element of the bulk and planar sheet model, then, it is not necessary to worry about the problem that the number of elements selected for each model will lead to the correct solution convergence or not. This is because the geometries of these two types of models are not complicated, the auto mesh method will automatically generate the number of elements for each model so that the solution will be convergence. However, if the geometry of the model is complicated, such as dome shape model, then, auto mesh can be used for those part of

the geometry which are not complicated. The complicated part can be defined by "user-controlled mesh" method. For example, in dome shape models, the complicated part of the geometry is that the bottom curve and the top side of the hot plate are tangent with each other, the joint part of these two boundaries is difficult to mesh. But it can be solved by defining the size and the number of elements which is needed for these two lines. The principal to generate this type of mesh is that you can decrease the size of the elements and increase the number of elements for the complicated part so that it looks like the originally geometry. When the mesh is generated, if there is no warning for low quality elements, then, it means that the mesh generated is good and the solution will be convergence. Otherwise, keep increasing the number of elements or decreasing the size of the elements until there is no warning for the mesh part. The "user-controlled mesh" was used for dome shape model because the geometry for dome shape is more complicated than bulk and planar sheet models. Examples of the meshes are provided in Figure 3.6 and Figure 3.7 for 10% bulk models and 5% dome shape models:
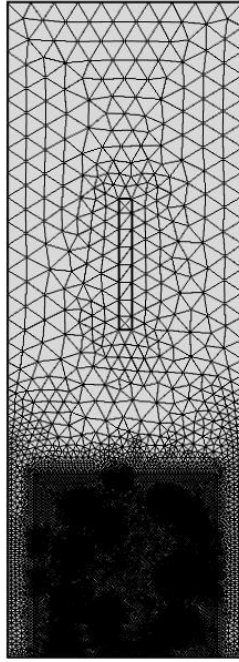
Figure 3. 6. Represents the auto-mesh for 10% PZT bulk samples, the element size is finer. The number of vertex elements is 88, the number of boundary elements is 952, the total number of elements is 21734 and the minimum element quality is 0.5264.
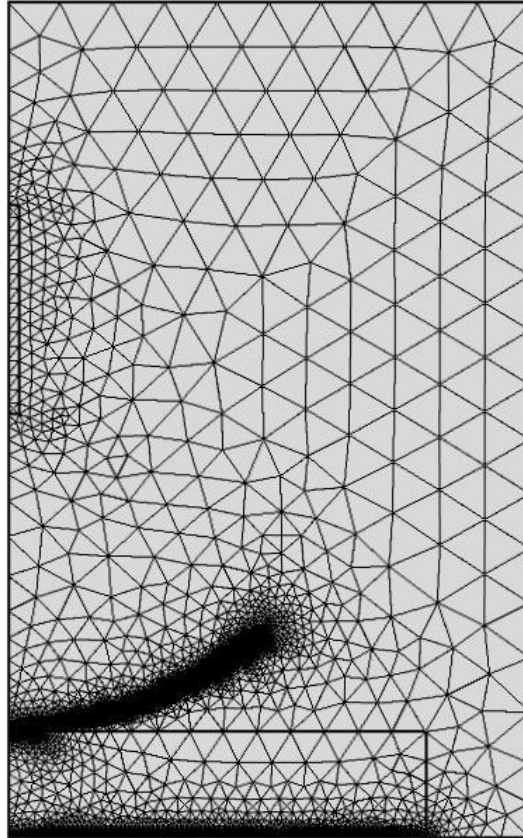
Figure 3. 7. Represents the user-controlled mesh for 5% PZT dome shape model. The size of elements of different parts is different. The number of vertex elements is 127, the number of boundary elements is 2673, the total number of elements is 43709 and minimum element quality is 0.002026.

3.8 Calculation process for the models

This step is the final step to set up a Comsol model. Once the finite element method is set up, the last step is to calculate the model which has been set up. In this study, five types of study were used to get the results for temperature distribution, stress, and strain, electric potential, capacitance and phase change of epoxy. The first one is the time-dependent study, which is used to find out the results for temperature distribution with time and stress and strain caused by thermal expansion with time. The range of time is set up from 0 to 10s and the time step is set as 0.1s. This means the output of results will be 0.1s for each step and the total results will end at 10s. Two interfaces are chosen for this study, which is "Solid Mechanics" and "Heat Transfer in Solid" because the results have no relationship with the other three interfaces. The Multiphysics couplings are chosen for this study, which is "Thermal Expansion 1" and "Temperature coupling 1". The second study is set up for calculating electric potential generated by deformation of the composites. The deformation is caused by thermal expansion. This study is also a transient type. The range of time and time step is the same with the first study. Two interfaces for this study are "Solid Mechanics" and "Electrostatics", which are used to get the results for direct piezoelectric effect. Two Multiphysics couplings are "Thermal Expansion" and "Piezoelectric Effect". The third study is stationary, which is used to get the capacitance of the whole domain. Two interfaces and two Multiphysics couplings are the same in the second study. The fourth study is both for

phase initialization and time-dependent, which is used to get the phase change and particle floating simulation. The range of time for this study is from 0 to 10s and the time step is 0.001s. Two physics interfaces are chosen as "Laminar Flow" and "Level Set". The Multiphysics coupling is chosen as "Two-Phase Flow, Level Set". The last study is frequency domain, which is used to get the voltage generated under certain stress and strain so that to calculate the value for dielectric constant and piezoelectric strain coefficient. The frequency is set up as 110HZ which is the same frequency when measuring the piezoelectric strain coefficient for the experimental data. The two physics interfaces and Multiphysics couplings are the same in the second study. The certain load and electrical displacement set up for this study is 0.25N and 1.168E-7m, where the load is the same value for the experimental load and the electric displacement is calculated by equation 2.13, where the applied external electric field is 0.2kV and d_{33} is 584 pC/N from the material property of PZT 5-A.

3.9 Piezoelectric and dielectric characterization

The ultimate goal of this study is to determine the piezoelectric and dielectric properties of the composites. Dielectric constant ε_r and piezoelectric strain coefficient d_{33} will be calculated according to the results get from the Comsol models. The dielectric constant is calculated by equation 3.29:

$$\varepsilon_r = \frac{Cd}{\varepsilon_0 A} \quad (3.29)$$

where C is the capacitance, d is the thickness of the sample, A is the area of the surface, ε_0 is the permittivity of free space - a vacuum - is equal to approximately 8.85 x 10^{-12}

Farads/meter (F/m). The empirical dielectric constants were compared to those predicted by an analytical model proposed by Maxwell's Equations:

$$\varepsilon_{eff}=\varepsilon_1+\alpha(\varepsilon_2-\varepsilon_1)\frac{\varepsilon_1+2\varepsilon_2+2(1-\alpha)(\varepsilon_1-\varepsilon_2)}{\alpha+1/3(1-\alpha)[\frac{(1-\alpha)\varepsilon_2}{\varepsilon_1}+\alpha+2]} \quad (3.30)$$

where ε_{eff} is the dielectric constant of the composite, ε_1 is the dielectric constant of the matrix medium and ε_2 is the dielectric constant of piezoelectric ceramics, α is the volume fraction of piezoelectric fillers.

Piezoelectric strain coefficient d_{33} is calculated by equation 3.31:

$$d_{33}=\frac{V\varepsilon_r\varepsilon_0 A}{Fd} \quad (3.31)$$

where V is the electric potential generated by piezoelectric, F is the boundary load added on the sample, which is 0.25N, A is the area of the unit cell and d is the thickness of the unit cell. ε_r is the dielectric constant calculated by equation 3.29 and ε_0 is mentioned before, the measured piezoelectric strain coefficient, d_{33}, was compared to the coefficients predicted by another model developed by Furukawa**Error! Reference source not found.**

$$d_{33}=\frac{1}{c}\Phi L_s L_E d_2 c_2 \quad (3.32)$$

where d_{33} is the piezoelectric coefficient, Φ is the volume fraction of piezoelectric fillers; the subscripts 1 and 2, denote the matrix and PZT inclusions respectively. $L_S=\frac{1}{\Phi}\frac{c_1-c}{c_1-c_2}$ and $L_E=\frac{1}{\Phi}\frac{\varepsilon_1-\varepsilon}{\varepsilon_1-\varepsilon_2}$, c, c_1, and c_2 are the Young's Moduli of the composite, matrix and PZT inclusions.

3.10 Curing condition study

In this study, how curing conditions will affect the piezoelectric and dielectric properties of the composites will be simulated in Comsol models. The curing process is a process that material will have a phase change when it absorbs the heat. In this study, it is the epoxy polymer change from gel form to solid form by the crosslinking procedure. Such a process is shown in figure 3.8 and 3.9. Figure 3.8 shows the chemical structure for epoxy DGEBA and figure 3.9 shows the 2D and 3D structures of fully curries epoxy DGEBA.
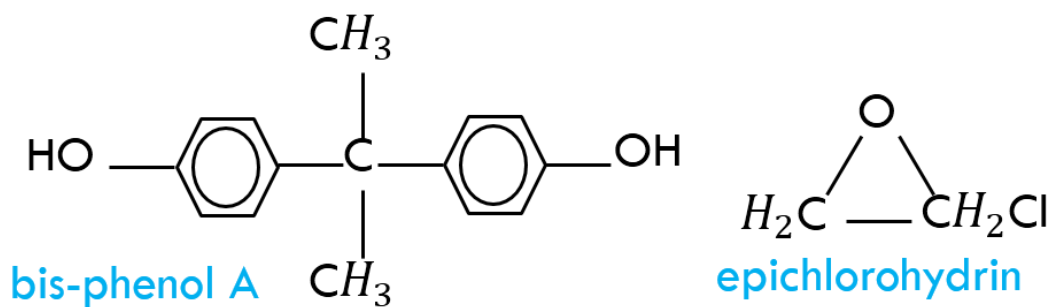
Figure 3. 8. Chemical structure for epoxy DGEBA

Figure 3.8 shows the chemical structure for epoxy DGEBA. It consists of two chemical groups, bis-phenol A group and epoxide group. During the kinetics of the curing process, the C-O bond of epoxide group needs to be broken in order to form a reactive $-CH_2$ site, capable to crosslink to the epoxy hardener molecule. This is called the crosslinking process.
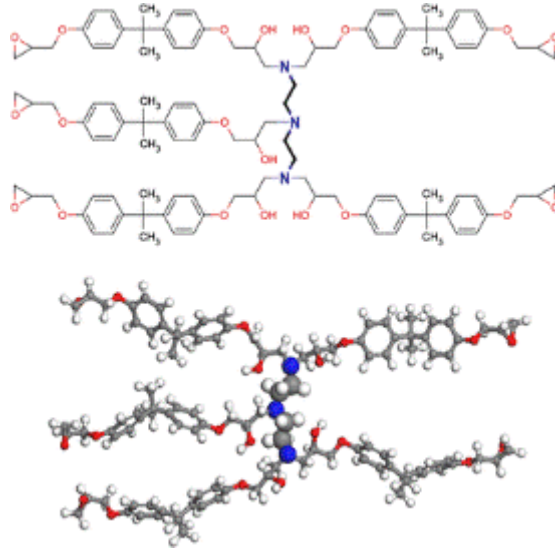
Figure 3. 9. Schematic 2D (top) and 3D (bottom) representations of a fully cross-linked set of DETA and EPON 828 molecules[42]

Two curing conditions will be studied in this work: ambient environment (at room temperature in air 20°C) and hotplate (at 75°C in air). The material chosen is epoxy partially cured compound. During heating and curing process, the material was assumed that they do not move around. Our model will compute the variation in time of the temperature, T, and the degree of cure, α, of the thermoset from the centerline of the composites Assuming no flow, the equation governing heat transfer in the thermoset precursor is:

$$\rho C_p \frac{\partial T}{\partial t} + \nabla \cdot (-k\nabla T) = -\rho H_r \frac{\partial \alpha}{\partial t} \qquad (3.33)$$

where ρ, C_p and κare the density, specific heat, and thermal conductivity of the material.

The degree of cure is αand as the material cures, it absorbs heat, thus there is a negative volumetric heat source that is a function of H_r, the heat of the reaction. The rate of change of the degree of cure is often described by:

$$\frac{\partial \alpha}{\partial t} = A e^{E_a/RT}(1-\alpha)^n \qquad (3.34)$$

where the Arrhenius equation defines the temperature-dependent reaction rate, with A being the frequency factor, E_a being the activation energy, R as the universal gas constant, and n is the order of the reaction.

Two physics interfaces used in Comsol models are "Heat Transfer in Solid" and "Domain ODEs and DAEs. In the first interface, all the boundary conditions and original conditions are the same with the introduction of physics which is mentioned before. The only difference is that a "Heat Source" condition was added in this interface, which is to add the right-hand side of equation 3.33 to the Comsol models. The second interface follows the governing equations 3.33 and 3.34. Two original conditions come with this interface, they are "Distributed ODE" and "Initial Values". In the first condition, the frequency source term need to be set up, which is the right-hand side of equation 3.34. The initial values for degree of cure α and the initial time derivative of α are both zero at the beginning. The material properties for the governing equations are given by Table 3.4, which is input in the Comsol models as global parameters[64].

Table 3. 4: Material properties for curing process of epoxy

Name	Expression	Unit	Description
E_a	35.8	J/mol	Activation Energy
A	110	1/s	Frequency Factor
H_r	1000	J/kg	Total Heat of Reaction
rho0	1200	kg/m^3	Density
C_p0	1250	J/(kg·K)	Specific Heat
k0	0.2	W/ (m·k)	Thermal Conductivity
n	5.45	1	Order

3.11 Comparison of model results with experimental results for particle distribution

For the experimental work, the surface topology, morphology, and distribution of the particles within the polymer matrix were observed with the aid of scanning electron microscope (SEM) and Energy Dispersive Spectroscopy (EDS) micrographs obtained from a Zeiss Sigma Field Emission Microscope[14]. In the SEM image, the displacement of the PZT particle can be seen after the curing process. In numerical models, the distribution of PZT particles in the composites will be simulated and it will show that the particles will move to the top side of the unit cell to generate some displacement [13, 14].

Chapter 4

Results and Discussion for Bulk Models

4.1 Temperature distribution of bulk composites

4.1.1 Temperature distribution of the centerline

In this section, the results of the temperature distribution of the centerline of the cross section of the composites will be discussed. As mentioned before, since the bulk sample composites are uniformly heated on the hot plate, the cross-section of the composites with the dimension of the diameter of the bulk samples in width and the thickness of the bulk samples in height can represent the properties of the whole domain. As mentioned before, it is 0.014m in width and 0.006m in height. This dimension is for the simulation of pure PZT models. However, in Chapter 3, as mentioned, the dimensions of PZT particles are very small, such that the regular computers cannot generate a huge amount of particle of PZT to reach the volume fraction of the

composites from 10% to 70 % PZT. So, the unit cell method is used to solve this problem. The unit cell is a small area that can globally represent the material properties of the whole domain. For the numerical method of bulk models, the dimension for the unit cell was chosen as a square of 70μm in length, which is much bigger than L/D ≥ 10/3, where L is the length for the unit cell and D is diameter for PZT particles[60].
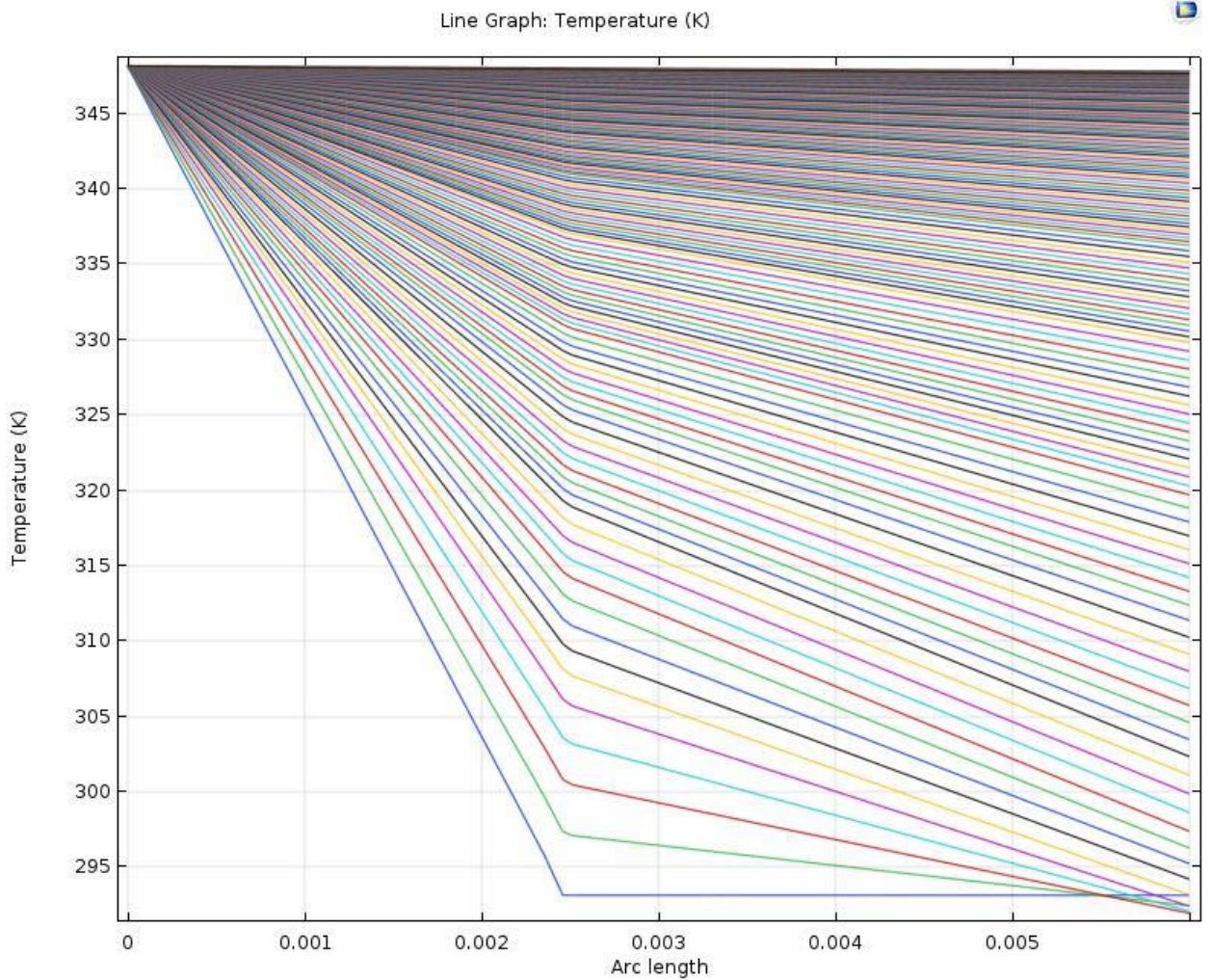
Figure 4. 1. Represents the temperature distribution of centerline of the cross section of the pure PZT bulk sample.

Figure 4.1 shows the temperature distribution of the centerline with the arc length changed with time, where arc length is the length of the centerline, which is the thickness of the bulk sample 0.006m. The arc length is the length for the centerline, which is the thickness in pure PZT or pure epoxy bulk models. The range of time is

from 0 to 300s with the time step of 1s. From the figure, the temperature at the bottom part of the sample is much higher than the temperature at the top part of the sample for each time step at the beginning. This is because the direction of heat transfer is from bottom to top. The temperature of the whole domain increases with increasing the time and arc length and finally get close to the fixed temperature 75C at the bottom side of the sample, which means the heat transfer process is done. The temperature distribution of the centerline for each time moment was described as different color. The first-time step is described in blue line at the bottom of the figure. The green line represents the second-time step and so on. Once the temperature becomes a horizontal straight line and stable, this means the heat transfer process is done. The loss of heat on the top side is caused by thermal dissipation because of the boundary condition of heat convection and surface radiation. Figure 4.2 is an example of the geometry set up for 10% PZT bulk model.
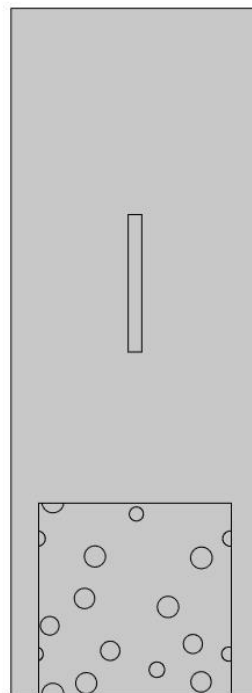
Figure 4. 2. The geometry of 10% PZT bulk model, which is generated by Mat lab script.

Since the dimension for the unit cell is very small, which is 70μm in length. Thus, the process of heat transfer is very fast in the unit cell. Even though the time step was set up as 0.001s, the temperature does not change in the range of time. The temperature will reach the fixed temperature 75C less than 0.001s, which is about 0.00001s for the whole domain of the unit cell. The temperature distribution of the centerline of the unit cell for 10% PZT bulk model is shown in figure 4.3, the horizontal axis represents the arc length of the bulk model, which is the thickness of the bulk model and the vertical axis represents the temperature.
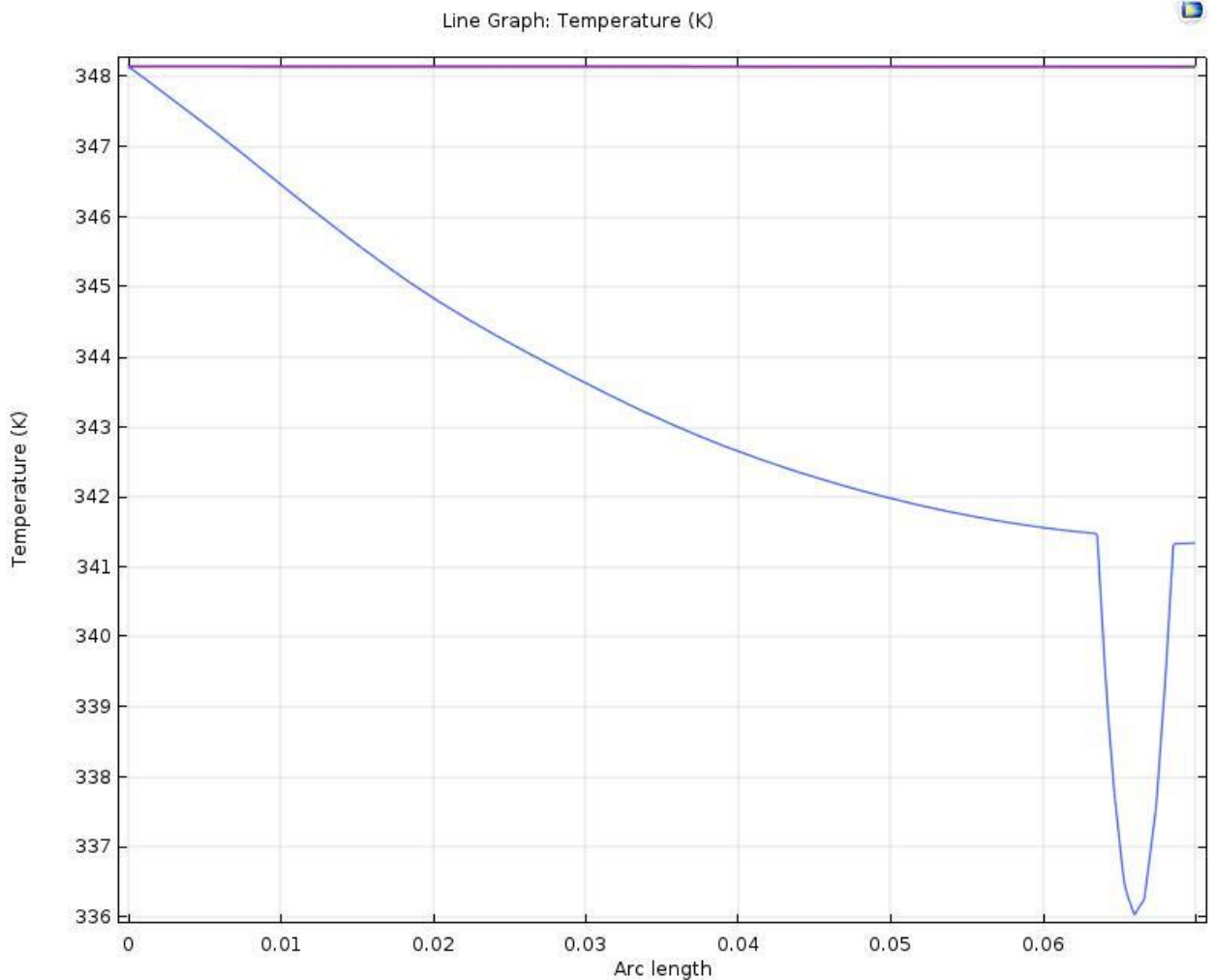
Figure 4. 3. The temperature distribution of the centerline of the unit cell for 10%-70% PZT bulk

model.

From the figure, the blue line is the temperature at time zero instant. However, the temperature for the rest of time steps coincident together which is represented by the pink horizontal line which is equal to the fixed temperature 348.15K at the bottom side, which means the heat transfer process finished less than the time step set up for the composite models which is 0.001s. This is because the unit cell is very thin. It cannot show the heat transfer process change with time in this time step. If the time step was set up much smaller, then, it is possible to show this process. However, there is limitation for Comsol that the time step could not be set up too small. If so, there will be some error shown on the screen. There is no thermal dissipation during this process. This is because the thickness of the unit cell is very tiny so that the effect from the boundary conditions for heat convection and surface radiation is neglected. In addition, since the dimension of the unit cell for all volume fraction PZT models are the same for bulk models, the temperature distributions of the centerline of the unit cell for the rest volume fraction models which are from 20% to 70% are the same with figure 4.3.

4.1.2 Temperature of the midpoint of the top side

In this section, the midpoint of the top side of the unit cell was chosen to see the final temperature of this fixed point when the heat transfer process is done and distribution change with time. This point is chosen as the midpoint on the top side of the pure PZT bulk model as Figure 3.1 shows. The horizontal axis represents the frequency and the vertical axis represents the temperature.
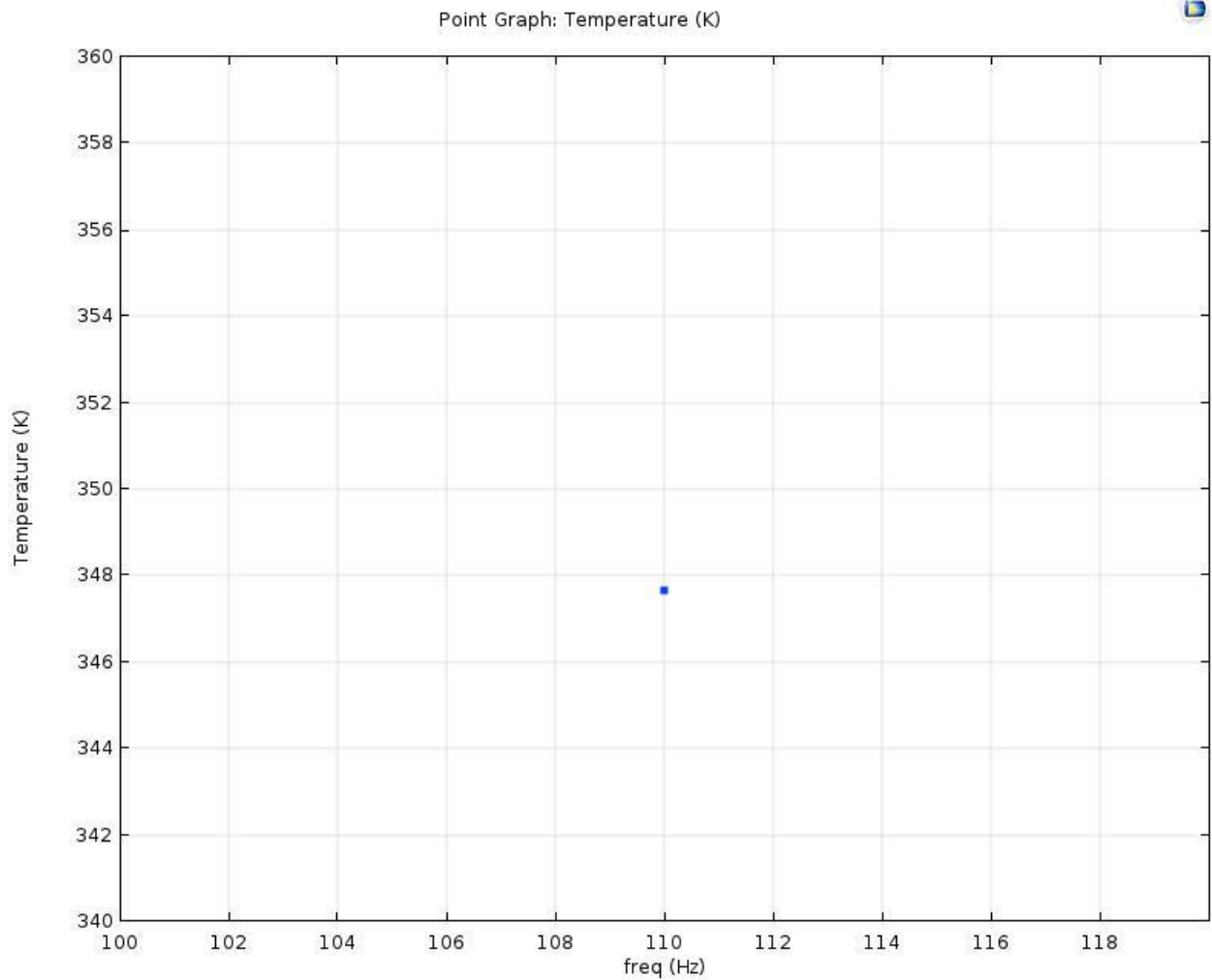
Figure 4. 4. Shows the final temperature of the midpoint at the top side of the pure PZT sample.

From figure 4.4, the temperature for this fixed point is a little bit lower than 348.15K, which is 347.65K because of thermal dissipation caused by heat convection and surface radiation. The horizontal axis represents the time and the vertical axis represents the temperature.
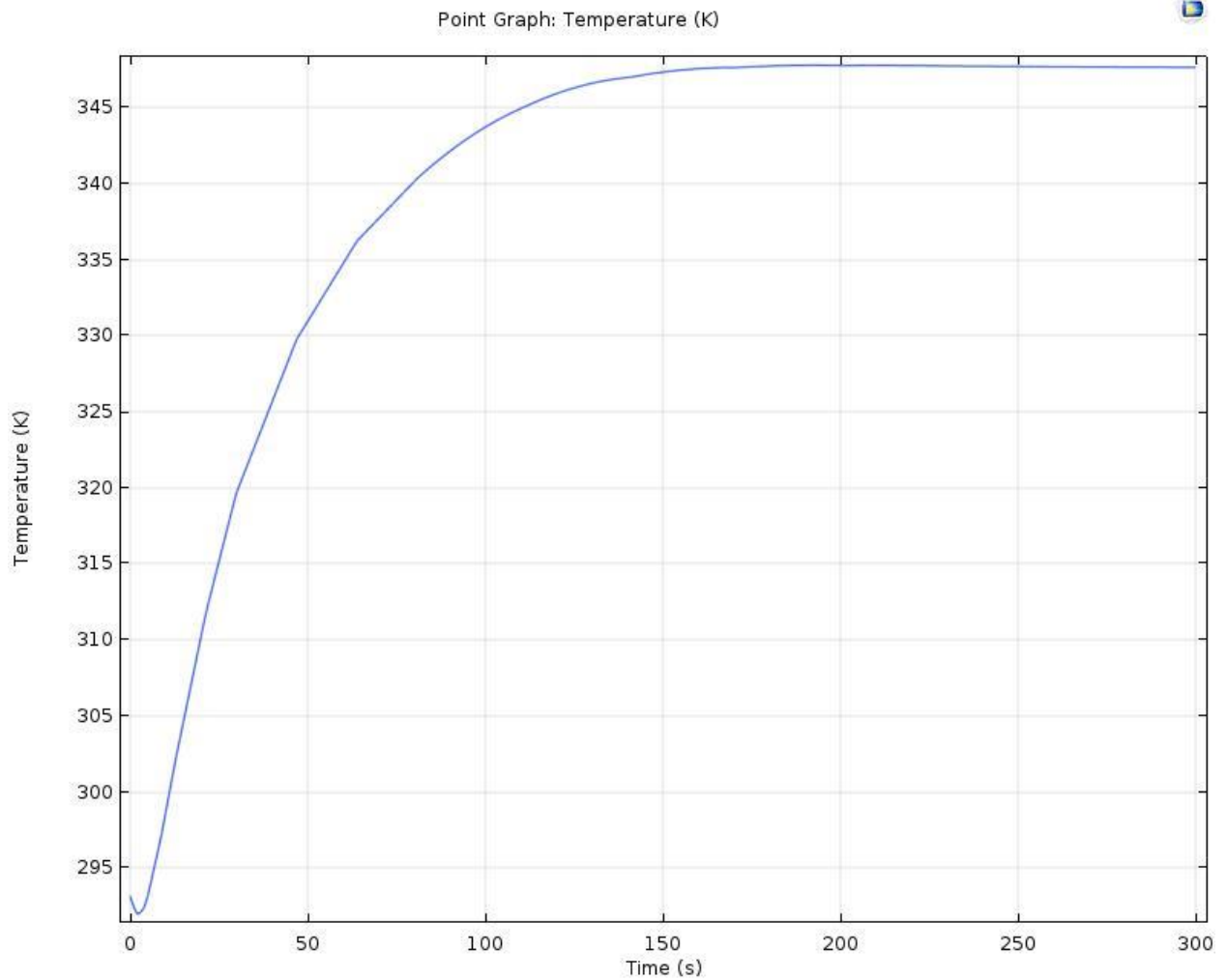
Figure 4. 5. Shows the midpoint value of temperature change with time of pure PZT bulk model.

Figure 4.5 gives us the results for temperature distribution of this midpoint change with time. From the figure, the temperature increases with increasing the time step and finally get to the value 347.65K which is the same as figure 4.4.

As mentioned in section 4.1.1, heat transfer process finishes very fast in the unit cell. So, the temperature distribution of the midpoint on the top side of the unit cell is same for all volume fraction PZT models which is shown by Figure 4.6. The horizontal axis represents the time and the vertical axis represents the temperature.
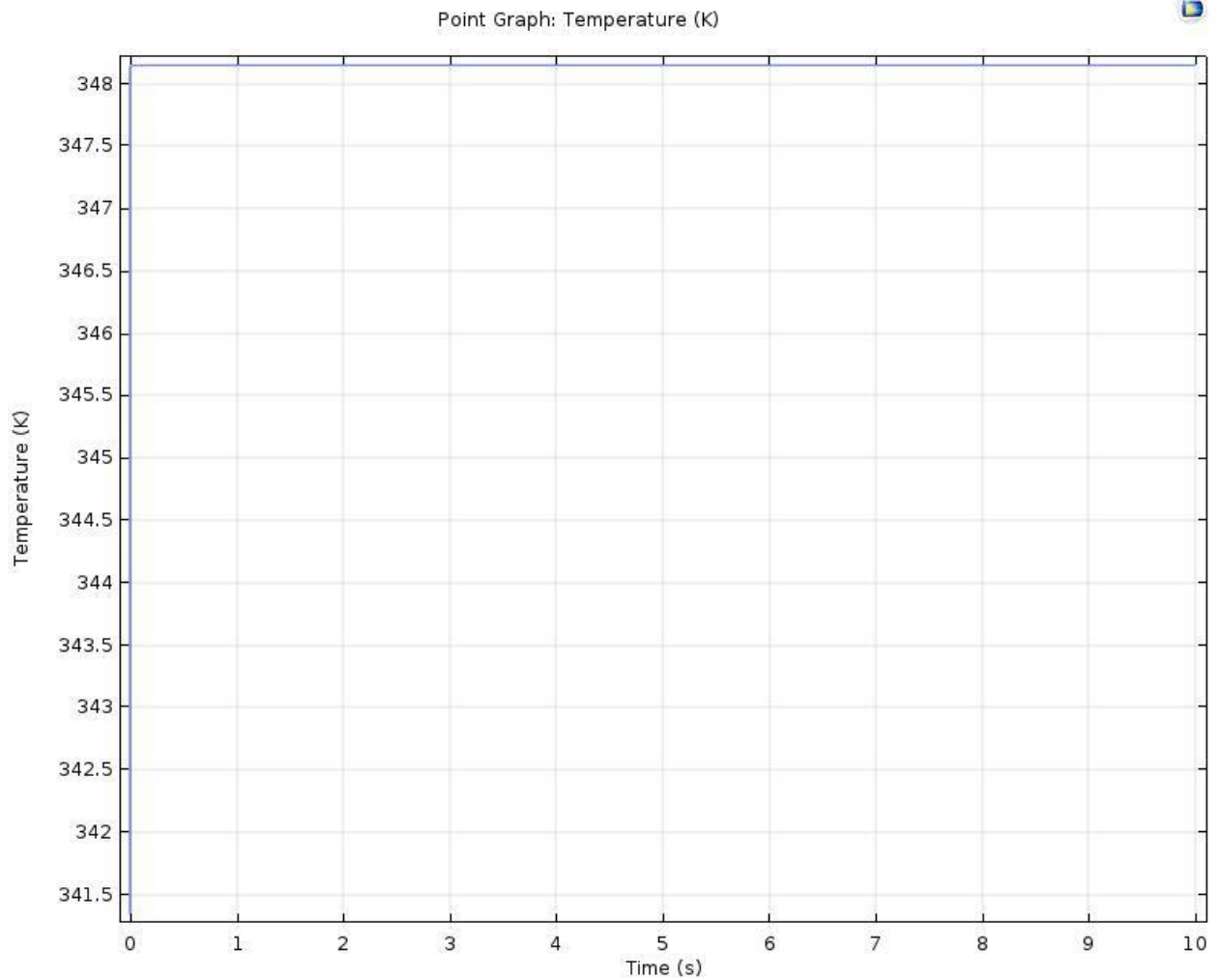
Figure 4. 6. Shows the temperature distribution of the midpoint on the top side of the unit cell for all composite PZT models from 10% to 70% PZT.

From figure 4.6, the temperature of this fixed-point jumps to348.15K even though the time step is only 0.001s, which means the heat transfer process finished in less than 0.001s. The temperature does not change with time because of the thickness of the unit cell is very thin.

4.1.3 Temperature distribution of pure epoxy fully cured model

In the first two sections, the temperature distribution of pure PZT bulk models was discussed. In this section, the result of the temperature distribution of epoxy fully cured bulk model will be shown. The dimension for the pure epoxy model is the same with

pure PZT model. The result of the centerline is shown in figure 4.7. The horizontal axis represents the arc length of the pure epoxy bulk model and the vertical axis represents the temperature. The different color of each line represents the temperature distribution of the centerline for each step. From the bottom to top is the temperature distribution at zero-time step and 300s step.
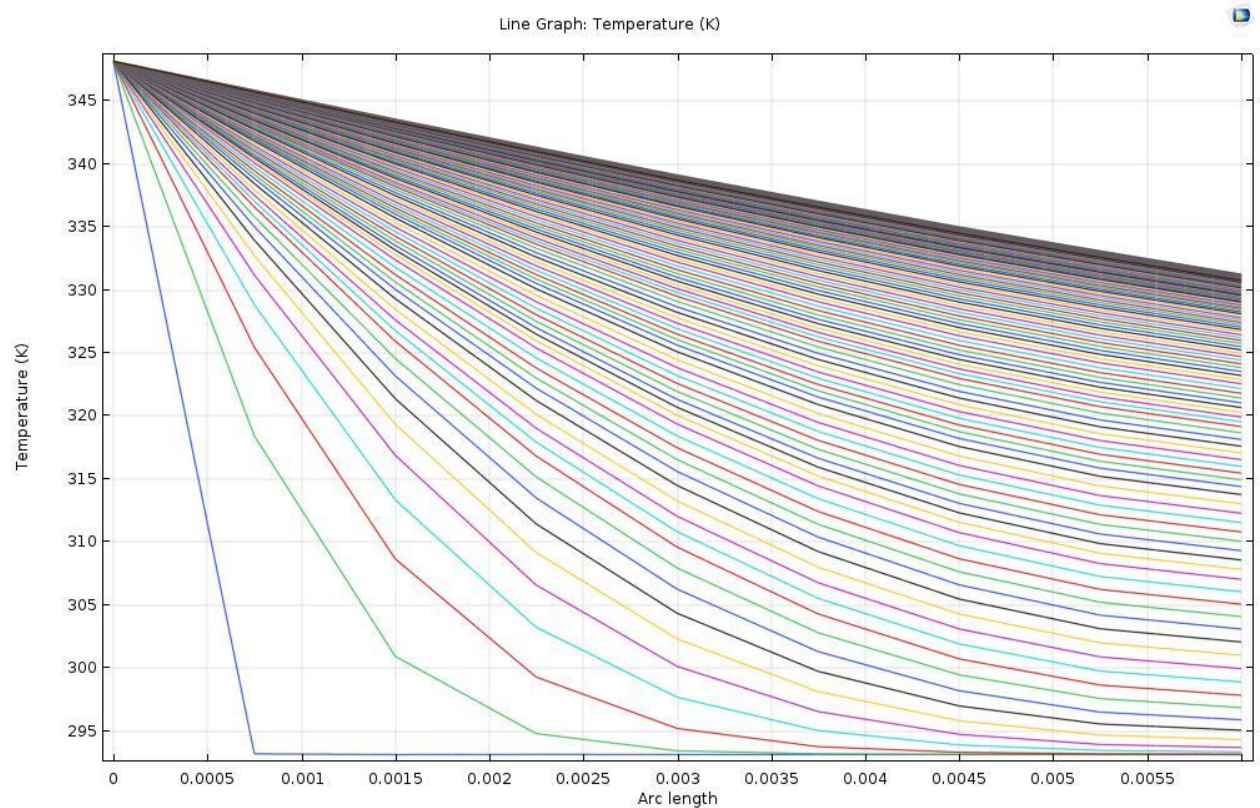
Figure 4. 7. Shows the temperature distribution of the centerline for pure epoxy fully cured with change of time. The blue line represents the temperature of the center line at 0s, green line represents T at 1s and so on.

From the diagram, the temperature distribution of the pure epoxy model is similar to pure PZT model which is shown in figure 4.1. But the final temperature on the top side of the sample is much lower than 75C. This is because the material properties for epoxy are different from PZT, which is affected more by heat transfer procedure and thermal dissipation has more related to heat convection and surface radiation. In this

case, some of the heat energy lost during the heat transfer process so that the final temperature on the top of the sample is less than the fixed temperature 75C. Figure 4.8 shows the result for the midpoint of the top side of the sample. The horizontal axis represents the time and the vertical axis represents the temperature.
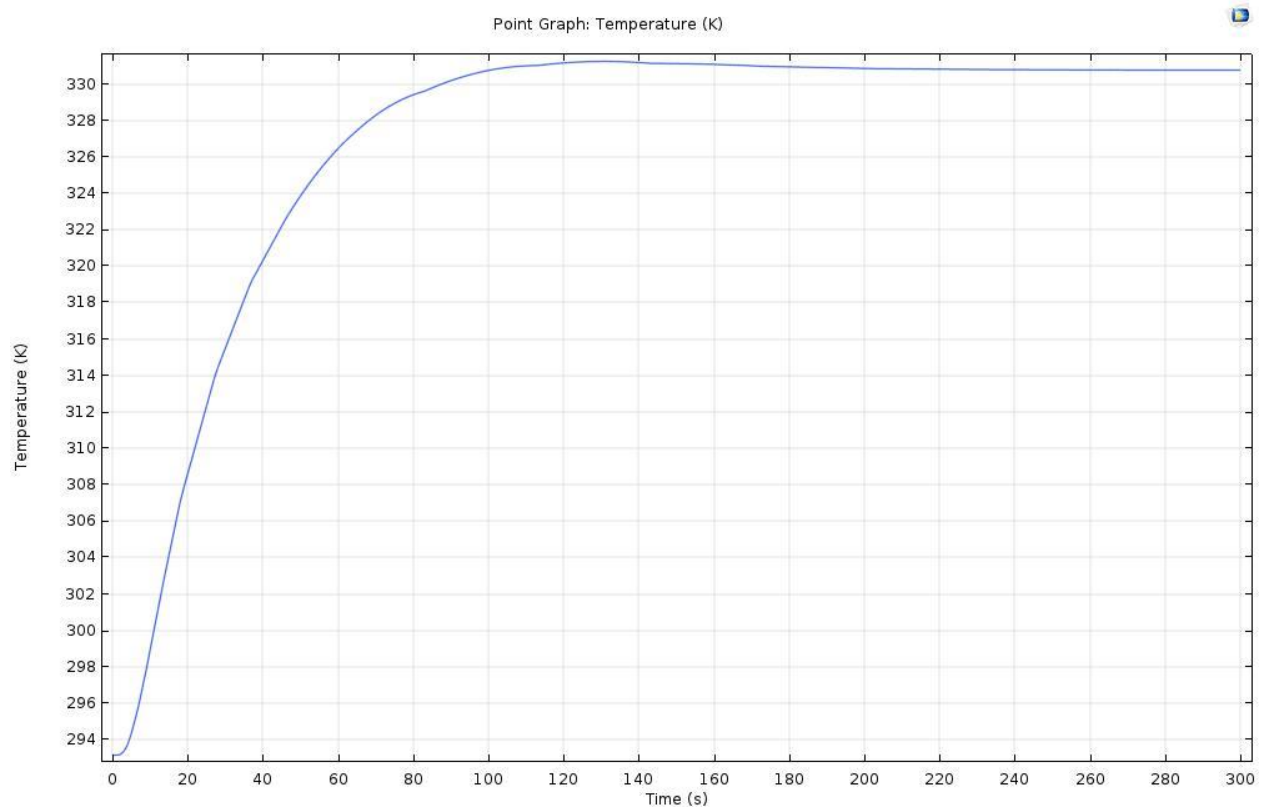
Figure 4. 8. Shows the temperature distribution of the midpoint of the top side for the pure epoxy fully cured bulk model.

From the figure, the temperature distribution of this fixed-point increases with increasing the time step and finally reach the temperature around 332K. The lost temperature is caused by thermal dissipation mentioned before.

4.1.4 Temperature distribution of pure epoxy partially cured model

In section 4.1.3, the temperature distribution of pure epoxy fully cured was discussed. In this section, the results for partially cured epoxy are shown. The difference

between these two types of epoxy is that fully cured epoxy is in solid form and partially cured epoxy is in gel form. In addition, the material properties are different. Figure 4.9 gives us the result for the centerline. The horizontal axis represents the arc length of the pure epoxy model and the vertical axis represents the temperature. The different color of each line represents the temperature distribution of the centerline for each step. From the bottom to top is the temperature distribution at zero-time step and 300s step.
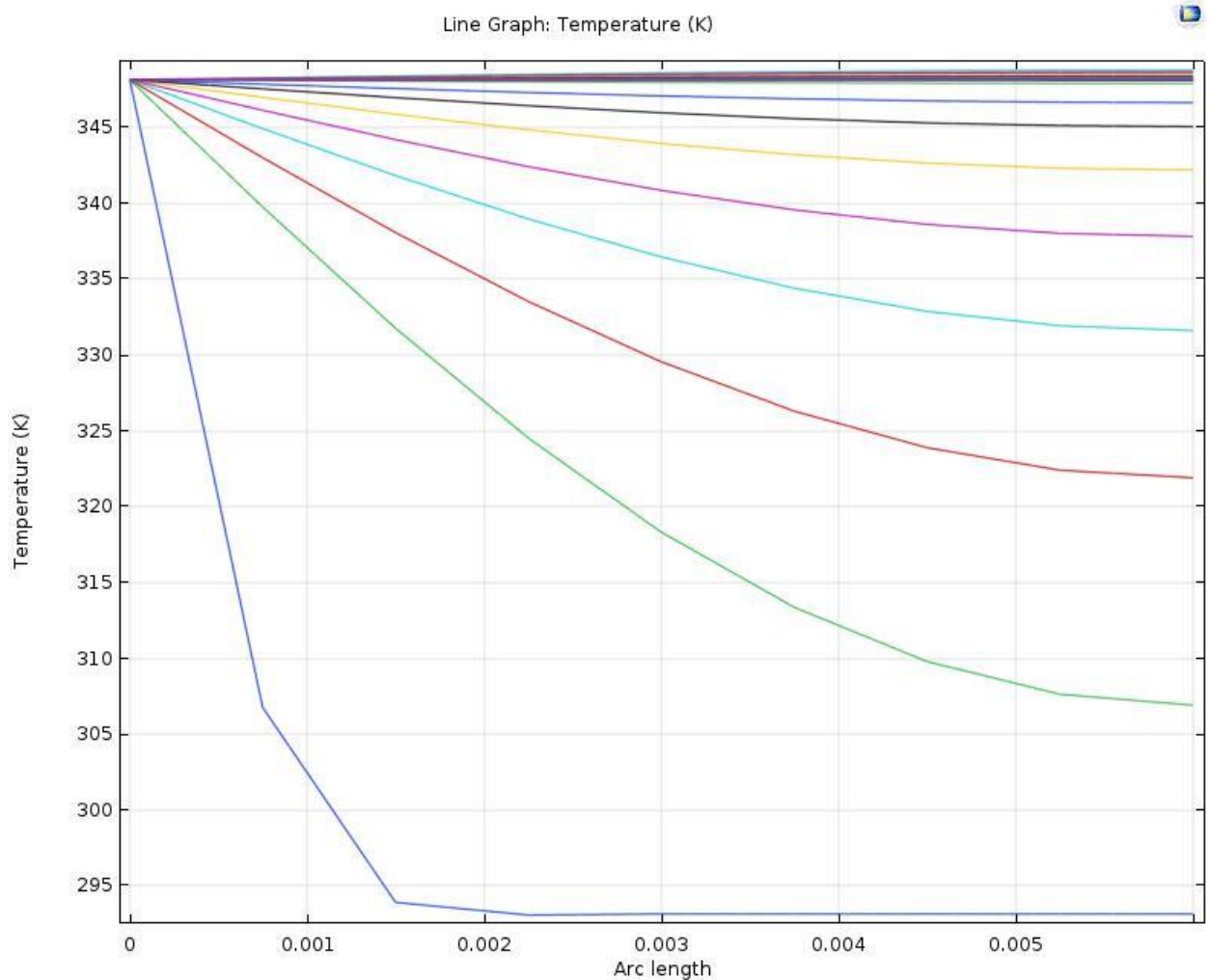
Figure 4. 9. Represents the temperature distribution of the centerline for the pure epoxy partially cured model.

From the figure, it is similar to figure 4.7, but it can reach the fix temperature 75C. This is because that the material properties for partially cured epoxy and fully cured epoxy are different. Since the partially cured epoxy is in gel form, it absorbs much more

heat during the heat transfer process and the heat transfer process is much quicker than in fully cured epoxy. This process is similar for heat transfer in the unit cell so that the effect of heat convection and surface radiation can be neglected. This phenomenon can be proved by figure 4.10, which is the result for the midpoint on the top side of the sample. The horizontal axis represents the time and the vertical axis represents the temperature.
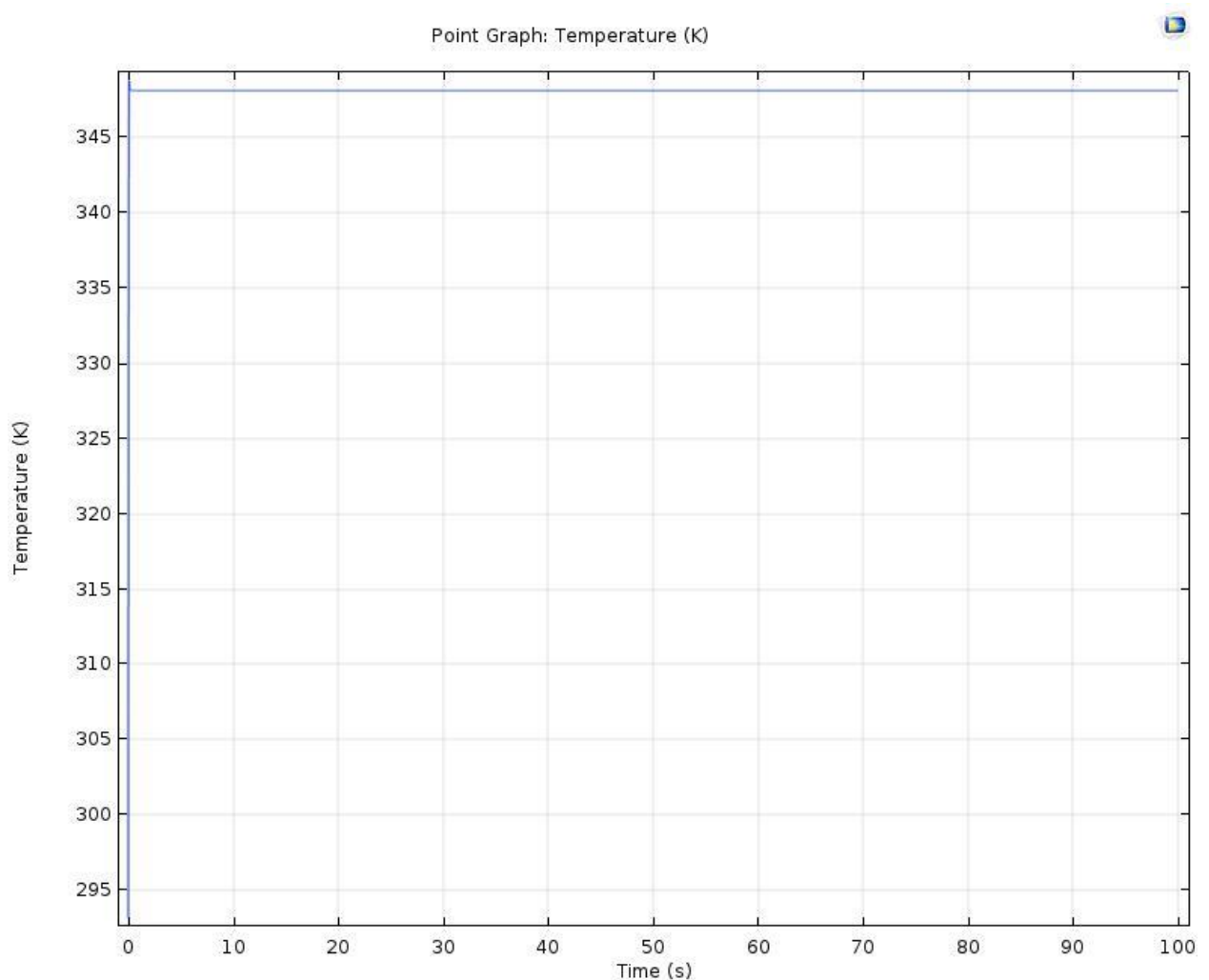
Figure 4. 10. Represents the temperature distribution of the midpoint of the top side of the sample for the pure epoxy partially cured model.

This figure is very similar to figure 4.6, which is for composite PZT models. This shows

the heat transfer process finishes very fast so that the thermal dissipation is almost zero.

4.2 Stress and strain caused by thermal expansion

In this section, the results for stress and strain caused by thermal expansion during the heat transfer process will be introduced for both centerline of the unit cell and midpoint on the top side of the unit cell.

4.2.1 Stress and strain of the centerline of the unit cell

The reason why the centerline of the cross section of the unit cell of the pure PZT model was chosen is that this centerline is from bottom side of the model to the top side of the model with the same direction of the heat transfer. All the points on this centerline can represent the properties at that horizontal interface if it considers that horizontal interfaces were cut through this centerline. In this case, all the information about mechanical and thermal properties can be obtained for the whole domain change with the time. Figure 4.11 and Figure 4.12 shows the centerline for pure PZT/epoxy model and composite PZT models.
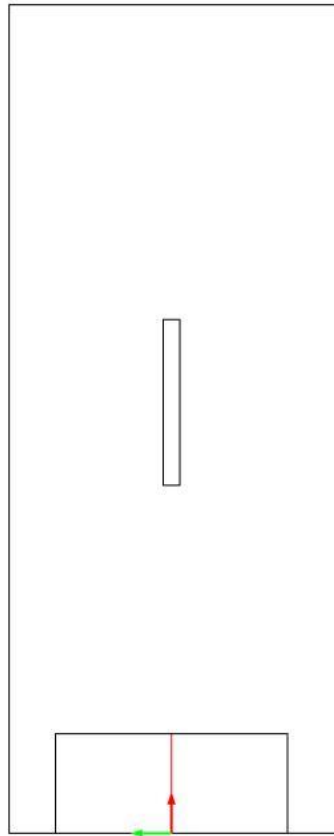
Figure 4. 11. Represents the centerline for pure PZT and pure epoxy bulk models. The red line in the middle is the centerline of bulk model.
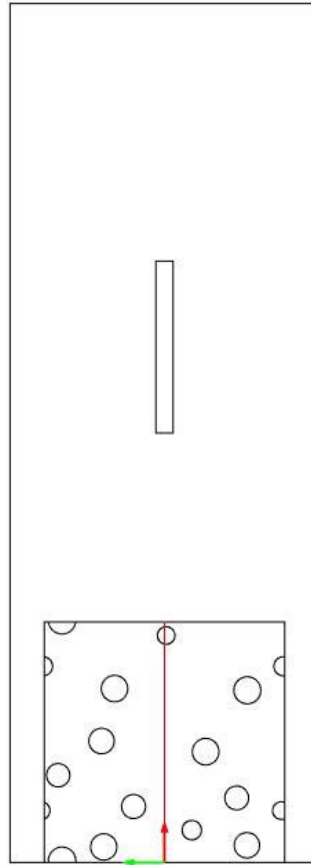
Figure 4. 12. Represents the centerline of the unit cell of the composite PZT bulk models. The red line is the centerline of the unit cell.

Since the two-phase materials epoxy DGEBA and PZT-5A have coefficients of thermal expansion, the composites will have some deformation due to the heat transfer process and this will generate stress and strain in the composite. In addition, thermal expansion of PZT and epoxy is different because the material properties of these two types of material are different. This will also induce stress and strain. The results for the pure PZT model are provided in Figure 4.13. The horizontal axis represents the temperature and the vertical axis represents the Von-Mises stress. Different color from left to right represent the stress change with each time step, which is from 0s to 300s.
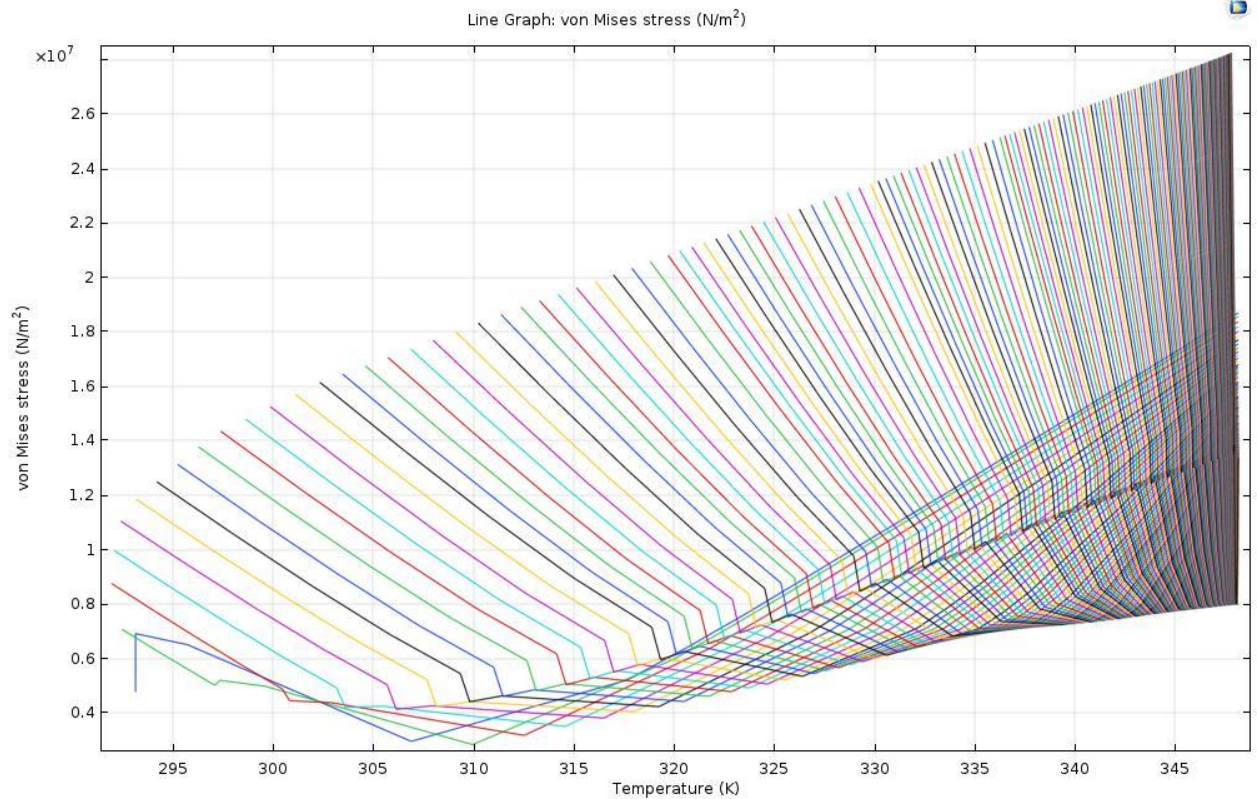
Figure 4. 13. Represents the von-Mises stress of the centerline for pure PZT bulk model.

Von-Mises stress is a value used to determine if a given material will yield or fracture, which represent a scalar field quantity obtained from the volume distortion energy density and used to measure the state of stress. From figure 4.13, von-Mises stress decreases with increasing the temperature at the beginning and keep increasing with increasing temperature after it reaches the minimum value for each time step. This means the samples have more deformation with high temperature and long-time step. The more deformation leads to a larger value of von-Mises stress in the samples. Figure 4.14 shows the result of the centerline of strain caused by thermal expansion for pure PZT bulk model. The horizontal axis represents the arc length of the model and the vertical axis represents the strain. Different color from the bottom to top represent the strain change with each time step, which is from 0s to 300s.
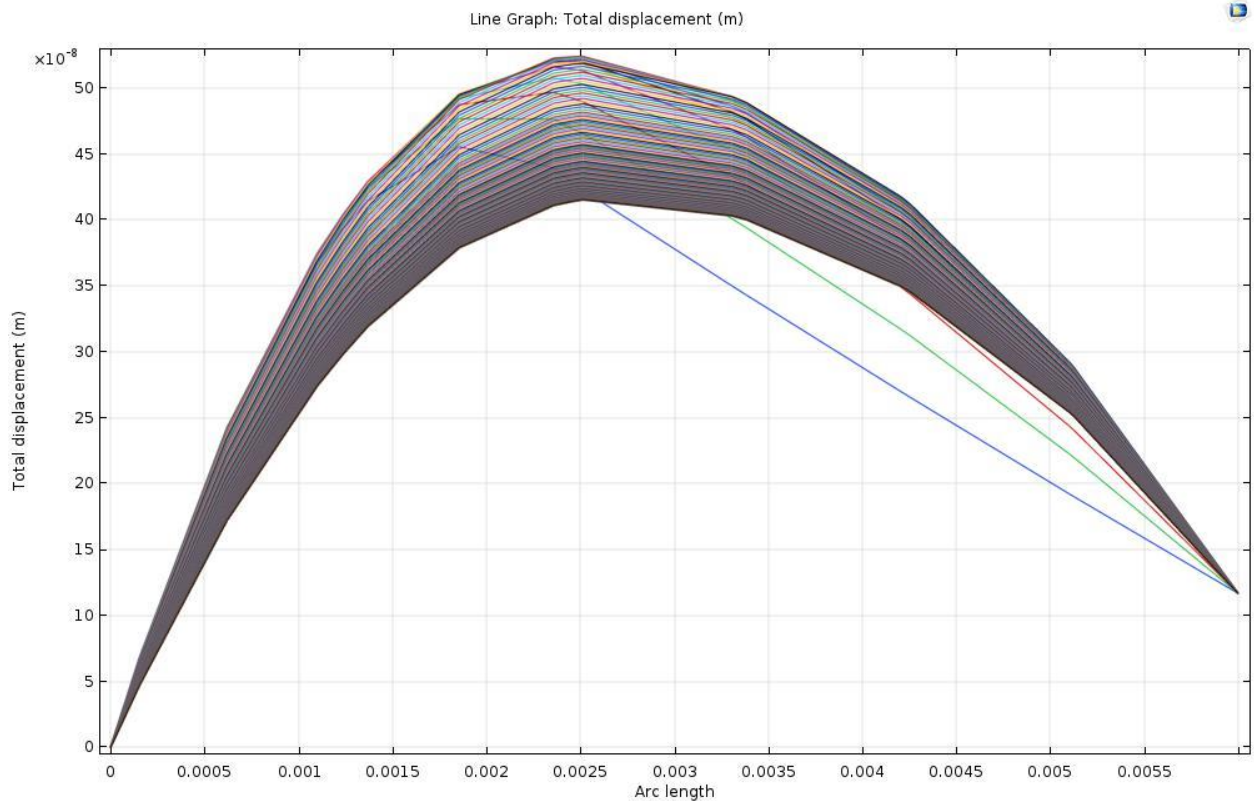
Figure 4. 14. Represents the strain of the centerline caused by thermal expansion.

From this figure, the strain increases in the bottom part of the sample and decreases in the top part of the sample. This is because the temperature of the bottom part is higher than the top part and heat transfer first happens in the bottom part of the sample. The largest deformation happens at the thickness about 0.0025m, which is close to the middle part of the sample. In addition, the strain for each time step globally increases with increasing time step and finally reach stable status.

Next, the results for pure epoxy bulk models will be introduced. First, the results for fully cured epoxy will be shown. Figure 4.15 gives the von-Mises stress of the centerline with respect to the arc length. The horizontal axis represents the arc length

of the model and the vertical axis represents the Von-Mises stress. Different color

from left to right represent the stress change with each time step, which is from 0s to

300s.

From the result, it shows that the stress decreases sharply close to the bottom

side of the sample, which generally has a higher temperature than the top part for each

time step. It then increases a little bit for each time step. In addition, von-Mises stress

generally increases in the polymer matrix with increasing time. Generally, the stress is

much larger within the matrix with higher temperature because a higher temperature

will lead to more thermal expansion during the heat transfer process.
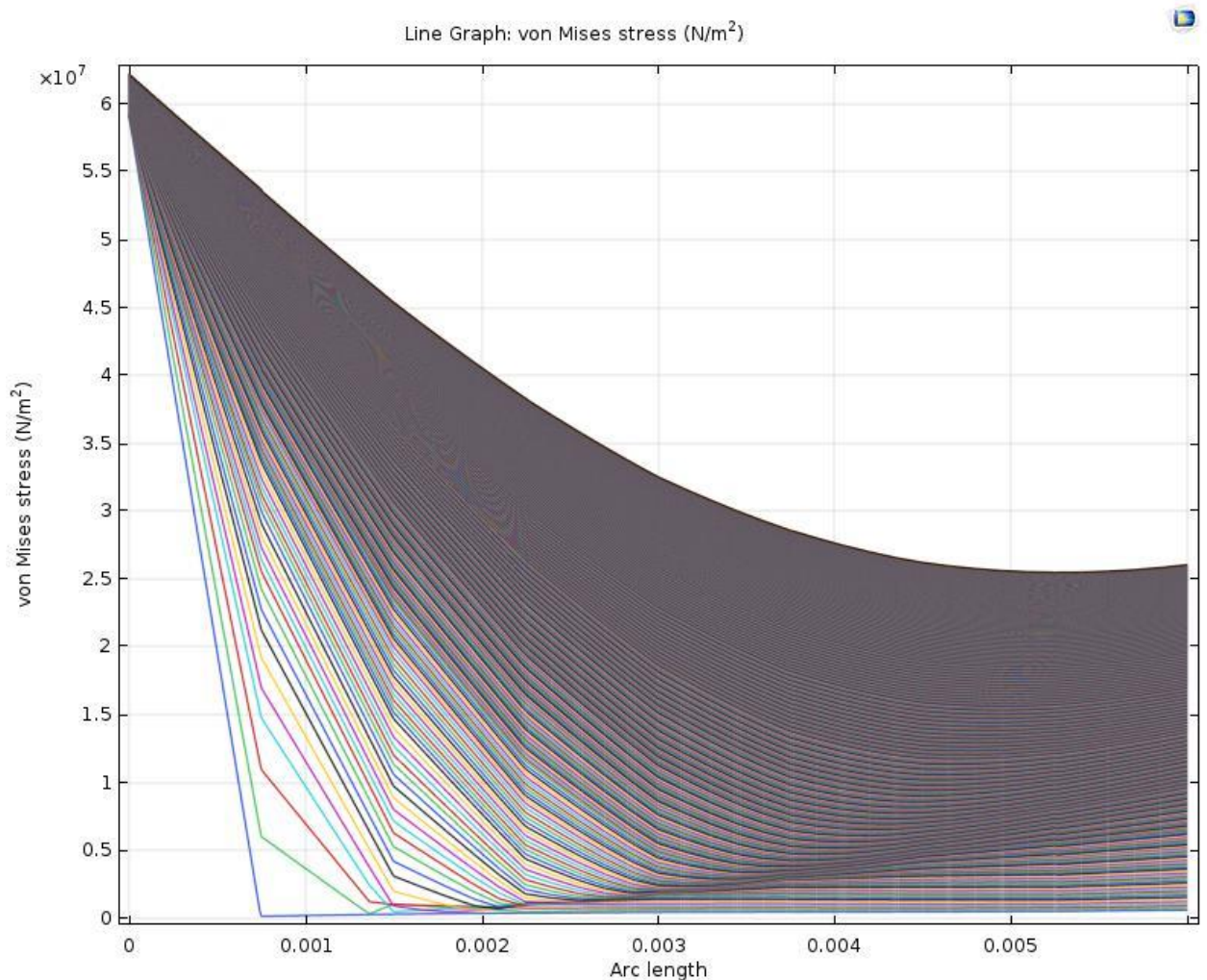
Figure 4. 15. Represents the von-mises stress of the centerline with respect to arc length change with

time step. Epoxy fully cured bulk model.

Figure 4.16 will show the result for the strain of the centerline of the polymer matrix. The horizontal axis represents the arc length of the model and the vertical axis represents the strain. Different color from the bottom to top represent the strain change with each time step, which is from 0s to 300s. From the figure, the strain increases fast at the beginning of the arc length, which is close to the bottom side of the polymer. Compared to Figure 4.15, it makes sense because that the part of polymer matrix has larger stress at the bottom side of the model which leads to more deformation inside the model close to the bottom side. But it becomes stable close to the top part at the beginning of the time step and finally increases for the whole domain with increasing the time step. This is because heat transfer procedure does not go through the whole domain at the beginning of the time step. Once the heat transfer process is done in the matrix, it will cause larger strains with increasing time.
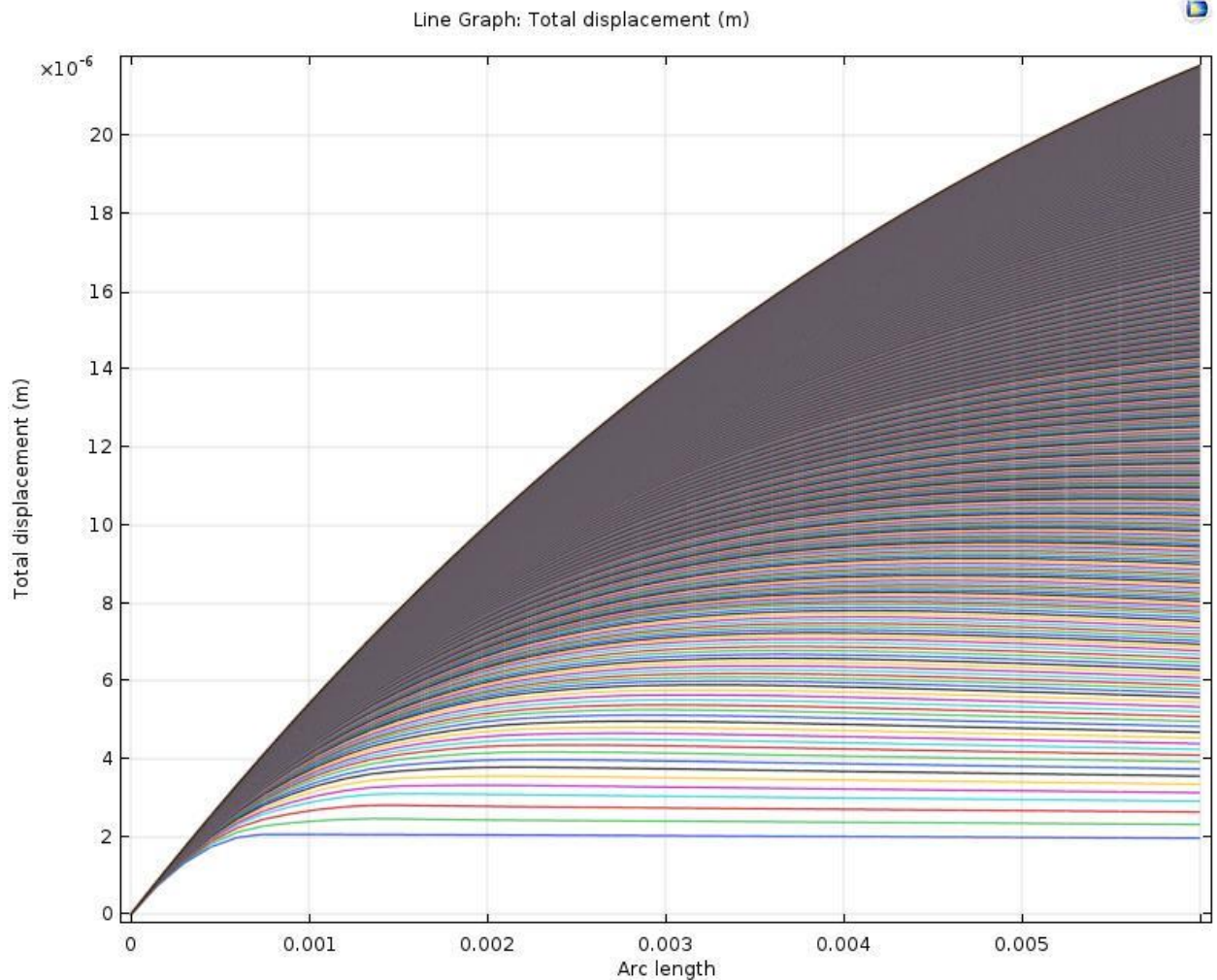
Figure 4. 16. Shows the result for the strain of the centerline caused by thermal expansion of pure epoxy fully cured bulk model.

If the material of epoxy was changed to partially cured, similar results got with fully cured epoxy. The only difference is that the value of von-Mises stress of the centerline is smaller than fully cured epoxy and strain is larger than fully cured epoxy. This is due to the difference of the material properties and the status of the polymer matrix. Moreover, the fully cured epoxy is in solid form and the partially cured epoxy is in gel form. It can generate more deformation than fully cure epoxy during the heat transfer process. However, the Young's Modulus of the fully cure epoxy is larger than the partially cured epoxy. Thus, the stress generated by the partially cure epoxy model is smaller than the fully cured epoxy model. The results are shown in Figure 4.17 and

4.18. The horizontal axis represents the arc length of the model and the vertical axis represents the stress and strain. Different color from the bottom to top represent the stress and the strain change with each time step, which is from 0s to 300s.
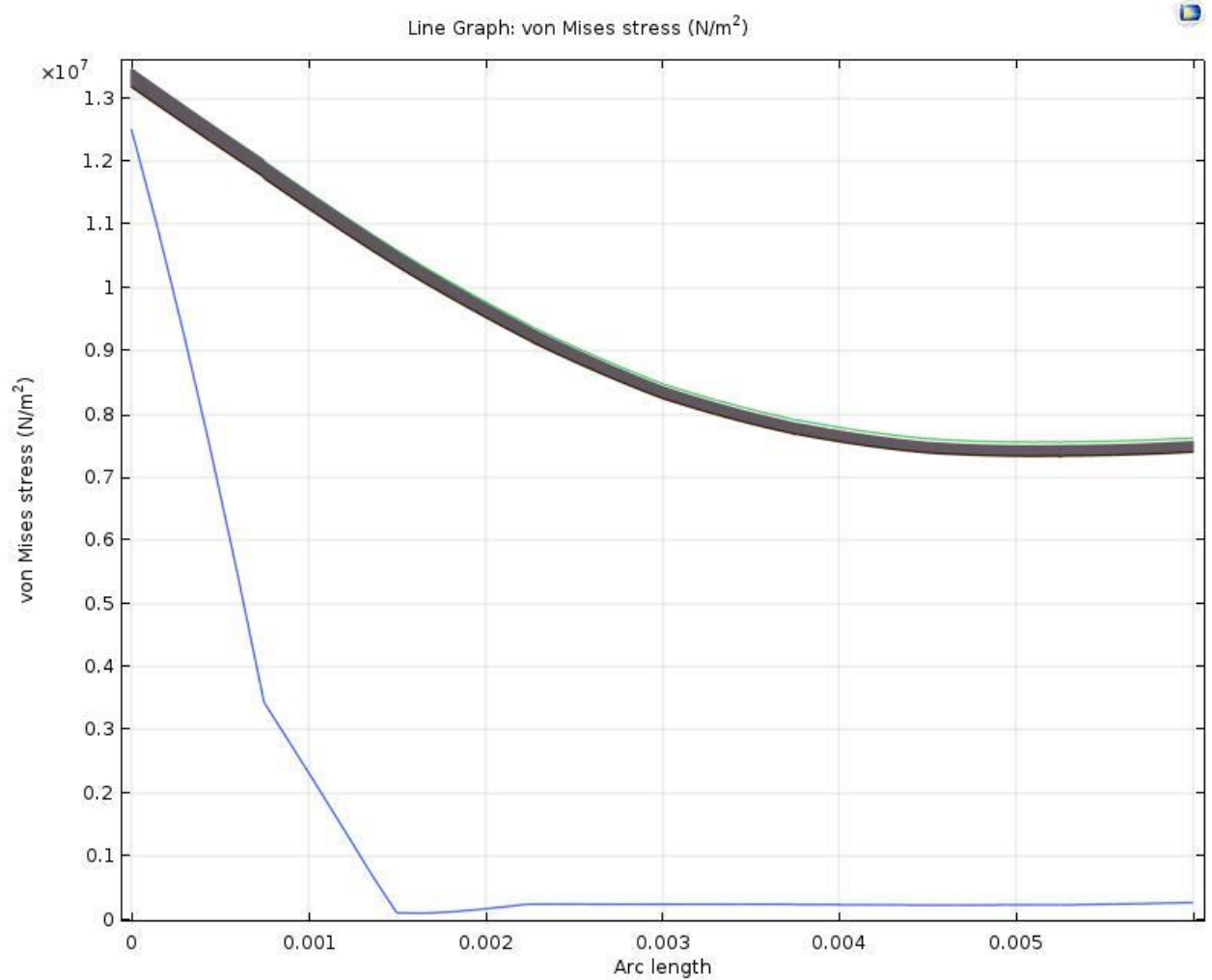
Figure 4. 17. Represents the von-Mises stress of the centerline for the pure epoxy partially cured bulk model.
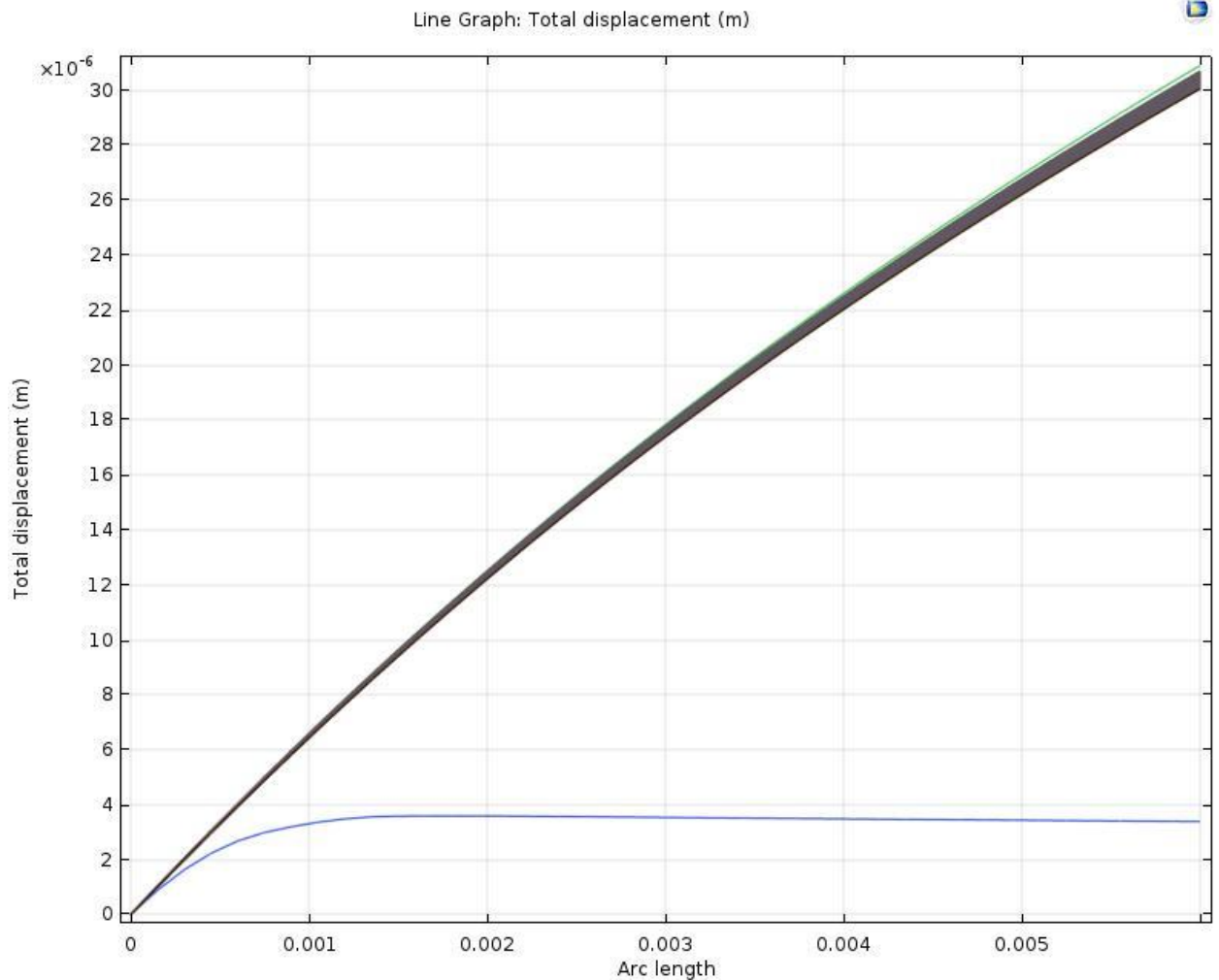
Figure 4. 18. Represents the strain caused by thermal expansion of the centerline for the pure epoxy partially cured bulk model.

The results listed before are pure PZT models and pure epoxy models. They have the same dimension of real samples fabricated by S.Banerjee.[74] Next, let us see the results for composite models. Figure 4.19 to Figure 4.25 are the results for von-Mises stress of the centerline from 10% PZT bulk model to 70% bulk model. The horizontal axis represents the arc length of the model and the vertical axis represents the stress. The blue curve represents the stress at the zero-time step and the purple curve represents the stress of the final time step.
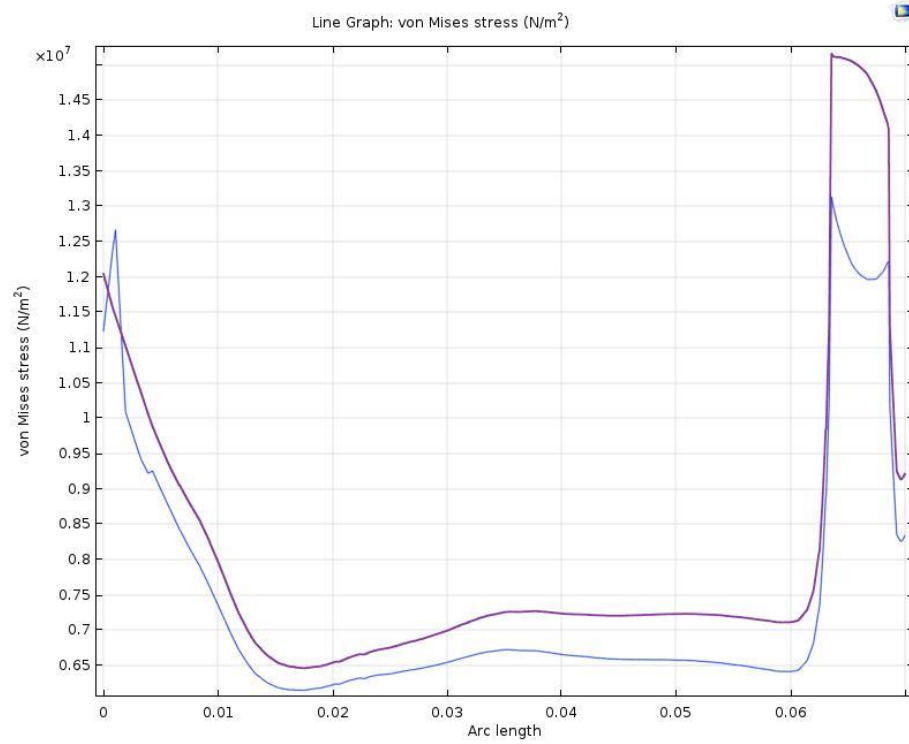
Figure 4. 19. Represents von-Mises stress of the centerline for 10% PZT bulk model.
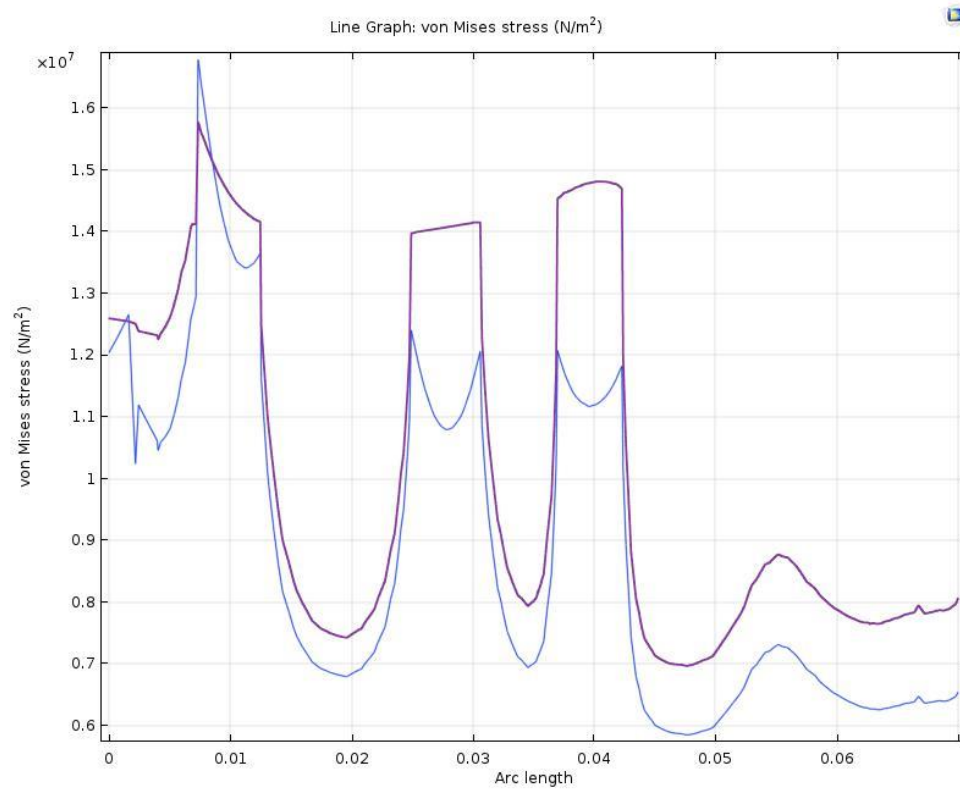
Figure 4. 20. Represents von-Mises stress of the centerline for 20% PZT bulk model.
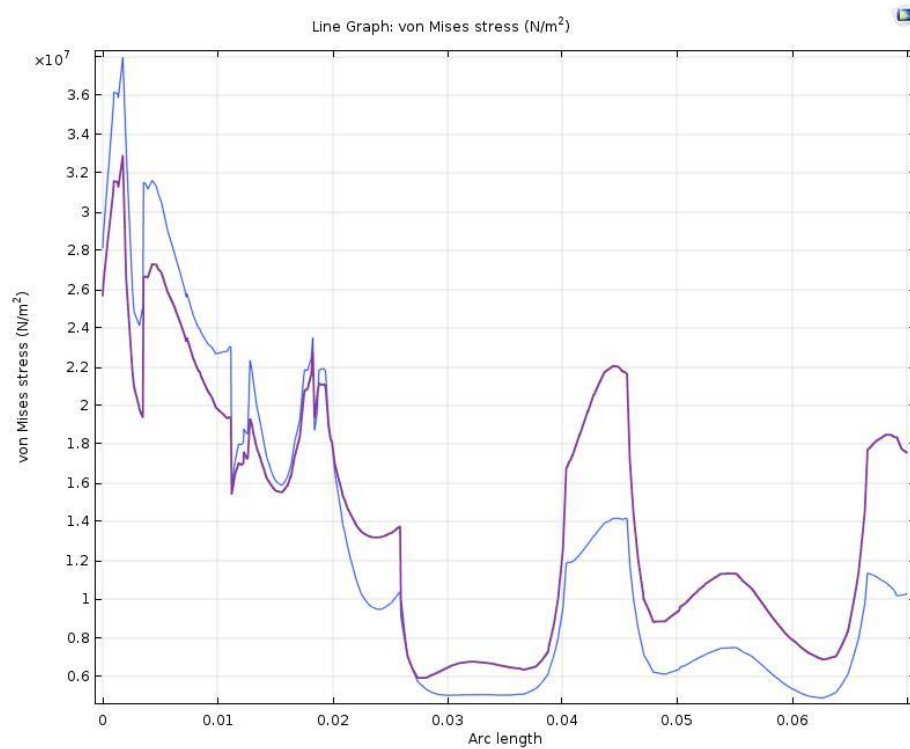
Figure 4. 21. Represents von-Mises stress of the centerline for 30% PZT bulk model.
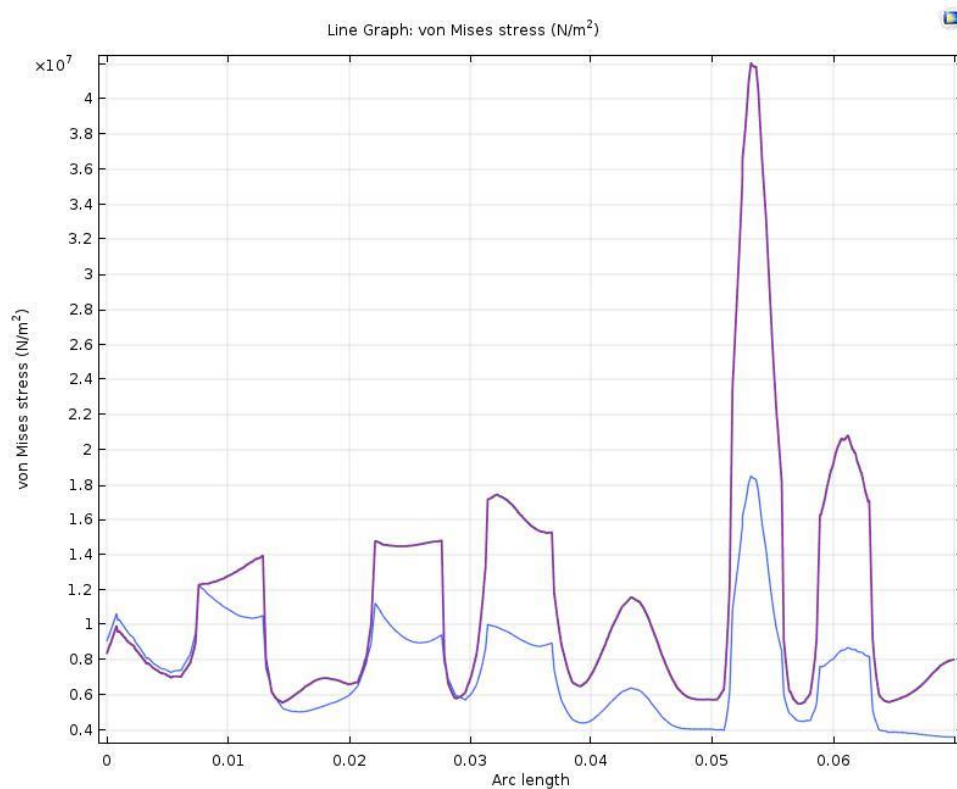
Figure 4. 22. Represents von-Mises stress of the centerline for 40% PZT bulk model.
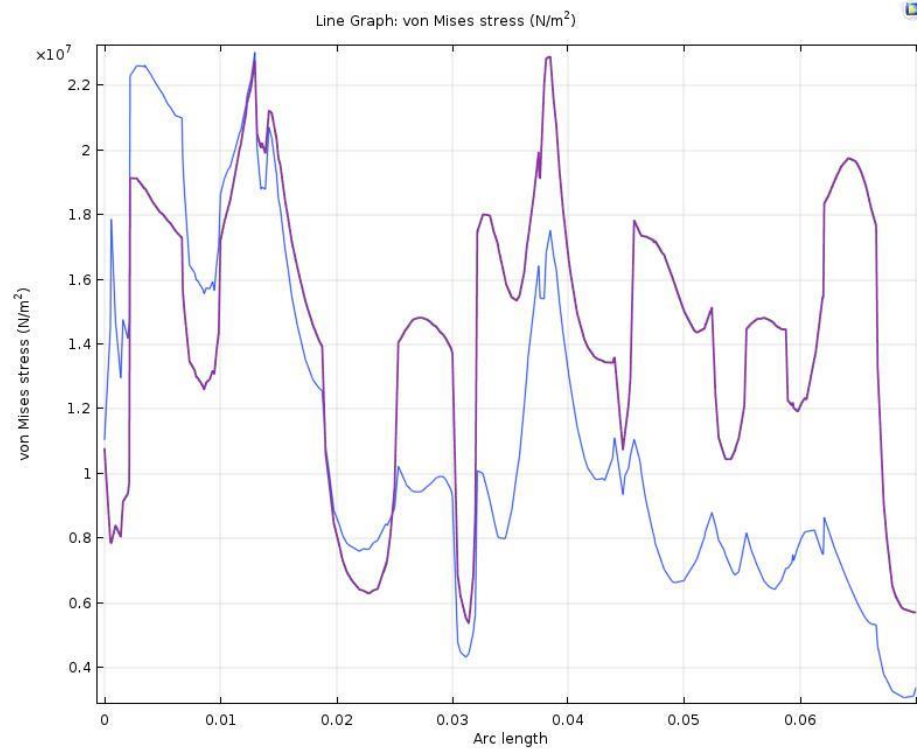
Figure 4. 23. Represents von-Mises stress of the centerline for 50% PZT bulk model.
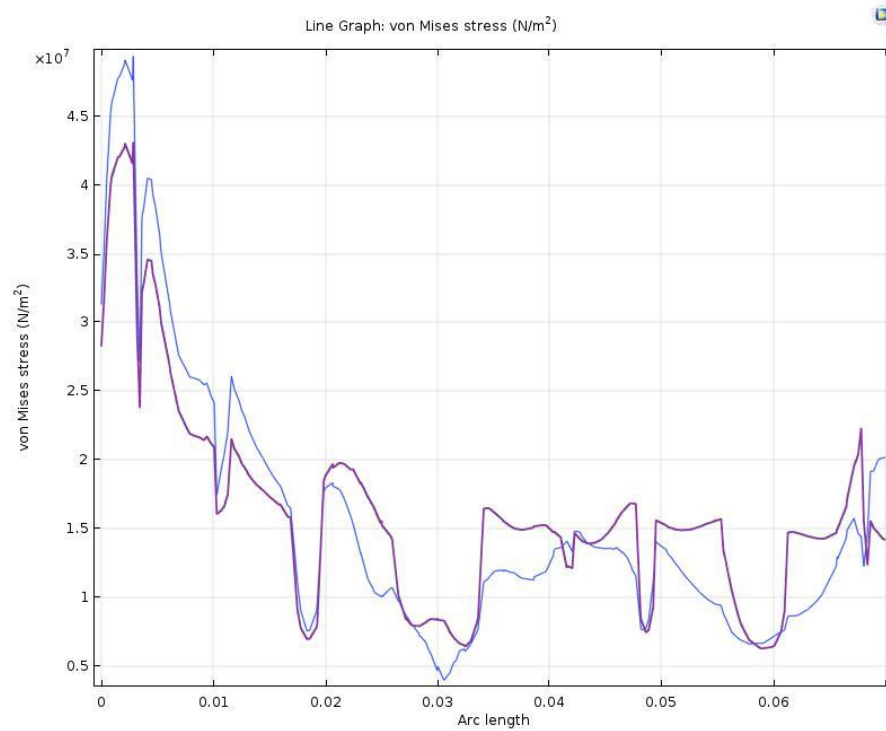
Figure 4. 24. Represents von-Mises stress of the centerline for 60% PZT bulk model.
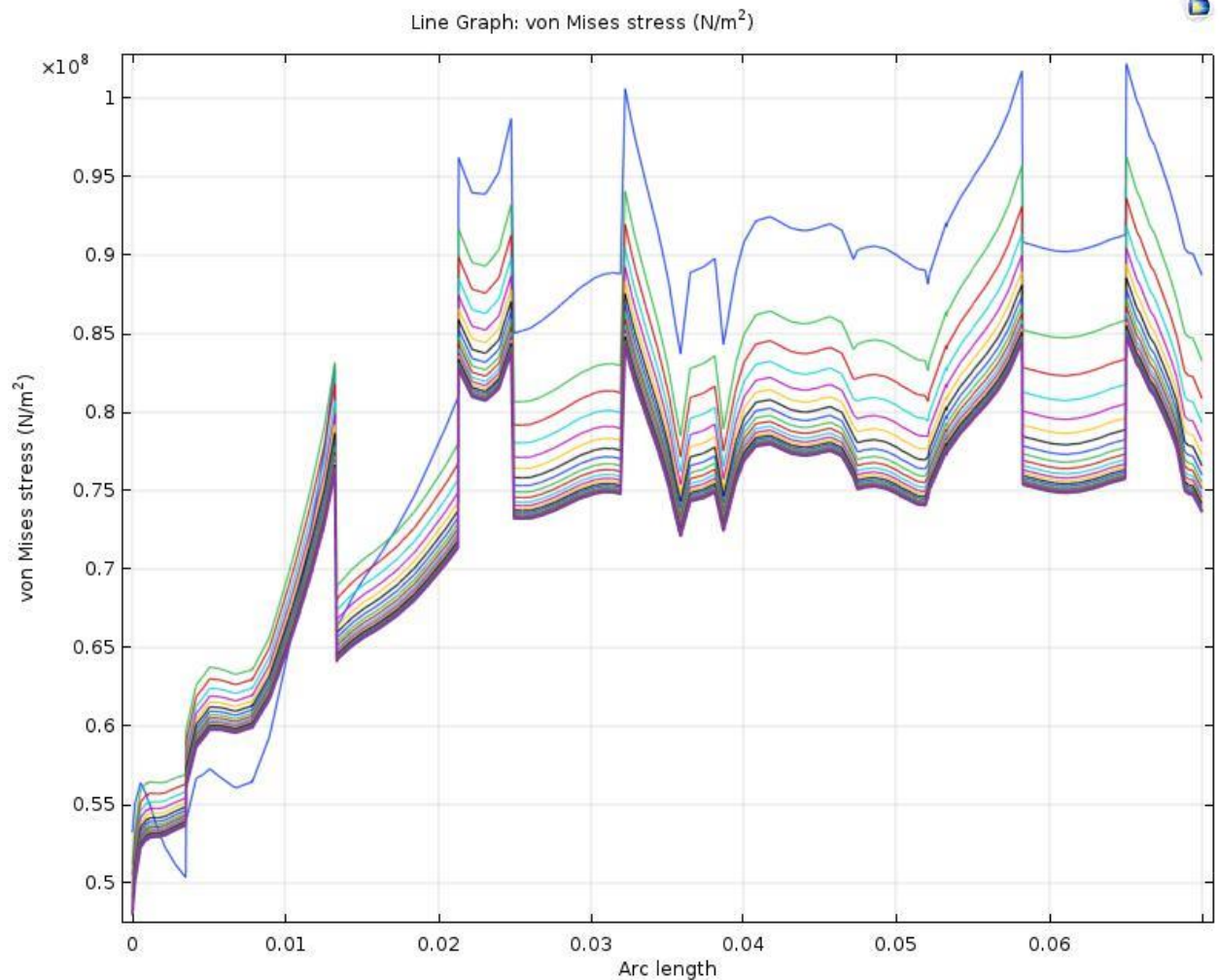
Figure 4. 25. Represents von-Mises stress of the centerline for 70% PZT bulk model change with time. The different colors represent the Von-Mises stress for each time step.

The above figures are von-Mises stress of the centerline for composite PZT models from 10% to 70%. From the figures, it shows that the von-Mises stress generally increases with increasing the volume fraction of PZT. The reason is that stress equal to Young's modulus of the material times strain. Young's modulus of PZT is much larger than epoxy DGEBA. That means the higher the volume fraction of PZT the composite has, the larger Young's modulus the composite has. Since the change of the strain is not too much of each volume fraction of the composite, this is why the stress increases with increasing the volume fraction of PZT. In addition, it is shown that the stress of the centerline dip down and go back up several times in each volume fraction PZT models.

The reason why the curve is not exponential or linear might be due to the position of PZT particles. The stress generated close to the PZT particles is different from the stress generated in polymer part. This may lead to the curve go up and down. It is hard to find which part of the centerline has the largest stress and smallest stress. They are in different place for different volume fraction models. Some of the smallest stress at 0.3mm, such as 30% and 50% PZT models. Some of the smallest stress occurs close to the bottom side of the unit cell and some of them happen close to the top side of the unit cell. The same thing happens for the largest stress. It is hard to find the rules for that. Next, the strain for the composite models will be introduced. The results for strain generated by thermal expansion for each volume fraction of PZT model are given through Figure 4.26 to 4.32. The horizontal axis represents the arc length of the model and the vertical axis represents the strain. The blue curve represents the stress at the zero-time step and the purple curve represents the strain of the final time step.
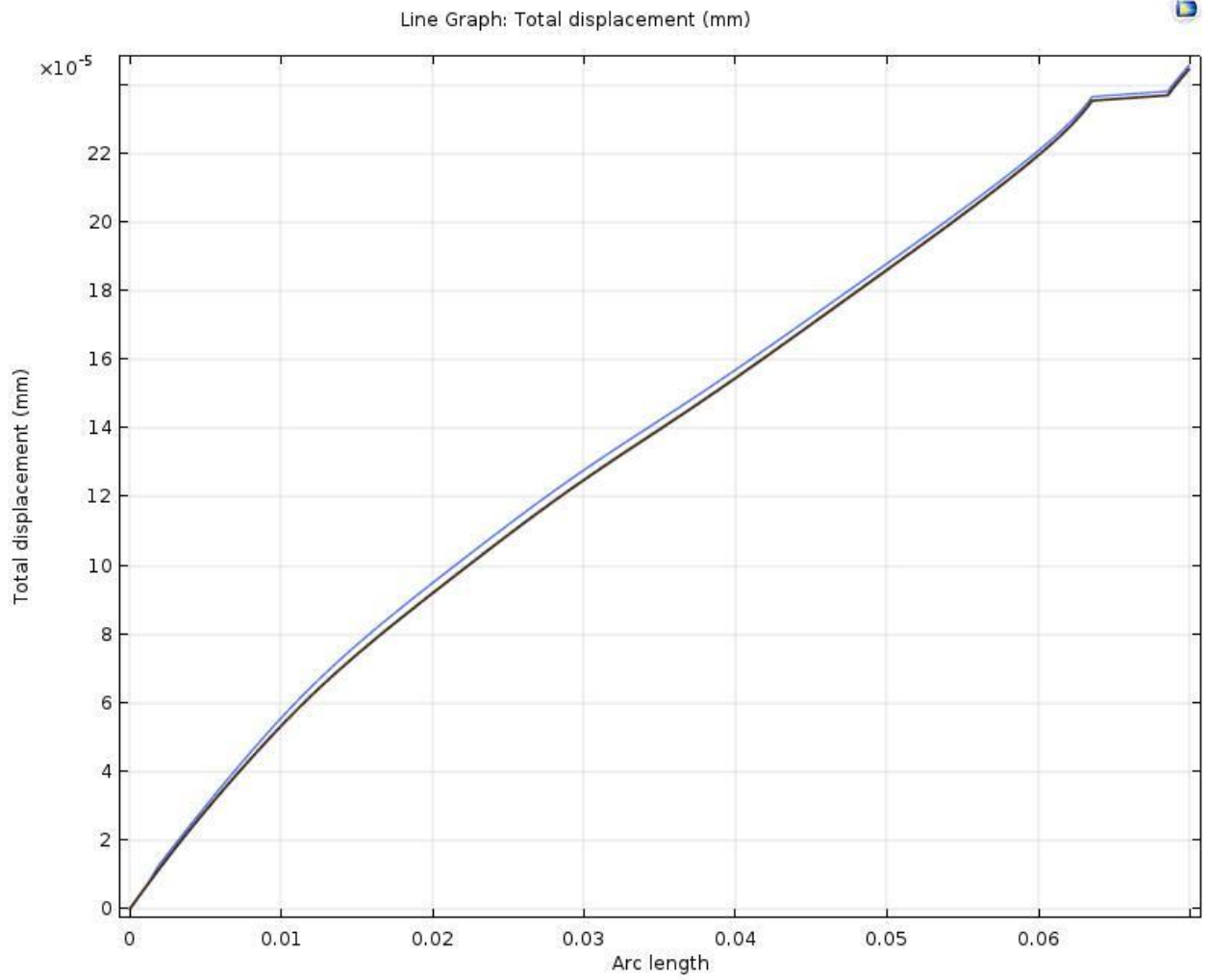
Figure 4. 26. Represents the strain of the centerline for 10% PZT bulk model.
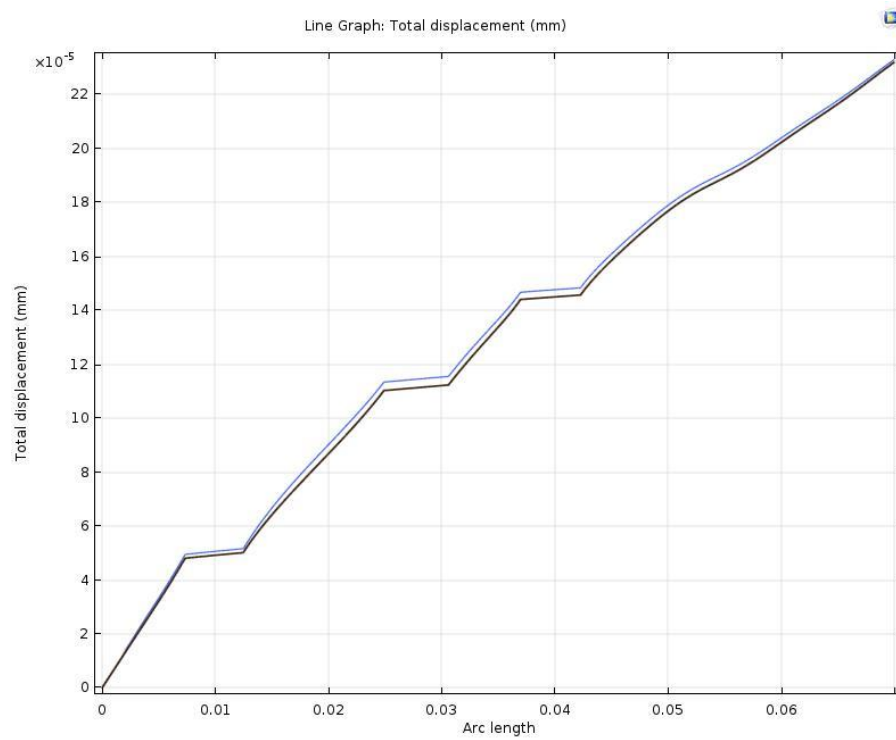
Figure 4. 27. Represents the strain of the centerline for 20% PZT bulk model.
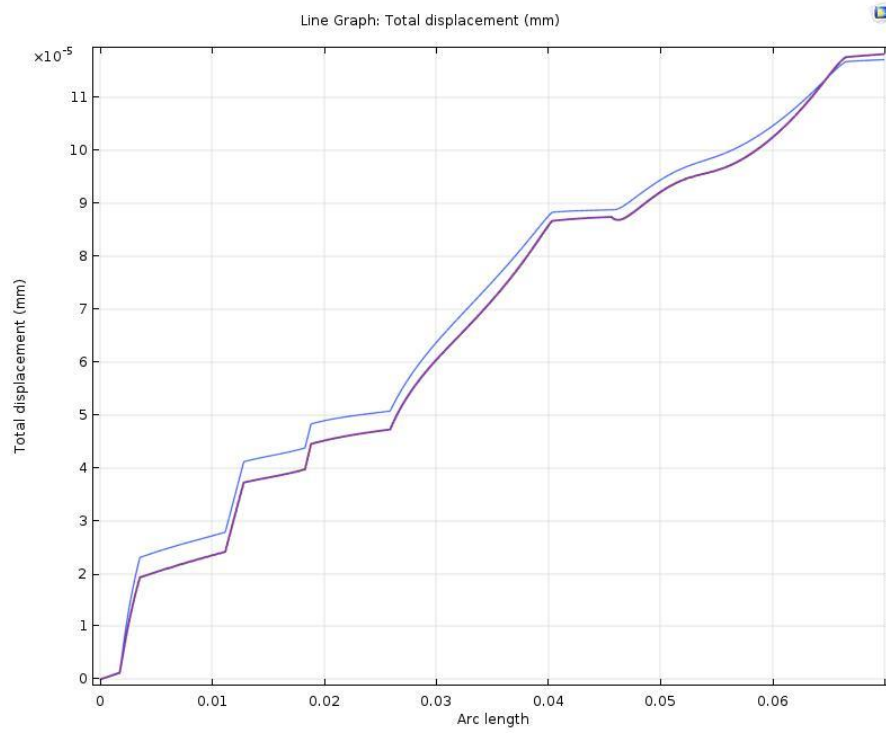
Figure 4. 28. Represents the strain of the centerline for 30% PZT bulk model.
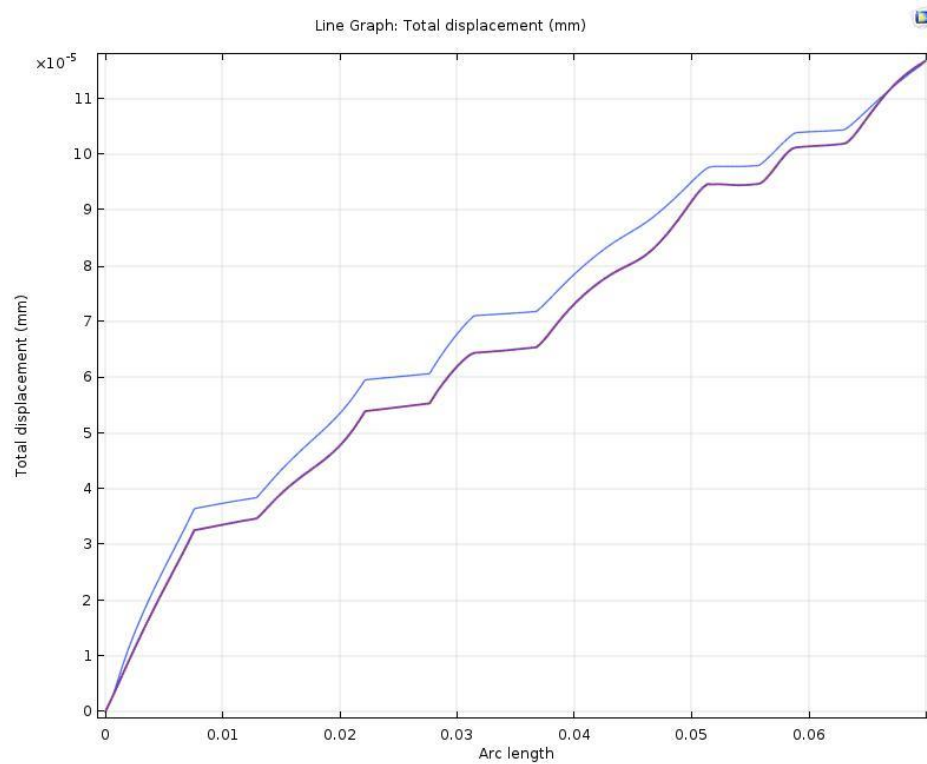
Figure 4. 29. Represents the strain of the centerline for 40% PZT bulk model.
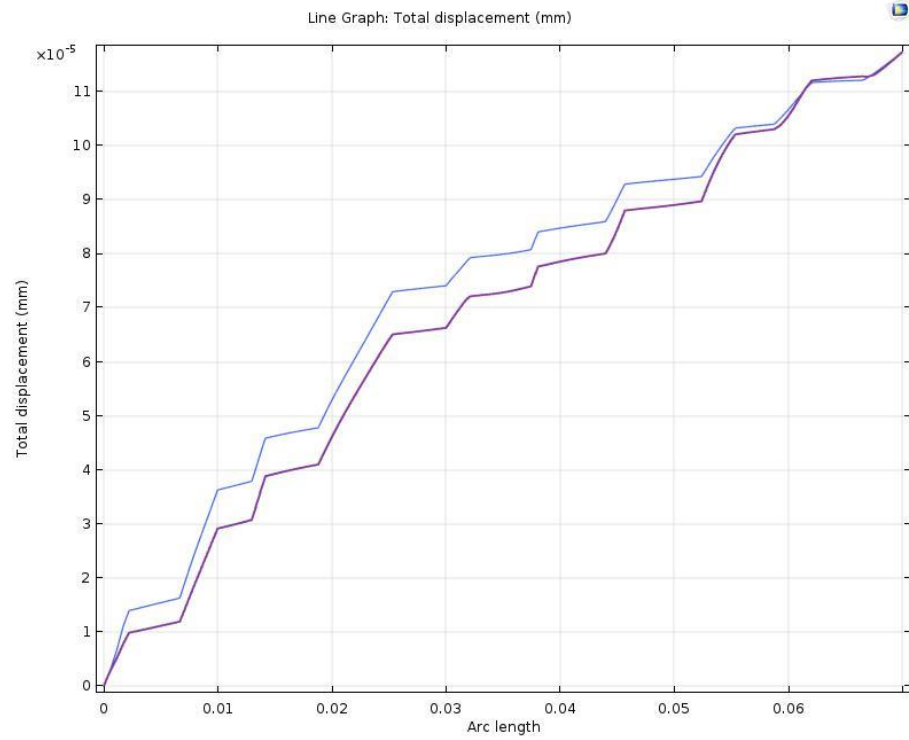
Figure 4. 30. Represents the strain of the centerline for 50% PZT bulk model
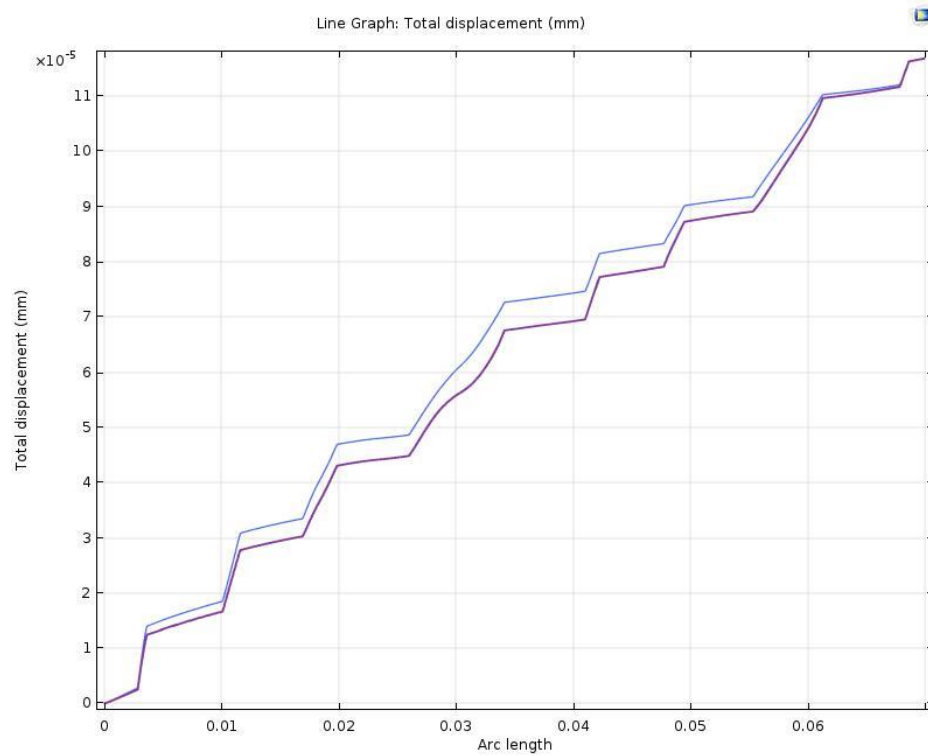
Figure 4. 31. Represents the strain of the centerline for 60% PZT bulk model.
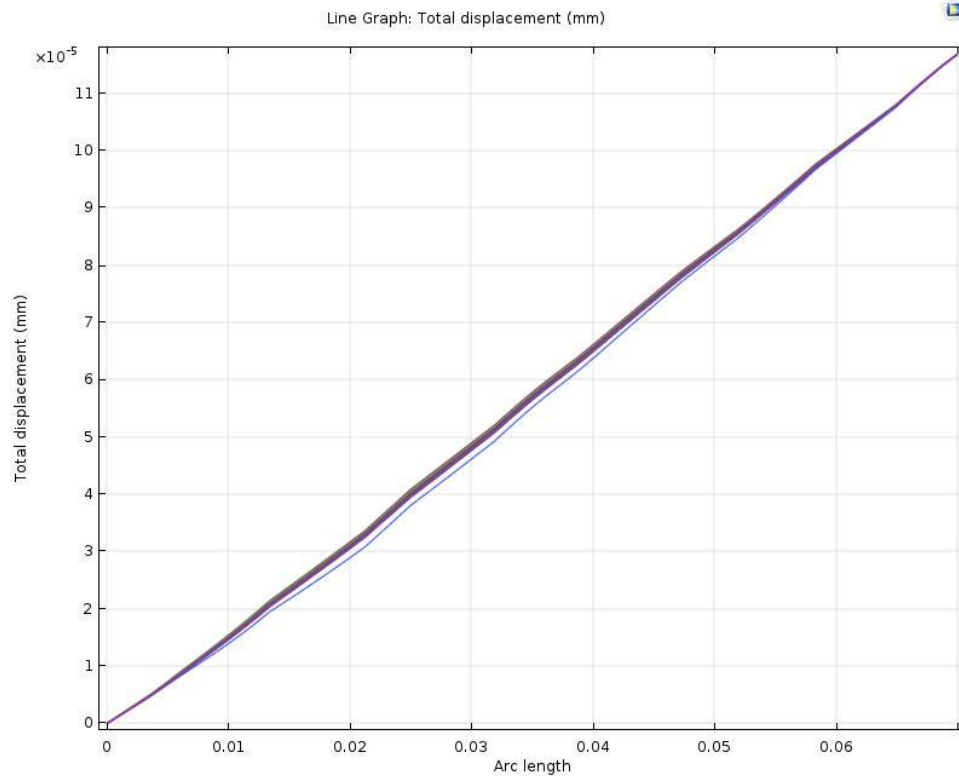
Figure 4. 32. Represents the strain of the centerline for 70% PZT bulk model.

From these figures, the strain of the centerline caused by thermal expansion decreases with increasing the volume fraction of PZT in general. This is because higher volume fraction PZT models have much higher Young's modulus than low volume fractions models. Thus, higher volume fractions PZT models are more stiffness than lower volume fractions PZT models. However, the shape of the strain for each volume fraction is similar, they increase with the arc length. But the values for each point on the arc length decrease with increasing the volume fractions of PZT. For 10% and 20% PZT models, the range of the strain is the same, which is much larger than the rest of the models. This is because for 10% and 20% models, the composites mainly consisted of epoxy DGEBA, which Young's modulus is much smaller than PZT and the polymer matrix is much easier to be deformed than PZT particles. In addition, it seems that the strain in 70% looks like linear while others' have steps. The reason lead to this

difference might be that in high percent volume fraction PZT models, PZT particles almost fulfill the area of the polymer matrix that it seems like PZT particles are uniformly distributed inside the matrix. Thus, the Young's Modulus of the composite is very similar for each part of the composite so that the generated strain looks like continuously.   Since the epoxy phase will be cured during the heat transfer process, composites with more epoxy materials might absorb much more heat during the heat transfer process when added the same heat source on it. The composites which absorb more heat may have much more deformation than higher volume fraction PZT models. That is why 10% and 20% composites models have almost the double range of the strain than other volume fractions PZT models. In this study, it seems like that the largest displacement caused by thermal expansion occurs at 10% PZT composite.

4.2.2 Stress and strain of the mid-point for the top side of the unit cell

In section 4.2.1, the stress and strain of the centerline of the unit cell was discussed. In this section, the results for stress and strain of the midpoint of the top side of the unit cell will be shown for each volume fraction of PZT bulk models. Such results for von-Mises stress will be given through Figure 4.33 to 4.39 for 10% to 70% PZT bulk models.
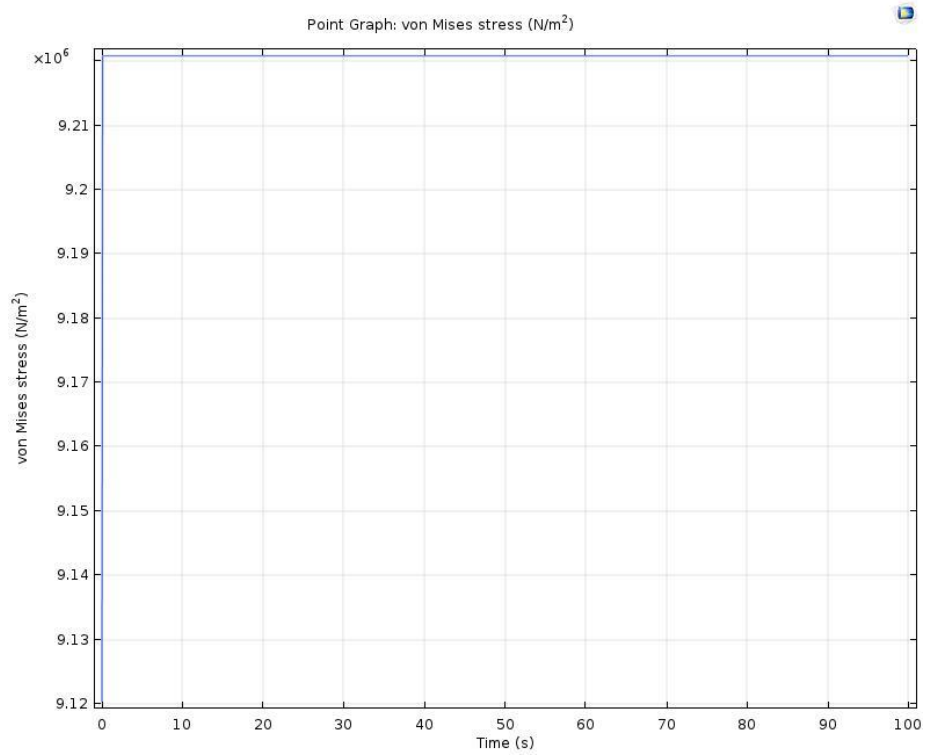
Figure 4. 33. Represents von-Mises stress of midpoint of the top side for 10% PZT bulk model.
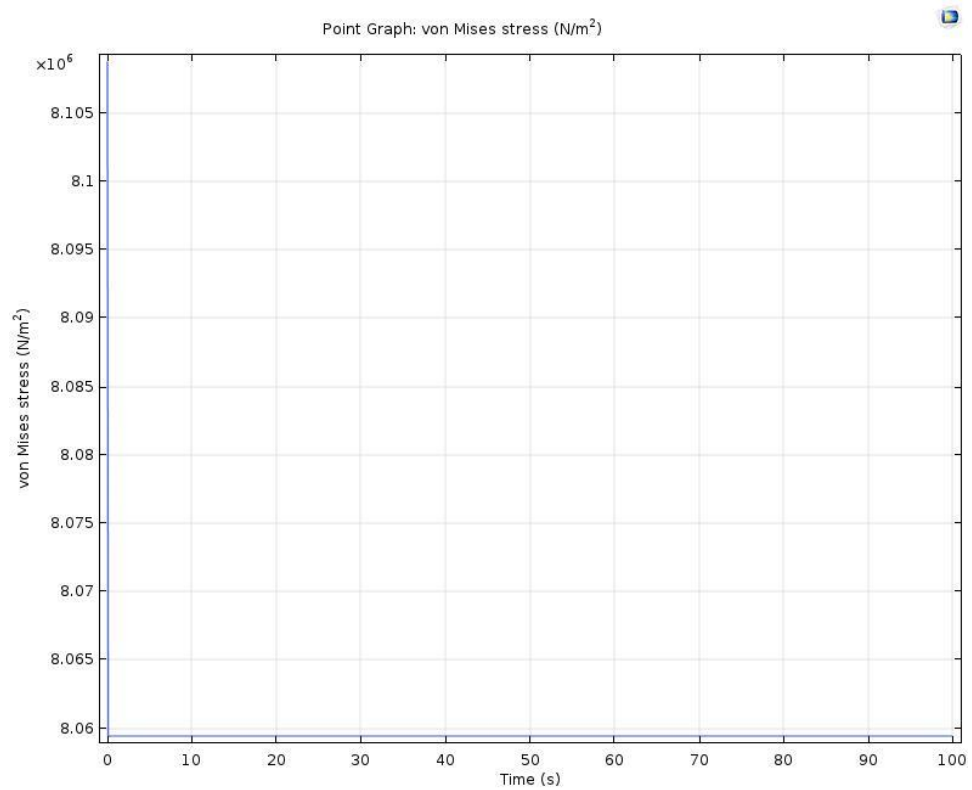
Figure 4. 34. Represents von-Mises stress of midpoint of the top side for 20% PZT bulk model.
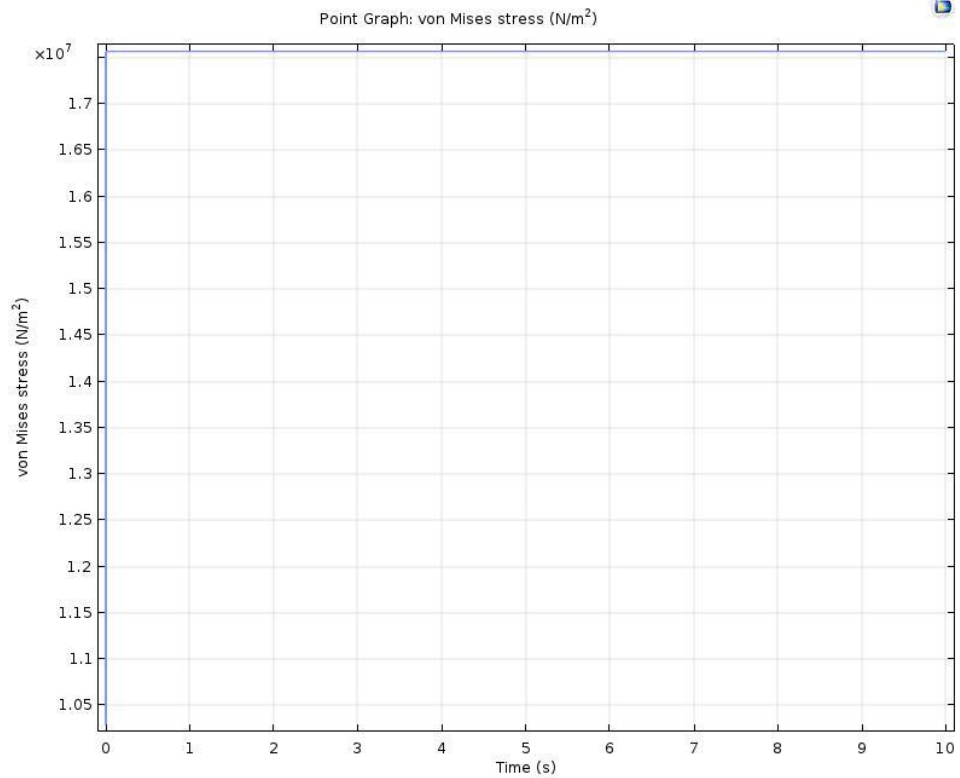
Figure 4. 35. Represents von-Mises stress of midpoint of the top side for 30% PZT bulk model.
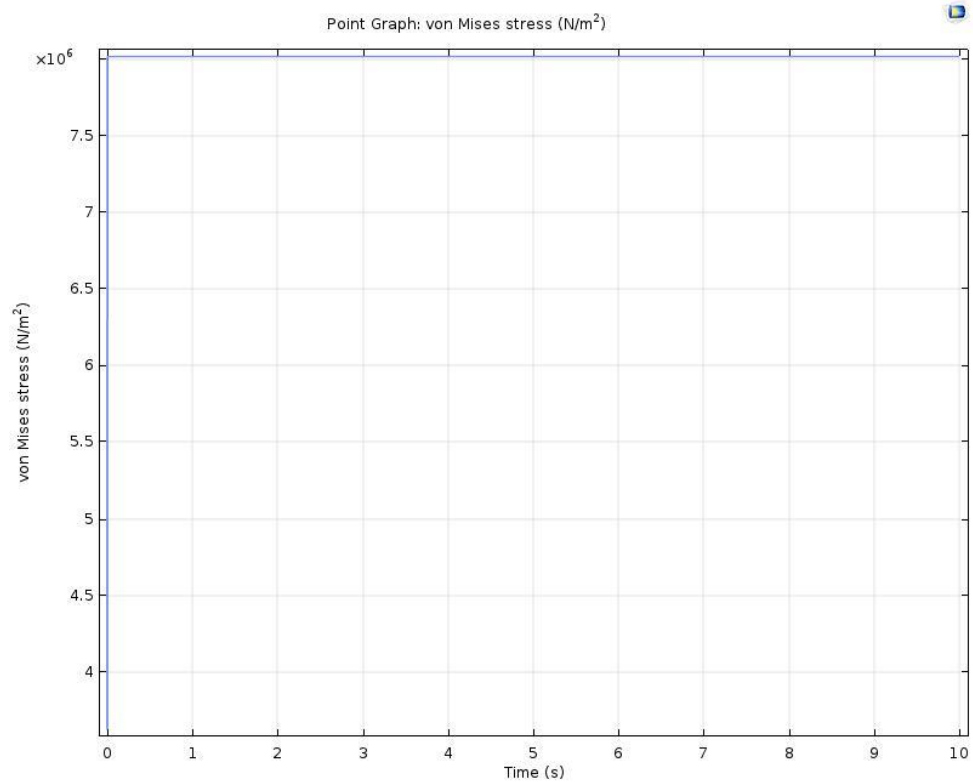
Figure 4. 36. Represents von-Mises stress of midpoint of the top side for 40% PZT bulk model.
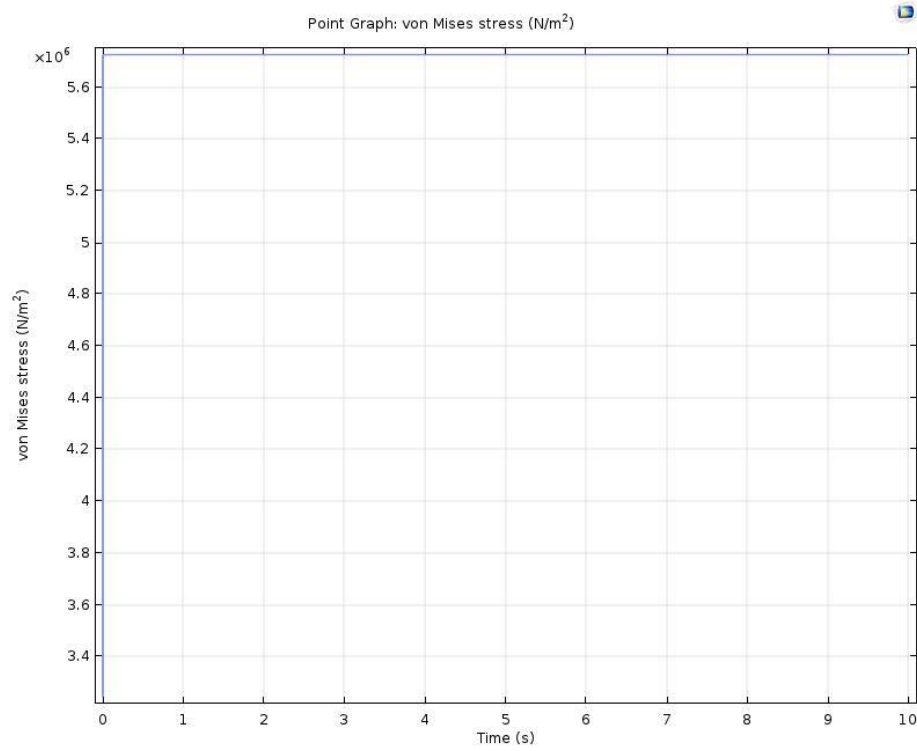
Figure 4. 37. Represents von-Mises stress of midpoint of the top side for 50% PZT bulk model.
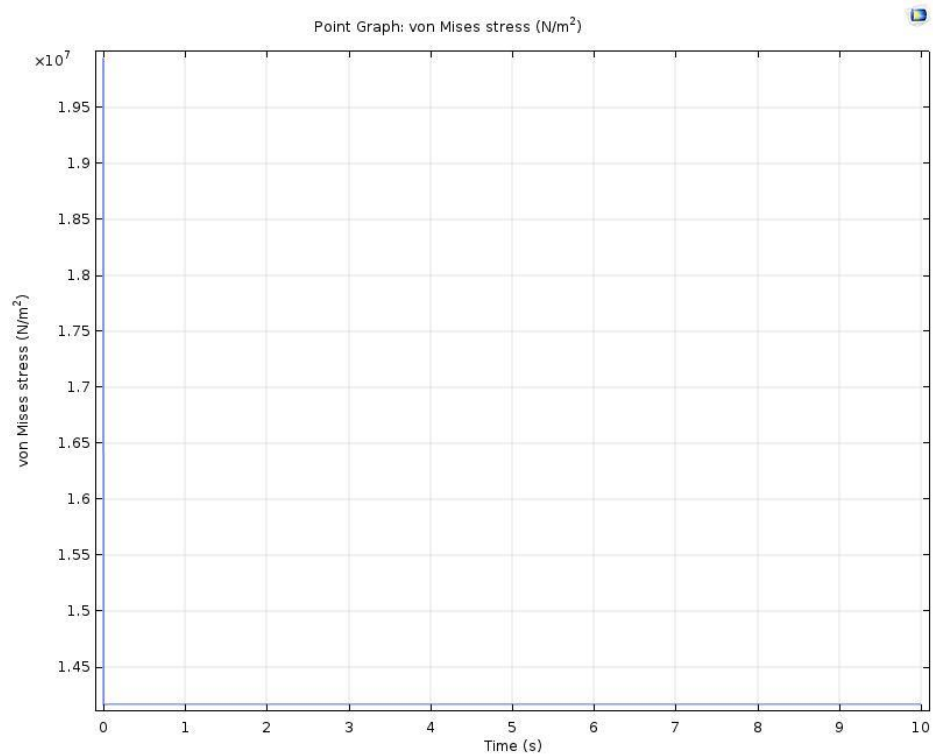
Figure 4. 38. Represents von-Mises stress of midpoint of the top side for 60% PZT bulk model.
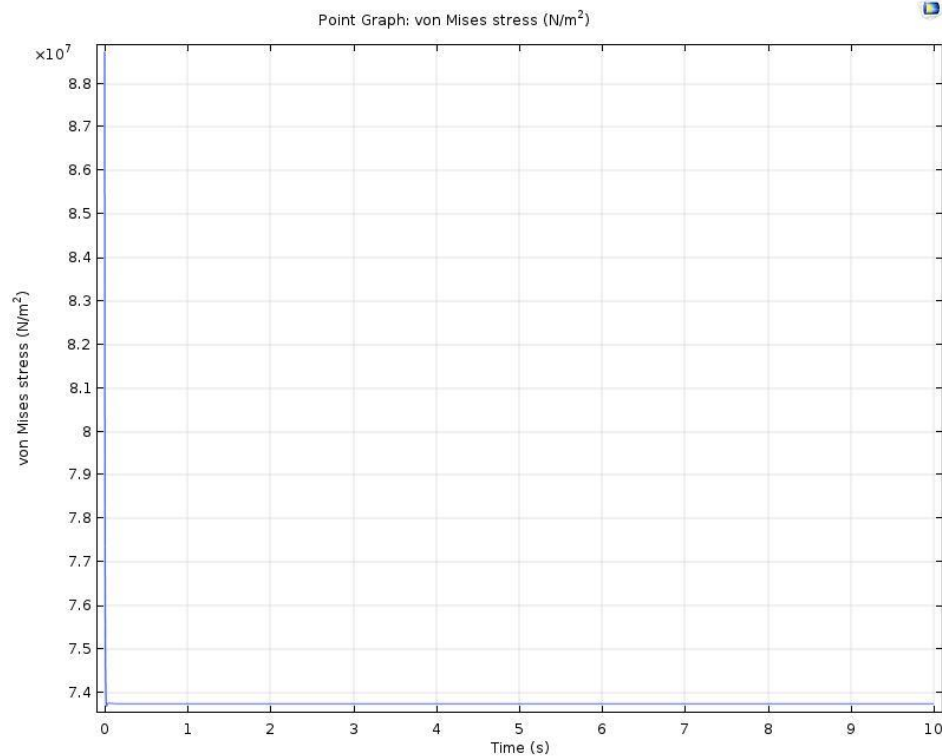
Figure 4. 39. Represents von-Mises stress of midpoint of the top side for 70% PZT bulk model.

From the figures, it shows that the stress at the midpoint is fixed at a constant for each volume fraction PZT models with changing time. This midpoint is on the top side of the unit cell. The result means the stress at this point was kept at the constant on the top side of the unit cell. It does not change with time since the heat transfer process finished very fast. The results decrease with the increasing volume fraction of PZT for some volume fraction models such as 10%, 20% and 40%, 50% models. But some higher volume fraction models have larger values than the lower volume fraction models, such as 30%, 60%, and 70%.

Next, let me show the results for the strain caused by thermal expansion of the midpoint on the top side of the unit cell for each volume fraction model. The results will be shown from Figure 4.40 to 4.46.
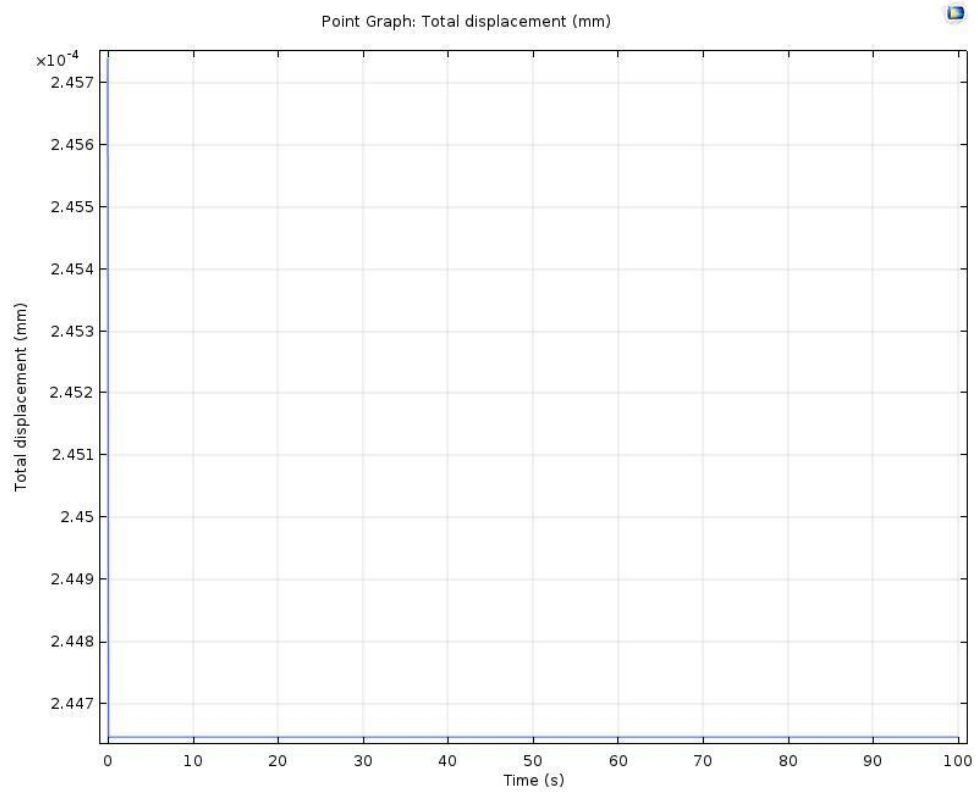
Figure 4. 40. Represents the strain of the midpoint of the top side for 10% PZT bulk model.
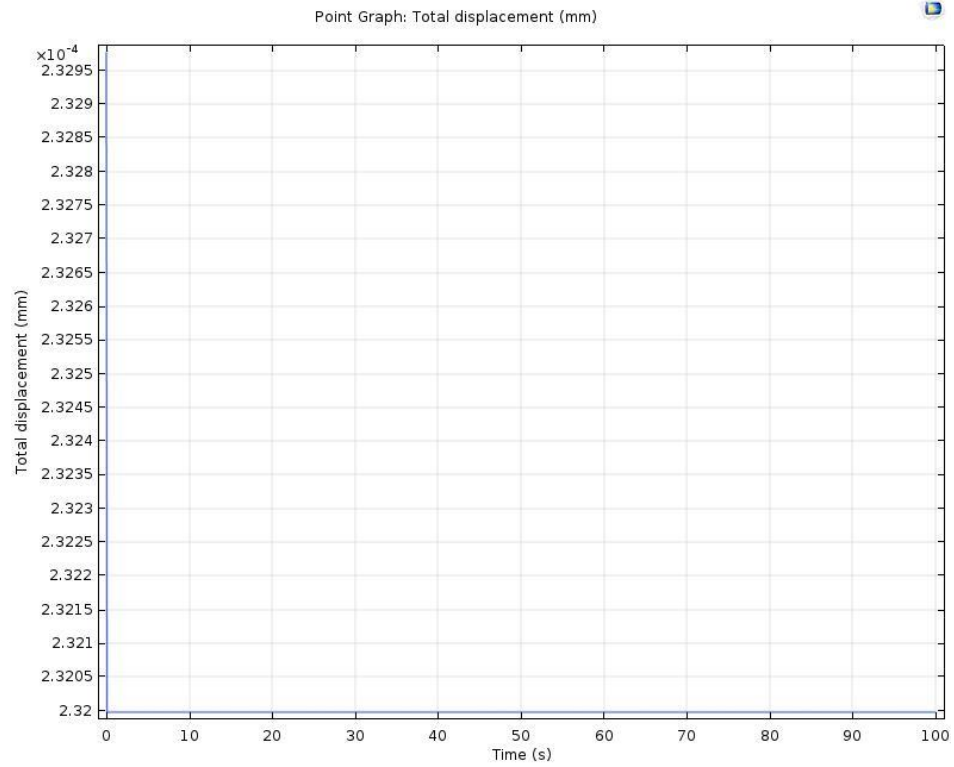
Figure 4. 41. Represents the strain of the midpoint of the top side for 20% PZT bulk model.
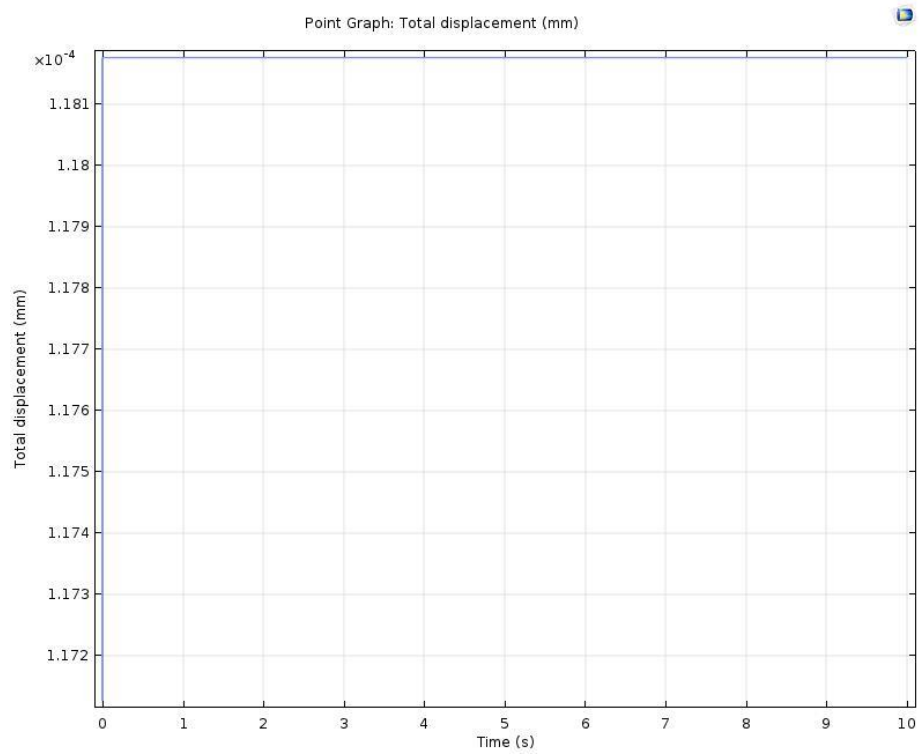
Figure 4. 42. Represents the strain of the midpoint of the top side for 30% PZT bulk model.
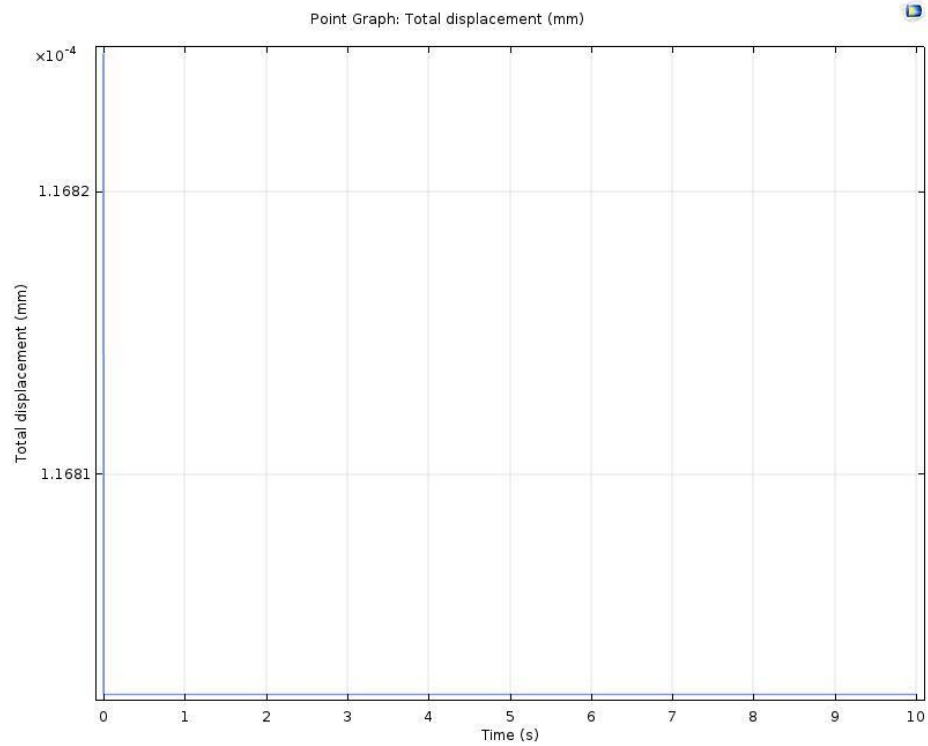
Figure 4. 43. Represents the strain of the midpoint of the top side for 40% PZT bulk model.
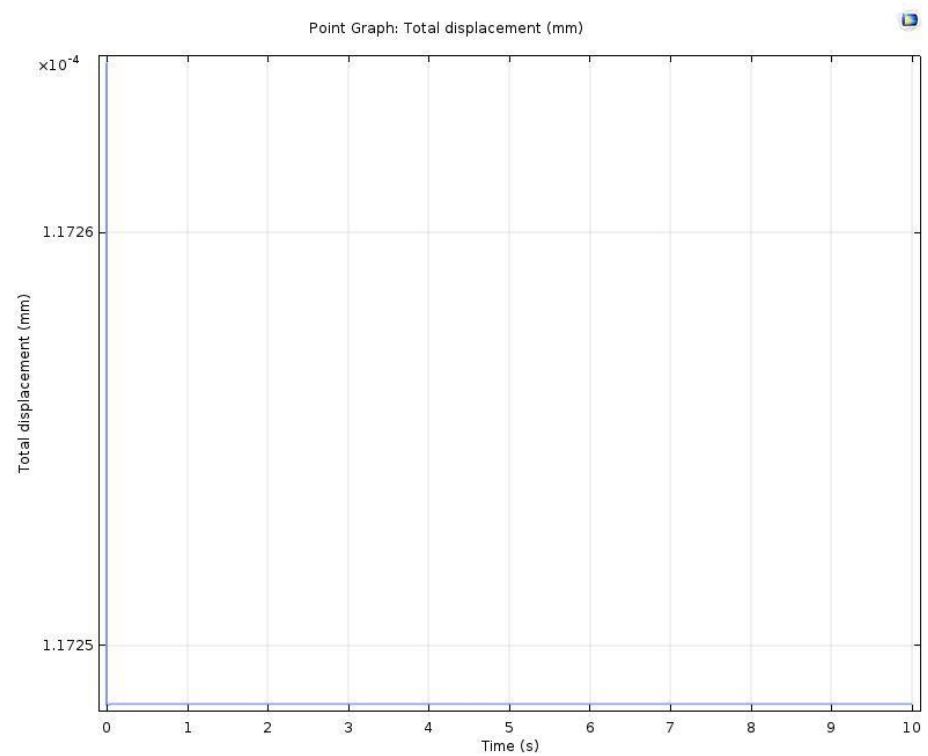
Figure 4. 44. Represents the strain of the midpoint of the top side for 50% PZT bulk model.
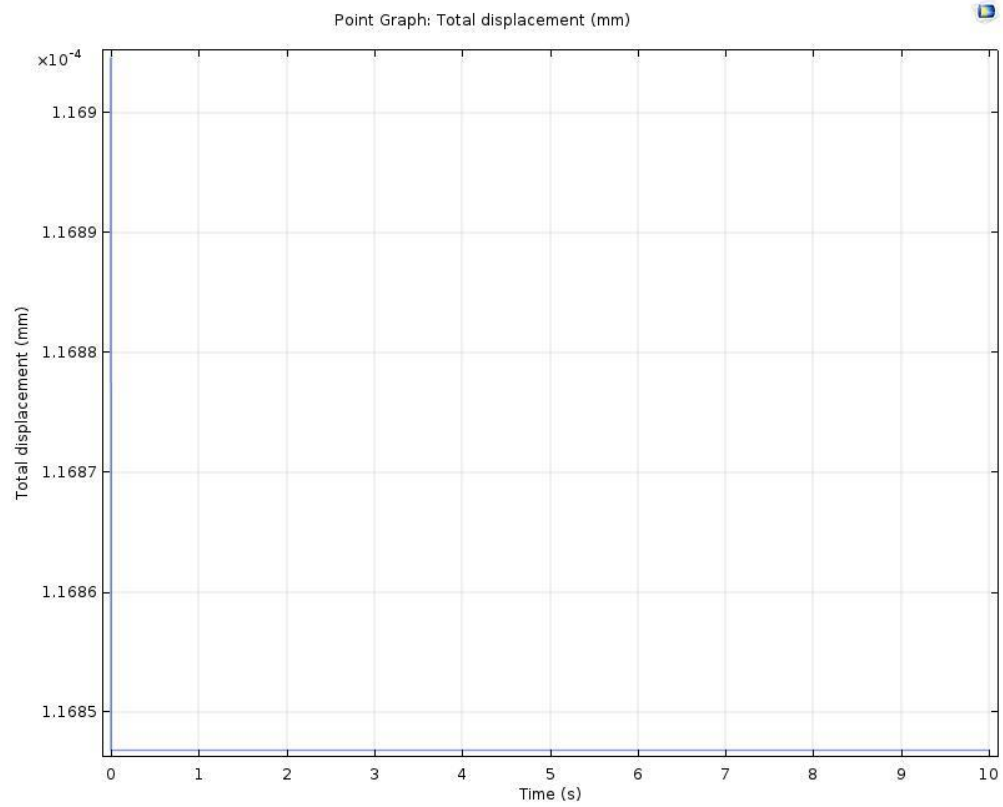
Figure 4. 45. Represents the strain of the midpoint of the top side for 60% PZT bulk model.
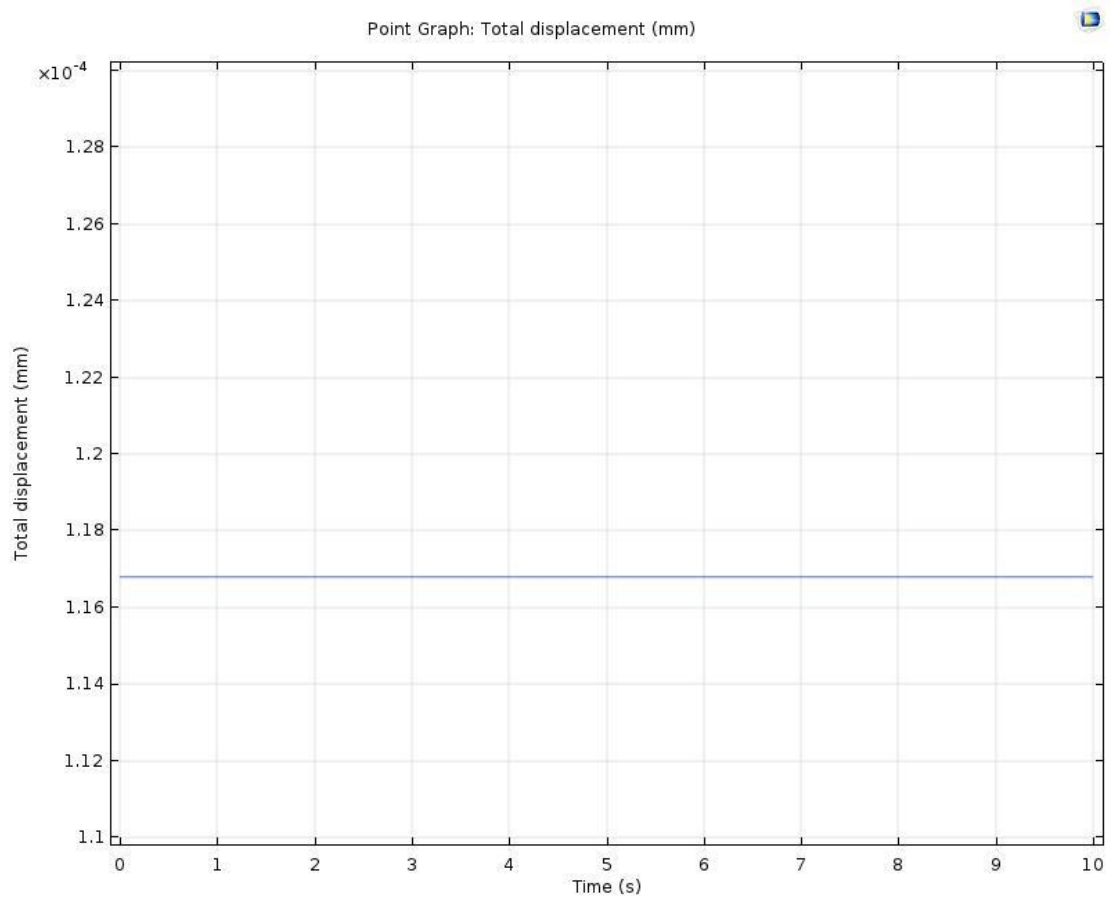
Figure 4. 46. Represents the strain of the midpoint of the top side for 70% PZT bulk model.

From the figures, it shows see that the strain of the midpoint of the top side of the unit cell decrease with increasing the volume fraction of PZT in general, except the 50% model. This is similar to the results for the strain of the centerline of the unit cell. The strain for all models is kept at a constant during the change of time. The minimum value for strain at the midpoint occurs at 40% PZT composite model and the largest value occurs at 10% PZT composite model. Actually, the midpoint of the top side is one of the points of the centerline. It is the end point on the arc length.

4.3 Electrical displacement and electric potential generated by each volume fraction PZT model.

In the above two sections in this Chapter, the results for thermal properties and solid mechanics results caused by thermal expansion was discussed. In this section, the results for piezoelectric effect related to solid mechanics will be discussed. First, the electrical displacement will be introduced. Electric displacement (D), also known as electric flux density, is the charge per unit area that would be displaced across a layer of conductor placed across an electric field. It is different from the strain discussed in section 4.2. In section 4.2, the strain is caused by thermal expansion and it describes the deformation of the composites. However, electric displacement describes the displacement of the charge per unit area when an external electric field is applied. In our study, the external electric field is applied in the -Z-direction. In the experimental part, the piezometer was used to measure the piezoelectric strain coefficient (d_{33}). In order to get the piezoelectric strain coefficient with each volume fraction, the boundary

load and electrical displacement were kept with the same value for all volume fraction

PZT models, which boundary load is 0.25N. The boundary load is in -Z-direction. As

the numerical results need to be compared with experimental data, the same conditions

of boundary load and electric displacement need to be set up in our Comosl models.

However, a problem is that the electrical displacement cannot be measured in the

experimental work. But it can be calculated according to equation 2.13 ($S_{33}=d_{33}.E_3$),

where S_{33} is the electrical displacement in Z-direction, d_{33} is piezoelectric strain

coefficient and E_3 is the applied external electric field in Z-direction. Since the

piezoelectric strain coefficient of pure PZT-5A can be checked from the material library

in Comsol, which is 584pc/N, and the applied external electric field is 0.2kV in bulk

models. Thus, the value of electrical displacement can be calculated as 1.168×10^{-7}m

for pure PZT bulk model. And the same value was kept for all volume fraction PZT

models which is the same as experimental work.

Once the value of the boundary load and electrical displacement for all the models

were get, the next step is to find out the electric potential (voltage) generated by the

direct piezoelectric effect. In experimental work, the dielectric constant was measured

at the frequency 110HZ. The same value of frequency was kept in the study in Comsol

models. Then the results for electric potential generated by direct piezoelectric effect is

listed in Table 4.1:

Table 4. 1: Electric potential generated by direct piezoelectric effect for each volume fraction PZT
model

Volume fraction PZT models	Electric potential(V)
Pure PZT	285.59

10%	42.056
20%	40.961
30%	38.407
40%	39.484
50%	42.948
60%	44.927
70%	118.72

From the table, it shows that pure PZT model gets the largest value of electric potential. This is because pure PZT model is one-phase material, which has a great piezoelectric effect. Once a boundary load was applied on the sample, it generates a large voltage. The electric potential decreases with the increasing volume fraction of PZT from 10% to 30% model. However, it increases with increasing the volume fraction of PZT from 40% to 70% composite models. Generally, a higher volume fraction of PZT composites may have a better piezoelectric effect. But since the composites are two-phase materials, epoxy may also affect the piezoelectric effect of the composites. From the table, the minimum value of electric potential occurs at 30% PZT composite model, which is 38.407V and largest value of electric potential happens at 70% PZT composite model, which is 118.72V. In this case, it shows that 70% PZT composite model has the best direct piezoelectric effect among these composite models and 30% PZT model has the lowest piezoelectric effect compared to other composite models.

4.4 Capacitance for each volume fraction of PZT model

Capacitance is the ability of a component or circuit to collect and store energy in the form of an electrical charge. In this study, the Maxwell capacitance can get from the Comsol models. In the results part, right click "Derived Value" and choose "Global Evaluation". Then the expression was input for Maxwell capacitance, which is "es.C11" into the setting window. Then if click the "Evaluation" button in the setting window, the Maxwell capacitance can directly get from the model. The capacitances for all volume fraction PZT composite models are listed in Table 4.2:

Table 4. 2: Maxwell capacitance for all volume fraction PZT composite models

Volume fraction PZT models	Maxwell capacitance(F)
Pure PZT	9.3329×10^{-12}
10%	8.8401×10^{-12}
20%	9.1797×10^{-12}
30%	9.5266×10^{-12}
40%	9.8420×10^{-12}
50%	1.0092×10^{-11}
60%	1.0177×10^{-11}
70%	1.1056×10^{-11}

From the table, it shows that the Maxwell capacitance increases with increasing the volume fraction of PZT composites from 10% to 70%. This means that a higher percentage volume fraction PZT models have better ability to store the energy of electrical charges. And since the capacitance of pure PZT model is not the largest one,

it is not a good idea to use this single-phase material to make capacitors. It might be better to use high volume fraction two-phase composites to make capacitors.

4.5 Curing condition study

In this section, the results for the curing process of epoxy DGEBA will be discussed. As mentioned before in Chapter 3, the degree of cure α will be expressed to describe the ability the epoxy DGEBA absorbs heat as the material cures. The epoxy will have phase change from gel form to sold form during the curing process. Two different curing conditions will be discussed in this section, one is curing on a hot plate at a fixed temperature 75C and the other one is curing in a room temperature 20C in the air.

4.5.1 Curing on a hot plate

First, the curing process of epoxy DGEBA on a hot plate at a fixed temperature 75C will be discussed. The reason why the temperature was chosen as 75C is because 75C is the Curie temperature of epoxy DGEBA. Above this temperature, the structure of epoxy DGEBA will be centrosymmetric and it will become stable. However, when the temperature is below this temperature, the structure is non-centrosymmetric and the epoxy is in gel form. In addition, the Curie temperature of PZT particles is much higher than 75C, so if the temperature was fixed at 75C, it cannot only get the phase change

of epoxy DGEBA and make the polymer matrix stable so as to keep the PZT particles inside the matrix, but also can still keep the piezoelectric and dielectric properties of PZT-5A so that the composites can still possess piezoelectric effect since the Curie temperature of PZT is much higher than 75C. Such properties are mentioned in Chapter 2, Perovskite Structure in Figure 2.16. Two interfaces are used in Comsol model to simulate this process, one is 'Heat transfer in solid" and the other one is "Domain ODEs and DAEs". The governing equations used for this process are mentioned in Chapter 3, equation 3.33 and 3.34 and the material properties used for this model are listed in table 3.8. The result for the degree of curie of the centerline of the cross section of pure epoxy DGEBA will be shown to express the curing process. The result is shown in Figure 4.47 and 4.48:

The value of the degree of cure is from 0 to 1. When it is close to zero, which means the epoxy is not cured and it is the gel form. When the curing process is done, the value of the degree of cure is equal to 1 or very close to 1. From the two figures, it shows that the epoxy DGEBA cured very fast at the beginning and it may take 1 week to be mostly cured, which the value of the degree of cure is close to 0.8. However, it may take very long to be fully cured as it shows from Figure 4.48. In experimental work, it takes about 8-10 hours to be fully cured. It has a great difference between Comsol models and the experimental work. The reason is that the data for the material properties of the epoxy DGEBA were not known. The thermal material properties used in this model get from the articles found online. Our lab does not have the instruments to measure the thermal properties of the epoxy DGEBA used in our experimental work.

That might be one of the reasons leads to the big difference. The other reason might be

that the epoxy is fully cured or not in our experimental work was unknown because it

cannot be measured. It might take more time to be fully cured.
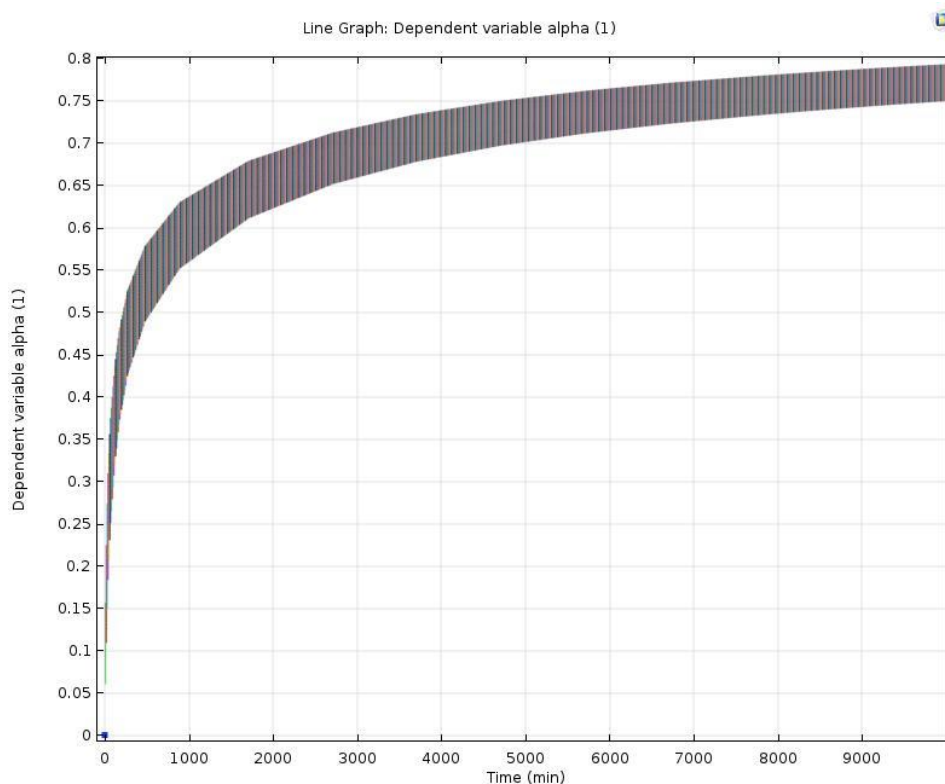
Figure 4. 47. Represents the degree of cure from 0 to 10000 mins at 75C.
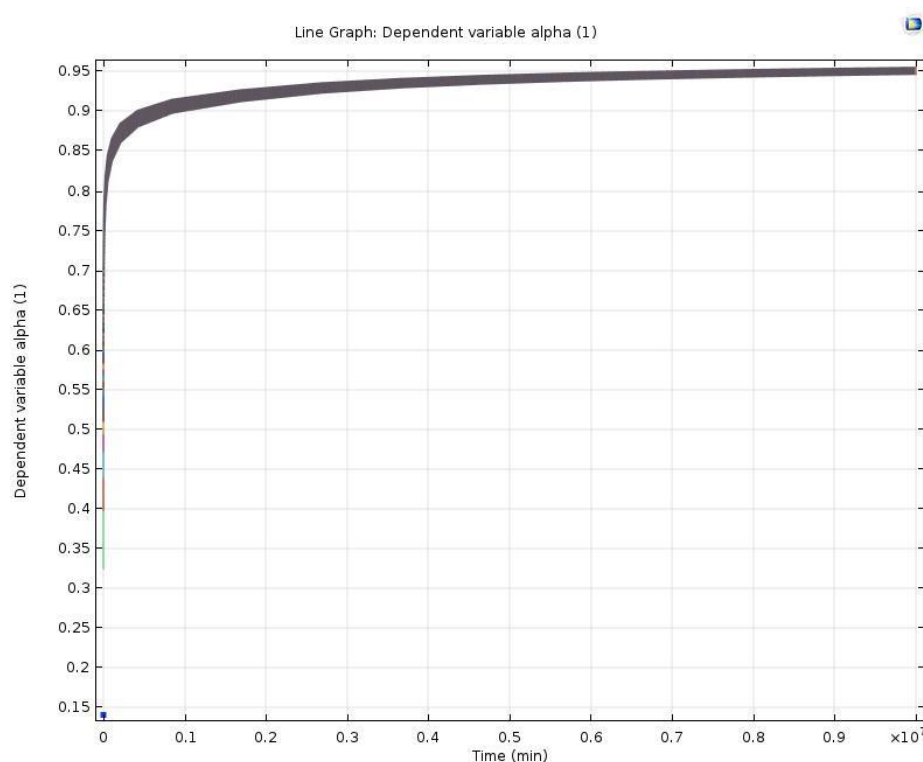
Figure 4. 48. Represents the degree of cure from 0 to 10^7 mins at 75C.

4.5.2 Curing in room temperature 20C in the air

Next, the curing process of epoxy DGEBA in room temperature 20C in the air will be discussed. Such a process is not affected by the heat transfer process because there is no temperature difference between air and the sample. The difference between this curing condition and the condition discussed in section 4.5.1 will be discussed. The result for the degree of cure of the centerline of the cross section of pure epoxy DGEBA is given by Figure 4.49:
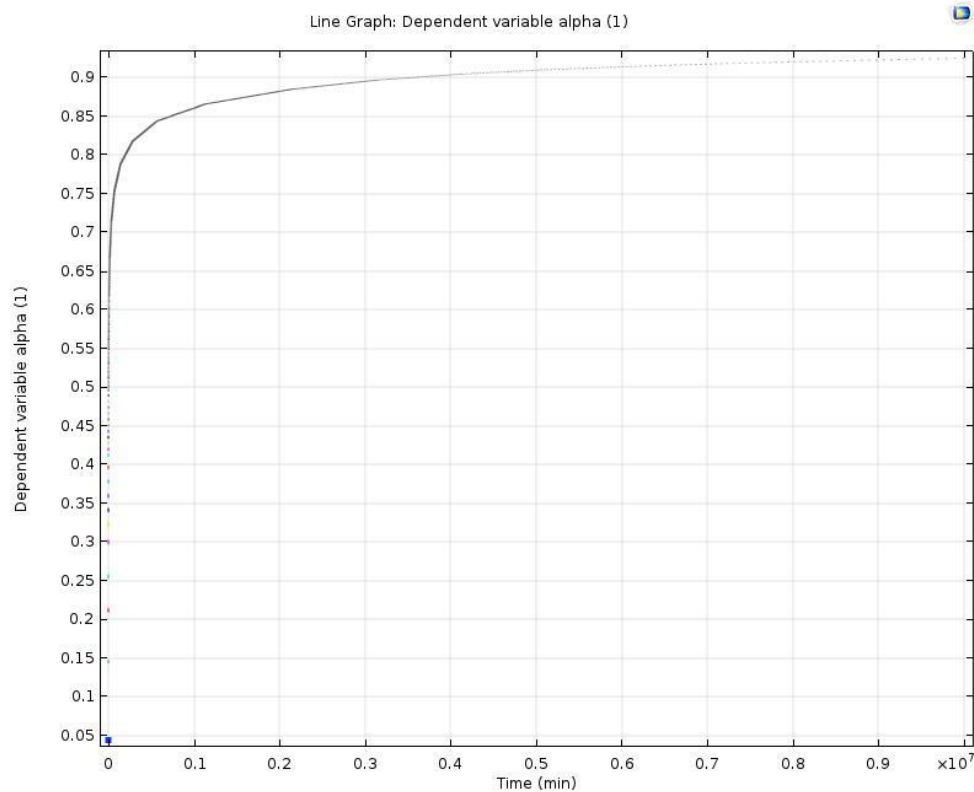
Figure 4. 49. Represents the degree of cure of the centerline in room temperature 20C.

From the figure, it shows that the epoxy DGEBA cannot be fully cured in room temperature even though the value of the time is extremely large. However, the same procedure was done in the experimental work. It takes about 3 weeks that the epoxy

DGEBA was fully cured at room temperature. There are several reasons for the different results between simulation work and experimental work. One reason is that the method used to simulate the curing process of epoxy in Comsol is suitable for heat transfer in solid models. It must have temperature difference which means it must have a heat transfer process during the curing process. Another reason as mentioned in section 4.5.1, the data of the material properties of the epoxy DGEBA used in our lab were not known since our lab does not have the instrument to measure the thermal properties of the epoxy. Thus, the values for the material properties which were input into the Comsol models might not be the same with the material used for experimental work. In addition, it is hard to control the room temperature as 20C for three weeks during the curing process of pure epoxy DGEBA. The temperature is changing during the experimental work. All these factors may lead to the huge difference between the simulation work and the experimental work.

4.5.3 Phase change of epoxy DGEBA during the curing process

In section 4.5.1 and 4.5.2, two different curing conditions for the curing process of epoxy DGEBA were discussed and the degree of cure α is expressed to describe such a process. In this section, the result for the phase change of epoxy DGEBA during the curing process for the simulation work will be shown. The process of the phase change of epoxy at a different time is shown from Figure 4.50 to 4.56. The blue part represents the solid form of the composite and the red part represents the gel form of the composite.

As time increases, the blue part will become larger, which means the composite was cured from gel form to solid form during the curing process.
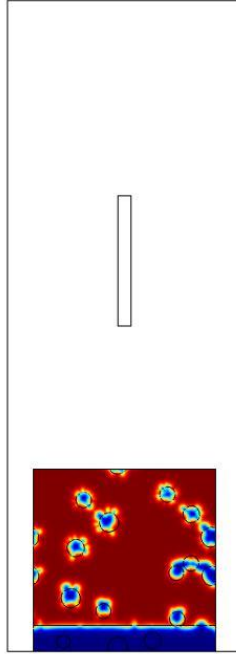
Figure 4. 50. Represents the phase change process of epoxy at 0s. The blue part represents the solid form and the red part represents the gel form.
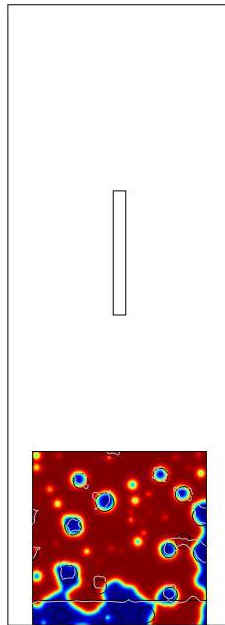
Figure 4. 51. Represents the phase change process of epoxy at 1s. The blue part represents the solid form and the red part represents the gel form. Red part becomes larger and blue part becomes smaller than 0s.
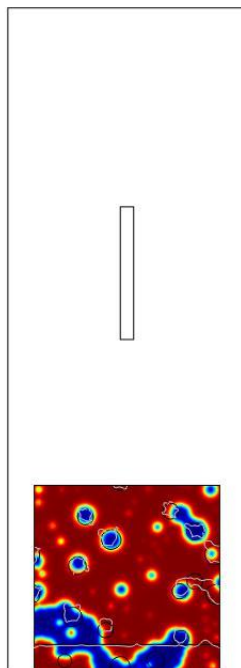
Figure 4. 52. Represents the phase change process of epoxy at 2s. The blue part represents the solid form and the red part represents the gel form. Red part becomes larger and blue part becomes smaller than 1s.
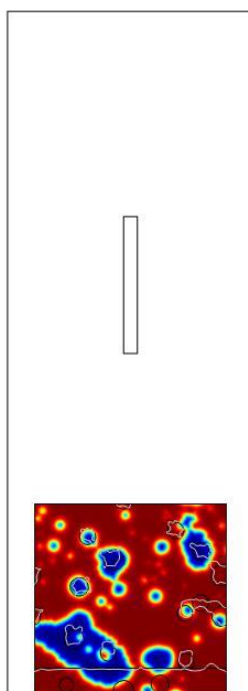
Figure 4. 53. Represents the phase change process of epoxy at 3s. The blue part represents the solid form and the red part represents the gel form. Red part becomes larger and blue part becomes smaller than 2s.
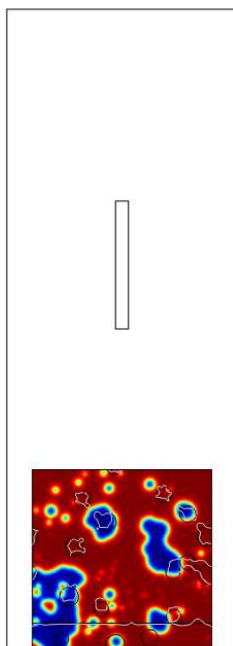
Figure 4. 54. Represents the phase change process of epoxy at 5s. The blue part represents the solid form and the red part represents the gel form. Red part becomes larger and blue part becomes smaller than 3s.
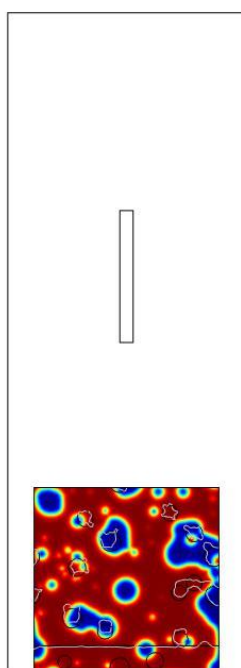
Figure 4. 55. Represents the phase change process of epoxy at 8s. The blue part represents the solid form and the red part represents the gel form. Red part becomes larger and blue part becomes smaller than 5s.
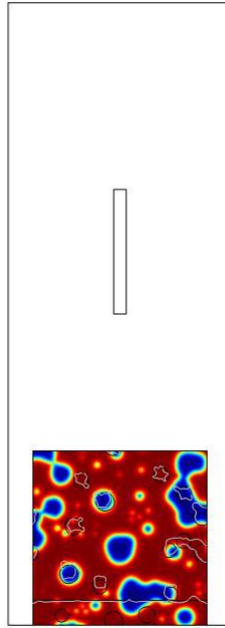
Figure 4. 56. Represents the phase change process of epoxy at 10s. The blue part represents the solid form and the red part represents the gel form. Red part becomes larger and blue part becomes smaller than 8s.

In these figures, the blue part represents material in solid form and red part represents material in liquid form (gel form). All these figures are 10% PZT composite model. The simulation is from 0 to 10s. As it shows, the bottom part of the unit cell was set up as a solid form because the epoxy starts curing of the bottom part. As it shows that the area of the blue part becomes larger with increasing time step. This is because the epoxy DGEBA is curing during this process and the material transfer from gel form to solid form during this process. Once the material is fully cured, all the matrix part will be solid and it will be represented by blue. The reason why the domain is not fully blue is that the time set up for this simulation is not enough for the epoxy to be fully cured. The reason why no more time was set up to do this simulation is that it takes too much time to run this model in Comsol. If the time was set up too long, it may lead to too much calculation that our computer cannot do it. Thus, only show part of this curing

process can be shown for the simulation work.

4.6 Particle distribution after curing process of epoxy DGEBA

In the last section, the curing process and phase change of epoxy DGEBA was discussed. But how will the PZT particles distribute after the curing process of epoxy polymer matrix? In this section, this question will be discussed. In experimental work, it was found that the PZT particles are accumulated at the top side of the epoxy polymer matrix instead of randomly distributed in the composites after the epoxy is fully cured through SEM image. Such a result is shown in Figure 4.57.
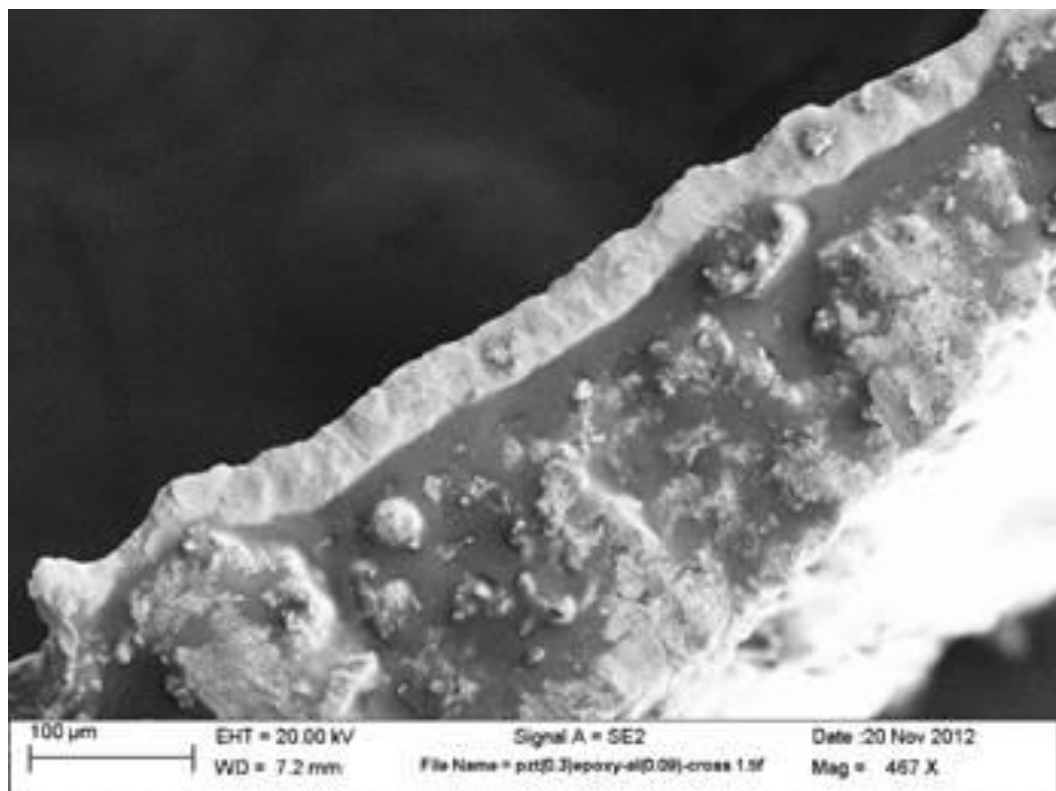
Figure 4. 57. Represents the SEM image for the particle distribution of PZT after the epoxy is fully cured [14].

As it shows that, SEM image shows the cross section of PZT-epoxy composite. The PZT particles are accumulated on the top side of the composite. This may because

that the direction of heat transfer process occurs from bottom to top in the composite. The temperature of the bottom part is much higher than the temperature of the top part of the composite at the beginning. In this case, the thermal load at the bottom part inside the composite may push the PZT particles to move to the top side of the composite. Another reason may be that the density of epoxy increases during the curing process. The change of the density of epoxy DGEBA during the curing process may lead to PZT particles floating up and accumulate at the top part of the composites. In simulation work, this process can be simulated in Comsol 5.3a. Such a process is given by Figure 4.58 to 4.65.
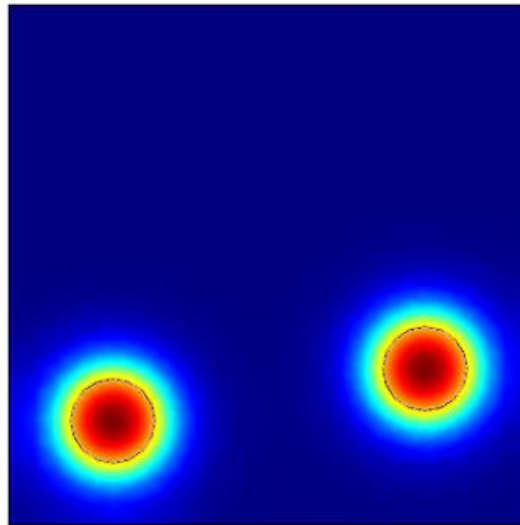
Figure 4. 58. Represents two particles floating up during the curing process at time 0s.
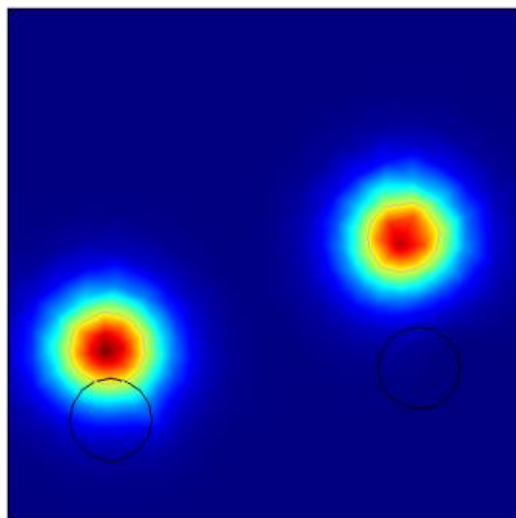
Figure 4. 59. Represents two particles floating up during the curing process at time 1s.
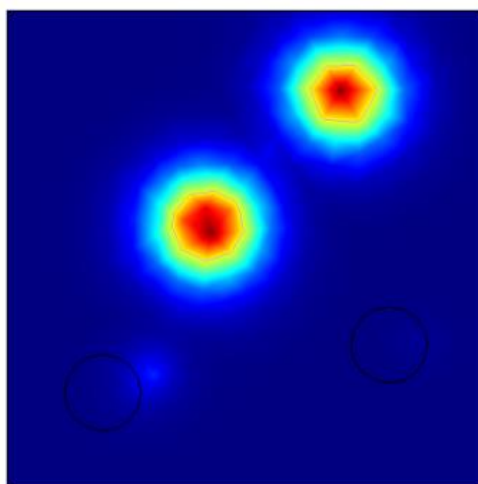
Figure 4. 60. Represents two particles floating up during the curing process at time 2s.
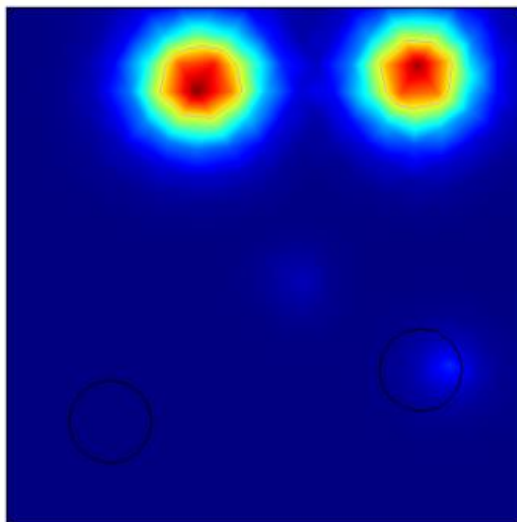
Figure 4. 61. Represents two particles floating up during the curing process at time 3s.
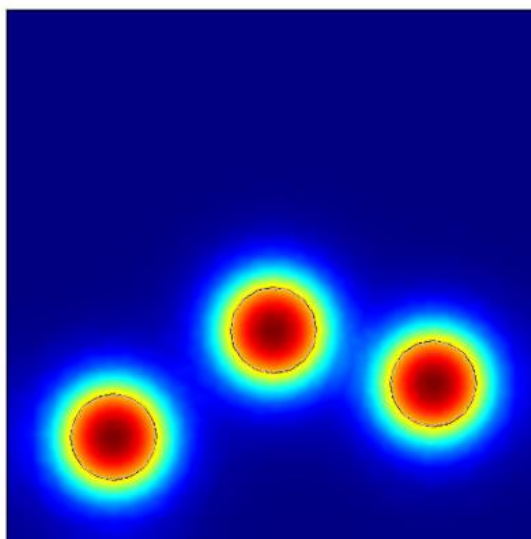
Figure 4. 62. Represents three particles floating up during the curing process at time 0s.
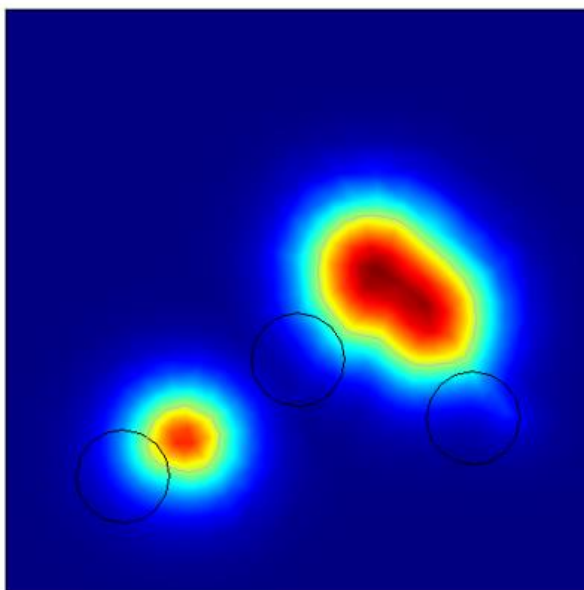
Figure 4. 63. Represents three particles floating up during the curing process at time 1s.
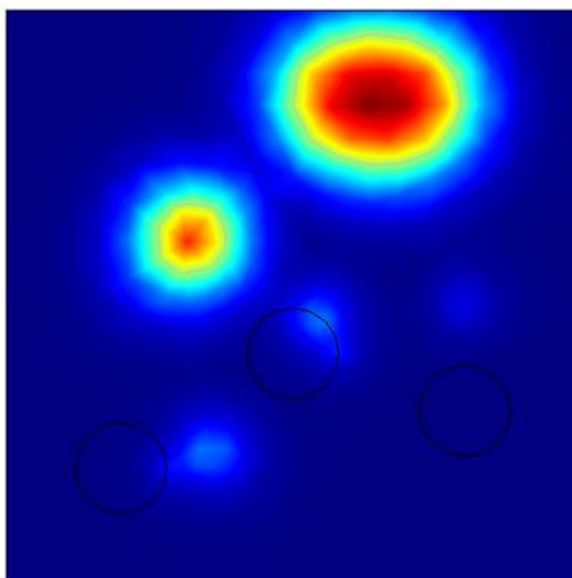
Figure 4. 64. Represents three particles floating up during the curing process at time 2s.
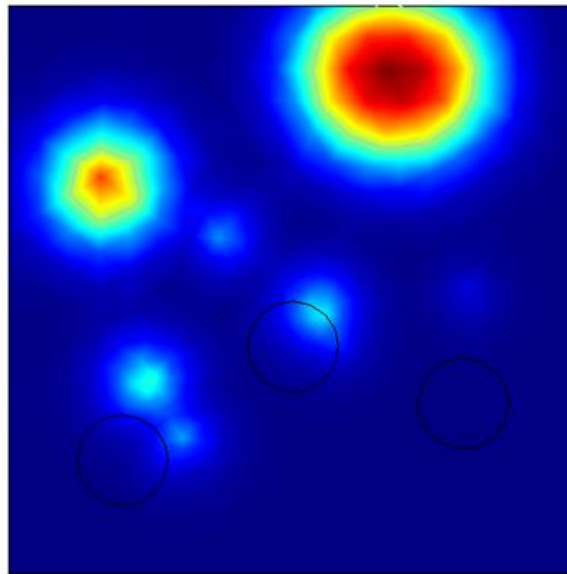
Figure 4. 65. Represents three particles floating up during the curing process at time 3s.

As the figures show that two types of models were done to simulate the PZT particles floating process during the phase change of epoxy DGEBA. The reasons why only did two particles and three particles are because there are some limitations for the computer to run Comsol models. One reason is that the dimension of the unit cell and PZT particles are very tiny and the numbers of PZT particles of each volume fraction are too many. It will take too much time to run the models for each volume fraction model for this particle floating process. In addition, there is no enough disk space for our lab computer to run this type of simulation. In order to show this process, the only thing can be done is to simulate two and three particles for this process.

For two PZT particles model, it shows that the two particles are floating up to the top side of the composite at different time step. The total time set up for this process is 3s and the time step is 0.1s for each step. They do not overlap with each other during

this process. The same process will happen in three particles model. However, two of the three particles overlapped with each other during this process. The reason why the particles overlap with each other depends on the distance between the particles. If the distance between the particles is small, then these particles will be overlapped with each other during the curing process. Otherwise, they will be separate. The reason why particles will move closely during this process is that there exist tensions inside the epoxy polymer matrix since the epoxy is in gel form at the beginning. The tensions will make the particles move closely during the phase change process of epoxy DGEBA.

4.7 Piezoelectric and dielectric properties of the composites

In this section, the results for piezoelectric and dielectric properties of the composites will be discussed for each volume fraction PZT model. In order to find out one of the hypotheses, mentioned in Chapter 2. The piezoelectric and dielectric properties of the composites for two different conditions will be discussed. One is considering the boundary conditions of heat convection and surface radiation. The other one is without considering these two boundary conditions. Dielectric constant ε_r and piezoelectric strain coefficient d_{33} will be calculated to express piezoelectric and dielectric properties. Such two values will be calculated by equation 2.5 and equation 3.31:

$$\varepsilon_r = \frac{Cd}{\varepsilon_0 A} \qquad (2.5)$$

$$d_{33} = \frac{V \varepsilon_r \varepsilon_0 A}{Fd} \qquad (3.31)$$

where C is the Maxwell capacitance, d is the thickness of the sample, A is the area of the surface, ε_0 is the permittivity of free space - a vacuum - is equal to approximately 8.85×10^{-12} Farads/meter(F/m), V is the electric potential, F is the fixed boundary load, which is 0.25N. In addition, the simulation results will be compared with both experimental results and results calculated by analytical models in this section as well.

4.7.1 Piezoelectric and dielectric properties of the composites with considering the boundary conditions in "heat transfer" in the solid interface.

First, the results for the dielectric constant and piezoelectric strain coefficient for the simulation work will be discussed with considering the boundary conditions for heat convection and surface radiation. Four models for each volume fraction PZT model were done and took the average value for dielectric constant and piezoelectric strain coefficient. The results for piezoelectric and dielectric constant are under frequency 110HZ. The results for the dielectric constant are given in Table 4.3:

Table 4. 3: dielectric constant for all volume fraction PZT samples from Comsol models

Volume fraction PZT models	Dielectric constant ε_r(F/m)
Pure PZT	1700
10%	71.18
20%	74.09
30%	76.89
40%	79.44

50%	81.45
60%	82.14
70%	89.23

From the table, the dielectric constant increases with increasing the volume fraction of PZT. The largest value of dielectric constant occurs at 70% PZT model, which is 89.23 F/m. Smallest value occurs at 10% PZT model, which is 71.18 F/m.

Since the dielectric constant for bulk samples were not measured in experimental work. It is impossible to compare the dielectric constant calculated by Comsol models with the experimental result. However, they can be compared with the results calculated by the analytical model. The analytical model used is Maxwell's Equations. The equation to calculate the dielectric constant of the composites is given by equation 3.30 and the results for the dielectric constant are given in Table 4.4

Table 4. 4: dielectric constant calculated by the analytical model

Volume fraction PZT models	Dielectric constant ε_r(F/m)
Pure PZT	1700
10%	72.31
20%	76.25
30%	78.45
40%	81.32
50%	83.36
60%	86.48
70%	92.23

From the table, it shows that the dielectric constant calculated by the analytical model increases with increasing the volume fraction of PZT. The results are very similar with the simulation data. Figure 4.66 shows the comparison of the simulation data and analytical model of dielectric constant:
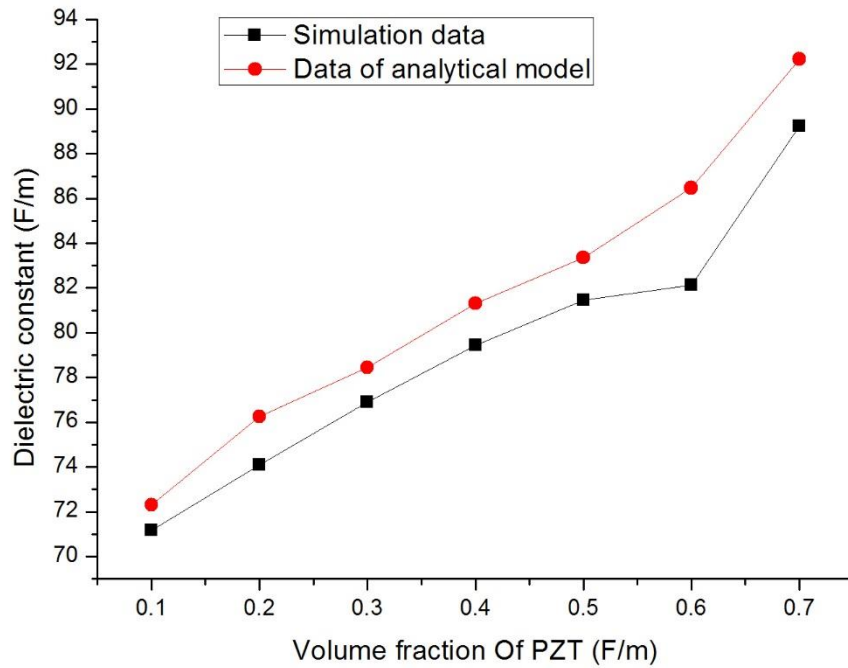
Figure 4. 66. Shows the results for dielectric constant for numerical data of the bulk composite models and the analytical data.

Next, the piezoelectric strain coefficient d_{33} will be discussed. This value is calculated by equation 3.31. The voltage V can get from each volume fraction by the Comsol models. The data for dielectric constant by table 4.3 were used. Boundary load F is kept at 0.25N. The results for the piezoelectric strain coefficient are given by Table 4.5:

Table 4. 5: piezoelectric strain coefficient of calculated by simulation work

Volume fraction PZT models	Piezoelectric strain coefficient d_{33} (pC/N)

Pure PZT	584
10%	7.42
20%	7.52
30%	7.32
40%	7.77
50%	8.67
60%	9.14
70%	26.25

From the table, it shows that the piezoelectric strain coefficient increases with increasing the volume fraction of PZT except 30% model. Thus, the minimum result occurs at 30% model which is 7.32pC/N and largest value occurs at 70% model which is 26.25pC/N. This result shows that higher volume fraction PZT composites have a better piezoelectric effect than lower volume fraction composites. This is quite making sense because PZT is the phase material that has the piezoelectric effect.

Next, let us compare the simulation result with the experimental result. Figure 4.66 gives the result for piezoelectric strain coefficient of the experimental work from S. Banerjee, which composites have the same shape, dimensions and volume fraction in experimental work[13]. The only difference is that his samples are three-phase composites with epoxy-PZT-aluminum, in which aluminum is used as conductive filler and was held as a constant at 20% for all volume fraction composites.
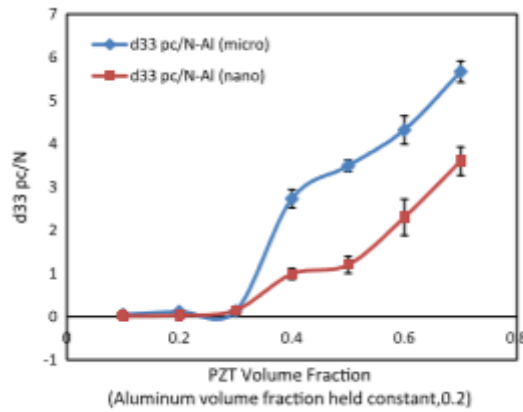
Figure 4. 67. The result for piezoelectric strain coefficient for PZT-epoxy-aluminum of the experimental data by S. Banerjee[13].
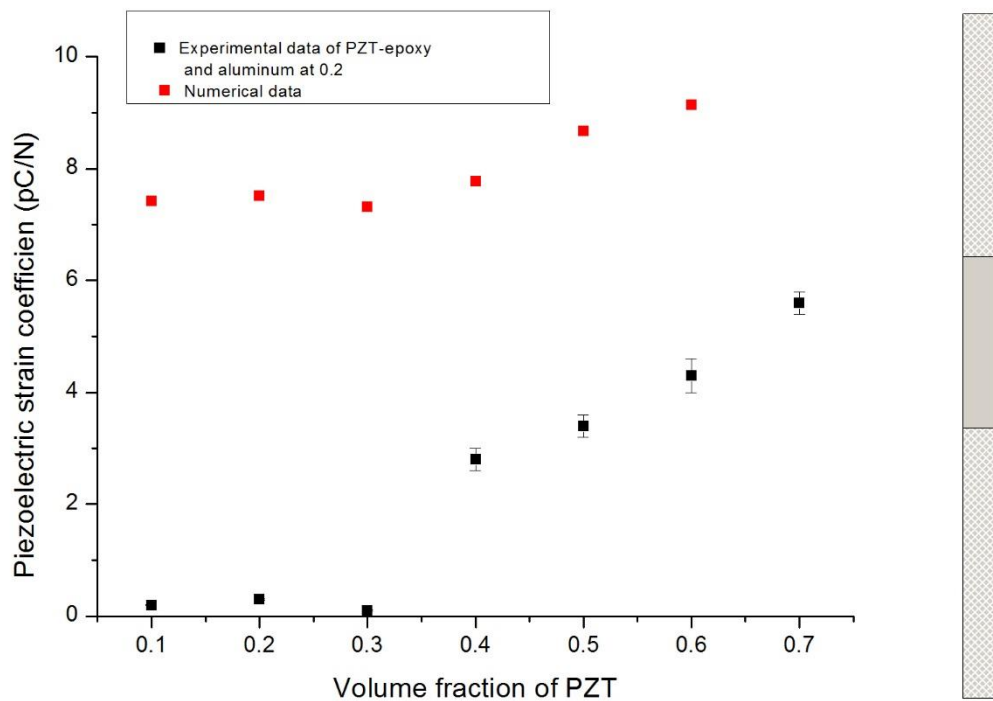
Figure 4. 68. The result for piezoelectric strain coefficient for PZT-epoxy-aluminum of the experimental data by S. Banerjee[13] and the numerical data of the bulk composite models.

From the figure, it shows that the piezoelectric strain coefficient of the experimental data has a similar trend of the simulation data. It increases with increasing the volume fraction of PZT. The difference is that the data for experimental work is a little bit smaller than the simulation results. The minimum value for the piezoelectric strain coefficient in experimental work also occurred at 30% PZT composite, which has

the same result as simulation data. In this figure, there are two types of results for piezoelectric strain coefficient, one is PZT particles in nano-dimension, the other one is in micro-dimension. The result for micro-dimension is larger than nano-dimension. In our simulation models, the unit for the dimension is in micro-dimension. Thus, the result for blue line is the result needs to be compared with the simulation result. Since the simulation work is ideal, the models set up in Comsol 5.3a are not affected by environmental and personal factors. Thus, it is making sense that the data for simulation work is larger than experimental data. The error between these two types of data may be caused by environmental factors, such as temperature change and by personal factors as well, such as fabrication procedures is not ideal. The most important factor which leads to the difference is that the PZT particles in Comsol models are not overlapped with each other in the composite. However, it is impossible to make all the PZT particles separate with each other in the composites so that the volume fraction of PZT of each composite sample may be smaller than that volume. In this case, the piezoelectric effect of the fabricated samples is lower than ideal models generated by Comsol. In addition, the experimental data is three-phase composites with fixed volume fraction of aluminum, however, the numerical model are only two-phase composites, which is PZT-epoxy. Thus, there is some difference between these two types of datas.

4.7.2 Piezoelectric and dielectric properties of the composites without considering the boundary conditions in "heat transfer" in a solid interface.

In the last section, the results for dielectric constant and piezoelectric strain coefficient were discussed with considering the boundary conditions of heat transfer, such as heat convection and surface radiation. However, in this section, these results will be discussed without considering such boundary conditions so as to see if there are a big difference in the results or not.

First, let us see the capacitance of each volume fraction PZT model without considering the boundary conditions of heat transfer. Table 4.6 gives the result for the capacitance of each volume fraction PZT model:

Table 4. 6: Maxwell capacitance without considering boundary conditions od heat transfer

Volume fraction PZT models	Maxwell capacitance(F)
Pure PZT	9.3329×10^{-12}
10%	8.8401×10^{-12}
20%	9.1549×10^{-12}
30%	9.5061×10^{-12}
40%	9.8357×10^{-12}
50%	1.0068×10^{-11}
60%	1.0177×10^{-11}
70%	1.1065×10^{-11}

From the table, it shows that the Maxwell capacitance has a similar trend with the

results for considering the boundary conditions heat transfer. It increases with increasing the volume fraction of PZT composite. Compared with the results in table 4.2, it is only a little different for the capacitance between two types of conditions. Some of the results for low volume fraction models are a little bit smaller than table 4.2 and the results for high volume fraction models are the same such as 60% and 70% models. In this case, it shows that the boundary conditions of heat transfer have only a little bit of influence on the Maxwell capacitance.

Next, let us discuss the results for the voltage generated by the piezoelectric effect without considering the boundary conditions of heat transfer. Table 4.7 gives the results for voltage of all volume fraction models.

Table 4. 7: electric potential generated by the piezoelectric effect without considering boundary conditions of heat transfer

Volume fraction PZT models	Electric potential(V)
Pure PZT	285.59
10%	43.168
20%	40.961
30%	38.407
40%	39.501
50%	42.977
60%	44.971
70%	118.73

From this table, it shows that the electric potential generated by the piezoelectric effect has almost the same results with table 4.1 which is the electric potential with

considering the boundary conditions of heat transfer. Only a few results of the models have a little bit larger voltage than table 4.1. In this case, the boundary conditions of heat transfer process have slightly affection on the piezoelectric effect.

Next, let us calculate the dielectric constant and piezoelectric strain coefficient by using the data from Table 4.6 and 4.7 to see the difference in the results between these two types of conditions. The results for the dielectric constant and piezoelectric strain coefficient are given by Table 4.8 and 4.9:

Table 4. 8: dielectric constant of all volume fraction models without considering the boundary conditions of heat transfer

Volume fraction PZT models	Dielectric constant ε_r(F/m)
Pure PZT	1700
10%	71.18
20%	73.89
30%	76.72
40%	79.38
50%	81.26
60%	82.14
70%	89.31

Table 4. 9: piezoelectric strain coefficient of all volume fraction models without considering the boundary conditions of heat transfer

Volume fraction PZT models	Piezoelectric strain coefficient d_{33} (pC/N)
Pure PZT	584
10%	7.61
20%	7.50
30%	7.30
40%	7.77

50%	8.65
60%	9.15
70%	26.28

From Table 4.8 and 4.9, it shows that the results for the dielectric constant and piezoelectric strain coefficient have only a little bit different with the results for considering the boundary conditions of the heat transfer process. The dielectric constant of some volume fraction models is a little bit smaller than the results in Table 4.3 and piezoelectric strain coefficient of some volume fraction models are a little bit smaller in low volume fraction models, such as 10%, 20%, and 30% models, but a little bit larger in high volume fraction models, such as 60% and 70% models, in comparison of table 4.5. In this case, it was found that the boundary conditions of heat transfer process have only a little bit of influence on piezoelectric and dielectric properties of the composites. Thus, the fourth hypothesis mentioned in Chapter 1 is proved. The results for dielectric constant and piezoelectric strain coefficient for two conditions are compared in Figure 4.68 and Figure 4.69.
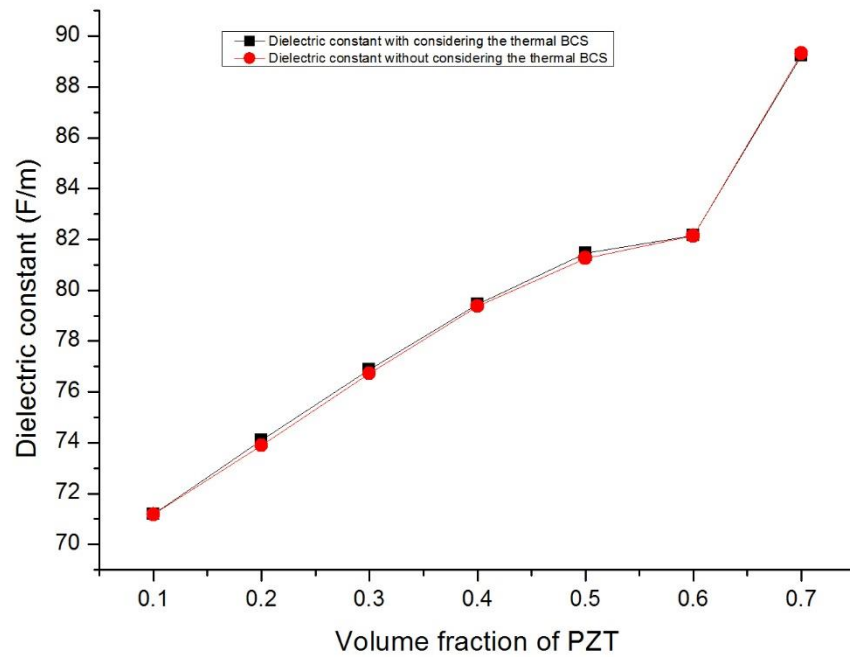
Figure 4. 69. Represents the dielectric constant of the bulk models for two types of conditions.
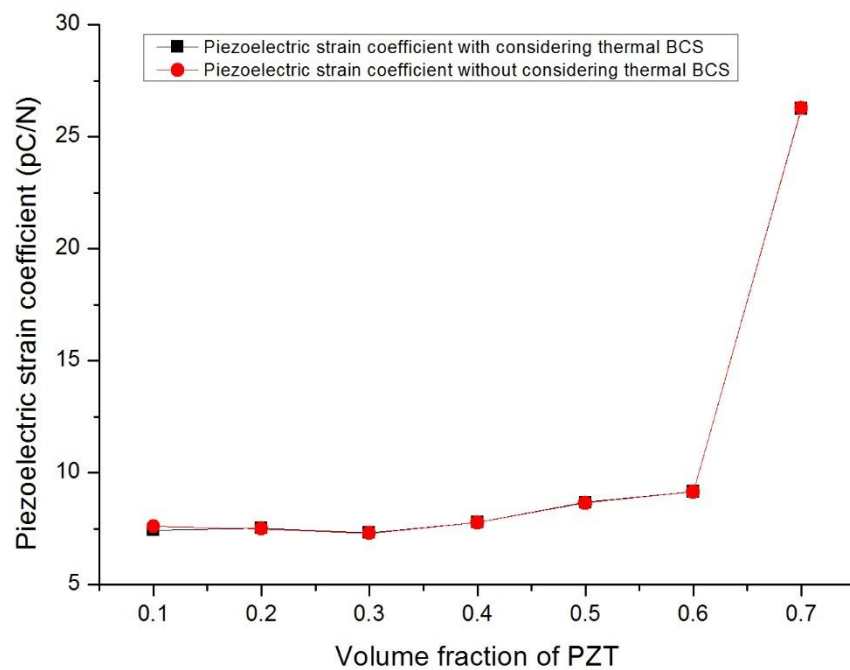
Figure 4. 70. Represents the piezoelectric strain coefficient of the bulk models for two types of conditions.

From the figures, the black line represents the dielectric constant with considering

the thermal boundary conditions (BCS), the red line represents he dielectric constant without considering the thermal boundary conditions. These two lines are mostly coincident with each other, which means the thermal BCS has slightly affect piezoelectric and dielectric properties for bulk composite models.

Chapter 5

Results and discussion for planar models

The difference for planar models and bulk models is that the thickness of the planar sample is much thinner than bulk sample. In this case, the unit cell chose for simulating planar models is different from the unit cell for bulk models. the rectangle unit cell was chosen to simulate the results for planar models because this type of unit cell is more similar to the real dimension of planar models. The dimension of the rectangle unit cell is 70µm in width and 30µm in thickness, as Figure 5.1 shows:
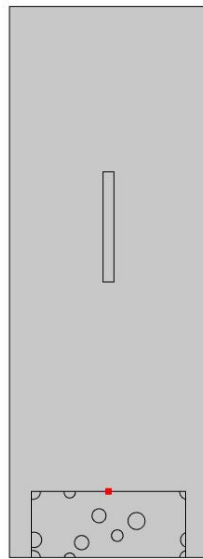
Figure 5. 1. Represents the rectangle unit cell for 10% planar model

5.1 Temperature distribution of planar composites

In this section, the temperature distribution for all volume fraction of PZT planar models of both centerline of the unit cell and the mid-point at the top surface of the unit cell will be discussed. The temperature distribution is related to heat transfer in the composites. This process will affect the curing process of the epoxy polymer and the

curing process will finally affect the piezoelectric and dielectric properties of the piezoelectric composites.

5.1.1 Temperature distribution of the centerline

In this section, the results of the temperature distribution of the centerline of the cross section of the composites will be discussed. As mentioned before, since the composites are uniformly heated on the hot plate, the cross-section of the composites with the dimension of the diameter of the planar samples in width and the thickness of the planar samples in height can represent the properties of the whole domain. As mentioned before, it is 0.0254m in width and 0.0002m in thickness. This dimension is for the simulation of pure PZT models. However, in chapter 3, the dimension for PZT particles as mentioned are very tiny that the regular computers cannot generate a huge amount of particle of PZT to reach the volume fraction of the composites from 10% to 70 % PZT so that the unit cell method is used to solve this problem. The unit cell as mentioned before is a small area that can globally represent the material properties of the whole domain. For the numerical method of bulk models, the dimension for the unit cell was chosen as a rectangle of 70μm in width and 30μm in thickness, which is much bigger than L/D ≥ 10/3, where L is the length for the unit cell and D is diameter for PZT particles[60].

First, let's start with pure PZT planar models. The model is with the same dimension of the samples fabricated by Zichen Lao. Figure 5.2 shows the temperature distribution of the centerline of the cross section of the planar model with the change

of time. The horizontal axis represents the arc length of the model and the vertical axis represents the temperature. The blue curve represents the temperature at the zero-time step and the rest of the different color line from the bottom to top represent the temperature distribution of other time step from 0s to 100s.
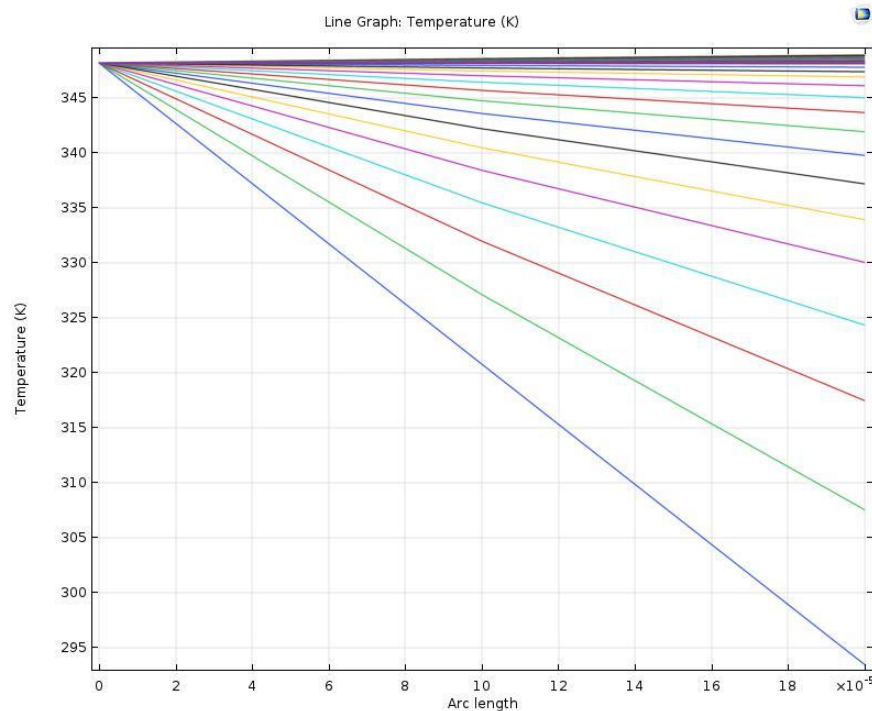
Figure 5. 2. Represents the temperature distribution of centerline of the cross section of the pure PZT planar sample.

Figure 5.2 shows the temperature distribution of the centerline with the arc length changed with time, where arc length is the length of the centerline, which is the thickness of the planar sample 0.0002m. The range of time is from 0 to 100s with the time step of 0.01s. From the figure, the temperature at the bottom part of the sample is much higher than the temperature at the top part of the sample for each time step at the beginning. This is because the direction of heat transfer is from bottom to top. The temperature of the whole domain increases with increasing the time and arc length and

finally get close to the fixed temperature 75C at the bottom side of the sample, which

means the heat transfer process is done. There is no lost temperature on the top side

because the temperature at both top side and the bottom side is 75C eventually, which

means the boundary conditions of heat transfer have no influence on thermal dissipation

during the heat transfer process because the thickness of the planar model is very thin.

Next, let us discuss the temperature distribution of the centerline of the cross

section of the composite models. The result for 10% to 70% model is given by Figure

5.3. The horizontal axis represents the arc length of the model and the vertical axis

represents the temperature. The blue curve represents the stress at the zero-time step

and the purple line represents the temperature distribution of the final time step 100s.
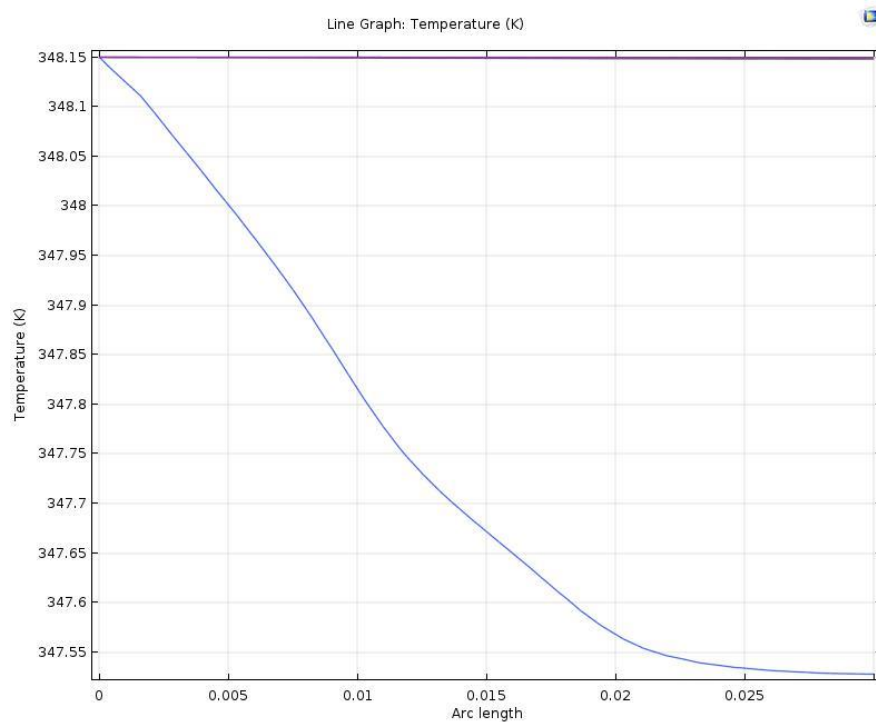
Figure 5. 3. The temperature distribution of the centerline of the unit cell for 10% to 70% PZT planar model.

It shows that the blue line is the temperature at time zero instant. However, the

temperature for the rest of time steps coincident together which is represented by the pink horizontal line which is equal to the fixed temperature 75C at the bottom side. There is no thermal dissipation during this process. This is because the thickness of the unit cell is very tiny so that the effect from the boundary conditions for heat convection and surface radiation is neglected. In addition, since the dimension of the unit cell for all volume fraction PZT models are the same for planar models. Thus, the temperature distributions of the centerline of the unit cell for all volume fraction models are the same with figure 5.3, which will not be put into the thesis again.

5.1.2 Temperature of the midpoint of the top side

In this section, the midpoint of the top side of the unit cell will be chosen to see the final temperature of this fixed point when the heat transfer process is done and distribution change with time. First, let us see the pure PZT planar model. The result is given in Figure 5.4:
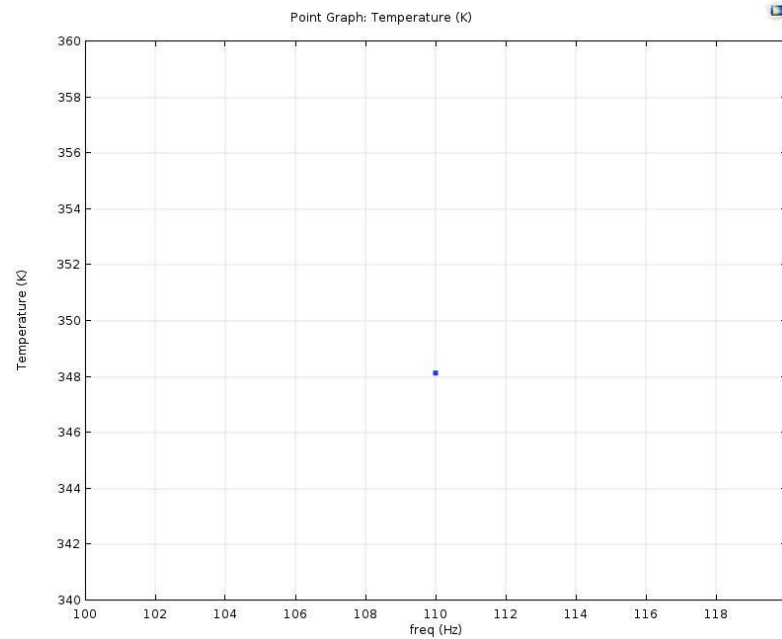
Figure 5. 4. Shows the final temperature of the midpoint at the top side of the pure PZT planar sample.

From Figure 5.4, the temperature for this fixed point is equal to 75C, which means there is no thermal dissipation and heat loss during the heat transfer process. It has the same result with figure 5.2. Next, let us see the result for composite models.
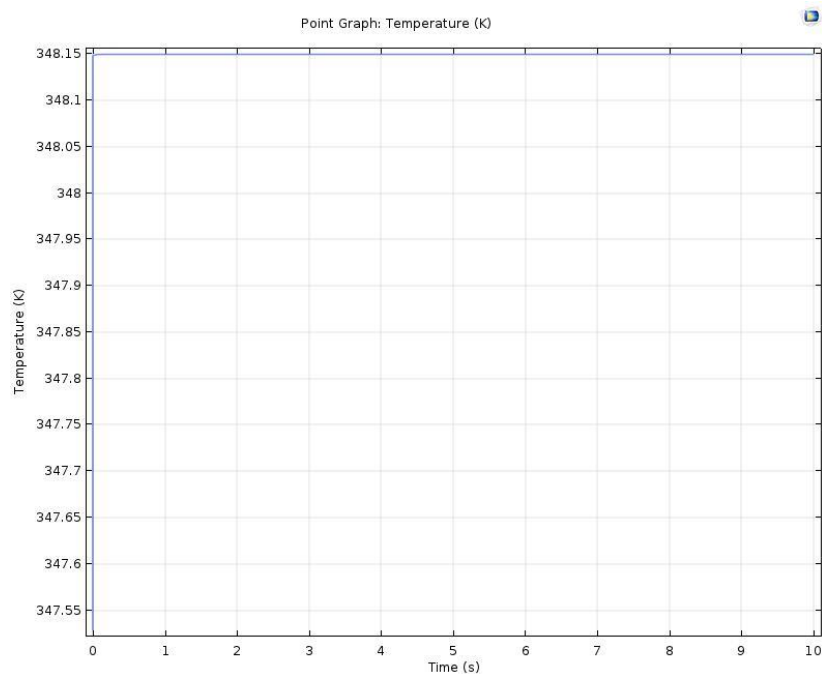
Figure 5. 5. Shows the temperature distribution of the midpoint on the top side of the unit cell for composite PZT planar models.

From Figure 5.5, the temperature of this fixed-point jumps to 75C superfast even

though the time step was set up as only 0.001s. It is impossible to see the process of

changing the temperature with time because of the thickness of the unit cell is very thin.

The rest of all volume fraction planar models have the same results as figure 5.5 so that

they will not be put into this section again.

5.1.3 Temperature distribution of pure epoxy fully cured planar model

In the first two sections, the temperature distribution of pure PZT and composite

planar models was discussed. In this section, the result of the temperature distribution

of epoxy fully cured planar model will be shown. The dimension for the pure epoxy

planar model is the same with pure PZT planar model. The result of the centerline is

shown in Figure 5.6. The horizontal axis represents the arc length of the model and the

vertical axis represents the temperature. The blue curve represents the temperature at

the zero-time step and the rest of the different color line from the bottom to top represent

the temperature distribution of other time step from 0s to 100s.
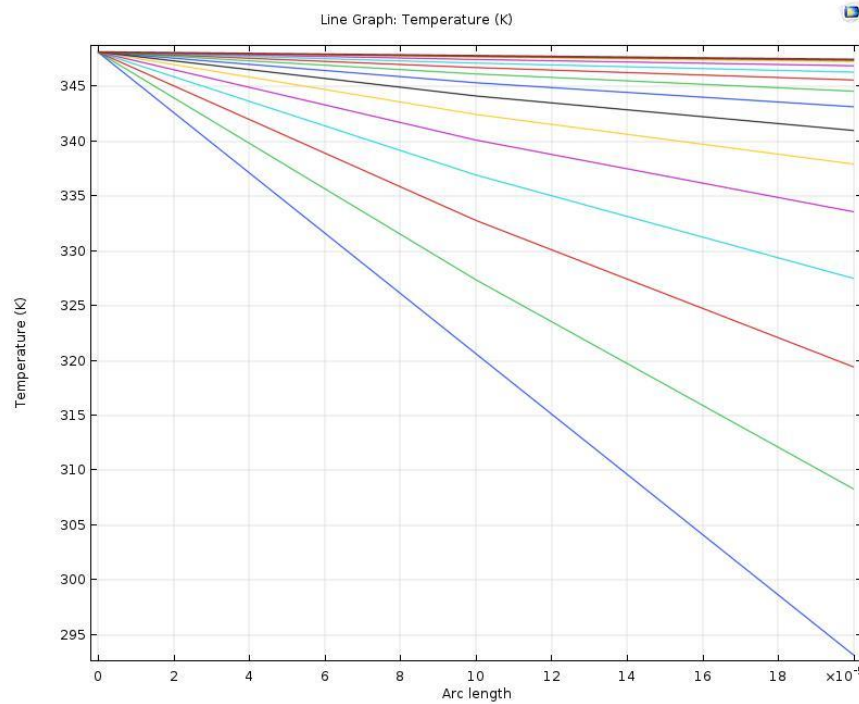
Figure 5. 6. Shows the temperature distribution of the centerline for pure epoxy fully cured planar model.

From the diagram, the temperature distribution of the pure epoxy model is similar to pure PZT model which is shown in figure 5.2. But the final temperature on the top side of the sample is a little bit lower than 75C, which is 347.47K. This is because the material properties for epoxy are different from PZT, which is affected more by heat transfer procedure and thermal dissipation has more related to heat convection and surface radiation even though the thickness of the planar model is very thin. The boundary conditions may still have a little bit of influence on thermal dissipation and heat loss. In this case, a little bit of the heat energy lost during the heat transfer process so that the final temperature on the top of the sample is less than the fixed temperature 75C. Figure 5.7 shows the result for the midpoint of the top side of the sample.
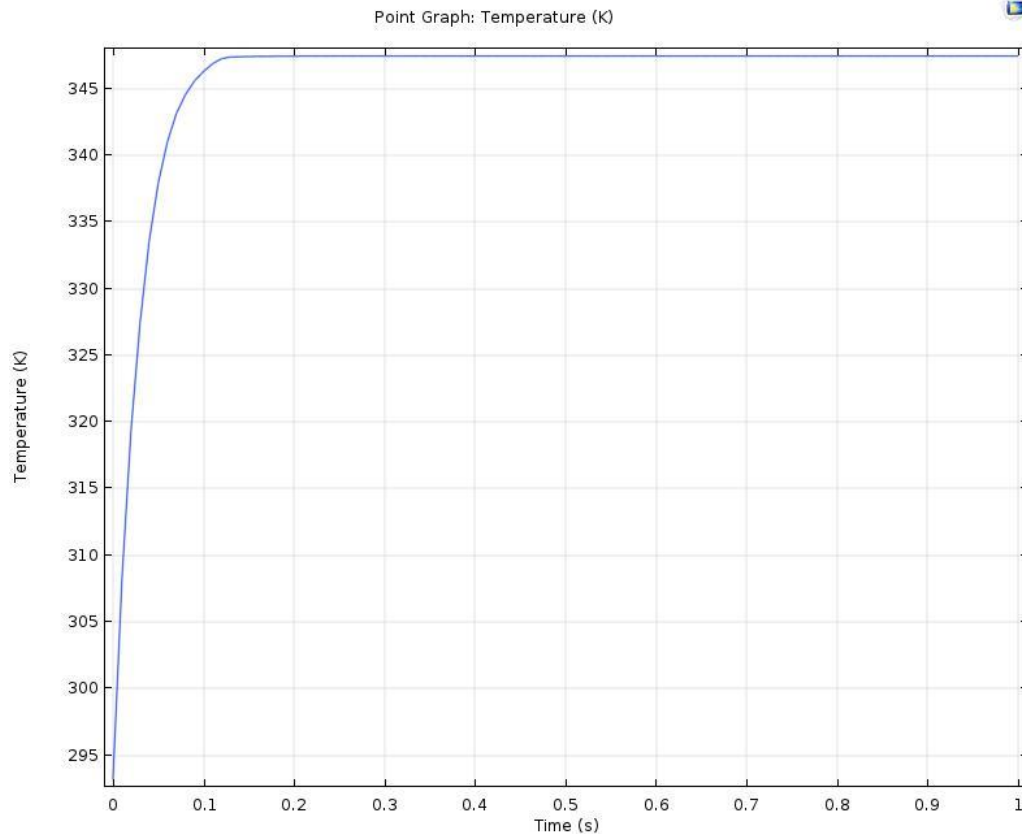
Figure 5. 7. Shows the temperature distribution of the midpoint of the top side for pure epoxy fully cured planar model.

From the figure, the temperature distribution of this fixed-point increases with increasing the time step and finally reach the temperature around 347.47K. The lost temperature is caused by thermal dissipation mentioned before.

5.1.4 Temperature distribution of pure epoxy partially cured planar model

In section 5.1.3, the temperature distribution of pure epoxy fully cured planar model was discussed. In this section, the results for partially cured epoxy will be shown. The difference between these two types of epoxy is that fully cured epoxy is in solid form and partially cured epoxy is in gel form. In addition, the material properties are different. Figure 5.8 gives us the result for the centerline. The difference of the

temperature distribution of planar sheet model from the bulk model is that the heat

transfer process in planar sheet model finished very fast in planar sheet model and there

is no heat loss in this type of model because the thickness of the model is very thin. The

horizontal axis represents the arc length of the model and the vertical axis represents

the temperature. The blue curve represents the temperature at the zero-time step and the

purple line represents the temperature distribution of the final time step 100s.
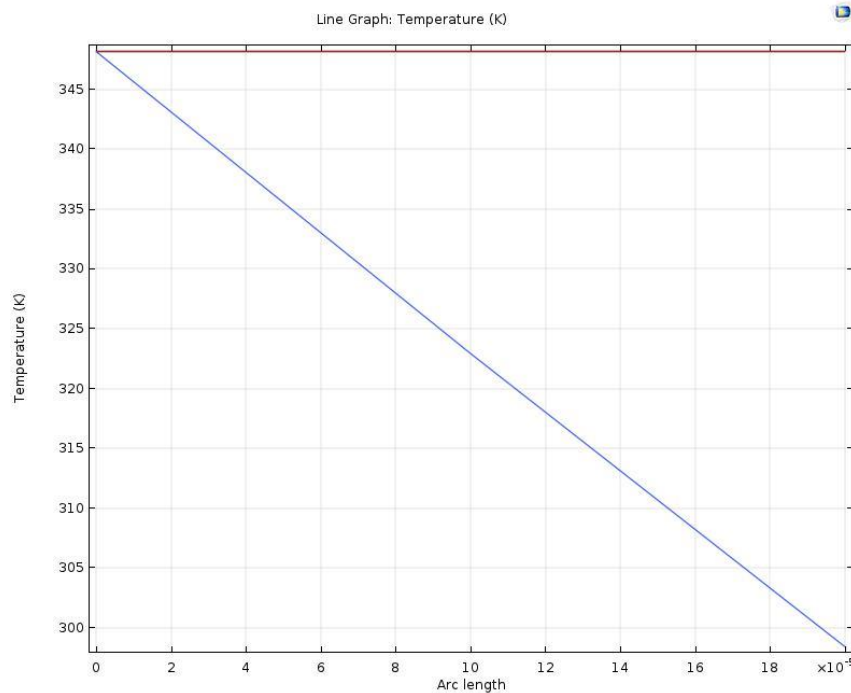
Figure 5. 8. Represents the temperature distribution of the centerline for pure epoxy partially cured
planar model.

From the figure, it shows that it is similar to Figure 5.6, it can reach the fix

temperature 75C. The difference is that the heat transfer process finishes much faster

than fully cured epoxy. This is because that the material properties for partially cured

epoxy and fully cured epoxy are different. Since the partially cured epoxy is in gel form,

it absorbs much more heat during the heat transfer process and the heat transfer process

is much quicker than in fully cured epoxy. This process is similar for heat transfer in the unit cell so that the effect of heat convection and surface radiation can be neglected. This phenomenon can be proved by Figure 5.9, which is the result for the midpoint on the top side of the sample.
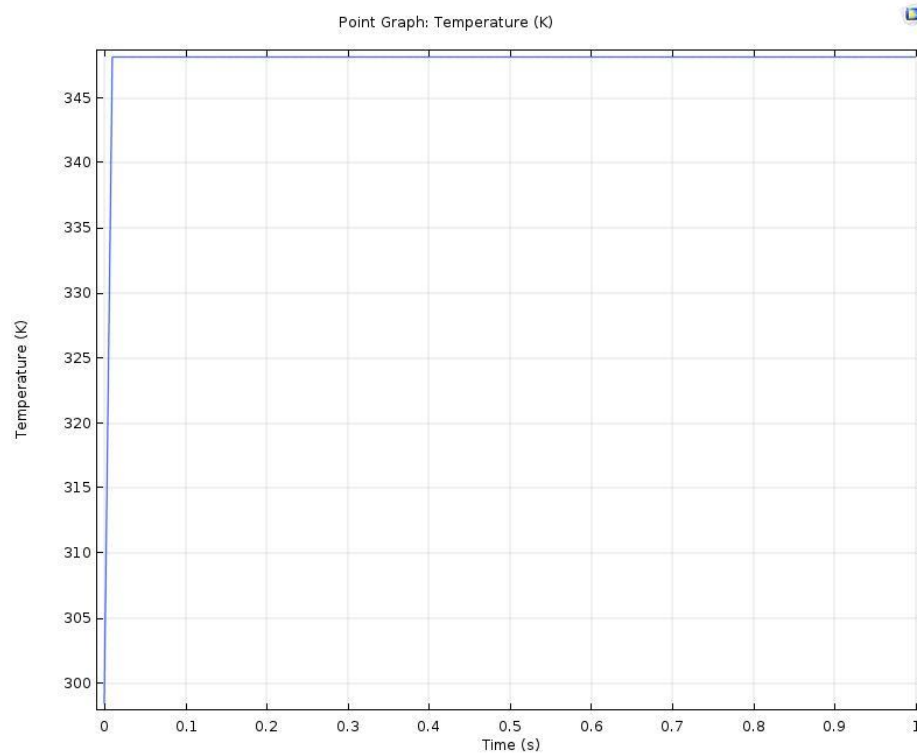
Figure 5. 9. Represents the temperature distribution of the midpoint of the top side of the sample for pure epoxy partially cured planar model.

This figure is very similar to Figure 5.7, which is for the pure epoxy fully cured planar model. The slight difference is that heat transfer in partially cured epoxy is faster than fully cured epoxy which is mentioned before. This shows the heat transfer process finishes very fast so that the thermal dissipation is almost zero. In this case, the boundary conditions for heat convection and surface radiation has a very tiny effect on the result, which represents that the fourth hypothesis mentioned in chapter 2 is correct.

5.2 Stress and strain caused by thermal expansion for planar sheet models

5.2.1 Stress and strain of the centerline of the unit cell

The reason why the centerline of the cross section of the unit cell was chosen of the pure PZT model is that this centerline is from bottom side of the model to the top side of the model with the same direction of the heat transfer. All the points on this centerline can represent the properties at that horizontal interface if it is considered that the horizontal interfaces were cut through this centerline. In this case, all the information about mechanical and thermal properties can get for the whole domain change with the time. As mentioned before since the two-phase materials epoxy DGEBA and PZT-5A have coefficients of thermal expansion, the composites will have some deformation due to the heat transfer process and this will generate stress and strain in the composite. First, let us see the results for pure PZT planar model and Figure 5.10 will show this result.
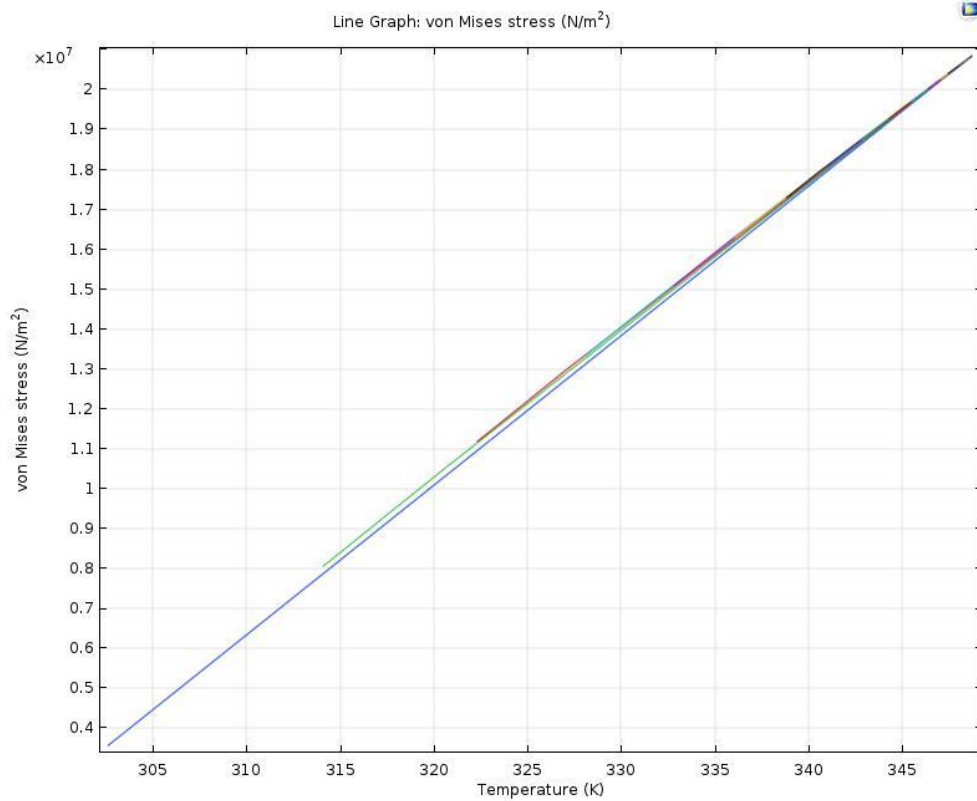
Figure 5. 10. Represents the von-Mises stress of the centerline for pure PZT planar model.

From Figure 5.10, von-Mises stress linearly increases with increasing the temperature. The stress only changes slightly with each time step. This means the samples have more deformation with high temperature and heat transfer process finish very fast in the model. The more deformation leads to a larger value of von-Mises stress in the samples. Figure 5.11 shows the result of the centerline of strain caused by thermal expansion for pure PZT planar model.
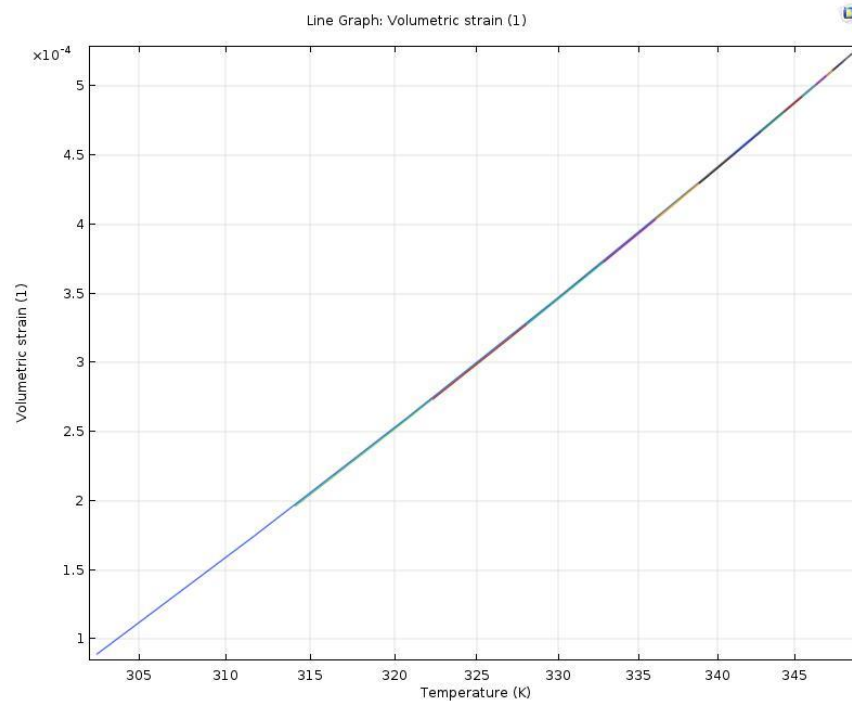
Figure 5. 11. Represents the strain of the centerline caused by thermal expansion of the pure PZT planar model.

From this figure, it shows that the strain is nearly linearly with increasing the temperature and slightly increases with increasing time step. This is similar to the change for von-Mises stress. This process indicates that heat transfer process finishes very fast in the sample because the thickness of the sample is very thin and higher temperature will lead to higher stress and strain.

Next, the results for pure epoxy planar models will be introduced. First, the results for fully cured epoxy will be shown. Figure 5.12 gives the von-Mises stress of the centerline with respect to the arc length. The horizontal axis represents the arc length of the model and the vertical axis represents the stress. The blue curve represents the stress at the zero-time step and the rest of the different color line from the bottom to top represent the temperature distribution of other time step from 0s to 100s.

From the result, it shows that the stress linearly decreases with the arc length. In addition, von-Mises stress generally increases in the polymer matrix with increasing time and finally keep at a constant. Generally, the stress is much larger within the matrix with higher temperature because a higher temperature will lead to more thermal expansion during the heat transfer process. The results in this part are linearly changed, which is different from the results in bulk models. The reason is that the thickness of the planar sheet model is much thinner than the bulk model, which will lead to the much faster heat transfer process.
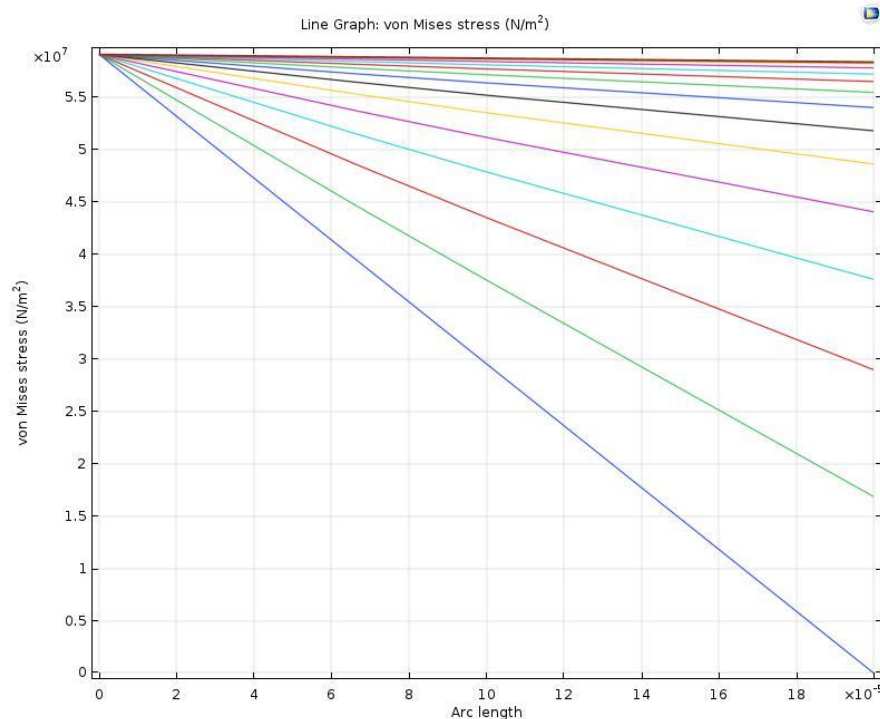
Figure 5. 12. Represents the von-mises stress of the centerline with respect to arc length change with time step. Epoxy fully cured planar model.

Figure 5.13 will show the result for the strain of the centerline of the polymer matrix. The horizontal axis represents the arc length of the model and the vertical axis represents the strain. The blue curve represents the strain at the zero-time step and the

rest of the different color line from the bottom to top represent the temperature distribution of other time step from 0s to 100s.

From the figure, the strain increases fast at the beginning of the arc length, which is close to the bottom side of the polymer. Compared to Figure 5.12, it makes sense because that the part of polymer matrix where has larger stress leads to more deformation inside the sample. But it becomes linearly increase with increasing the time step and finally increases for the whole domain with increasing the time step. This is because heat transfer procedure does not go through the whole domain at the beginning of the time step. Once the heat transfer process is done in the matrix, it will cause larger strains with increasing time.
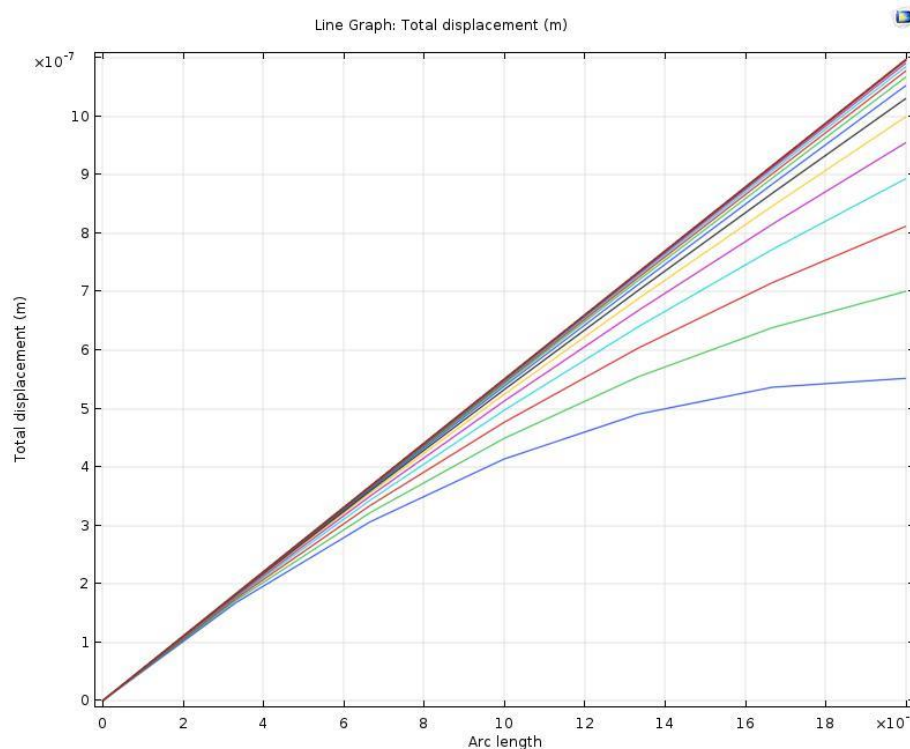
Figure 5. 13. Shows the result for the strain of the centerline caused by thermal expansion of pure epoxy fully cured planar model.

If the material of epoxy was changed as partially cured, similar results were got

with fully cured epoxy. The only difference is that the value of von-Mises stress of the centerline is smaller than fully cured epoxy. But the strain has similar results with fully cured epoxy. The difference is that the heat transfer process went through much faster than fully cured epoxy that there is no difference for each time step. This is due to the difference of the material properties and the status of the polymer matrix. The results are shown in Figure 5.14 and 5.15. The horizontal axis represents the arc length of the model and the vertical axis represents the stress and strain. The blue curve represents the stress at the zero-time step and the purple line represents the stress and strain of the final time step 100s.
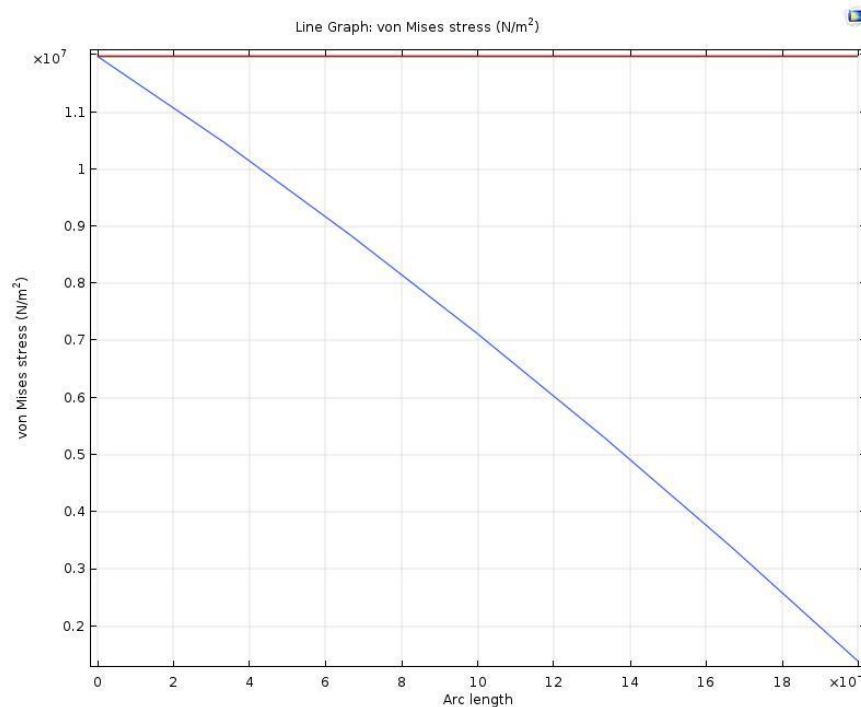

Figure 5. 14. Represents the von-Mises stress of the centerline for pure epoxy partially cured planar model.
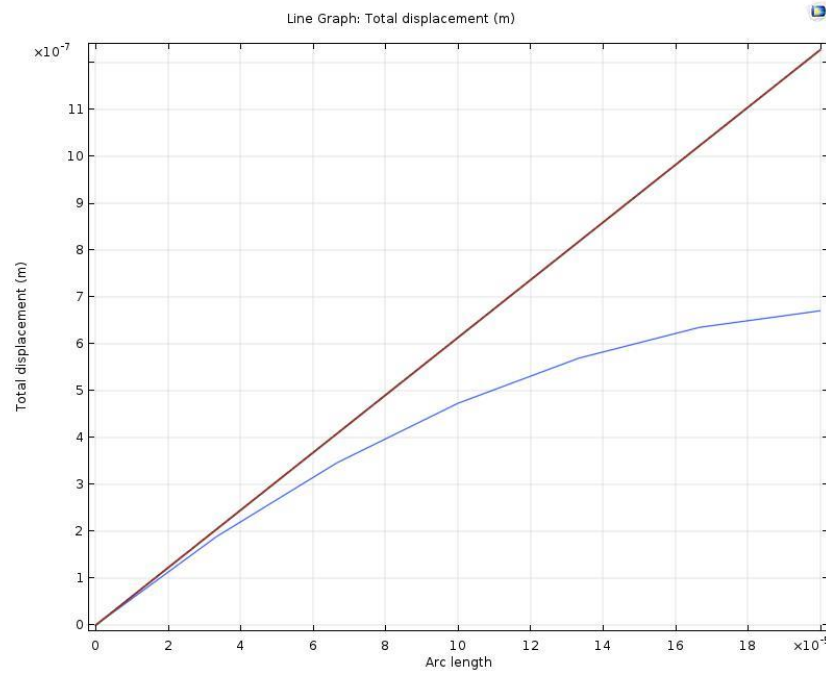
Figure 5. 15. Represents the strain caused by thermal expansion of the centerline for pure epoxy partially cured planar model.

The results listed before are pure PZT models and pure epoxy models. They have the same dimension of real samples fabricated by Zichen Lao in our group. Next, let us see the results for composite models. Figure 5.16 to figure 5.22 are the results for von-Mises stress of the centerline from 10% PZT bulk model to 70% bulk model. The unit cell used for the planar sheet model is thinner than the bulk model, which is the rectangle not the square. But the results for stress and strain are in the similar range for the bulk models. This is because stress and strain are caused by thermal expansion, which is affected by the thermal properties and mechanical properties of the composite. It does not have too much relation of the geometry of the model. In the following figure, blue curve represents stress at zero second and the purple curve represents the stress at other time step.
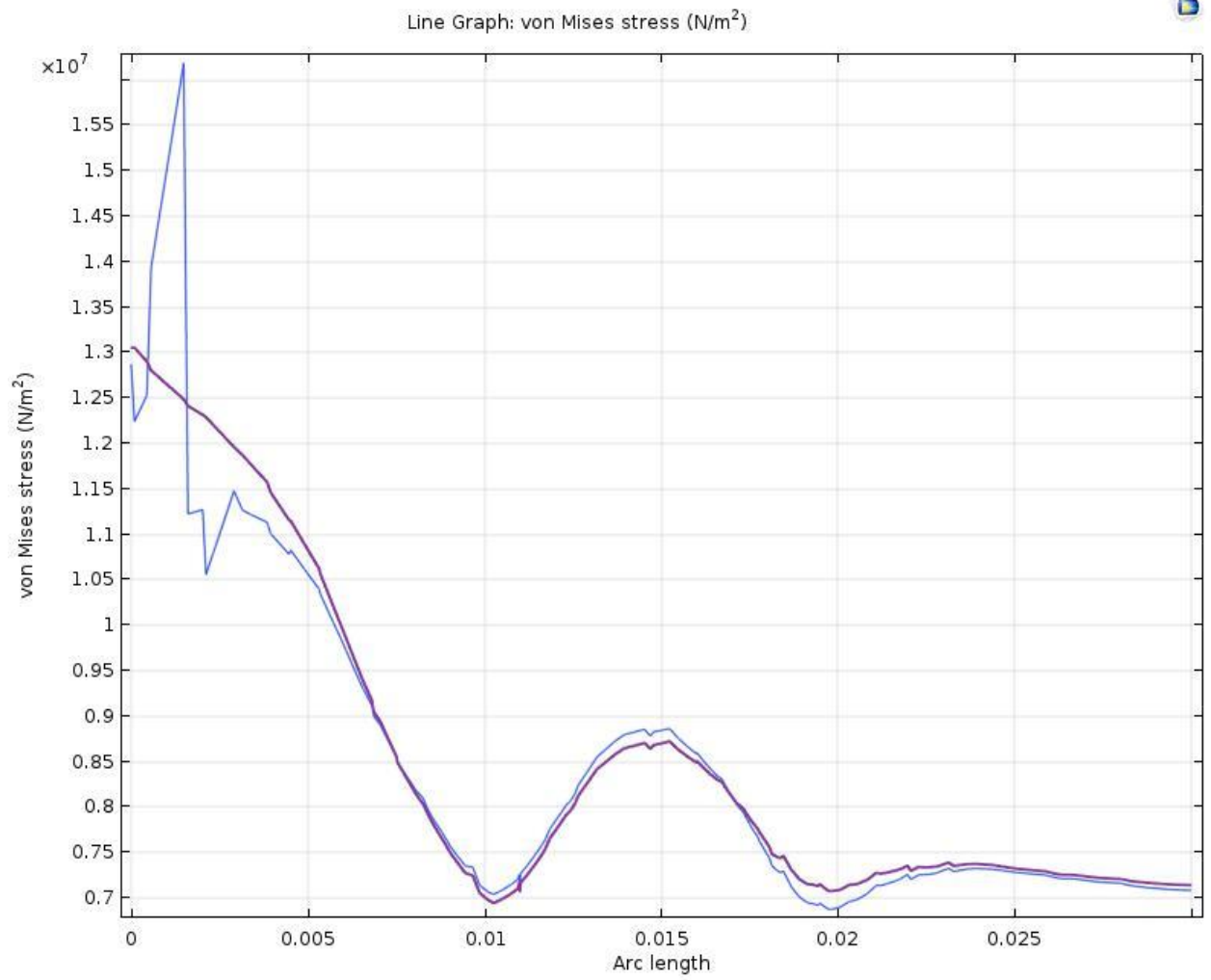
Figure 5. 16. Represents von-Mises stress of the centerline for 10% PZT planar model.
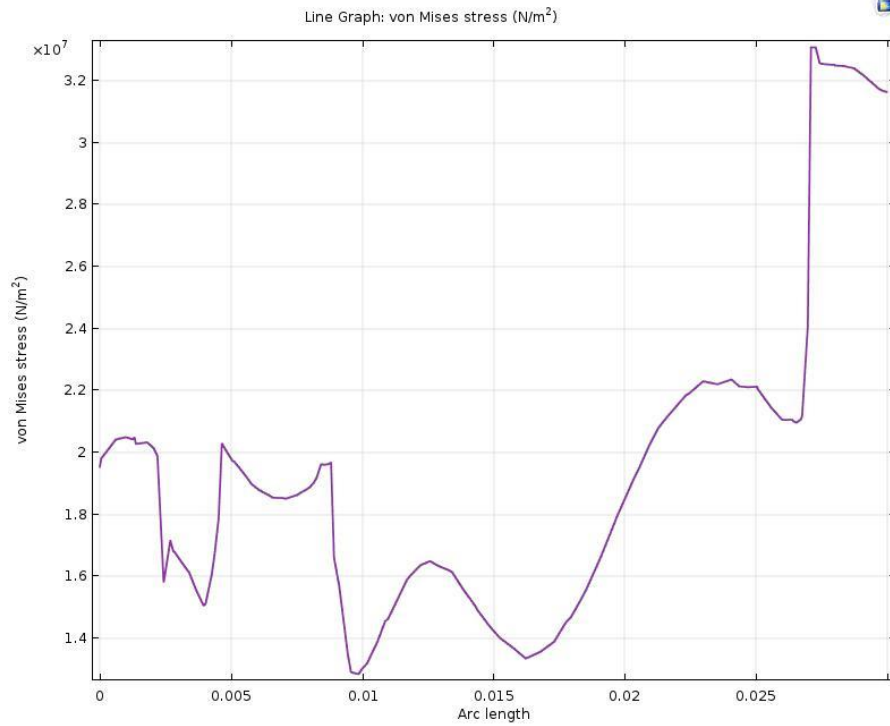
Figure 5. 17. Represents von-Mises stress of the centerline for 20% PZT planar model.
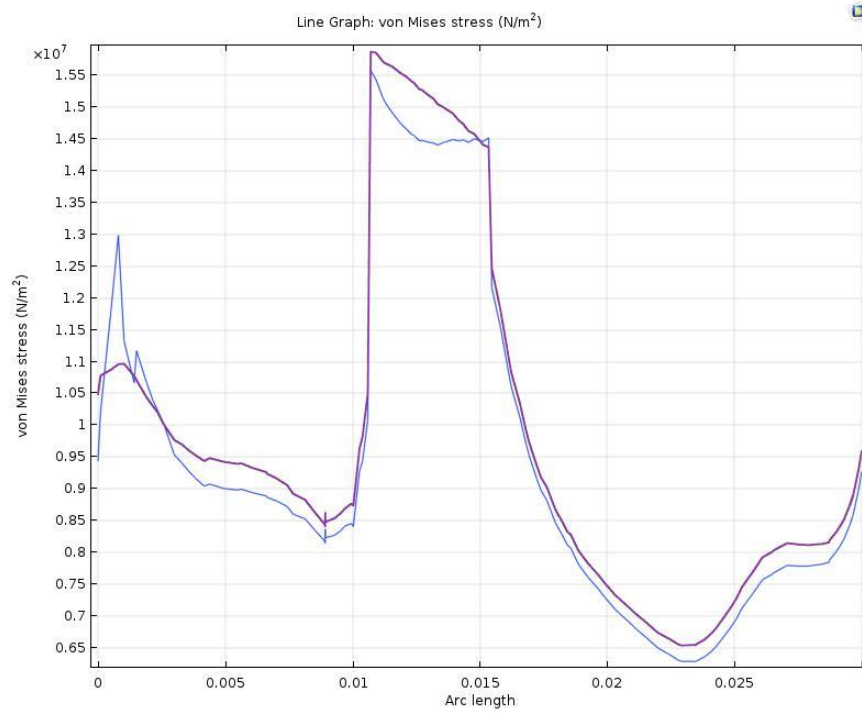
Figure 5. 18. Represents von-Mises stress of the centerline for 30% PZT planar model.
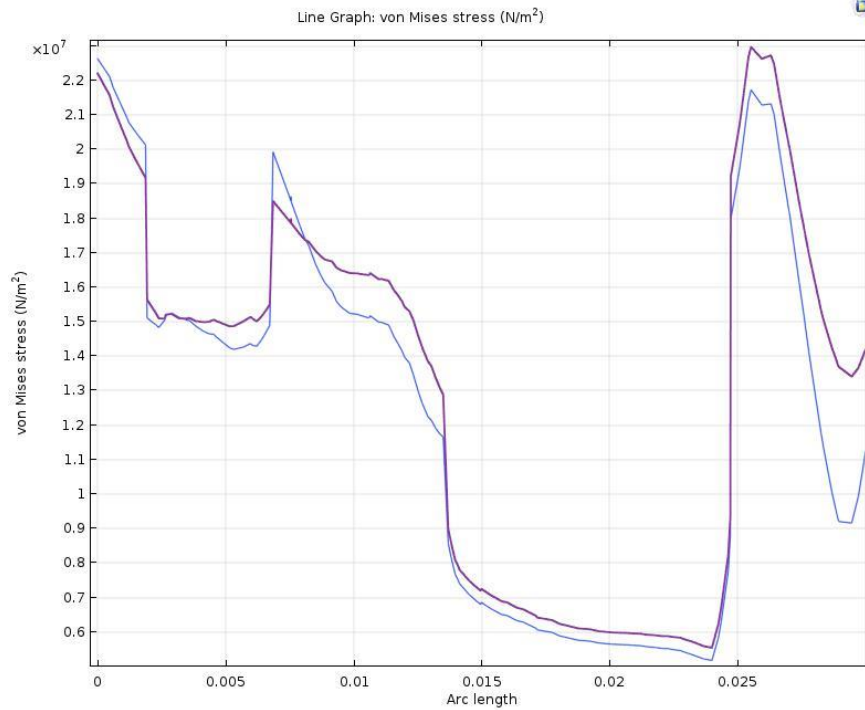
Figure 5. 19. Represents von-Mises stress of the centerline for 40% PZT planar model.
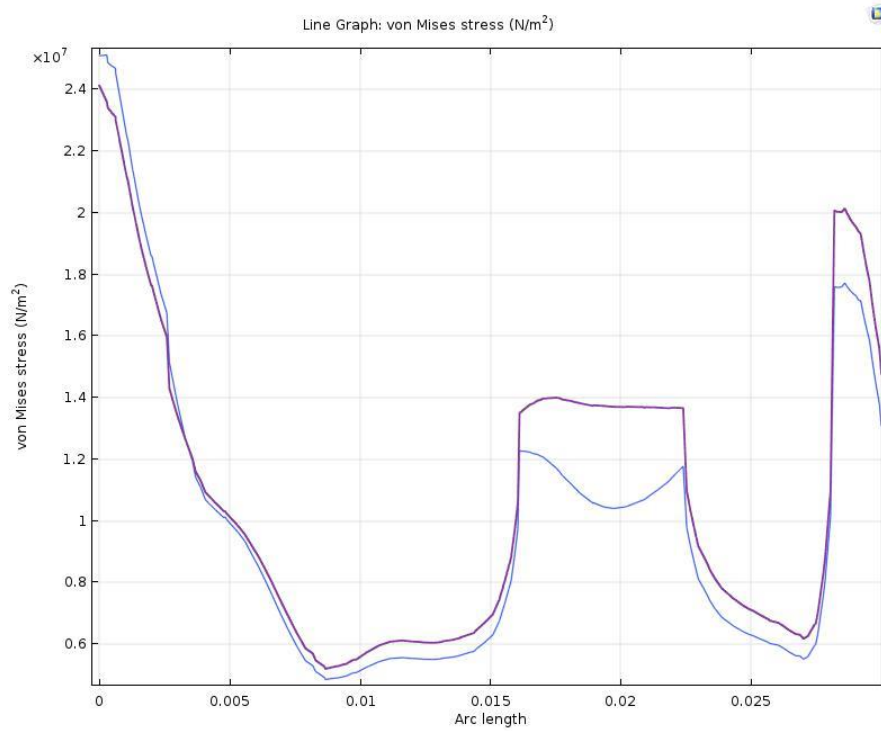
Figure 5. 20. Represents von-Mises stress of the centerline for 50% PZT planar model.
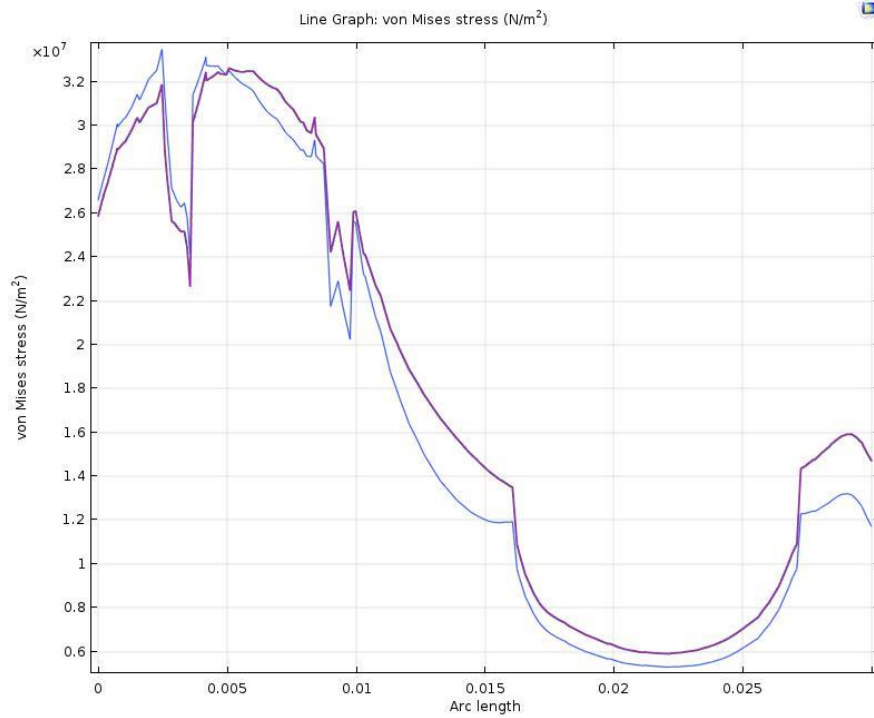
Figure 5. 21. Represents von-Mises stress of the centerline for 60% PZT planar model.
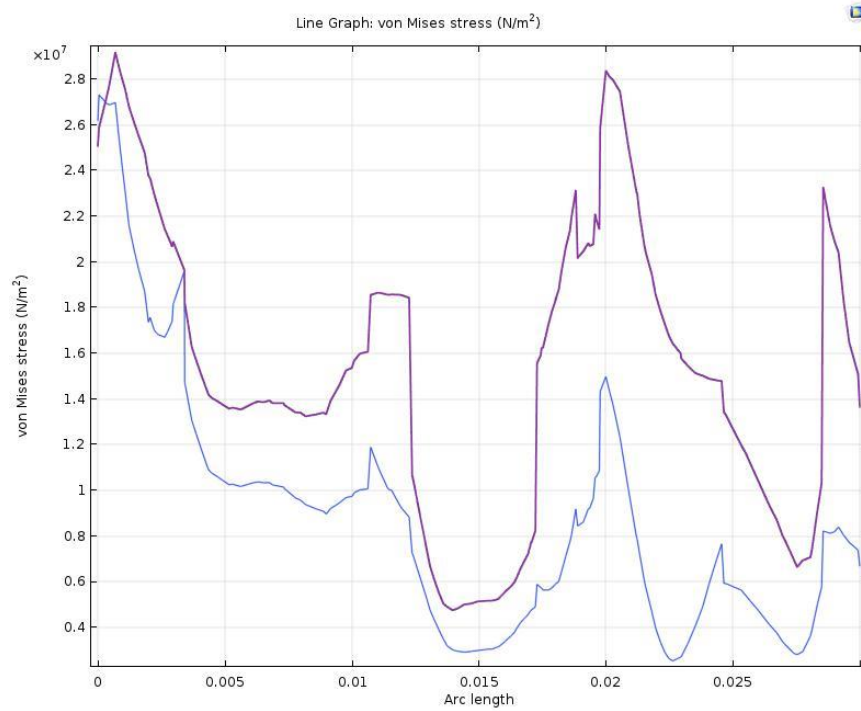
Figure 5. 22. Represents von-Mises stress of the centerline for 70% PZT planar model.

The above figures are von-Mises stress of the centerline for composite PZT models from 10% to 70%. From the figures, it shows that the von-Mises stress generally

increases with increasing the volume fraction of PZT except 10% and 70% planar models. The reason is that of stress equal to Young's modulus of the material times strain. Young's modulus of PZT is much larger than epoxy DGEBA. That means the higher the volume fraction of PZT the composite has, the larger Young's modulus the composite has. Since the change of the strain is not too much of each volume fraction of the composite. That is why the stress increases with increasing the volume fraction of PZT. In addition, it is shown that the stress of the centerline dip down and go back up several times in each volume fraction PZT models. The reason why the curve is not exponential or linear might be due to the position of PZT particles. The stress generated close to the PZT particles is different from the stress generated in polymer part. This may lead to the curve go up and down. It is hard to find which part of the centerline has the largest stress and smallest stress. They are in different place for different volume fraction models. Some of the smallest stress occurs close to the bottom side of the unit cell and some of them happen close to the top side of the unit cell. The same thing happens for the largest stress. It is hard to find the rules for that. The largest value occurs in 20% model. Next, the strain for the composite models will be introduced. The results for strain generated by thermal expansion for each volume fraction of PZT model are given through Figure 5.23 to 5.29. The horizontal axis represents the arc length of the model and the vertical axis represents the strain. The blue curve represents the strain at the zero-time step and the purple line represents the strain of the final time step 100s. The results of the strain for the planar sheet models is in a similar range of the bulk models. It does not have too much influence by the different geometry for the unit cell.
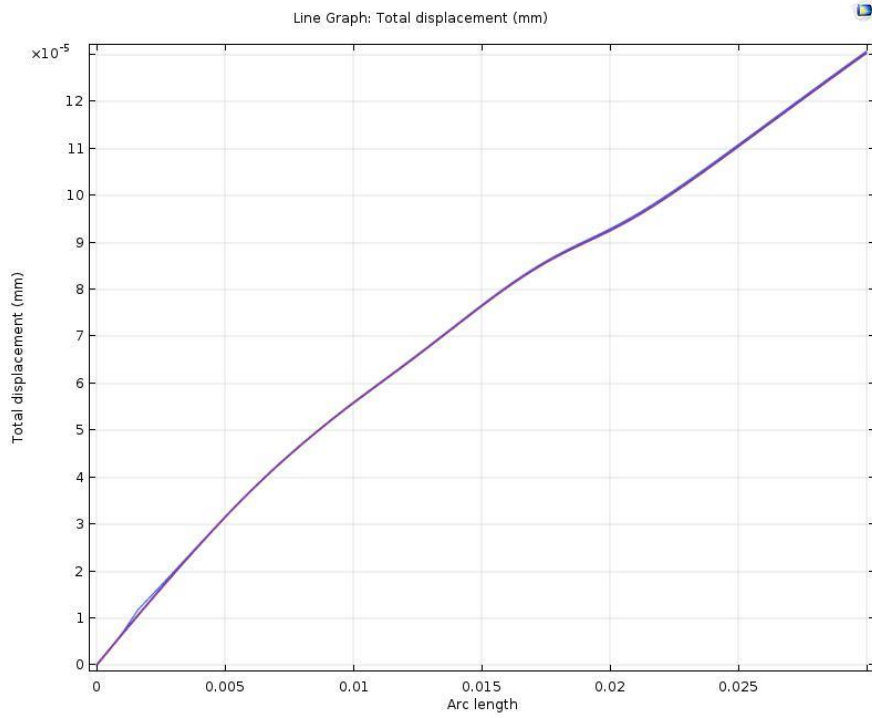
Figure 5. 23. Represents a strain of the centerline for 10% PZT planar model.
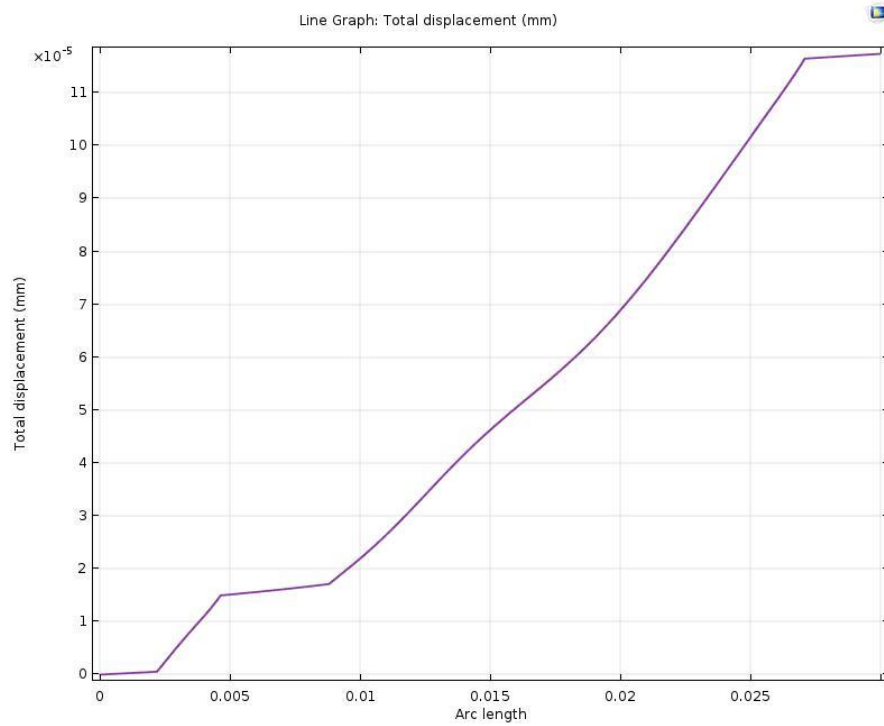
Figure 5. 24. Represents a strain of the centerline for 20% PZT planar model.
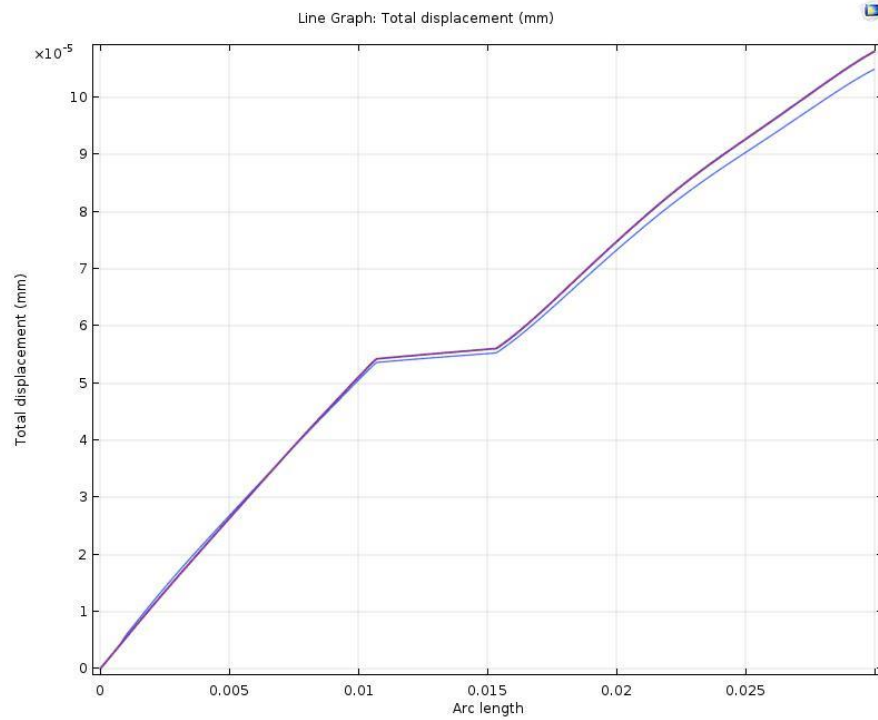
Figure 5. 25. Represents a strain of the centerline for 30% PZT planar model.
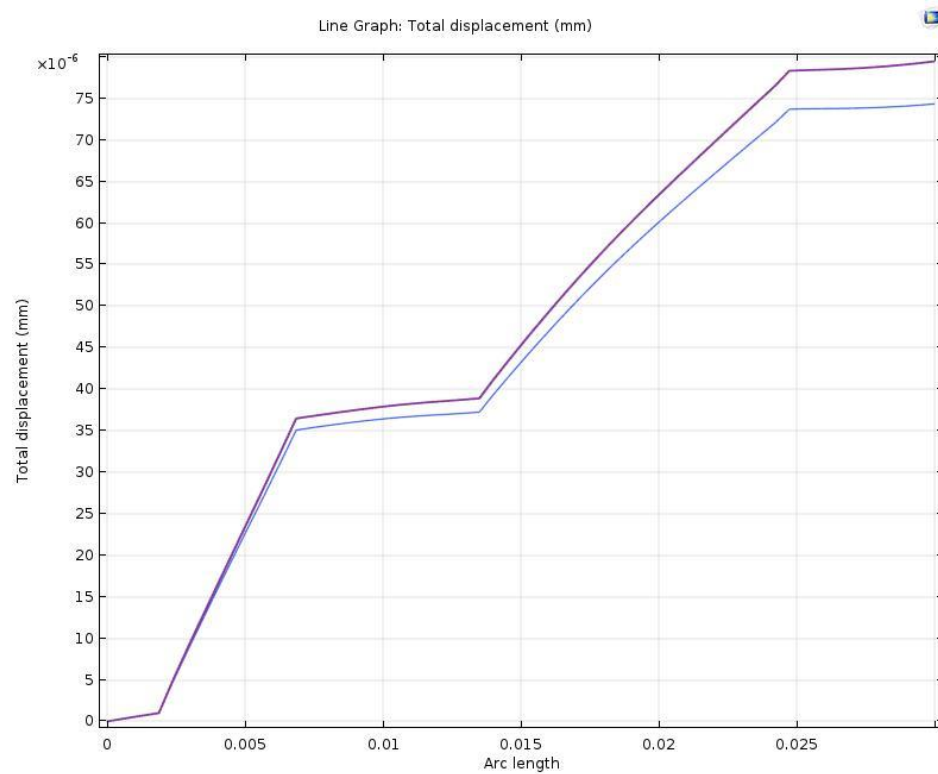
Figure 5. 26. Represents a strain of the centerline for 40% PZT planar model.
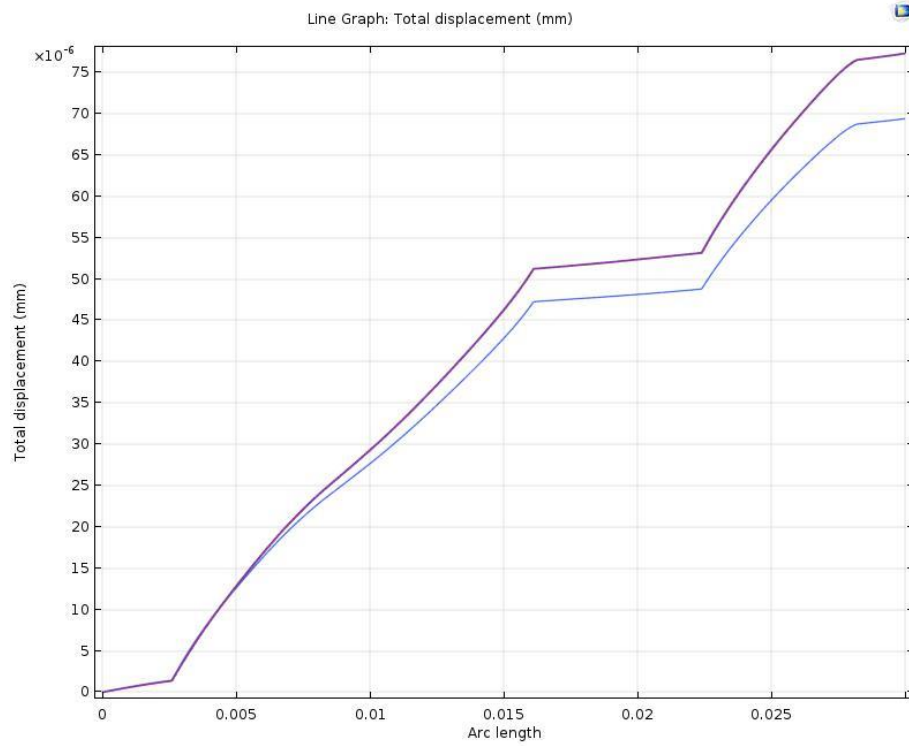
Figure 5. 27. Represents a strain of the centerline for 50% PZT planar model.
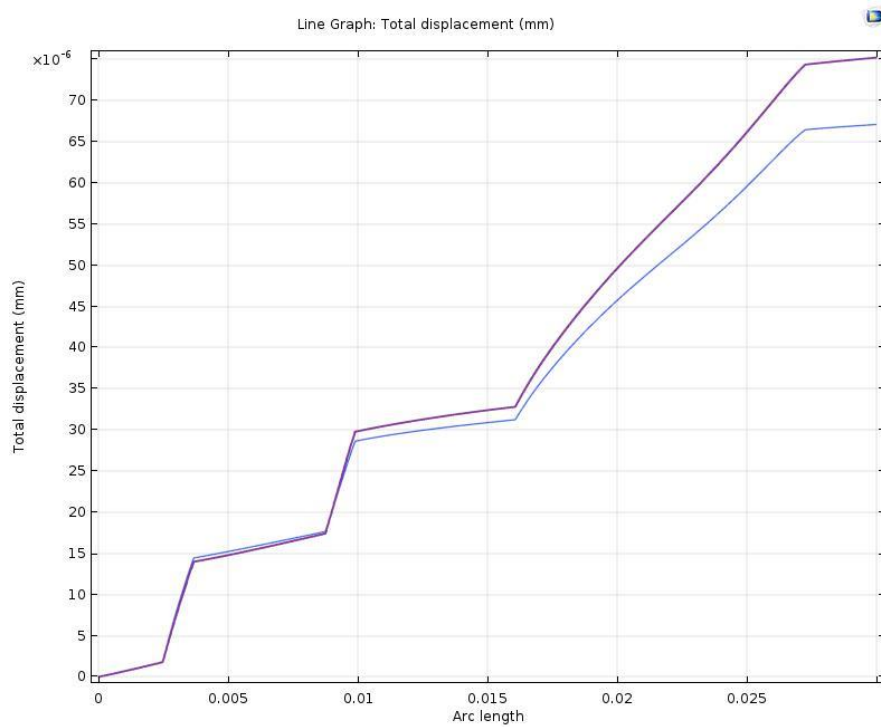
Figure 5. 28. Represents a strain of the centerline for 60% PZT planar model.
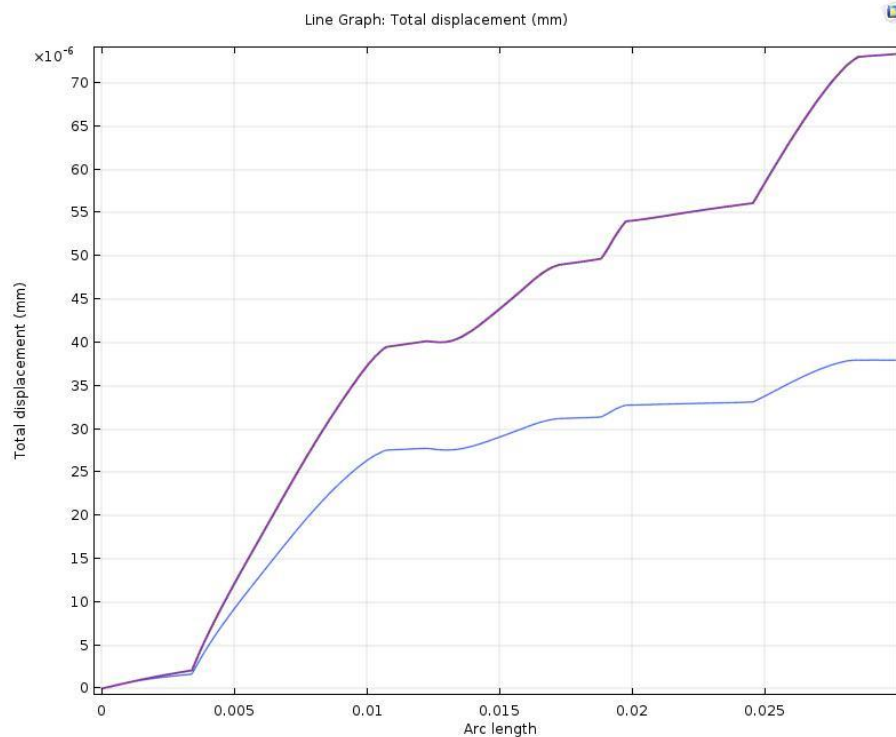
Figure 5. 29. Represents a strain of the centerline for 70% PZT planar model.

From these figures, it was found that the strain of the centerline caused by thermal expansion decreases with increasing the volume fraction of PZT in low volume fraction models, such as 10%, 20%, and 30%. But it almost keeps at the same range in high volume fraction models, such as 40%, 50%, 60%, and 70%. This is because higher volume fraction PZT models have much higher Young's modulus than low volume fractions models. Thus, higher volume fractions PZT models are more stiffness than lower volume fractions PZT models. However, the shape of the strain for each volume fraction is similar, they increase with the arc length. But the values for each point on the arc length decrease with increasing the volume fractions of PZT, such as point 0.005mm. For 10% and 20% PZT models, the range of the strain is similar, which is much larger than the rest of the models. This is because, for 10% and 20% models, the composites mainly consist of epoxy DGEBA, which Young's modulus is much smaller

than PZT and the polymer matrix is much easier to be deformed than PZT particles. Since the epoxy phase will be cured during the heat transfer process, composites with more epoxy materials might absorb much more heat during the heat transfer process when add the same heat source on it. The composites which absorb more heat may have much more deformation than higher volume fraction PZT models. That is why 10% and 20% composites models have almost the double range of the strain than other volume fractions PZT models. In this study, it seems like that the largest displacement caused by thermal expansion occurs at 10% PZT composite and the lowest occurs at 70% planar model.

5.2.2 Stress and strain of the mid-point for the top side of the unit cell

In section 5.2.1, the stress and strain of the centerline of the unit cell will be discussed. In this section, the results for stress and strain of the midpoint of the top side of the unit cell will be shown for each volume fraction of PZT planar models. Such results for von-Mises stress will be given through Figure 5.30 to 5.36 for 10% to 70% PZT bulk models. The horizontal axis represents the time and the vertical axis represents the stress.
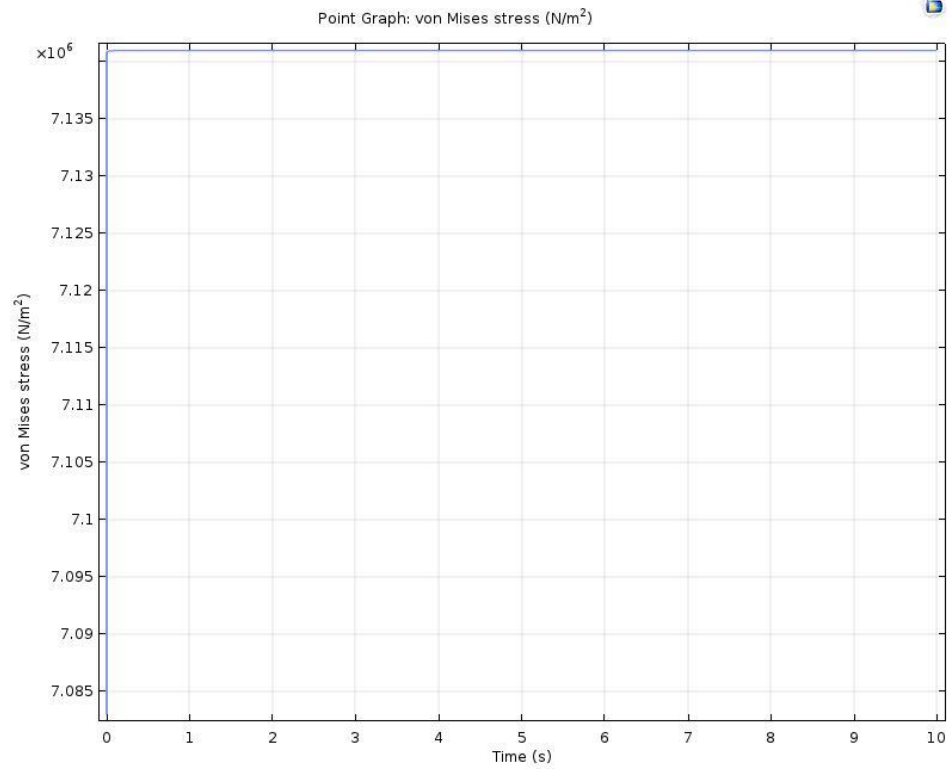
Figure 5. 30. Represents von-Mises stress of midpoint of the top side for 10% PZT planar model.
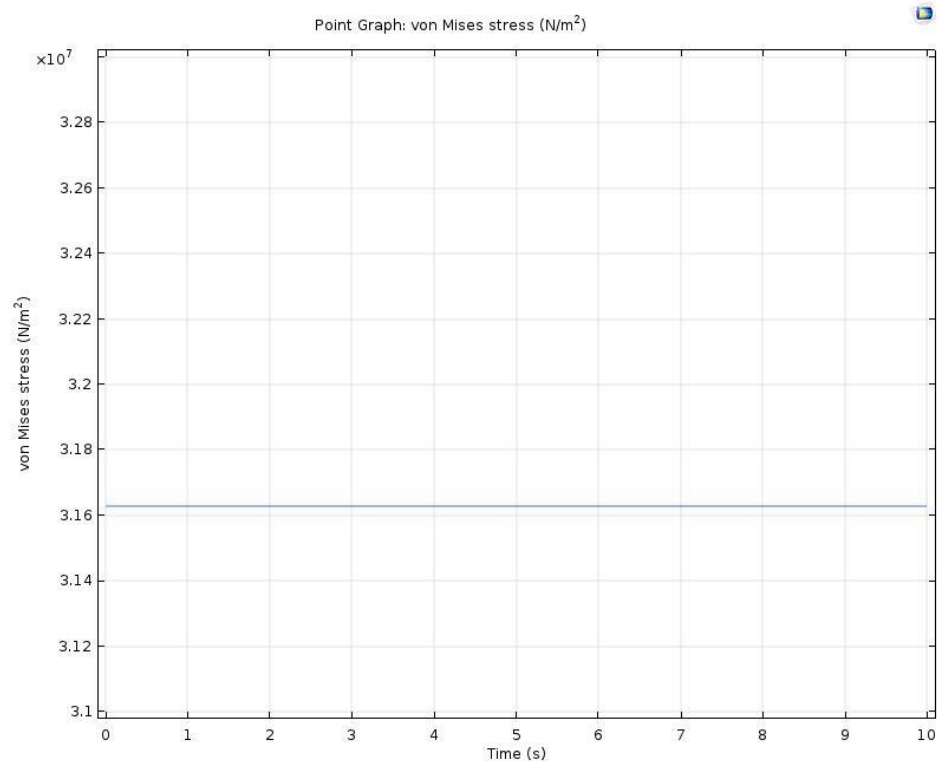
Figure 5. 31. Represents von-Mises stress of midpoint of the top side for 20% PZT planar model.
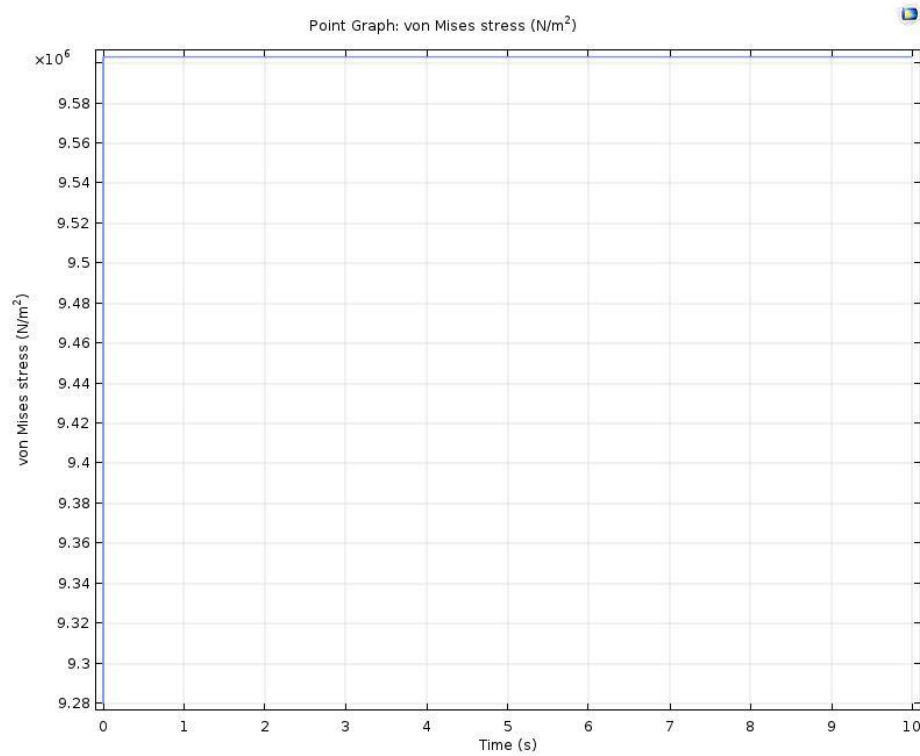
Figure 5. 32. Represents von-Mises stress of midpoint of the top side for 30% PZT planar model.
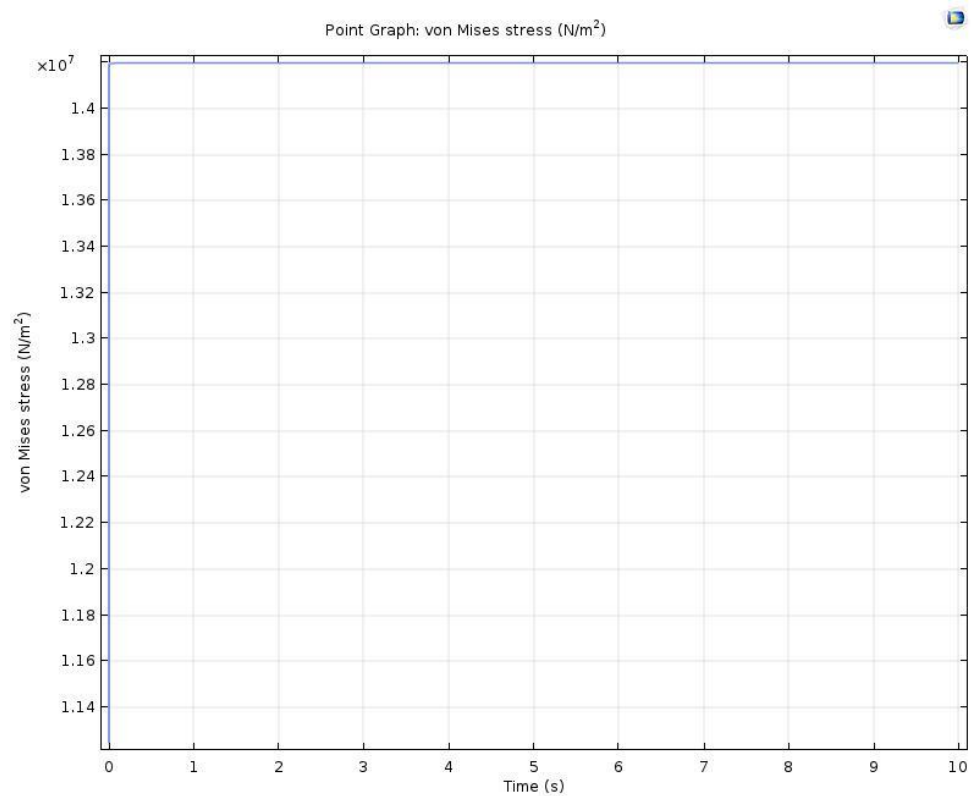
Figure 5. 33. Represents von-Mises stress of midpoint of the top side for 40% PZT planar model.
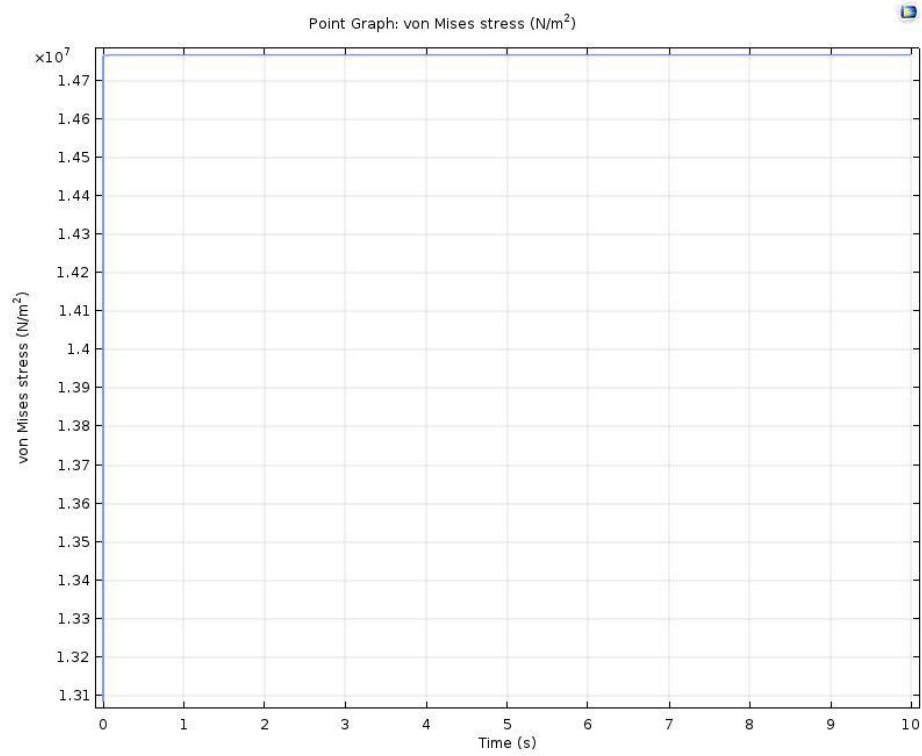
Figure 5. 34. Represents von-Mises stress of midpoint of the top side for 50% PZT planar model.
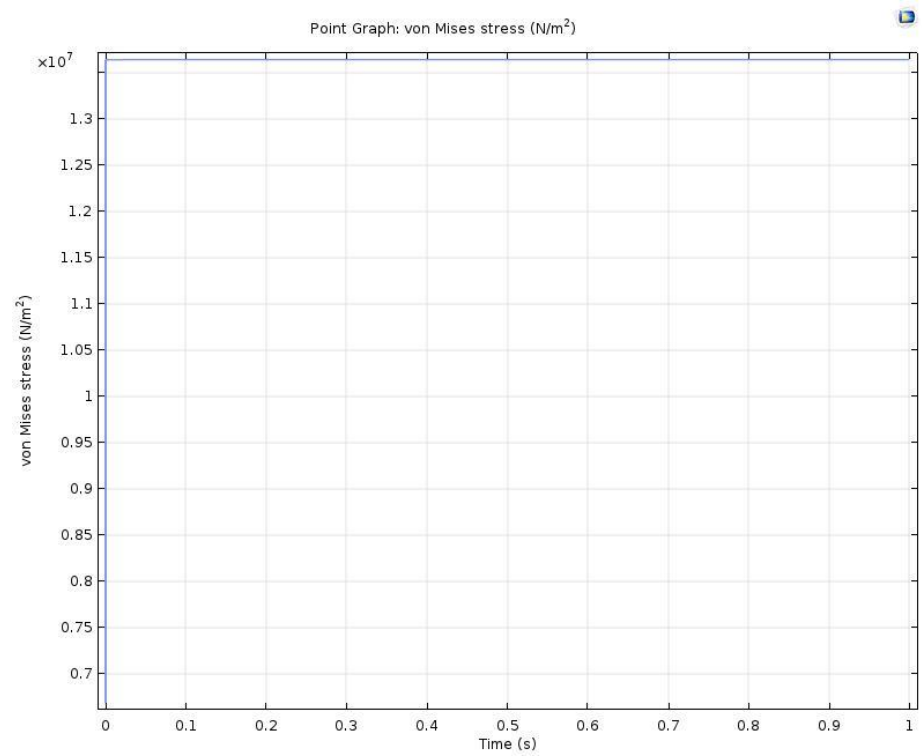
Figure 5. 35. Represents von-Mises stress of midpoint of the top side for 60% PZT planar model.
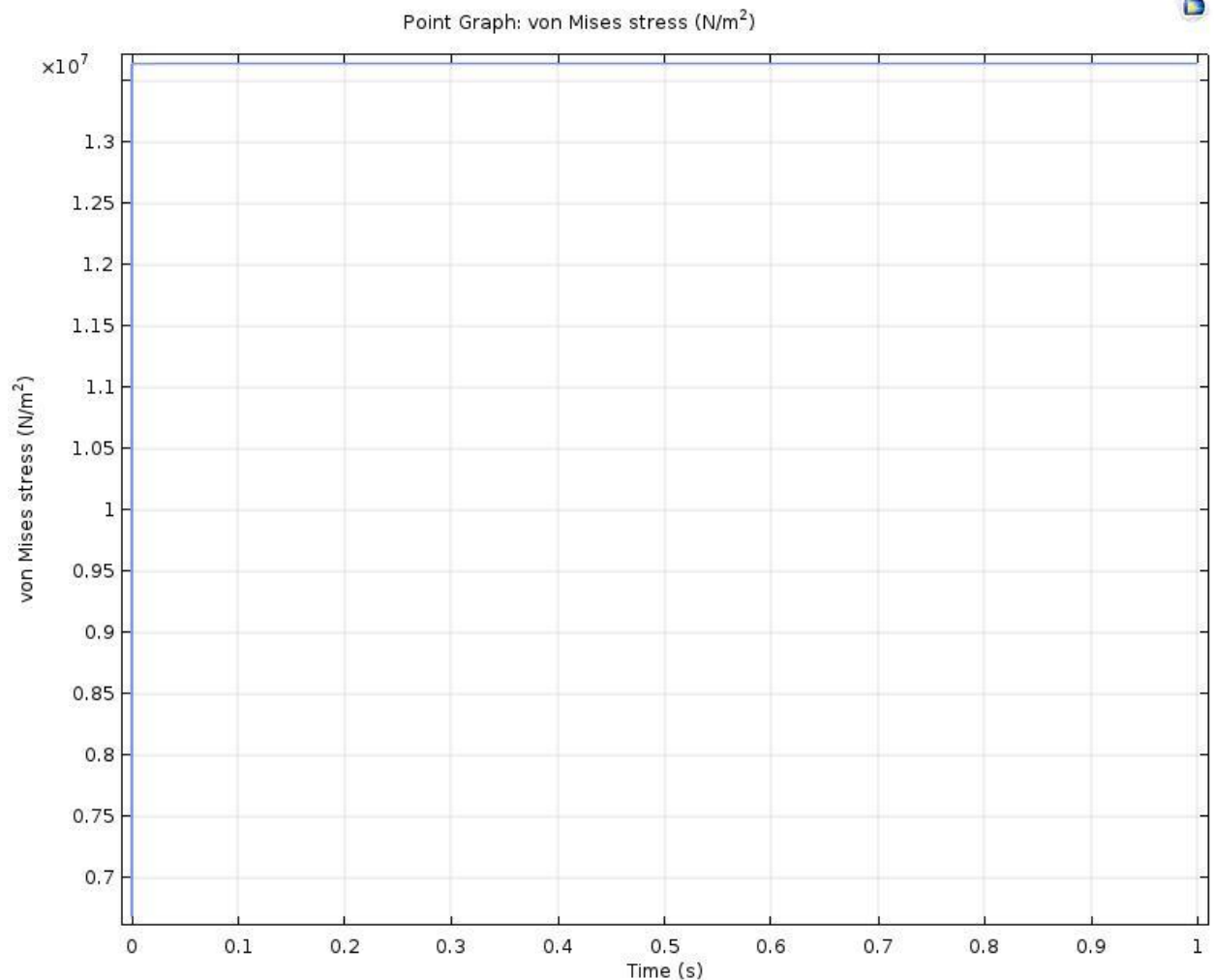
Figure 5. 36. Represents von-Mises stress of midpoint of the top side for 70% PZT planar model.

From the figures, it shows that the stress at the midpoint is fixed at a constant for each volume fraction PZT models with changing time. The results increase with the increasing volume fraction of PZT for some volume fraction models such as 10%, 20%,30%, 40%, 50% models. But some higher volume fraction models have a little bit smaller values than the lower volume fraction models, such as 60% and 70% and they have very similar results. 20% model has the largest value for von-Mises stress which is the same mention as the result from the centerline.

Next, let me show the results for the strain caused by thermal expansion of the

midpoint on the top side of the unit cell for each volume fraction model. The results will be shown from Figure 5.37 to 5.43. The horizontal axis represents the time and the vertical axis represents the strain.
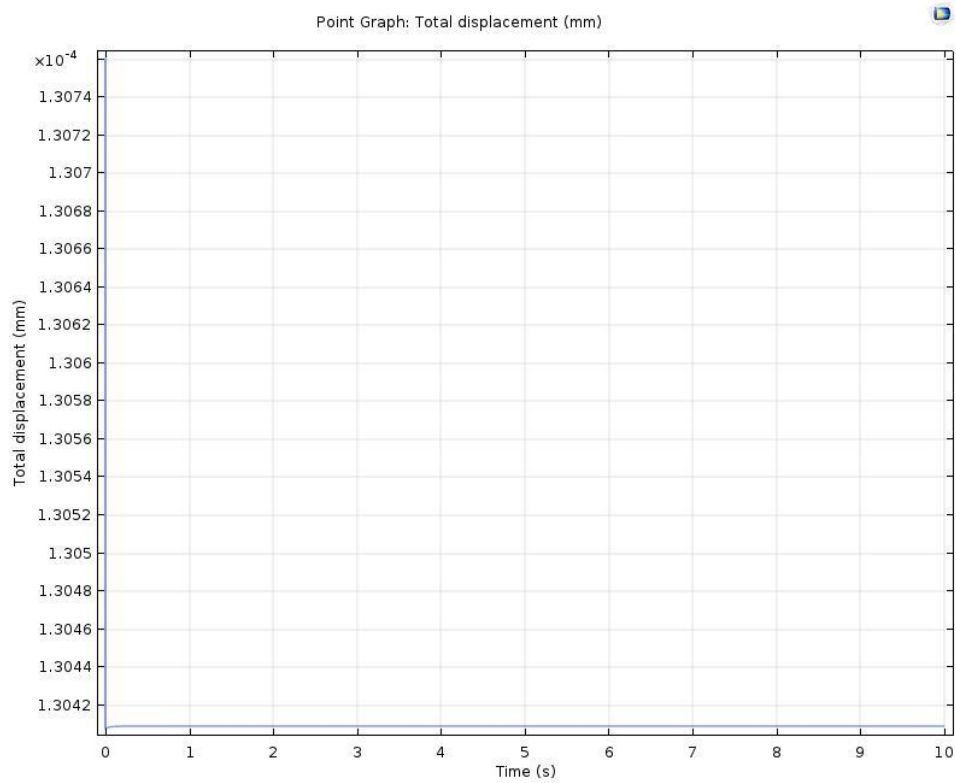
Figure 5. 37. Represents a strain of the midpoint of the top side for 10% PZT planar model.
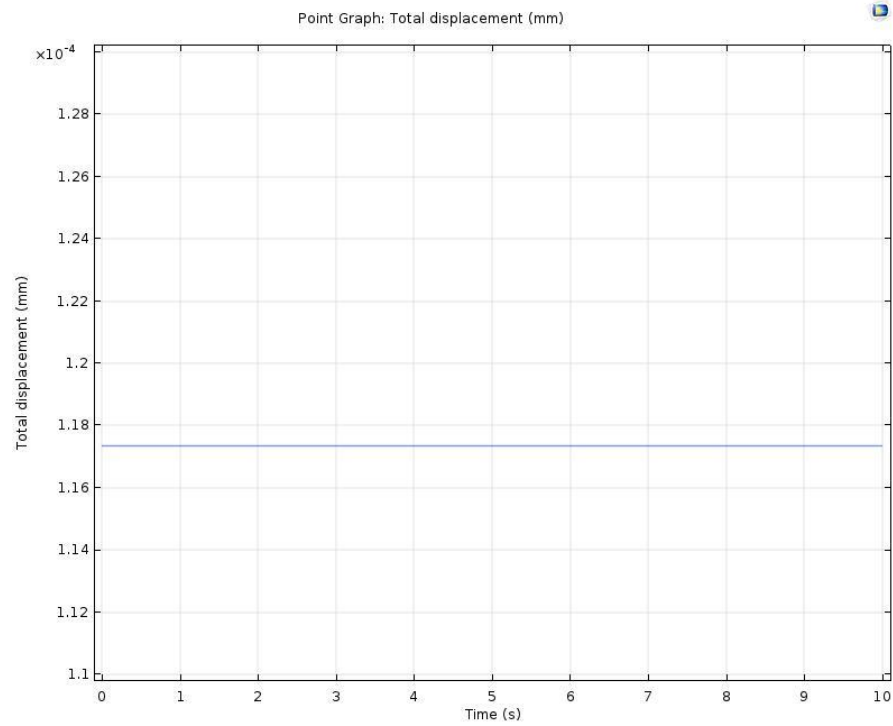
Figure 5. 38. Represents a strain of the midpoint of the top side for 20% PZT planar model.
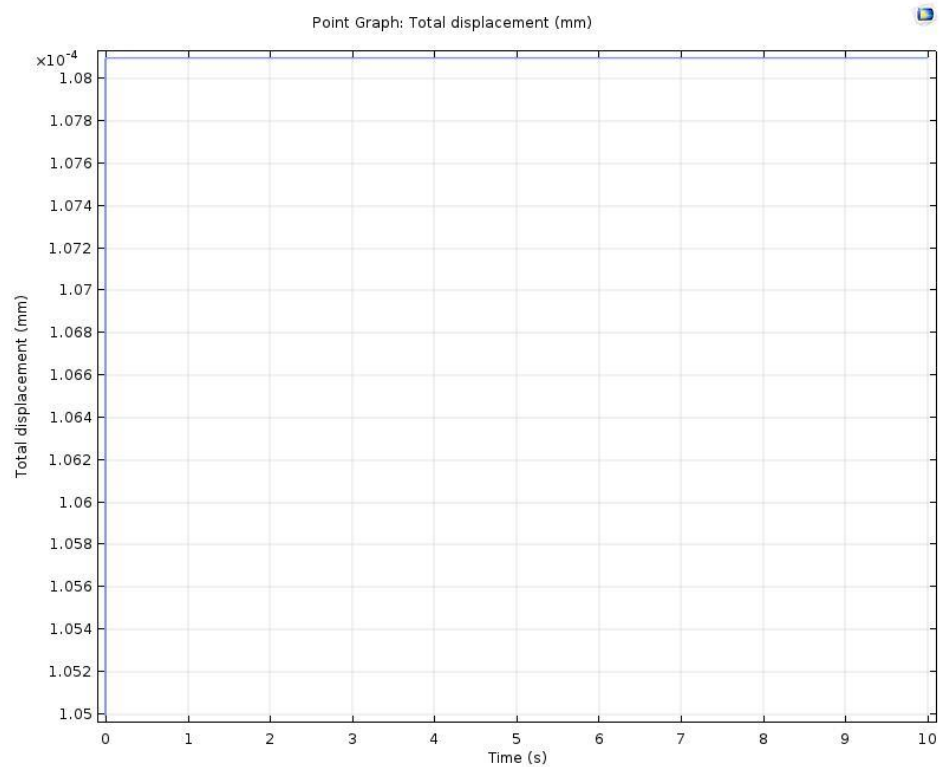
Figure 5. 39. Represents a strain of the midpoint of the top side for 30% PZT planar model.
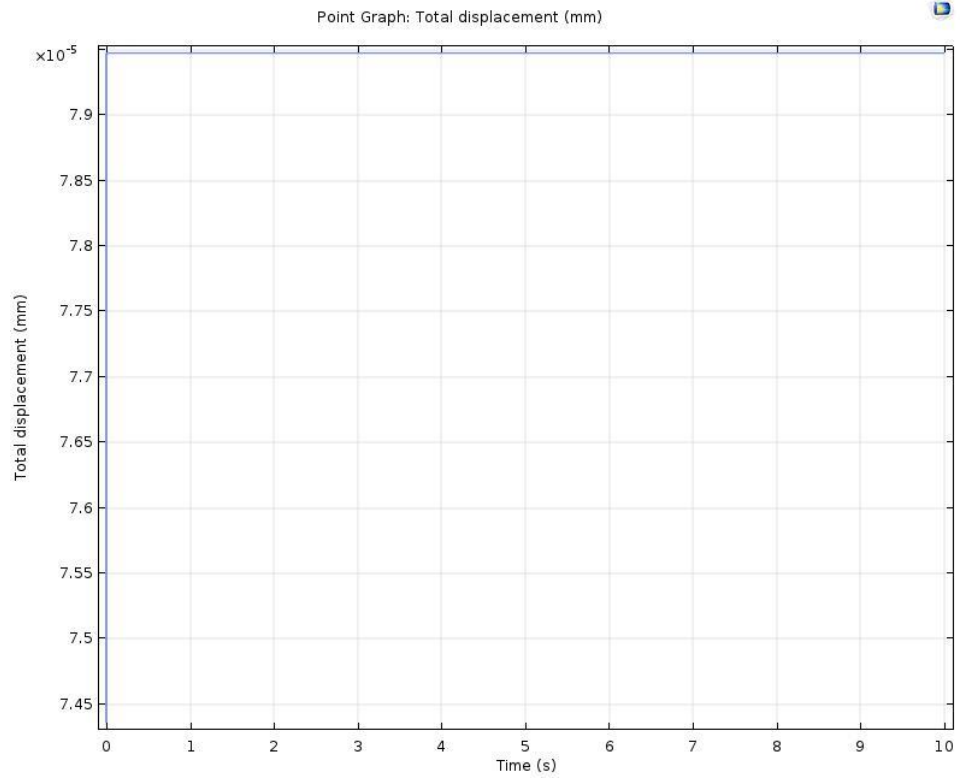
Figure 5. 40. Represents a strain of the midpoint of the top side for 40% PZT planar model.
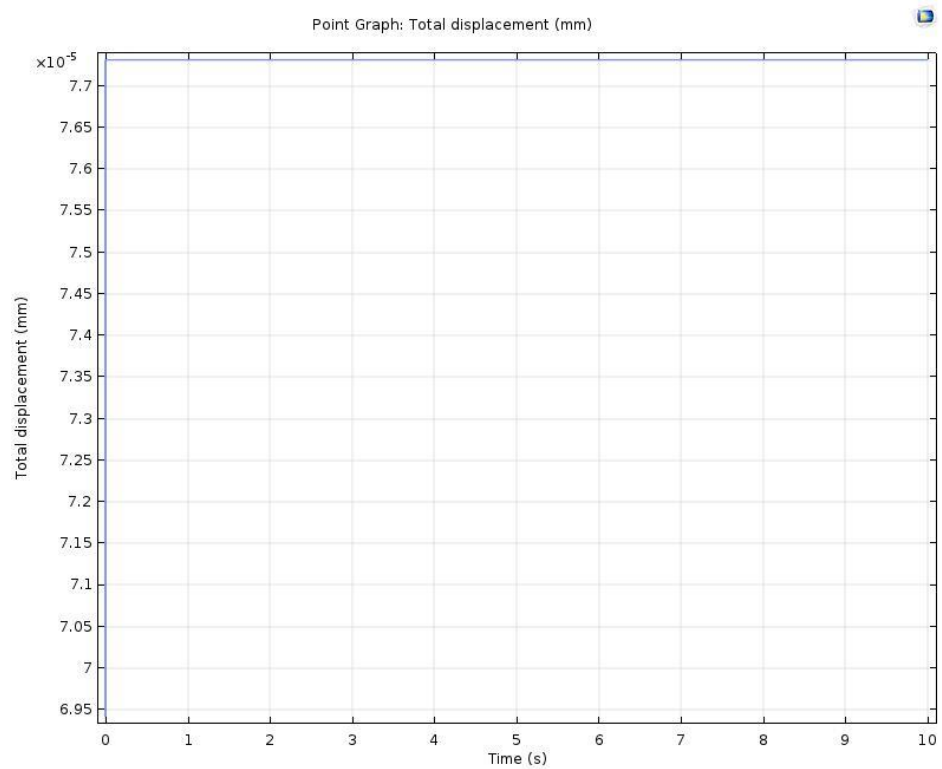
Figure 5. 41. Represents a strain of the midpoint of the top side for 50% PZT planar model.

Point Graph: Total displacement (mm)
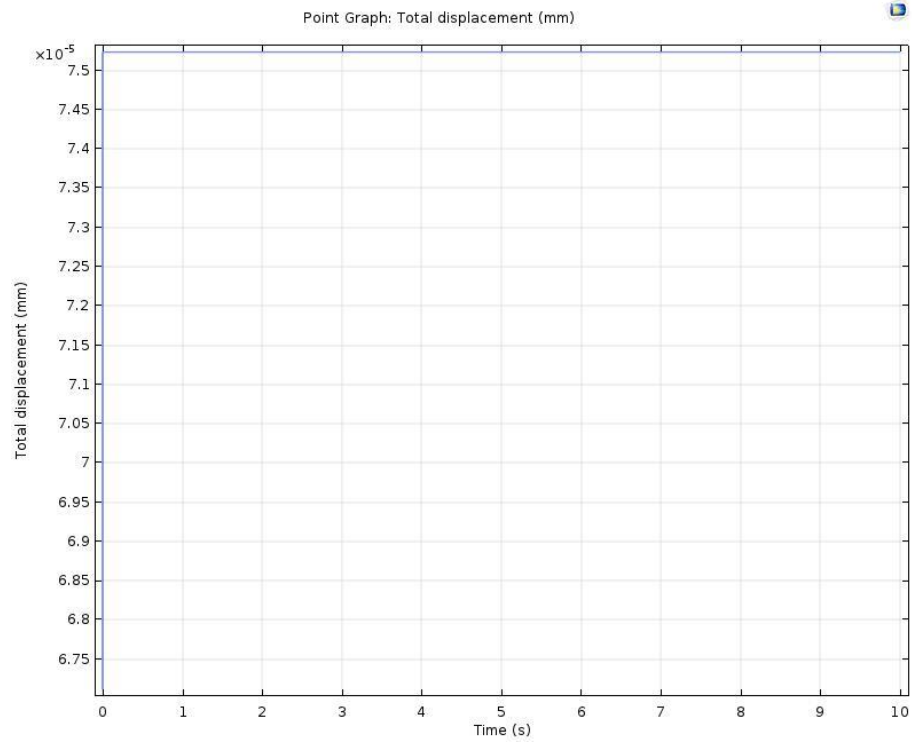
Figure 5. 42. Represents a strain of the midpoint of the top side for 60% PZT planar model.

Point Graph: Total displacement (mm)
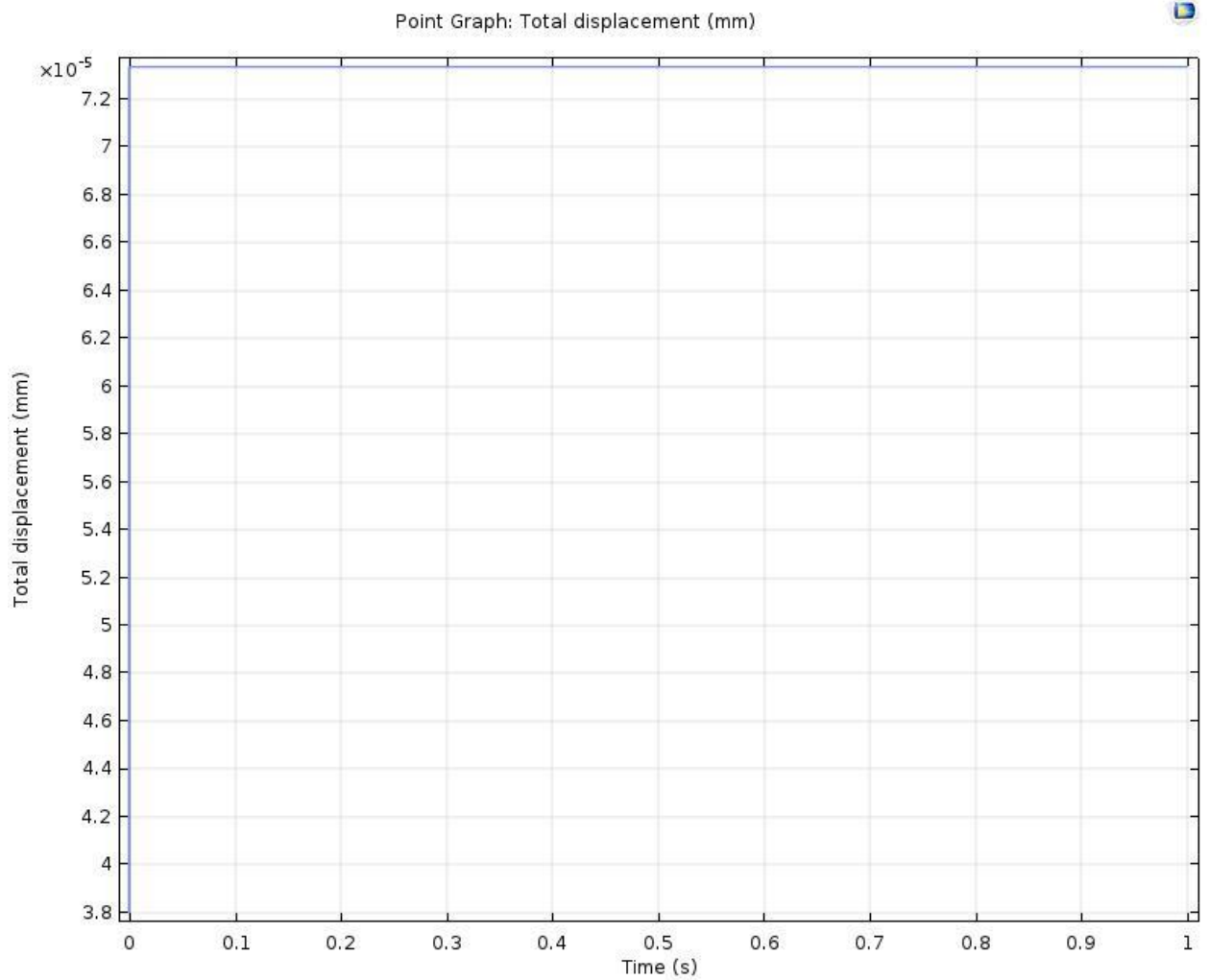
Figure 5. 43. Represents a strain of the midpoint of the top side for 70% PZT planar model.

From the figures, it shows that the strain of the midpoint of the top side of the unit cell decrease with increasing the volume fraction of PZT in general. This is similar to the results for the strain of the centerline of the unit cell. The strain for all models is kept at a constant during the change of time. The minimum value for strain at the midpoint occurs at 70% PZT composite model and the largest value occurs at 10% PZT composite model. Actually, the midpoint of the top side is one of the points of the centerline. It is the end point on the arc length.

5.3 Electrical displacement and electric potential generated by each volume fraction PZT model.

In the above two sections in this Chapter, the results for thermal properties and solid mechanics results caused by thermal expansion were discussed. In this section, the results for piezoelectric effect related to solid mechanics will be discussed. First, the electrical displacement will be introduced. Electric displacement (D), also known as electric flux density, is the charge per unit area that would be displaced across a layer of conductor placed across an electric field. It is different from the strain discussed in section 5.2. In section 5.2, the strain is caused by thermal expansion and it describes the deformation of the composites. However, electric displacement describes the displacement of the charge per unit area when an external electric field is applied. In

our study, the external electric field is applied in the -Z-direction. In the experimental

part, the piezometer was used to measure the piezoelectric strain coefficient (d_{33}). In

order to get the piezoelectric strain coefficient with each volume fraction, the boundary

load and electrical displacement were kept as the same value for all volume fraction

PZT models, which boundary load is 0.25N. The boundary load is in -Z-direction. As

the numerical results need to be compared with experimental data, the same conditions

of boundary load and electric displacement need to be set up in our Comosl models.

However, a problem is that the electrical displacement cannot be measured in the

experimental work. But it can be calculated according to equation 2.13 ($S_{33}=d_{33}.E_3$),

where S_{33} is the electrical displacement in Z-direction, d_{33} is piezoelectric strain

coefficient and E_3 is the applied external electric field in Z-direction. Since the

piezoelectric strain coefficient of pure PZT-5A can be checked from the material library

in Comsol, which is 584pc/N, and the applied external electric field is 0.2kV in planar

models. Thus, the value of electrical displacement can be calculated as 1.168×10^{-7}m

for pure PZT planar model. This same value for all volume fraction PZT models was

kept which is the same as experimental work.

Once the value of the boundary load and electrical displacement for all the models were

got, the next step is to find out the electric potential (voltage) generated by the direct

piezoelectric effect. In experimental work, the dielectric constant was measured at the

frequency 110HZ. The same value of frequency was kept in the study in Comsol models.

Then the results for electric potential generated by direct piezoelectric effect is listed in

Table 5.1:

Table 5. 1: Electric potential generated by direct piezoelectric effect for each volume fraction PZT planar model

Volume fraction PZT models	Electric potential(V)
Pure PZT	253.37
10%	16.916
20%	17.346
30%	22.336
40%	26.077
50%	27.74
60%	30.753
70%	31.567

From the table, it shows that pure PZT model gets the largest value of electric potential. This is because pure PZT model is one-phase material, which has a great piezoelectric effect. Once a boundary load was applied on the sample, it generates a large voltage. The electric potential increases with increasing the volume fraction of PZT composite models. Generally, a higher volume fraction of PZT composites may have a better piezoelectric effect. But since the composites are two-phase materials, epoxy may also affect the piezoelectric effect of the composites. From the table, the minimum value of electric potential occurs at 10% PZT composite model, which is 16.916and largest value of electric potential happens at 70% PZT composite model, which is 31.567 V. In this case, it shows that 70% PZT composite model has the best direct piezoelectric effect among these composite models and 10% PZT model has the lowest piezoelectric effect compared to other composite models. Compared with the

electric potential generated in the bulk models, the electric potential generated in the planar sheet models is smaller than the bulk models. This is because the dimension of the planar sheet models is smaller than the bulk model, especially the thickness is much smaller in planar sheet models. It will lead to large deformation in the bulk composite models than in planar sheet models if a same boundary load is applied on the two types of models.

5.4 Capacitance for each volume fraction of PZT model

Capacitance **i**s the ability of a component or circuit to collect and store energy in the form of an electrical charge. In this study, the Maxwell capacitance can be got from the Comsol models. In the results part, right click "Derived Value" and choose "Global Evaluation". Then the expression can be input for Maxwell capacitance, which is "es.C11" into the setting window. Then if click the "Evaluation" button in the setting window, t the Maxwell capacitance can be got directly from the model. The capacitances for all volume fraction PZT composite models are listed in Table 5.2:

Table 5. 2: Maxwell capacitance for all volume fraction PZT composite models

Volume fraction PZT models	Maxwell capacitance(F)
Pure PZT	1.1653×10^{-11}
10%	6.6612×10^{-12}
20%	6.7341×10^{-12}
30%	6.8176×10^{-12}
40%	6.8741×10^{-12}

50%	6.9065×10^{-12}
60%	6.9171×10^{-12}
70%	6.9367×10^{-12}

From the table, it shows that the Maxwell capacitance increases with increasing the volume fraction of PZT composites from 10% to 70%. This means that a higher percentage volume fraction PZT models have better ability to store the energy of electrical charges. Compared the capacitance with the bulk models, they are smaller in planar sheet models than in the bulk models. The reason is still that the area of the planar sheet models is smaller than the area of the bulk models. Maxwell capacitance is measured from the whole domain. Larger domain will lead to larger capacitance.

5.5 Curing condition study

In this section, the results for the curing process of epoxy DGEBA will be discussed. As mentioned before in Chapter 3, the degree of cure α will be expressed to describe the ability the epoxy DGEBA absorbs heat as the material cures. The epoxy will have phase change from gel form to sold form during the curing process. Two different curing conditions will be discussed in this section, one is curing on a hot plate at a fixed temperature 75C and the other one is curing in a room temperature 20C in the air. The difference is that the dimension of the model is different from the bulk model, which is much smaller and thinner than the bulk model.

5.5.1 Curing on a hot plate

First, the curing process of epoxy DGEBA on a hot plate at a fixed temperature 75C will be discussed. The reason why the temperature was chosen as 75C is because 75C is the Curie temperature of epoxy DGEBA. Above this temperature, the structure of epoxy DGEBA will be centrosymmetric and it will become stable. However, when the temperature is below this temperature, the structure is non-centrosymmetric and the epoxy is in gel form. In addition, the Curie temperature of PZT particles is much higher than 75C, so if fixed the temperature at 75C, it cannot only get the phase change of epoxy DGEBA and make the polymer matrix stable so as to keep the PZT particles inside the matrix, but also it can still keep the piezoelectric and dielectric properties of PZT-5A so that the composites can still possess piezoelectric effect since the Curie temperature of PZT is much higher than 75C. Such properties are mentioned in Chapter 2, Perovskite Structure in Figure 2.16. Two interfaces are used in Comsol model to simulate this process, one is 'Heat transfer in solid" and the other one is "Domain ODEs and DAEs". The governing equations used for this process are mentioned in Chapter 3, equation 3.33 and 3.34 and the material properties used for this model are listed in table 3.8. The result for the degree of curie of the centerline of the cross section of pure epoxy DGEBA will be shown to express the curing process. The result is shown in Figure 5.44 and 5.45:

The value of the degree of cure is from 0 to 1. When it is close to zero, which

means the epoxy is not cured and it is the gel form. When the curing process is done, the value of the degree of cure is equal to 1 or very close to 1. From the two figures, it shows that the epoxy DGEBA cured very fast at the beginning and it may take 1 week to be mostly cured, which the value of the degree of cure is close to 0.8. However, it may take very long to be fully cured as it shows from Figure 5.45. In experimental work, it takes about 8-10 hours to be fully cured. It has a great difference between Comsol models and the experimental work. The reason is that the data for the material properties of the epoxy DGEBA were unknown. The thermal material properties used in this model were got from the articles found online. It is impossible to measure the thermal properties of the epoxy DGEBA used in our experimental work since there is no such instruments in our lab. That might be one of the reasons leads to the big difference. The other reason might be that the epoxy is fully cured or not in our experimental work is unknown because it cannot be measured. It might take more time to be fully cured. In addition, if the results were compared with the bulk model, it shows that it takes much faster for the planar model to be fully cured than bulk model because it is much thinner than the bulk model.
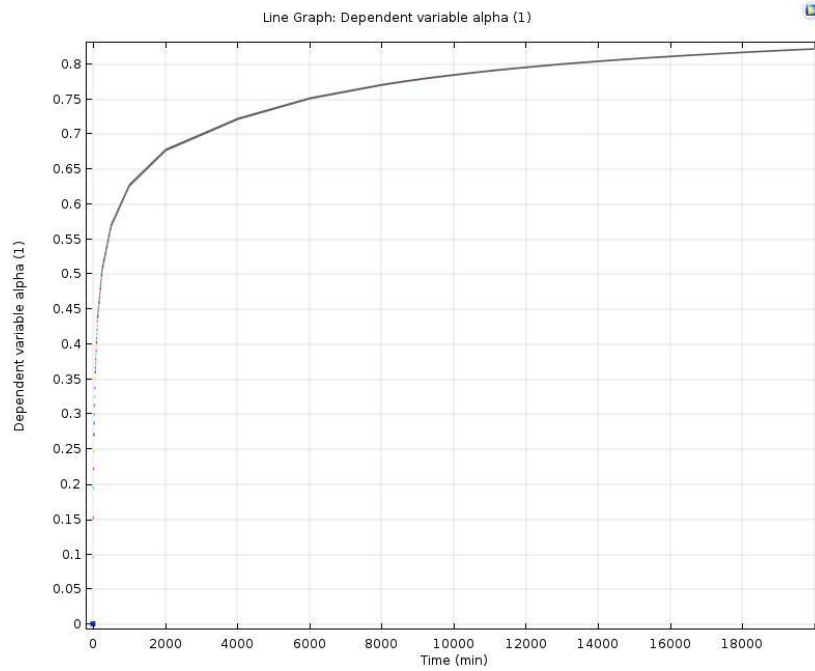
Figure 5. 44. Represents the degree of cure from 0 to 20000 mins at 75C.
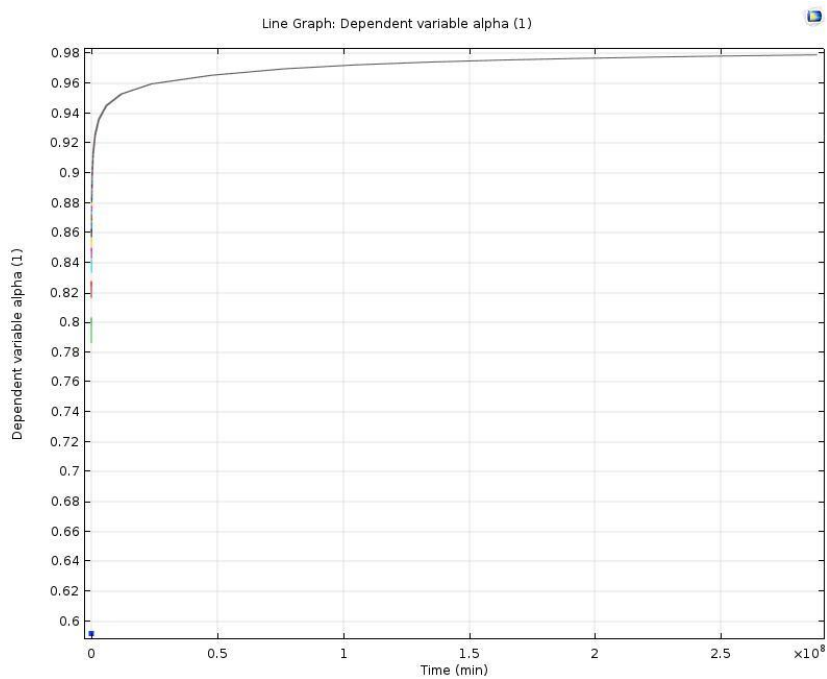
Figure 5. 45. Represents the degree of cure from 0 to 5×10^{8} mins at 75C.

5.5.2 Curing in room temperature 20C in the air

Next, the curing process of epoxy DGEBA in room temperature 20C in the air will

be discussed. Such a process is not affected by the heat transfer process because there

is no temperature difference between air and the sample. The difference between this curing condition and the condition discussed in section 5.5.1 will be shown. The result for the degree of cure of the centerline of the cross section of pure epoxy DGEBA is given by Figure 5.46:
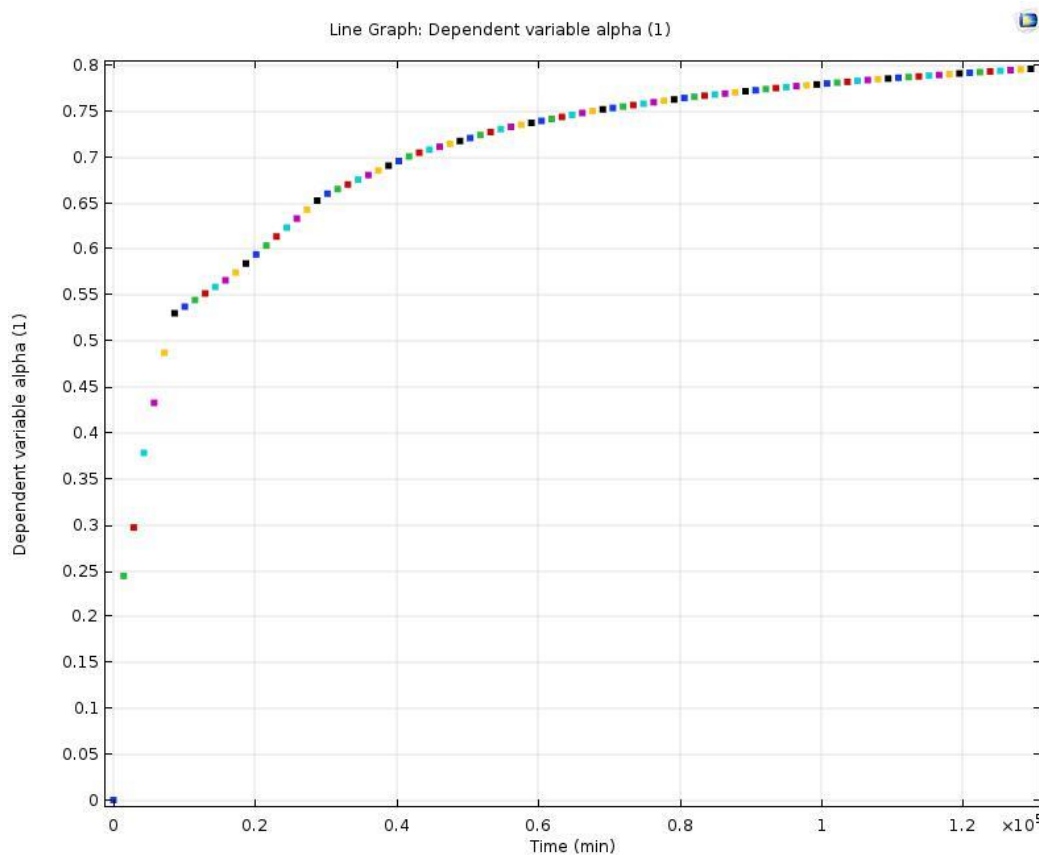
Figure 5. 46. Represents the degree of cure of the centerline in room temperature 20C.

From the figure, it shows that the epoxy DGEBA cannot be fully cured in room temperature even though the value of the time set up is extremely large. It takes about 90 days to get the value of the degree of cure about 0.8. However, the same procedure was done in the experimental work. It takes about 3 weeks that the epoxy DGEBA was fully cured at room temperature. There are several reasons for the different results between simulation work and experimental work. One reason is that the method used to simulate the curing process of epoxy in Comsol is suitable for heat transfer in solid

models. It must have temperature difference which means it must have a heat transfer process during the curing process. Another reason as mentioned in section 5.5.1, the data of the material properties of the epoxy DGEBA used in our lab were unknown since there is no instrument to measure the thermal properties of the epoxy in our lab. Thus, the values for the material properties input into the Comsol models might not be the same with the material used for experimental work. In addition, it is hard to control the room temperature as 20C for three weeks during the curing process of pure epoxy DGEBA. The temperature is changing during the experimental work. All these factors may lead to the huge difference between the simulation work and the experimental work.

5.6 Particle distribution after curing process of epoxy DGEBA

In Chapter 4, the process of particle floating of PZT after the curing process of epoxy DGEBA for bulk models was discussed. In this section, the similar results will be shown for the planar model. Like the bulk model, two particles floating and three particles floating process will be done. Such results will be shown from Figure 5.47 to 5.54.
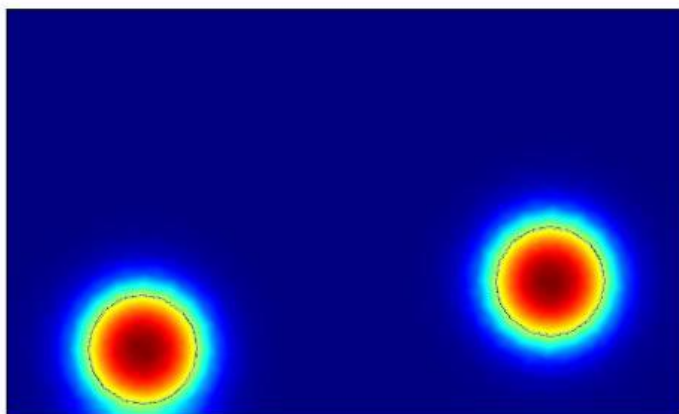
Figure 5. 47. Represents two particles floating up during the curing process at time 0s.
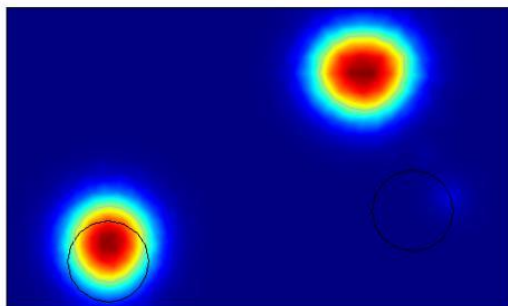
Figure 5. 48. Represents two particles floating up during the curing process at time 1s.
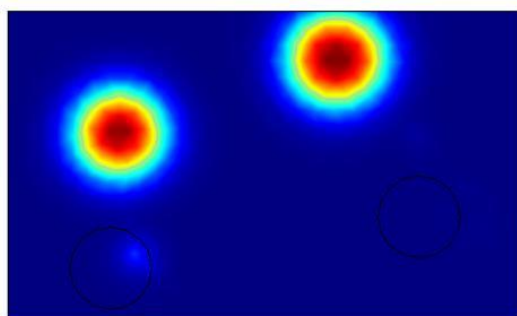
Figure 5. 49. Represents two particles floating up during the curing process at time 2s.
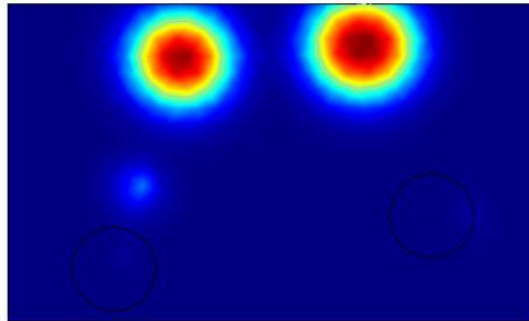
Figure 5. 50. Represents two particles floating up during the curing process at time 3s.
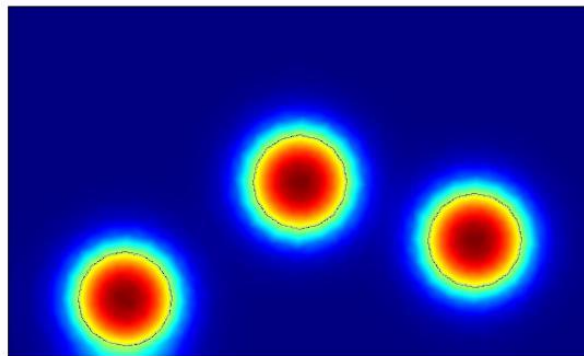
Figure 5. 51. Represents three particles floating up during the curing process at time 0s.
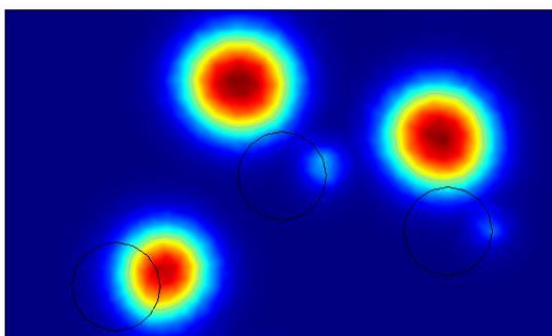
Figure 5. 52. Represents three particles floating up during the curing process at time 1s.
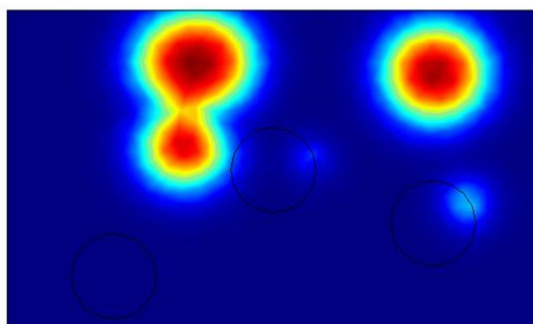
Figure 5. 53. Represents three particles floating up during the curing process at time 2s.
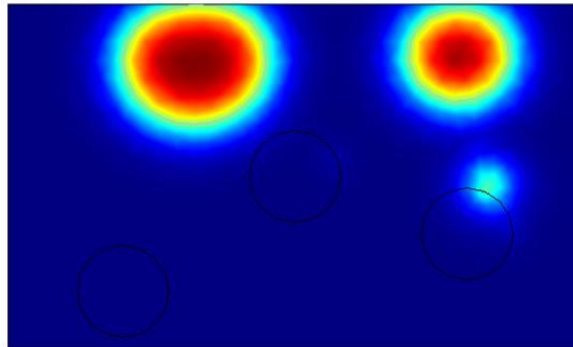
Figure 5. 54. Represents three particles floating up during the curing process at time 3s.

As the figures show that two types of models were done to simulate the PZT particles floating process during the phase change of epoxy DGEBA. The reasons why only did two particles and three particles are because there are some limitations for the computer to run Comsol models. One reason is that the dimension of the unit cell and PZT particles are very tiny and the numbers of PZT particles of each volume fraction are too many. It will take too much time to run the models for each volume fraction model for this particle floating process. In addition, there is no enough disk space for our lab computer to run this type of simulation. In order to show this process, the only thing that can be done is to simulate two and three particles for this process.

For two PZT particles model, it shows that the two particles are floating up to the top side of the composite at different time step. The total time set up for this process is 3s and the time step is 0.1s for each step. They do not overlap with each other during this process. The same process can be done for three particles model. However, two of

the three particles overlapped with each other during this process. The reason why the particles overlap with each other depends on the distance between the particles. If the distance between the particles is small, then these particles will be overlapped with each other during the curing process. Otherwise, they will be separate. The reason why particles will move closely during this process is that there exist tensions inside the epoxy polymer matrix since the epoxy is in gel form at the beginning. The tensions will make the particles move closely during the phase change process of epoxy DGEBA. Compared with the same procedure in the bulk models, there is no difference in the process. This is because what factor decides the PZT particles will overlap with each other is the distance between them and there is no relation to the geometry of the unit cell.

5 .7 Piezoelectric and dielectric properties of the composites

In this section, the results for piezoelectric and dielectric properties of the composites for each volume fraction PZT model will be discussed. In order to find out one of the hypotheses, mentioned in Chapter 2. The piezoelectric and dielectric properties of the composites for two different conditions will be discussed. One is considering the boundary conditions of heat convection and surface radiation. The other one is without considering these two boundary conditions. Dielectric constant ε_r and piezoelectric strain coefficient d_{33} will be calculated to express piezoelectric and

dielectric properties. Such two values will be calculated by equation 2.5 and equation

3.31:

$$\varepsilon_r = \frac{Cd}{\varepsilon_0 A} \qquad (2.5)$$

$$d_{33} = \frac{V\varepsilon_r\varepsilon_0 A}{Fd} \qquad (3.31)$$

where C is the Maxwell capacitance, d is the thickness of the sample, A is the area of

the surface, ε_0 is the permittivity of free space - a vacuum - is equal to approximately

8.85×10^{-12} Farads/meter(F/m), V is the electric potential, F is the fixed boundary load,

which is 0.25N. In addition, the simulation results will be compared with both

experimental results and results calculated by analytical models in this section as well.

5.7.1 Piezoelectric and dielectric properties of the composites with considering the boundary conditions in "heat transfer" in the solid interface.

First, the results for the dielectric constant and piezoelectric strain coefficient will

be discussed for the simulation work with considering the boundary conditions for heat

convection and surface radiation. Four models were done for each volume fraction PZT

model and take the average value for dielectric constant and piezoelectric strain

coefficient. The results for piezoelectric and dielectric constant are under frequency

110HZ. The results for the dielectric constant are given in Table 5.3:

Table 5. 3: dielectric constant for all volume fraction PZT samples from Comsol models

Volume fraction PZT models	Dielectric constant ε_r(F/m)
Pure PZT	1700

10%	29.63
20%	29.96
30%	30.33
40%	30.58
50%	30.72
60%	30.77
70%	30.86

From the table, the dielectric constant increases with increasing the volume fraction of PZT. The largest value of dielectric constant occurs at 70% PZT model, which is 30.86 F/m. The smallest value occurs at 10% PZT model, which is 29.63 F/m. The dielectric constant of the planar composite models is smaller than the dielectric constant of bulk composite models in Chapter 4. The reason is that the dimension of planar models is smaller than bulk models so that the capacitance of each planar composite model is smaller than bulk models. Thus, the dielectric constant of planar models is smaller than bulk models. The results for dielectric constant of the planar sheet composite models are given by Figure 5.55:
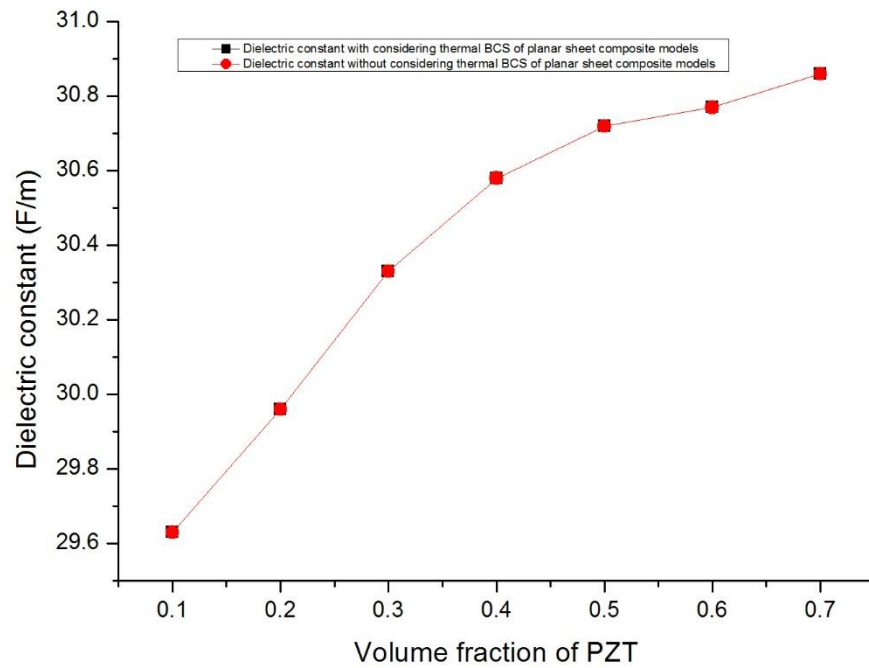
Figure 5. 55. Represents the dielectric constant of the planar sheet composite models.

Since the dielectric constant were not measured for planar samples in experimental work. The dielectric constant cannot be calculated by Comsol models with the experimental result. However, they can be compared with the results calculated by the analytical model. The analytical model used is Maxwell's Equations. The equation to calculate the dielectric constant of the composites is given by equation 3.30 and the results for the dielectric constant are given in Table 5.4

Table 5. 4: dielectric constant calculated by the analytical model

Volume fraction PZT models	Dielectric constant ε_r(F/m)
Pure PZT	1700
10%	120.8
20%	246.25
30%	380.97
40%	526.03

50%	682.66
60%	852.31
70%	1036.67

From the table, it shows that the dielectric constant calculated by the analytical model increases with increasing the volume fraction of PZT., which is mentioned in Chapter 4. There is no difference between the results here and in Chapter 4. This is because the equation of the dielectric constant of the analytical model has no relation of the dimension of the geometry. It is only related to the dielectric constant of each material in the composite. However, they are much larger than the simulation data. The reason for this difference is because the equation for the dielectric constant of the analytical model is only related to the dielectric constants of the matrix material and particle fillers. It does not consider the shape and dimension of the composites. In addition, it is not related to the capacitance as well. It is an ideal model without considering other factors. But in our model, the dielectric constant is calculated by equation 2.5, which is related to the dimension of the sample and capacitance. The capacitance is affected by material properties of the composite, the external electric field and boundary conditions added for each interface. But the similar part is that both two types of data increase with increasing the volume fraction of PZT.

Next, the piezoelectric strain coefficient d_{33} will be discussed. This value is calculated by equation 3.31. The voltage V can be got for each volume fraction by the Comsol models. The data for dielectric constant were used by table 5.3. Boundary load

F is kept at 0.25N. The results for the piezoelectric strain coefficient are given by Table

5.5:

Table 5. 5: piezoelectric strain coefficient of calculated by simulation work

Volume fraction PZT models	Piezoelectric strain coefficient d_{33} (pC/N)
Pure PZT	584
10%	1.24
20%	1.29
30%	1.68
40%	1.98
50%	2.11
60%	2.34
70%	2.41

From the table, it shows that the piezoelectric strain coefficient increases with

increasing the volume fraction of PZT model. Thus, the minimum result occurs at 10%

model which is 1.24pC/N and largest value occurs at 70% model which is 2.41pC/N.

This result shows that higher volume fraction PZT composites have a better

piezoelectric effect than lower volume fraction composites. This is quite making sense

because PZT is the phase material that has the piezoelectric effect. The piezoelectric

strain coefficient of planar models is also smaller than the bulk models since the voltage

generated by the direct piezoelectric effect and dielectric constant of planar models are

all smaller than bulk models.

Next, let us compare the simulation result with experimental results. The planar

composite samples were fabricated by Zichen Lao in our group and the piezoelectric

strain coefficient is also measured by him. He fabricated 10%, 20%, 30%, 40%, and 60%

planar samples and he made 3 samples for each volume fraction PZT composite and

the results are the averaged results for each volume fraction composites. The results are

shown in Table 5.6:

Table 5. 6: piezoelectric strain coefficient calculated by experimental work

Volume fraction PZT models	Piezoelectric strain coefficient d_{33} (pC/N)
10%	1.067
20%	1.4
30%	1.53
40%	1.80
60%	2.16

From the table, it shows that the experimental results for piezoelectric strain

coefficient are very similar with the simulation work, which means the simulation

models are correct and the experimental work has a good procedure to fabricate the

samples. Generally, the simulation results are a little bit larger than the experimental

results except 20% composite. This makes sense because the simulation models are

ideally considered but the experimental work is not. They are affected by many factors

such as fabrication procedure, particle distribution and so on. However, the results of

this type of work got for both the experimental part and simulation part were very good.

The results of the piezoelectric strain coefficient for both experimental work and

numerical work are given by Figure 5.56:
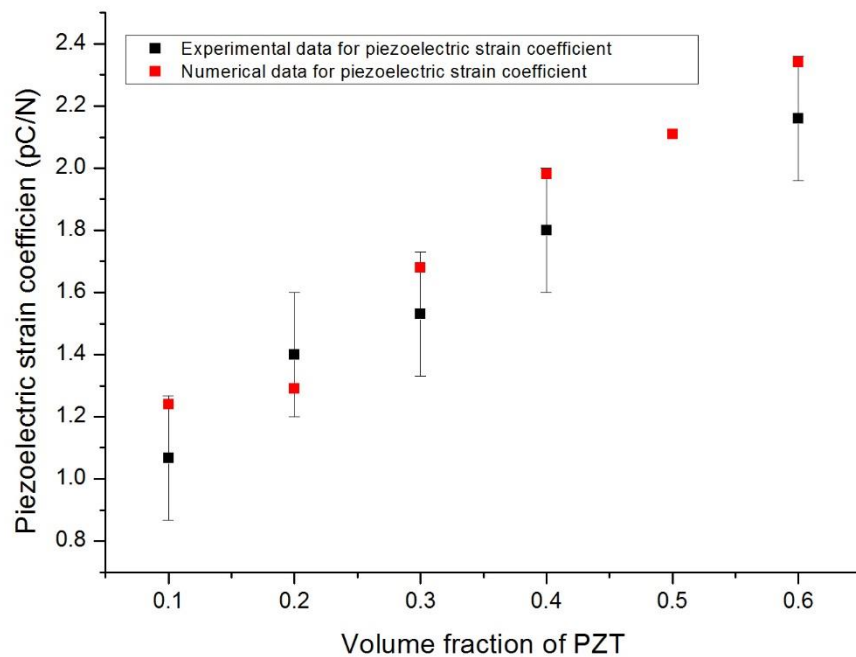
Figure 5. 56. Represents the piezoelectric strain coefficient for both experimental work and numerical work of the planar sheet composite models.

From this figure, black points represent the experimental data of piezoelectric strain coefficient of the planar sheet composite models. Red points represent the piezoelectric strain coefficient of the numerical work. It shows that the numerical data are generally inside the error bar of the experimental data which means the simulation results are pretty good. The results increase with increasing the volume fraction of PZT which means higher volume fraction of PZT composite planar sheet samples have better piezoelectric property than lower volume fraction of PZT samples.

5.7.2 Piezoelectric and dielectric properties of the composites without considering the boundary conditions in "heat transfer" in the solid interface.

In the last section, the results for dielectric constant and piezoelectric strain coefficient was discussed with considering the boundary conditions of heat transfer, such as heat convection and surface radiation. However, in this section, these results will be discussed without considering such boundary conditions so as to see if there are a big difference between the results or not.

In Chapter 4, it was proved that there is no big difference for both conditions, which means boundary conditions of heat transfer process do not have much influence on piezoelectric and dielectric properties of the composites. For here, let us see if the same thing will happen in planar composites which have different geometry of bulk models.

First, let us see the capacitance of each volume fraction PZT model without considering the boundary conditions of heat transfer. Table 5.7 gives the result for the capacitance of each volume fraction PZT model:

Table 5. 7: Maxwell capacitance without considering boundary conditions od heat transfer

Volume fraction PZT models	Maxwell capacitance(F)
Pure PZT	1.1653×10^{-11}
10%	6.6612×10^{-12}
20%	6.7341×10^{-12}
30%	6.8176×10^{-12}

40%	6.8741×10^{-12}
50%	6.9065×10^{-11}
60%	6.9171×10^{-11}
70%	6.9367×10^{-11}

From the table, it shows that the Maxwell capacitance has the same trend with the results for considering the boundary conditions heat transfer. It increases with increasing the volume fraction of PZT composite. Compared with the results in table 5.2. The results for capacitance are totally same. In this case, it shows that the boundary conditions of heat transfer have only a no influence on the Maxwell capacitance.

Next, let us discuss the results for the voltage generated by the piezoelectric effect without considering the boundary conditions of heat transfer. Table 5.8 gives the results for voltage of all volume fraction models.

Table 5. 8: electric potential generated by the piezoelectric effect without considering boundary conditions of heat transfer

Volume fraction PZT models	Electric potential(V)
Pure PZT	253.37
10%	16.916
20%	17.346
30%	22.336
40%	26.077
50%	27.74
60%	30.753
70%	31.567

From this table, it shows that the electric potential generated by the piezoelectric effect has the same results with table 5.1 which is the electric potential with considering the boundary conditions of heat transfer. All of the results are the same as table 5.1. In this case, the boundary conditions of heat transfer process have no affection on the piezoelectric effect of planar models.

Next, let us calculate the dielectric constant and piezoelectric strain coefficient by using the data from table 4.6 and 4.7 to see the difference in the results between these two types of conditions. The results for the dielectric constant and piezoelectric strain coefficient are given by Table 5.9 and 5.10:

Table 5. 9: dielectric constant of all volume fraction models without considering the boundary conditions of heat transfer

Volume fraction PZT models	Dielectric constant ε_r(F/m)
Pure PZT	1700
10%	29.63
20%	29.96
30%	30.33
40%	30.58
50%	30.72
60%	30.77
70%	30.86

Table 5. 10: piezoelectric strain coefficient of all volume fraction models without considering the boundary conditions of heat transfer

Volume fraction PZT models	Piezoelectric strain coefficient d_{33} (pC/N)

Pure PZT	584
10%	1.24
20%	1.29
30%	1.68
40%	1.98
50%	2.11
60%	2.34
70%	2.41

From Table 5.9 and 5.10, it shows that the results for the dielectric constant and piezoelectric strain coefficient are totally the same with the results with boundary conditions of heat transfer. This is because the capacitance and voltage are totally the same with table 5.1 and 5.2. Thus, the boundary conditions of heat transfer have no influence on piezoelectric and dielectric properties for planar models. The results of the piezoelectric strain coefficient for two types of boundary conditions are given in Figure 5.57 and Figure 5.58:
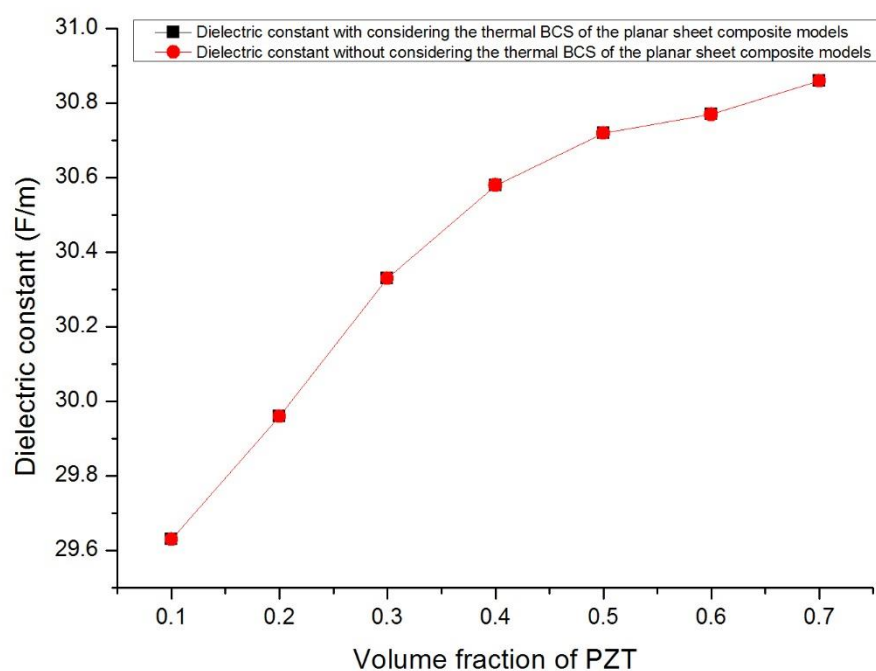
Figure 5. 57. Represents the dielectric constant for both two types of thermal boundary conditions of the planar sheet composite models.
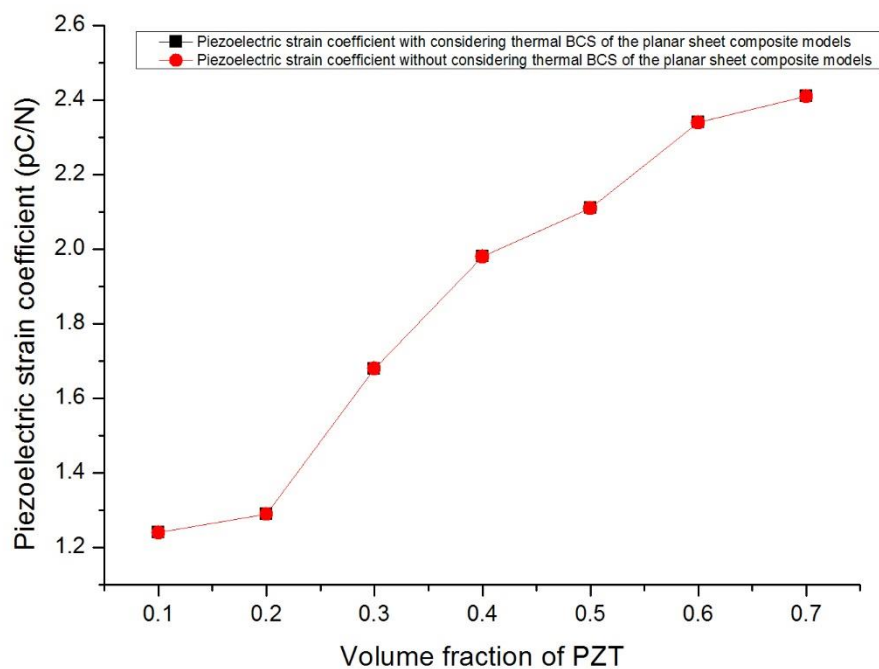
Figure 5. 58. Represents the piezoelectric strain coefficient for both two types of thermal boundary conditions of the planar sheet composite models.

Chapter 6

Results and discussion for dome shape models

Compared with bulk models and planar models, the difference of the dome shape model is that the geometry is not like a regular shape such as a square or rectangle. It is deformed by planar sheet and has two curved boundaries. Another difference in this type of model is that the unit cell method was not used to simulate the results. This is because that no related references were found which use unit cell method to solve this type of geometry problems and the unit cell method is only useful in regular shape models, such as square and rectangle. In this case, in order to solve the problem, the scale method was tried to use to scale the original model into a much smaller one which keeps the same shape of the geometry of the dome shape. But in this case, the number of PZT particles in the scaled model will be much less than the original one. The scale factor for all dome shape models is 0.1 so that the area of the scaled model is 100 times smaller than the original geometry. In order to prove that this method is right, 5% PZT and 10% PZT dome shape models were tried to simulate with both original dimension and scaled ones. It was found that the results for capacitance and voltage generated by piezoelectric effect are very similar, which means the piezoelectric and dielectric properties of both two models are very similar. This means the scaled method is working. Thus, the scaled method was used for all volume fraction dome shape composite models. However, there is a big difference between scaled method and unit cell method. For unit cell method, a script to generate PZT particles in the unit cell was

written to get each volume fraction models, all the PZT particles inside the unit cell are separated and they are not overlapped with each other. In this case, the volume fraction of PZT particles for each volume fraction models keeps at the exact values for each model. But for dome shape models, how to write a script to separate the PZT particles inside the dome shape model is a problem for me. Thus, some of the PZT particles are overlapped with each other. In this case, the volume fraction of PZT of each composite model is an approximation value. The results get from my models may be a little bit smaller than the ideal model with exactly volume fraction values models. Actually, in experimental work, no matter how good the fabrication procedure is, some of the PZT particles are definitely overlapped with each other. Thus, even though the scaled method is not perfect, it is still working for the simulation work. The third difference for dome shape model is that 2D axis-symmetric module was used in Comsol to generate the geometry, but the 2D module for bulk and planar models. This is because only an interface of the whole geometry was studied. For the dome shape model, if the 2D module was used, it is not like the original geometry if it is extruded into a 3D shape. However, in 2D axis-symmetric module, it is the same shape with the original geometry if the interface was rotated with Y-axis. The geometry of the 10% PZT scaled dome shape model is given by Figure 6.1 as an example:
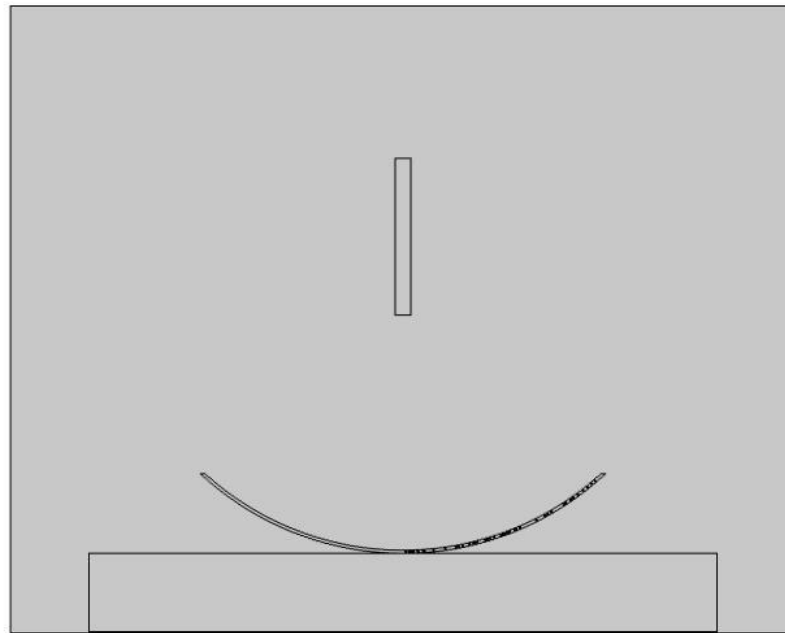
Figure 6. 1. Represents the geometry of scaled 10% dome shape model

6.1 Temperature distribution of dome shape composites

In this section, the temperature distribution will be discussed for all volume fraction of PZT composites of both bottom and up curves of the dome shape models. The temperature distribution is related to heat transfer in the composites.

6.1.1 Temperature distribution of the bottom curve

In this section, the results of the temperature distribution of the bottom curve of the cross section of the dome shape composites will be discussed. As mentioned before, since the composites are axis-symmetric with Y-axis, the interface of the dome shape can represent the properties of the whole domain. As mentioned before, it is 0.0254m in width and 0.0002m in thickness. This dimension is for the simulation of pure PZT and pure epoxy models. However, in chapter 3, as introduced that the dimension for

PZT particles are very tiny that the regular computers cannot generate huge amount of particle of PZT to reach the volume fraction of the composites from 10% to 70% PZT so that the unit cell method is used to solve this problem. However, in this chapter, the scaled method was used to solve this problem instead of unit cell method since there is no types of unit cell which is suitable for dome shape models. The scale factor is 0.1 for all composite models. But the dimension for pure PZT and pure epoxy models are the same with the original dimension of the fabricated samples.

First, let's start with pure PZT planar models. The model is with the same dimension of the samples fabricated by Wanlin Du[14]. Figure 6.2 shows the temperature distribution of the bottom curve of the cross section of the dome shape model with the change of arc length. The horizontal axis represents the arc length of the bottom curve and the vertical axis represents the temperature. The different colors from the bottom to top represent the temperature distribution at each time step from zero-step to 300s.
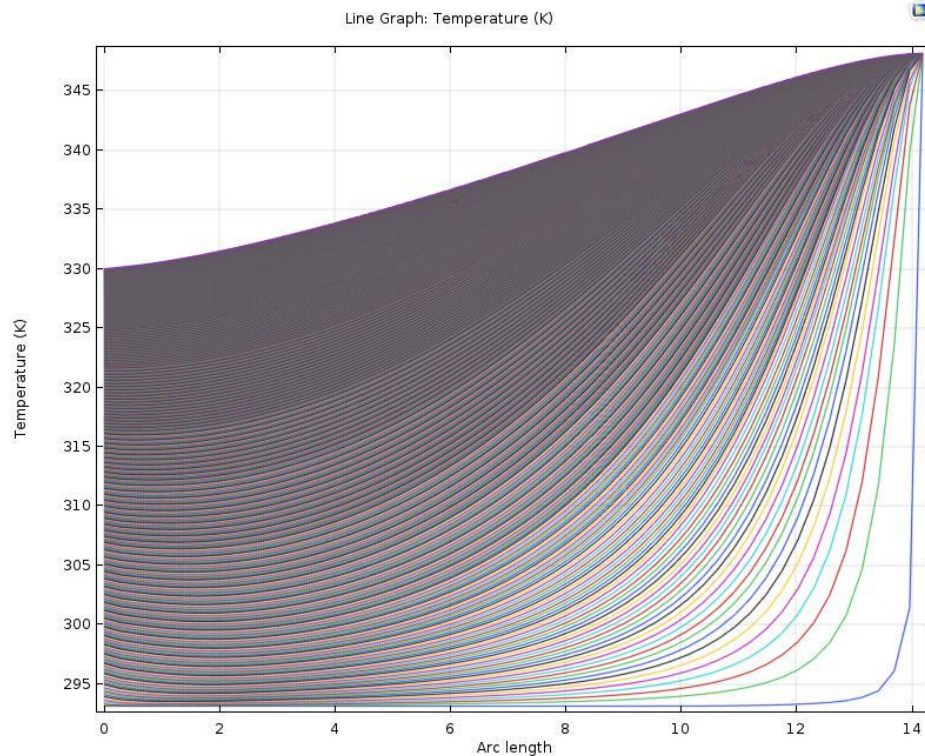
Figure 6. 2. Represents the temperature distribution of bottom curve of the cross-section of the pure PZT dome shape sample with the arc length.

Figure 6.2 shows the temperature distribution of the bottom curve with the arc length changed with time, where arc length is the length of the bottom curve. The range of time is from 0 to 300s with the time step of 0.1s. From the figure, the temperature at the bottom curve increases with the arc length and increases with increasing the time step.

Next, let us discuss the temperature distribution of the bottom curve of the cross section of the composite models. The result for 10% to 70% dome shape model is given by Figure 6.3. The horizontal axis represents the arc length of the bottom curve and the vertical axis represents the temperature. The blue line represents the temperature distribution at zero-time step and the purple curve represents the temperature distribution of the final time step 100s.

It shows that the blue line is the temperature at time zero instant. However, the rest

of the temperature at each time step are almost coincident together which is almost equal to the applied temperature 75C. This because the scaled method is similar to the unit cell method that the dimension of the dome shape model is very thin so that the heat transfer process finished very fast during the time step. For the bottom curve, the temperature increases a little bit with increasing the arc length. Since the scaled method was used for all volume fraction composite dome shape models, the thickness of the dome shape models is very tiny that the temperature distribution for all volume fraction models is same which are like Figure 6.3. Thus, the temperature distribution for other volume fraction models will not be put into the thesis again.
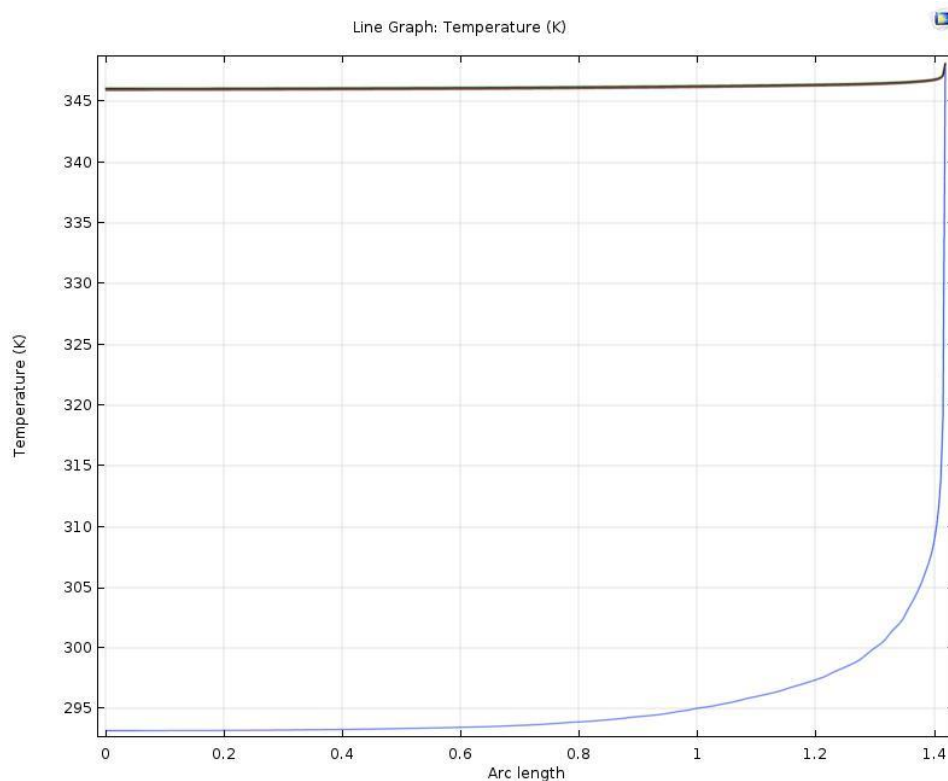
Figure 6. 3. The temperature distribution of the bottom curve for 10% PZT dome shape model.

6.1.2 Temperature distribution of the up curve

In this section, the temperature distribution of the upcurve of the dome shape

models will be discussed. First, let us see the pure PZT model. The temperature distribution of the up curve of pure PZT model is given by Figure 6.4. The horizontal axis represents the arc length of the up curve and the vertical axis represents the temperature. The different colors from the bottom to top represent the temperature distribution at each time step from zero-step to 300s.
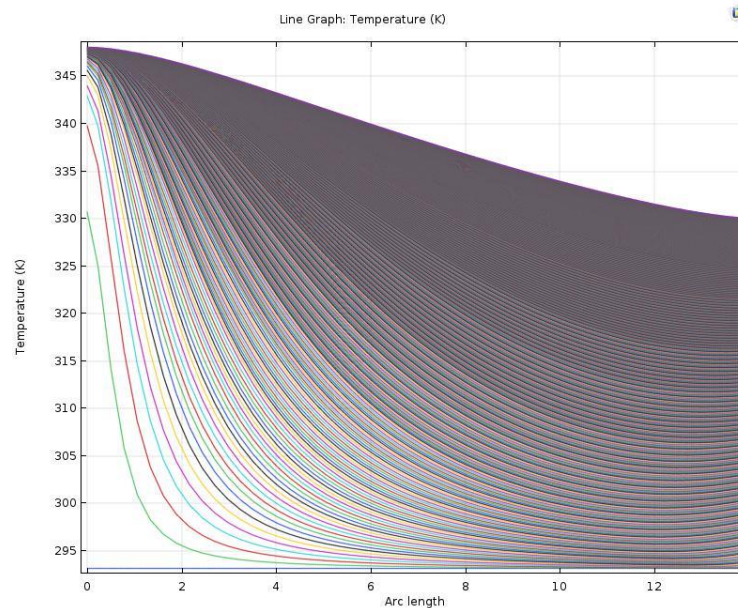
Figure 6. 4. Represents the temperature distribution of upcurve of the cross-section of the pure PZT dome shape sample with the arc length.

From the figure, it shows that the temperature distribution of the up curve is opposite with bottom curve. It decreases with the arc length for each time step but increases with increasing the time step. Next, let us discuss the temperature distribution of the upcurve of the cross-section of the composite models. The result for 10% dome shape model is given by Figure 6.5. The horizontal axis represents the arc length of the up curve and the vertical axis represents the temperature. The blue line represents the temperature distribution at zero-time step and the purple curve represents the temperature distribution of the final time step 100s.
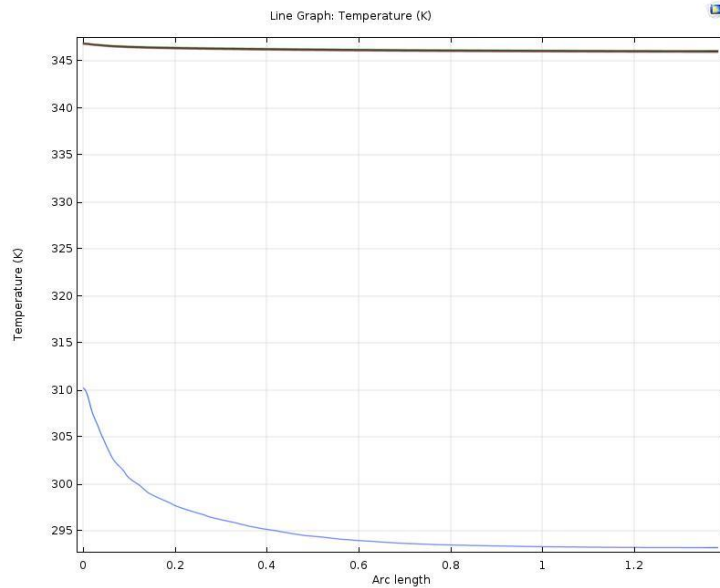
Figure 6. 5. Represents the temperature distribution of upcurve of the cross-section of the 10% PZT dome shape sample with the arc length.

From the figure, the blue line is the temperature at time zero. However, the rest of the temperature at each time step are almost coincident together which is almost equal to the applied temperature 75C. This is very similar to the temperature distribution of the bottom curve. The difference is that the temperature of the up curve is a little bit higher at the beginning of the arc length than at the end of the arc length, which is just the opposite to the bottom curve.

6.1.3 Temperature distribution of pure epoxy fully cured dome shape model

In the first two sections, the temperature distribution of pure PZT and composite dome shape models was discussed. In this section, the result of temperature distribution of epoxy fully cured dome shape model will be shown. The dimension for the pure

epoxy dome shape model is the same with pure PZT dome shape model. The result of the bottom curve is shown in Figure 6.6. The horizontal axis represents the arc length of the bottom curve and the vertical axis represents the temperature. The different colors from the bottom to top represent the temperature distribution at each time step from zero-step to 300s.
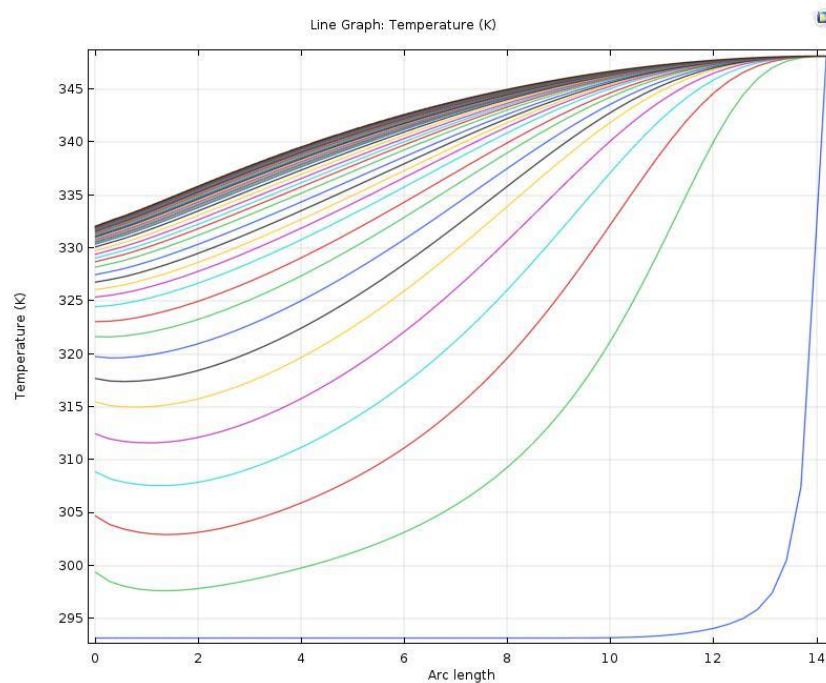
Figure 6. 6. Shows the temperature distribution of the bottom curve for pure epoxy fully cured dome shape model.

From the diagram, the temperature distribution of the pure epoxy model is similar to pure PZT model which is shown in figure 6.2. The difference is that the temperature for epoxy changes more at the beginning of the arc length. This is because the material properties for epoxy are different from PZT, which is affected more by heat transfer procedure and thermal dissipation has more related to heat convection and surface radiation even though the thickness of the planar model is very thin. The boundary conditions may still have a little bit of influence on thermal dissipation and heat loss. In this case, a little bit of the heat energy lost during the heat transfer process so that the

final temperature on the top of the sample is less than the fixed temperature 75C.

Next, let us see the result for the up curve. The temperature distribution of the up curve is given by Figure 6.7. The horizontal axis represents the arc length of the up curve and the vertical axis represents the temperature. The different colors from the bottom to top represent the temperature distribution at each time step from zero-step to 300s.
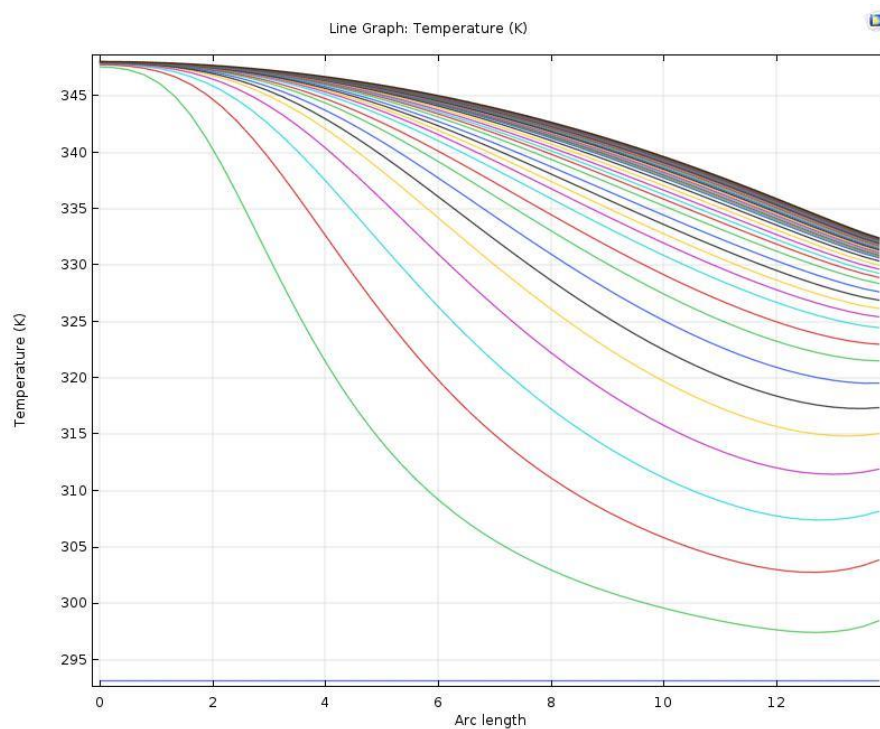
Figure 6. 7. Shows the temperature distribution of the up curve for pure epoxy fully cured dome shape model.

From the figure, it shows that the temperature distribution of the up curve is opposite to the bottom curve. It decreases with increasing the arc length but increases with increasing the time step, which means the temperature is much higher close to the Y-axis.

6.1.4 Temperature distribution of pure epoxy partially cured dome shape model

In section 6.1.3, the temperature distribution of pure epoxy fully cured dome shape model was discussed. In this section, the results for partially cured epoxy will be shown. The difference between these two types of epoxy is that fully cured epoxy is in solid form and partially cured epoxy is in gel form. In addition, the material properties are different. Figure 6.8 gives us the result for the bottom curve. The horizontal axis represents the arc length of the bottom curve and the vertical axis represents the temperature. The different colors from the bottom to top represent the temperature distribution at each time step from zero-step to 300s.
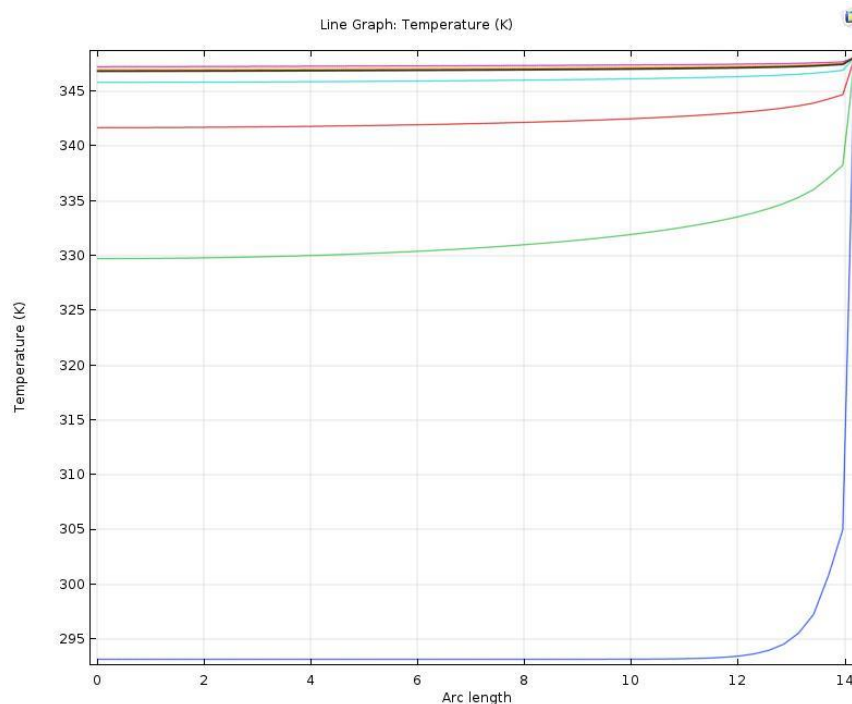
Figure 6. 8. Shows the temperature distribution of the bottom curve for pure epoxy partially cured dome shape model.

From the figure, it shows that it is similar to temperature distribution for epoxy

fully cured. The difference is that the heat transfer process finishes faster in partially

cured epoxy. This is because of the difference of the material properties between the

two types of epoxy. Since the partially cured epoxy is in gel form, it will absorb more

heat energy when the same temperature is applied so as to have the phase change to

become into solid form.

Next, let us see the result for the up curve. The temperature distribution of the up

curve is given by Figure 6.9. The horizontal axis represents the arc length of the up

curve and the vertical axis represents the temperature. The different colors from the

bottom to top represent the temperature distribution at each time step from zero-step to

300s.
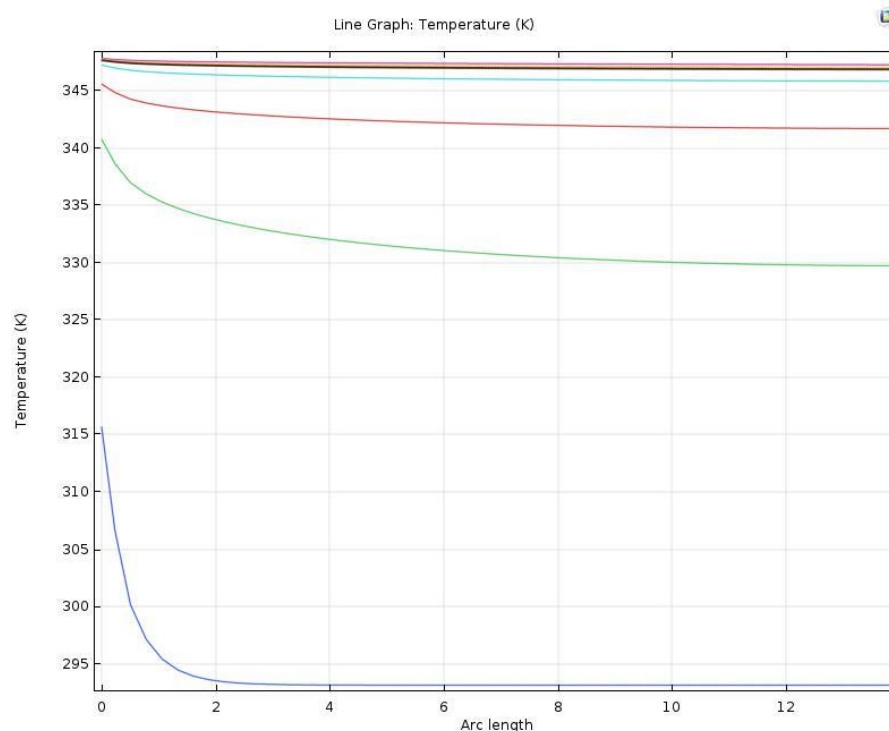
Figure 6. 9. Shows the temperature distribution of the up curve for pure epoxy partially cured dome shape model.

From the figure, the temperature distribution for the up curve is opposite to bottom

curve. It decreases with increasing the arc length and increases with increasing the time step, which is similar to fully cured epoxy.

6.2 Stress and strain caused by thermal expansion

In this section, the results for stress and strain caused by thermal expansion during the heat transfer process for both bottom curve and the up curve of the dome shape composite models will be discussed.

6.2.1 Stress and strain of the bottom curve of the dome shape models

First, let us discuss the results of stress and strain for the bottom curve of the dome shape models. The stress and strain for the bottom curve of pure PZT dome shape models are given by Figure 6.10 and 6.11. The horizontal axis represents the arc length of the bottom curve and the vertical axis represents the stress and strain. The different colors from the bottom to top represent the stress and strain at each time step from zero-step to 300s.
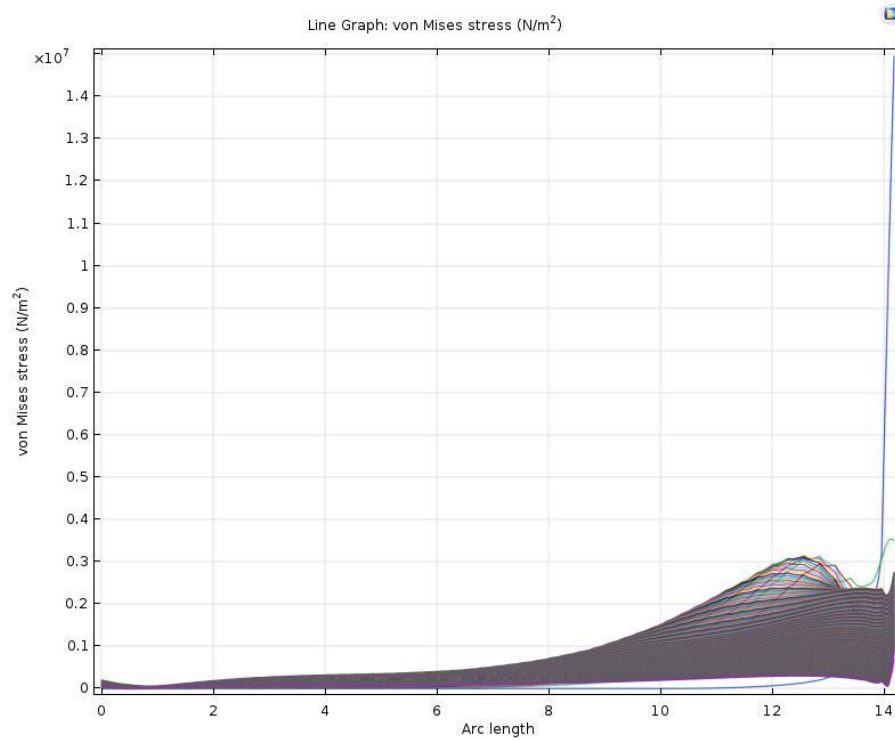
Figure 6. 10. Represents the von-Mises stress of the bottom curve for pure PZT dome shape model.
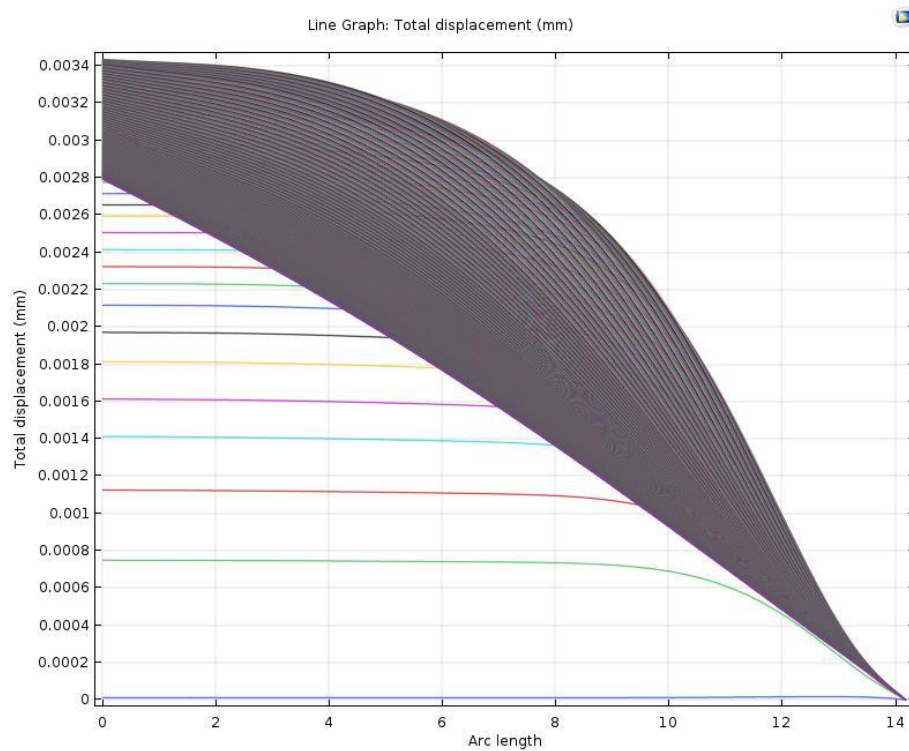
Figure 6. 11. Represents the strain of the bottom curve caused by the thermal expansion of the pure PZT dome shape model.

From the figures, it shows that the von-Mises stress increases with increasing the

arc length and time step. But the difference between high stress and low stress is not too big. However, the distribution of the strain is just the opposite. It decreases with the arc length and increases with time step. This is because the temperature is higher close to Y-axis so that the deformation of the bottom curve is larger near the Y-axis than the at the arc length of far away from the Y-axis.

Next, let us see the results for pure epoxy fully cured and pure epoxy partially cured dome shape models. The stress and strain of the bottom curve are given by Figure 6.12 to 6.15. The horizontal axis represents the arc length of the bottom curve and the vertical axis represents the stress and strain. The different colors from the bottom to top represent the stress and strain at each time step from zero-step to 300s.
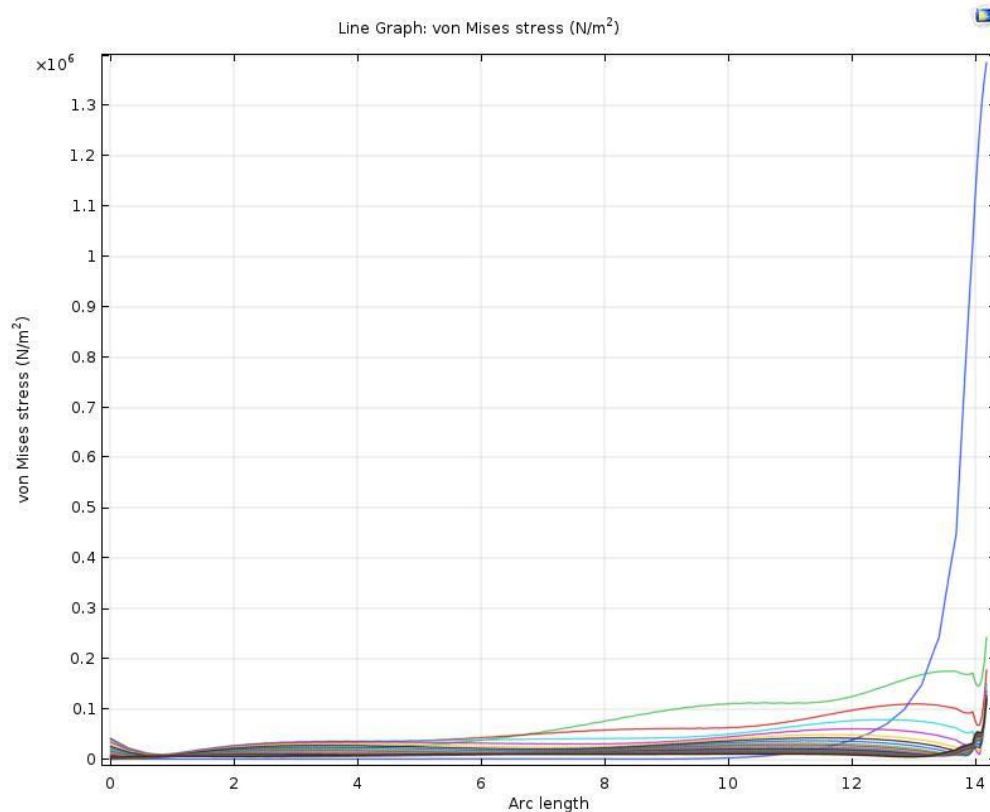

Figure 6. 12. Represents the von-mises stress of the bottom curve with respect to arc length change with time step. Epoxy fully cured dome shape model.
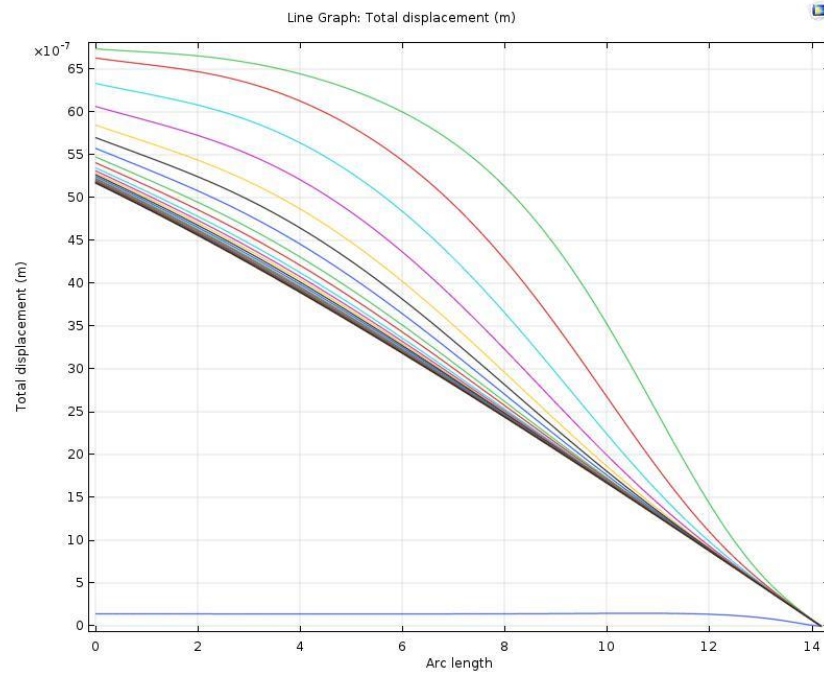
Figure 6. 13. Represents the strain of the bottom curve with respect to arc length change with time step. Epoxy fully cured dome shape model.
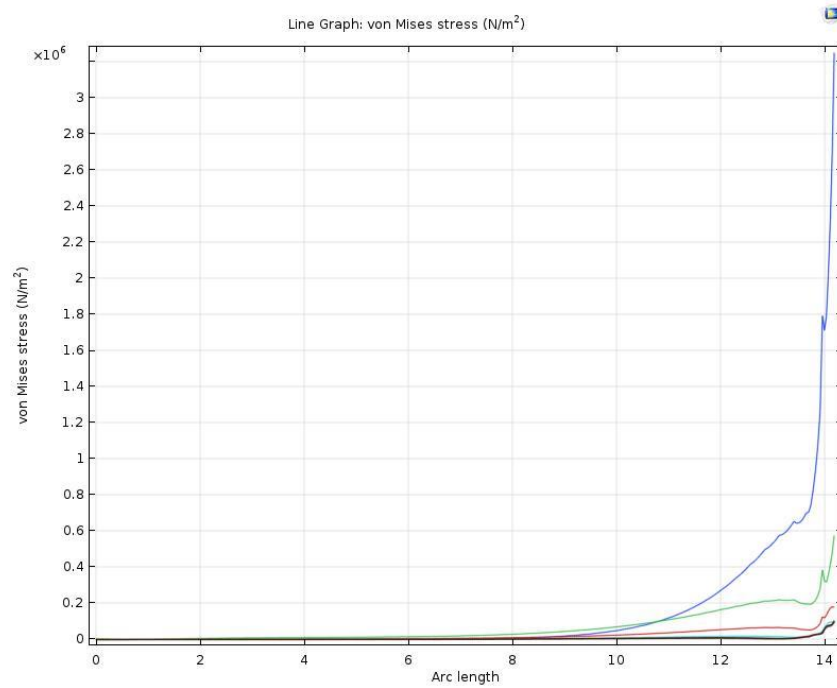
Figure 6. 14. Represents the von-mises stress of the bottom curve with respect to arc length change with time step. Epoxy partially cured dome shape model.
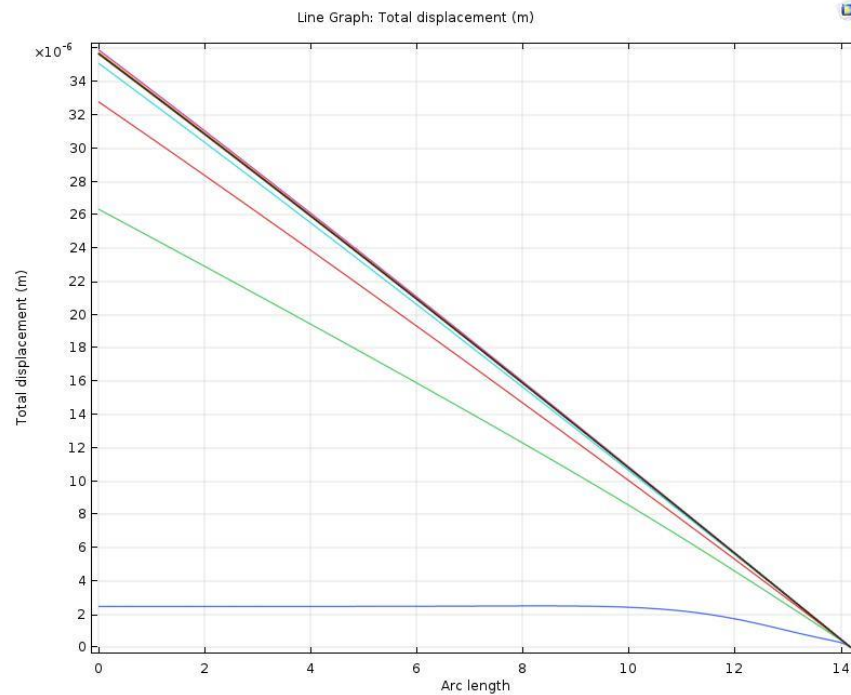
Figure 6. 15. Represents the strain of the bottom curve with respect to arc length change with time step. Epoxy partially cured dome shape model.

For the fully cured epoxy model, the distribution of von-Mises stress and strain for bottom curve are very similar to the distribution of pure PZT dome shape model. However, for the partially cured epoxy model, the deformation is much larger than fully cured epoxy. It is almost linearly decreasing with arc length for the strain. This is because partially cured epoxy is in gel form. It can absorb more heat during the heat transfer process and it will have phase change from gel form to solid form during this process. This will lead to more deformation than fully cured epoxy.

The results listed before are pure PZT models and pure epoxy models. They have the same dimension of real samples fabricated by Wanlin Du in our group[14]. Next, let us see the results for composite models. Figure 6.16 to figure 6.22 are the results for von-Mises stress of the bottom curve from 10% PZT dome shape model to 70% dome shape model. The horizontal axis represents the arc length of the bottom curve and the vertical axis represents the stress. The blue curve represents the stress at zero-time step

and the black curve represents the stress at the final time step.
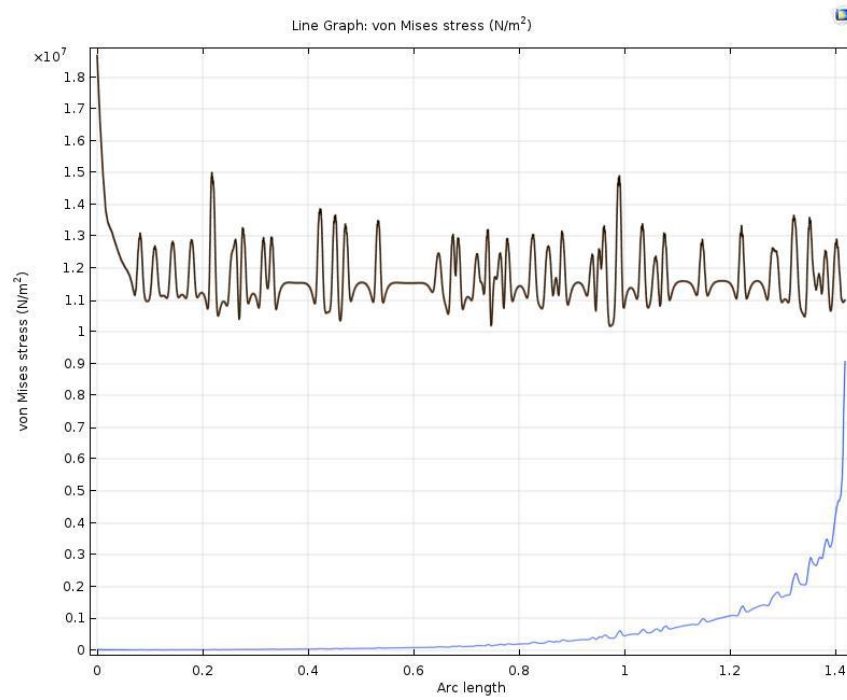
Figure 6. 16. Represents von-Mises stress of the bottom curve for 10% PZT dome shape model.
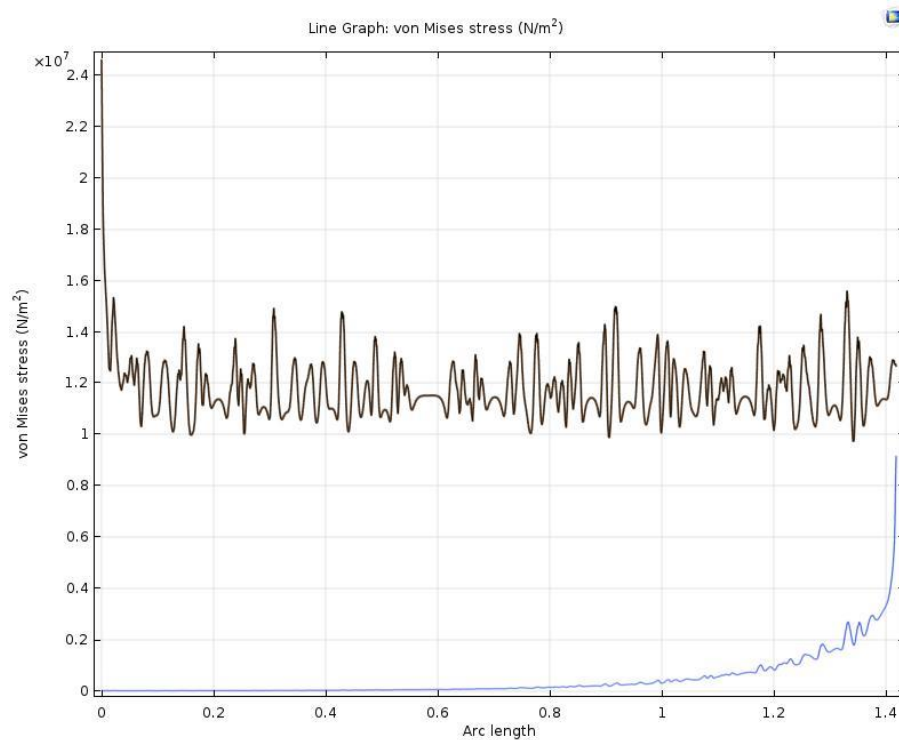
Figure 6. 17. Represents von-Mises stress of the bottom curve for 20% PZT dome shape model.
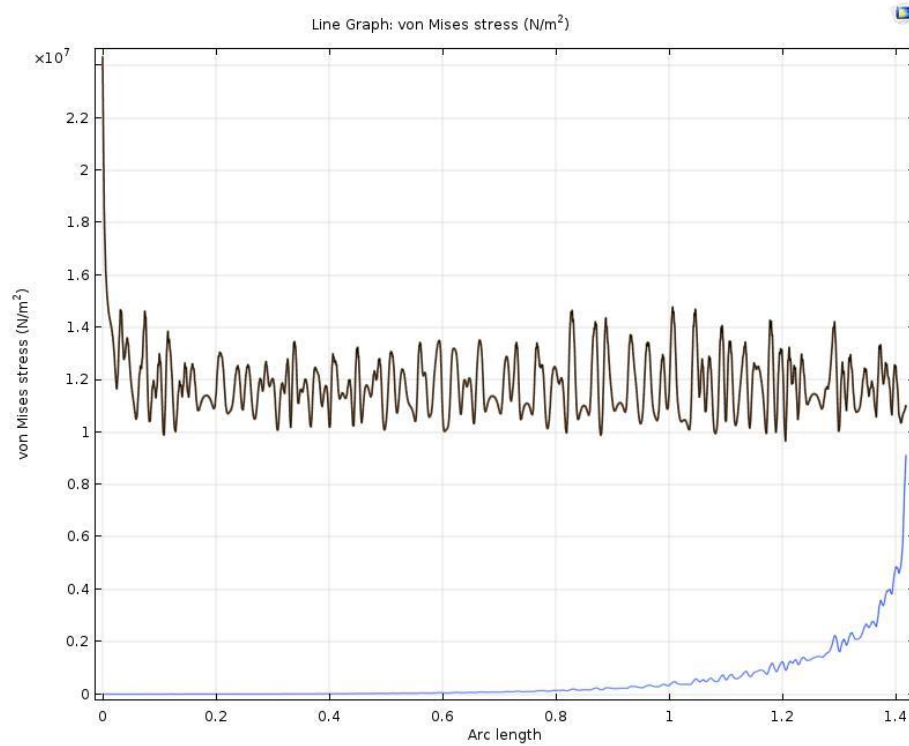
Figure 6. 18. Represents von-Mises stress of the bottom curve for 30% PZT dome shape model.
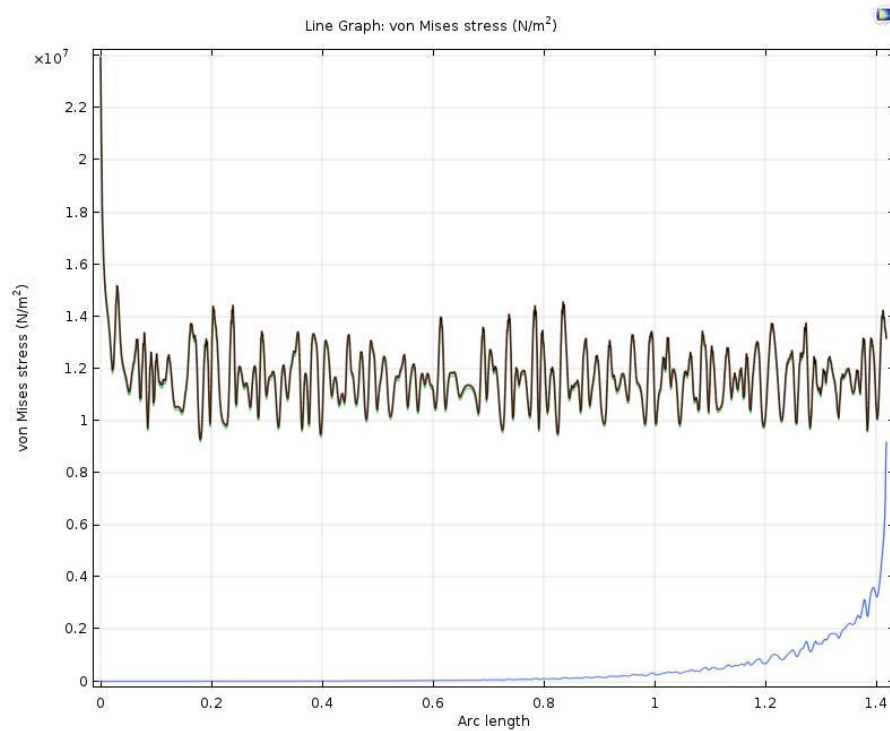
Figure 6. 19. Represents von-Mises stress of the bottom curve for 40% PZT dome shape model.
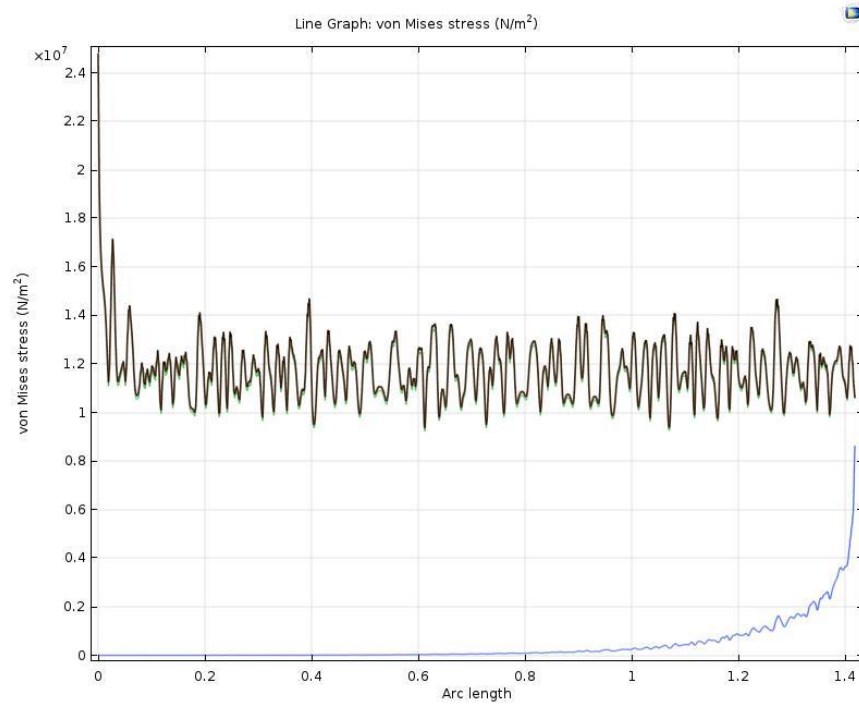
Figure 6. 20. Represents von-Mises stress of the bottom curve for 50% PZT dome shape model.
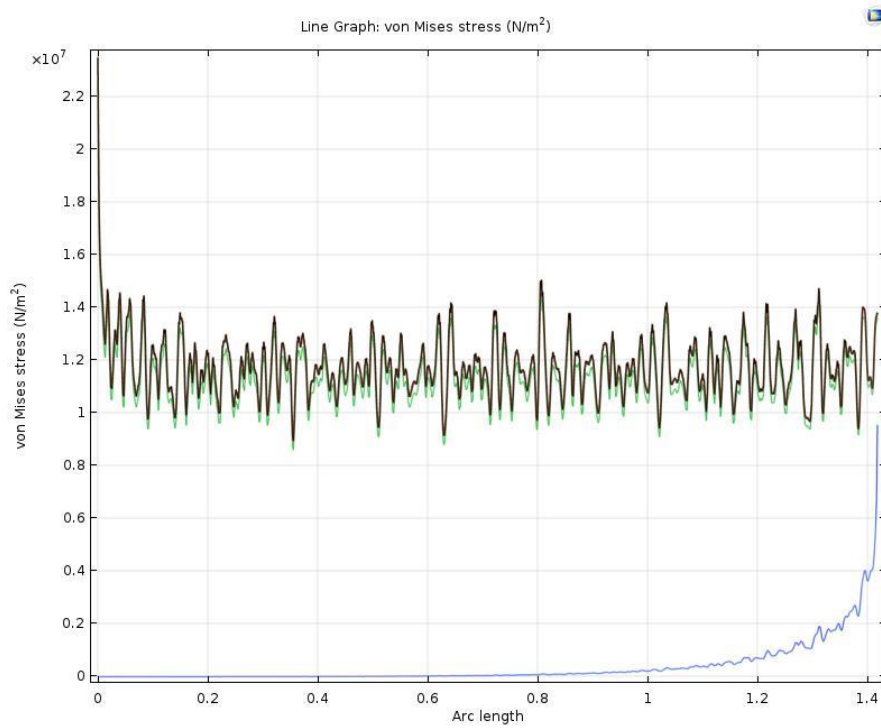
Figure 6. 21. Represents von-Mises stress of the bottom curve for 60% PZT dome shape model.
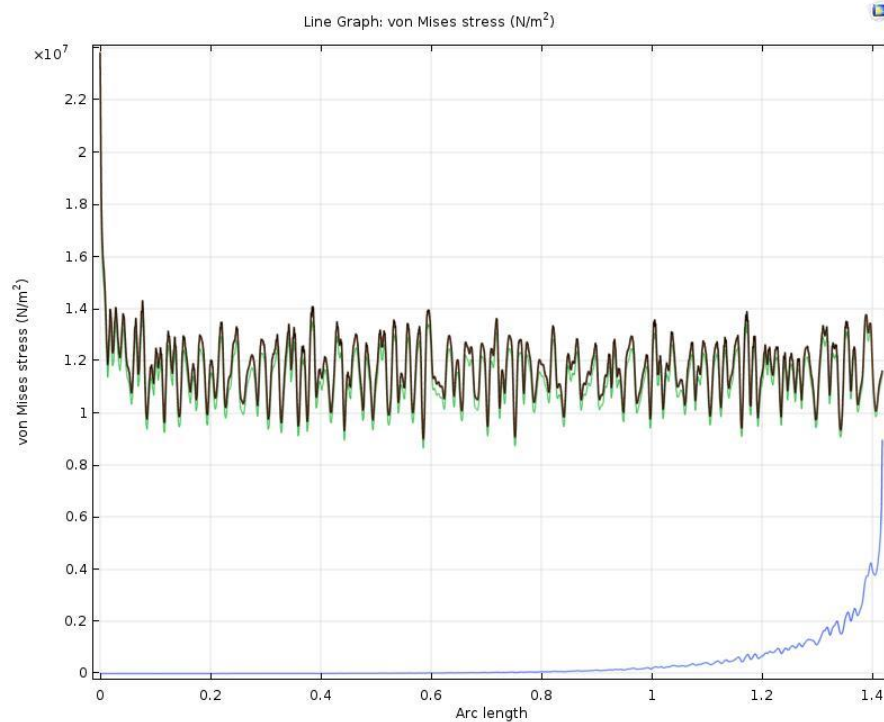
Figure 6. 22. Represents von-Mises stress of the bottom curve for 70% PZT dome shape model.

From the figures, it shows that the von-mises stress of the bottom curve for each volume fraction dome shape models are very similar. The range of the stress is almost between $1×10^7$ to $1.6×10^7$ N/m^2. The reason is that the bottom curve was set up as a fixed boundary as a constraint boundary condition for "Solid Mechanics" physics for Comsol models, otherwise, the results will not be convergence. In this case, the stress for the bottom curve is very similar for each volume fraction PZT models.

Since the bottom curve is fixed, there is no deformation for the bottom curve during the heat transfer process. Thus, the displacement for the bottom curve keeps at zero during the heat transfer process for all volume fraction dome shape models. The result is given by Figure 6.23. The horizontal axis represents the arc length of the bottom curve and the vertical axis represents the strain.
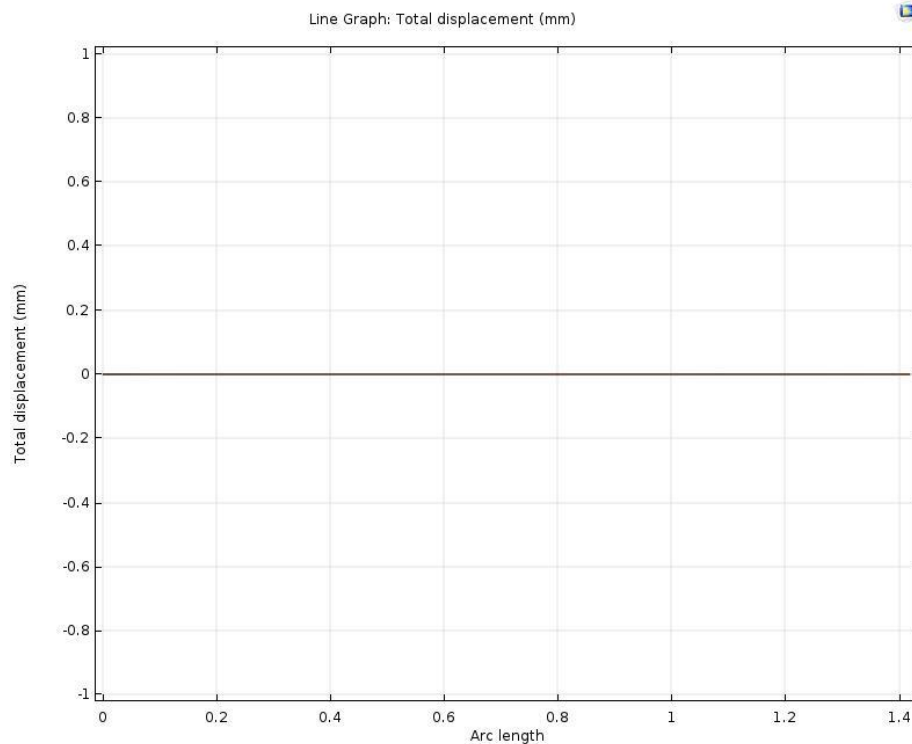
Figure 6. 23. Represents the strain of the bottom curve for all volume fraction PZT dome shape models.

6.2.2 Stress and strain of the upcurve of the dome shape models

In section 6.2.1, the stress and strain of the bottom curve of the dome shape models was discussed. In this section, the results for stress and strain of the up curve for each volume fraction of PZT dome shape models will be shown. As before, let us see the results for pure PZT dome shape model first. The von-Mises stress and strain for the up curve of pure PZT dome shape model is given by Figure 6.24 and 6.25. The horizontal axis represents the arc length of the up curve and the vertical axis represents the stress and strain. The different color curve from the bottom to top represent the stress and strain from zero-time step to final time step.

From the figures, it shows that the von-Mises stress decreases with increasing the arc length and increases with increasing the time step. The strain of the up curve

increases with increasing arc length and time step. The distribution of stress and strain

is opposite to the bottom curve and the range of the displacement for both bottom and

up curves is same but the stress of the up curve is smaller than the bottom curve.
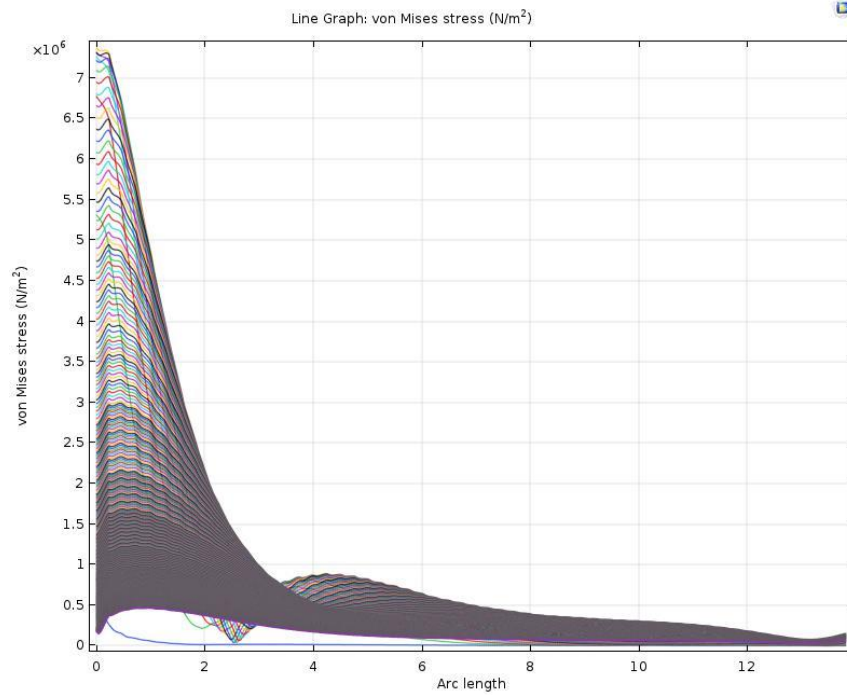
Figure 6. 24. Represents the von-Mises stress of the up curve for pure PZT dome shape model.
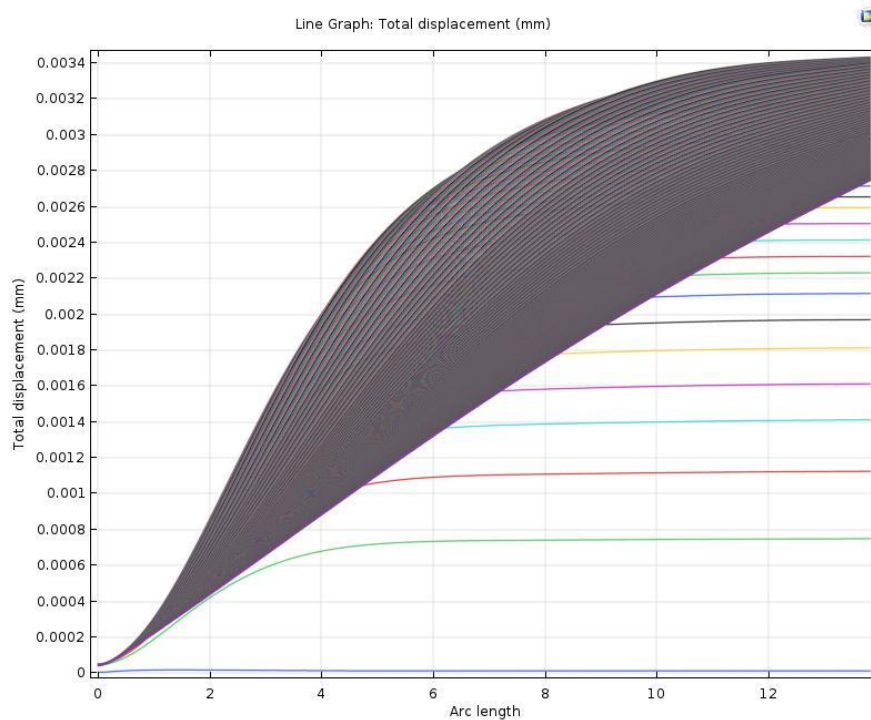
Figure 6. 25. Represents the strain of the up curve for pure PZT dome shape model.

Next, let us discuss the result for pure epoxy models of both fully cured epoxy and partially cured epoxy. The results for stress and strain of the up curve for both two types of epoxy models are given by Figure 6.26 to 6.29. The horizontal axis represents the arc length of the up curve and the vertical axis represents the stress and strain. The different color curve from the bottom to top represent the stress and strain from zero-time step to final time step.
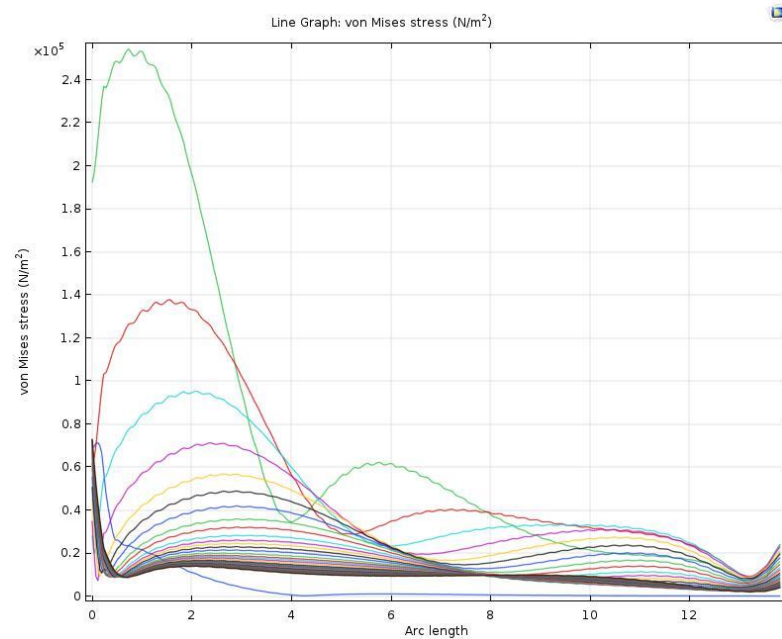
Figure 6. 26. Represents the von-mises stress of upcurve with respect to arc length change with time step. Epoxy fully cured dome shape model.
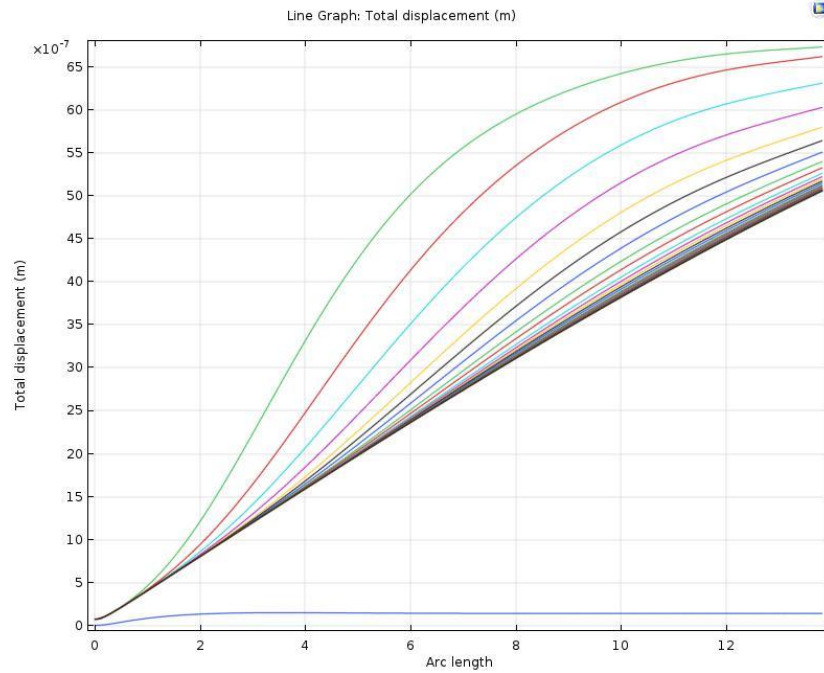
Figure 6. 27. Represents the strain of the up curve with respect to arc length change with time step. Epoxy fully cured dome shape model.
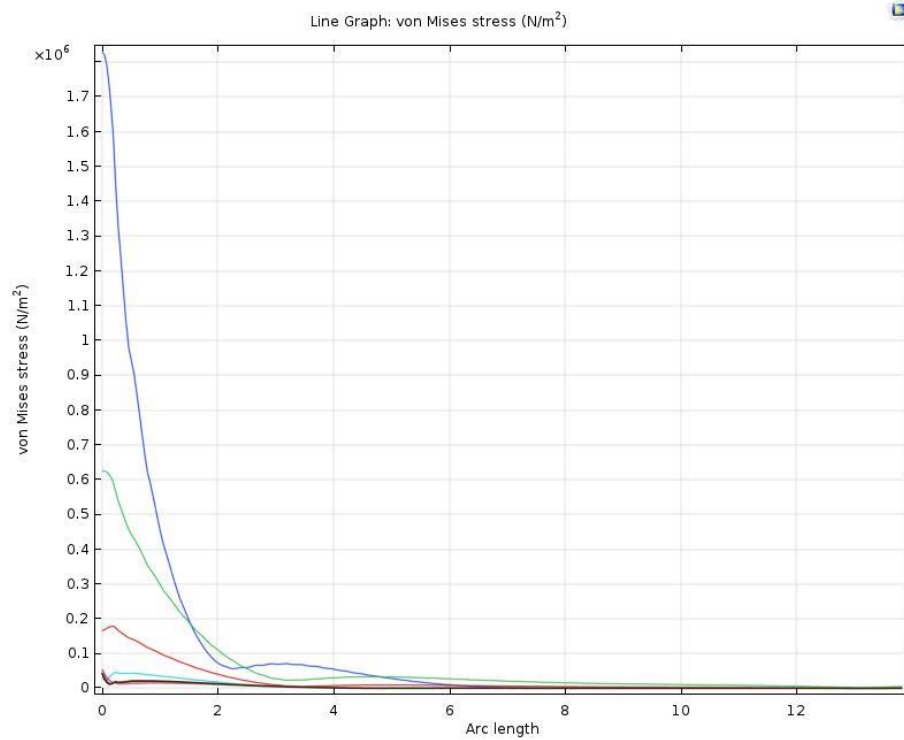
Figure 6. 28. Represents the von-mises stress of the up curve with respect to arc length change with time step. Epoxy partially cured dome shape model.
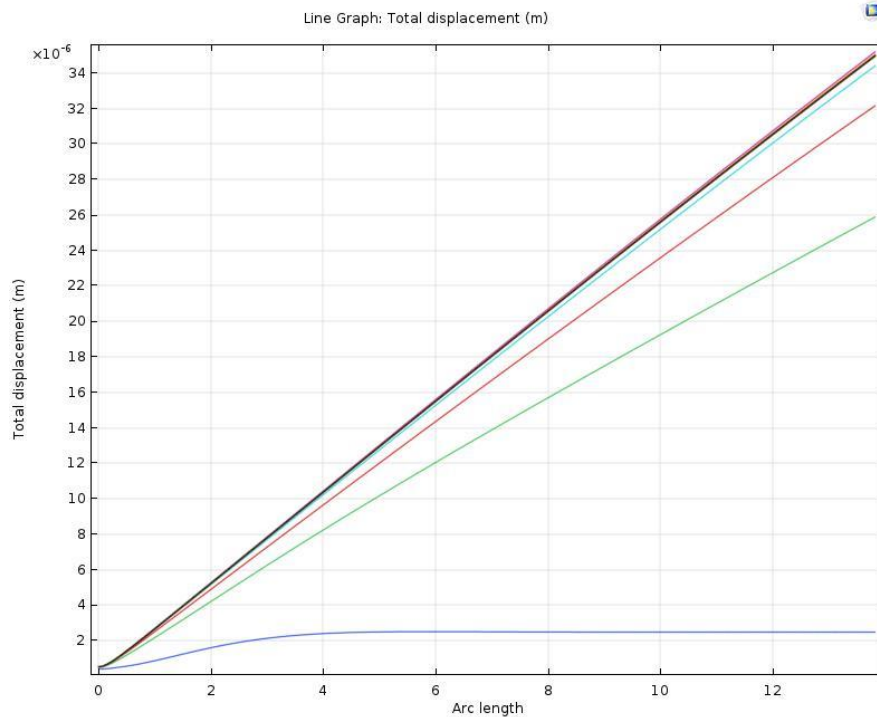
Figure 6. 29. Represents the strain of the up curve with respect to arc length change with time step. Epoxy partially cured dome shape model.

From the figures, the distributions of stress and strain of the up curve for both two types of epoxy are opposite to the bottom curve. The von-Mises stress of both two types of epoxy models for upcurve is generally decreases with increasing the arc length, but the strain increases with increasing the arc length. The range of the stress and strain is similar to the bottom curve.

Next, let us see the results for composite PZT dome shape models. First, the results for the von-Mises stress of the up curve for each volume fraction composite model will be shown. The results are shown in Figure 6.30 to 6.36. The horizontal axis represents the arc length of the up curve and the vertical axis represents the stress. The blue curve represents the stress at zero-time step and the black curve represents the stress at the final time step.
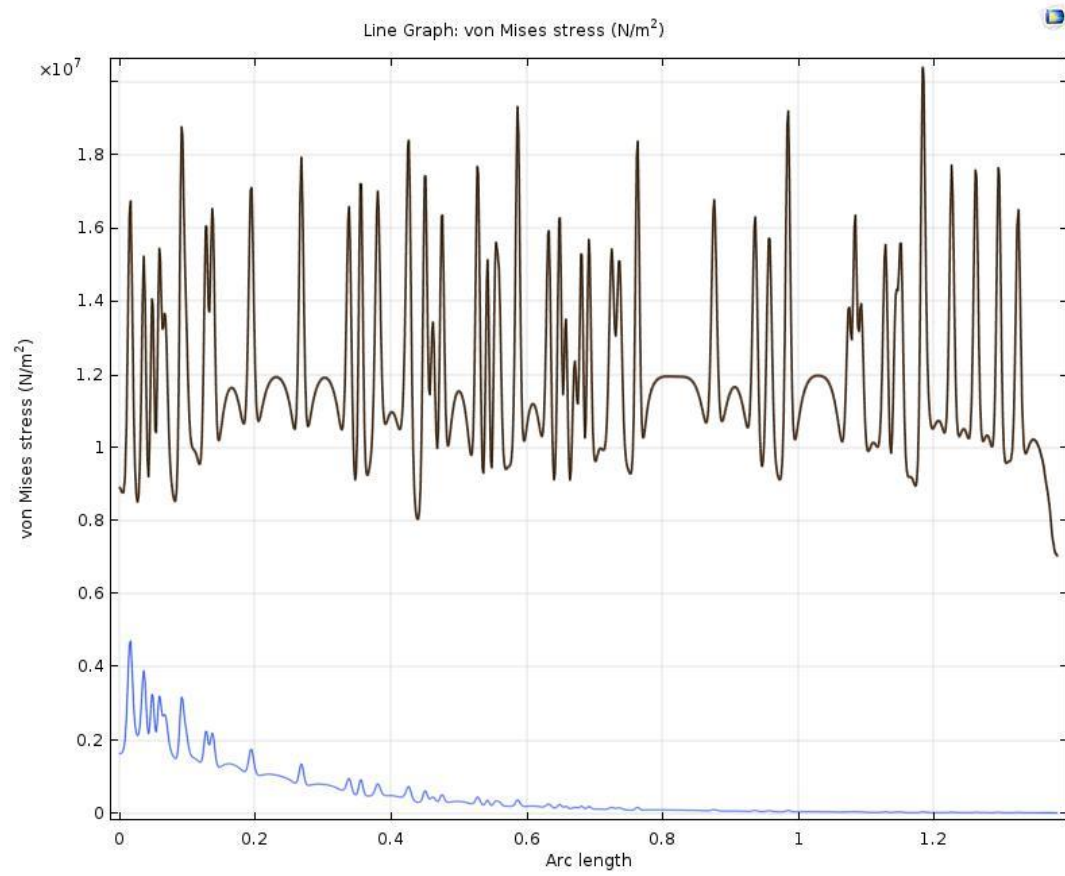
Figure 6. 30. Represents von-Mises stress of the up curve for 10% PZT dome shape model.
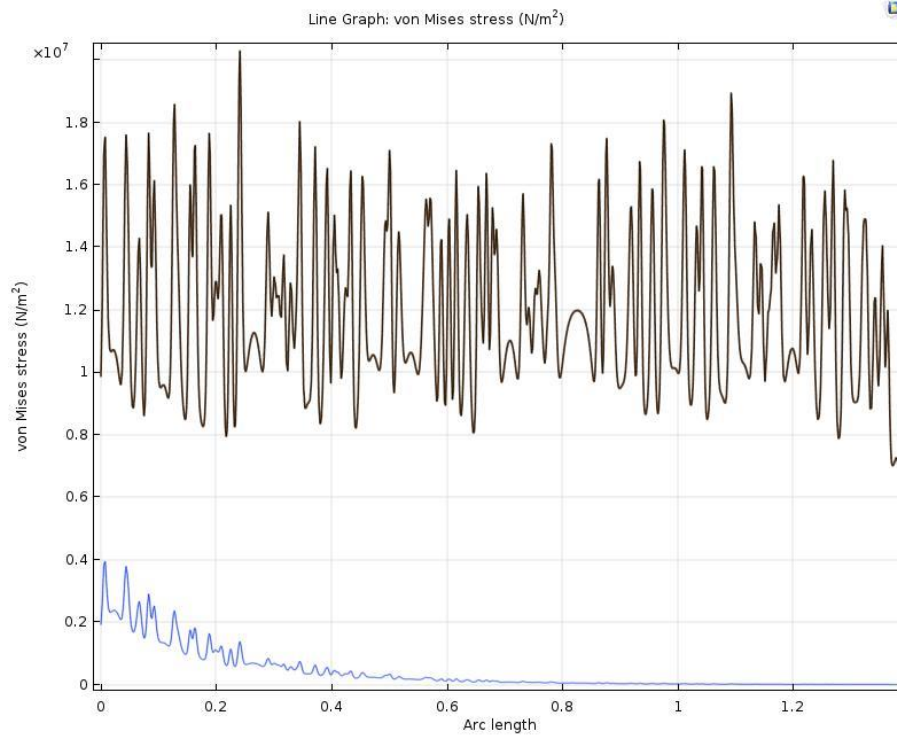
Figure 6. 31. Represents von-Mises stress of the up curve for 20% PZT dome shape model.
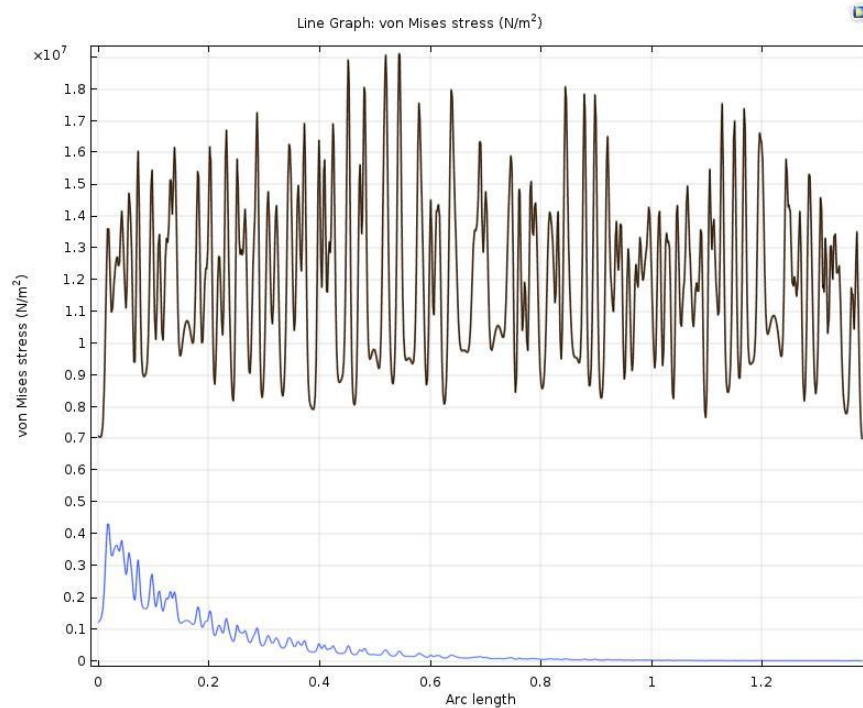
Figure 6. 32. Represents von-Mises stress of the up curve for 30% PZT dome shape model.
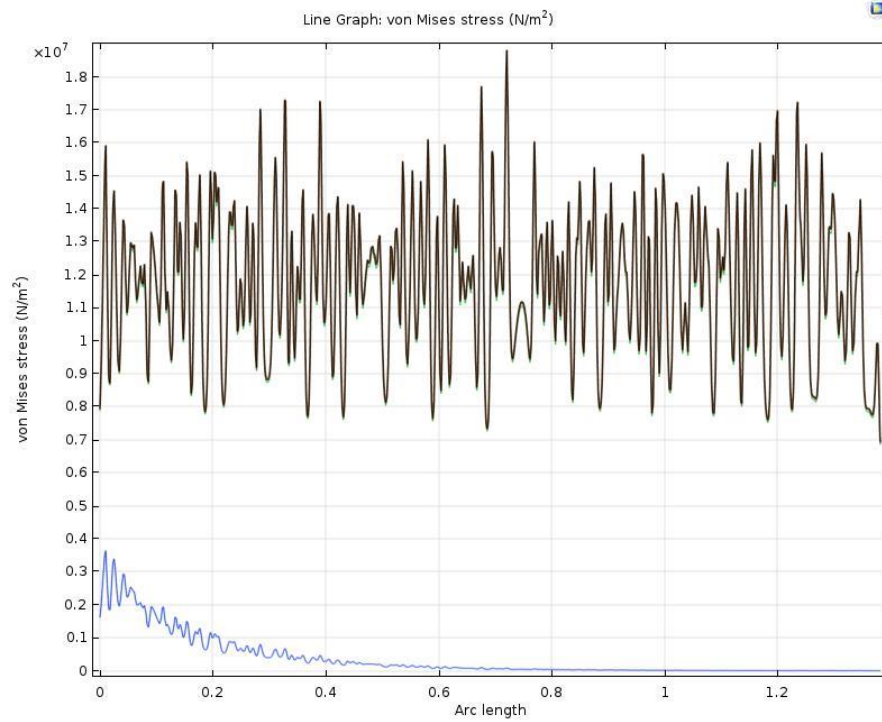
Figure 6. 33. Represents von-Mises stress of the up curve for 40% PZT dome shape model.
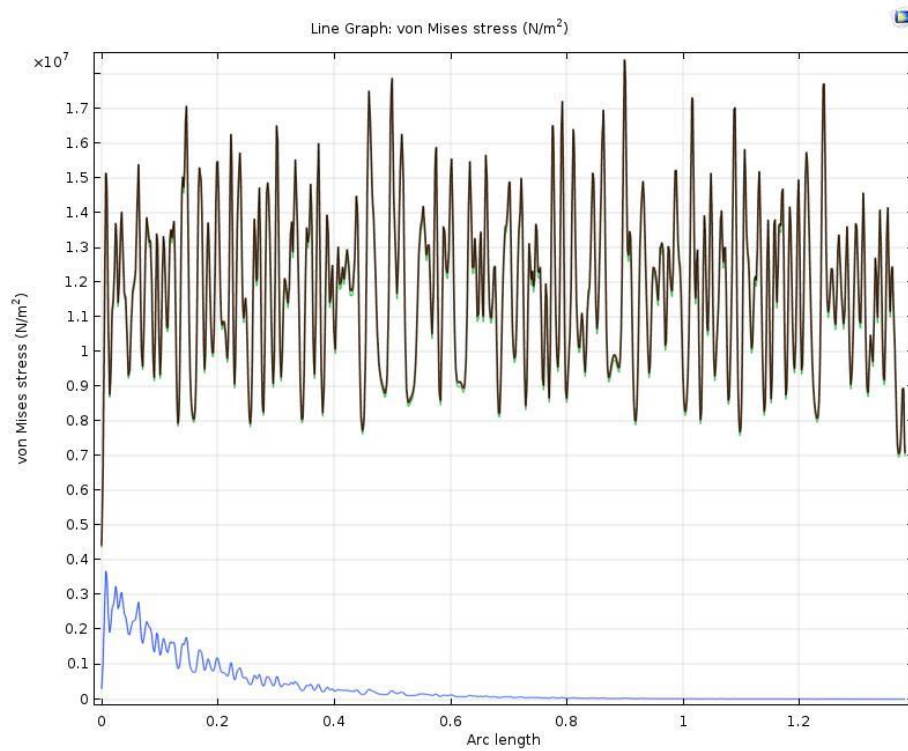
Figure 6. 34. Represents von-Mises stress of the up curve for 50% PZT dome shape model.
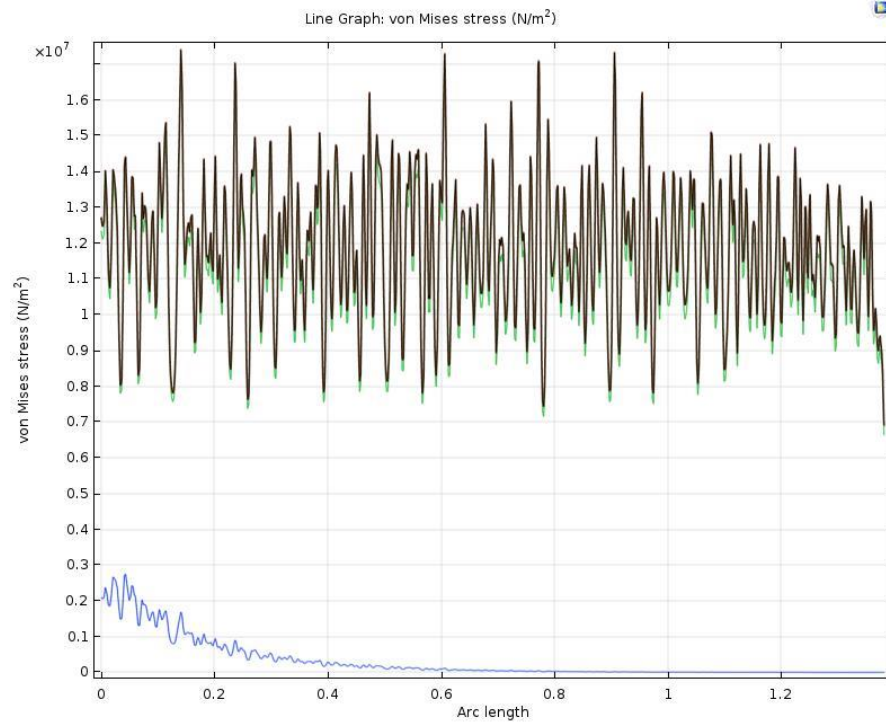
Figure 6. 35. Represents von-Mises stress of the up curve for 60% PZT dome shape model.
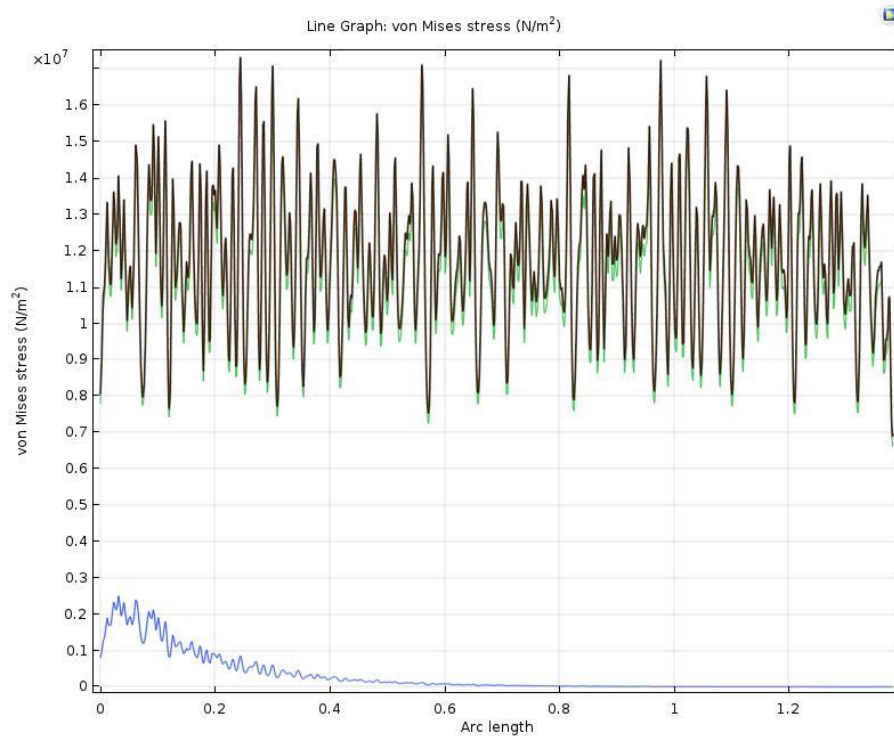
Figure 6. 36. Represents von-Mises stress of the up curve for 70% PZT dome shape model.

From the figures, the range of the distribution of the von-Mises stress is very similar for each volume fraction composite models. It is almost between $0.8{\times}10^7$ to $2.0{\times}10^7$ N/m^2. There is no big difference for different volume fraction PZT dome

shape models. It is not like the distributions of the stress in bulk and planar models. The reason is that in bulk and planar models, the heat source is added directly at the bottom boundary of the composite samples. Thus, the main type of heat transfer process is heat conduction in the solid interface. However, in a dome shape model, the heat source is not directly added on the bottom curve. Thus, the main type of heat transfer process is heat convection and surface radiation. There is more heat loss during these two types of the heat transfer process. Since, the stress is equal to strain times Young's Modulus of the composite, the range of the strain of the up curve is very similar for each volume fraction models which will be shown in the next part, so the range of the stress is very similar if the Young's Modulus does not change too much for the composites.

Next, let us see the results for the strain of the up curve for each volume fraction composite models. The results are given by Figure 6.37 to 6.43. The horizontal axis represents the arc length of the up curve and the vertical axis represents the strain. The blue curve represents the strain at zero-time step and the black curve represents the strain at the final time step.
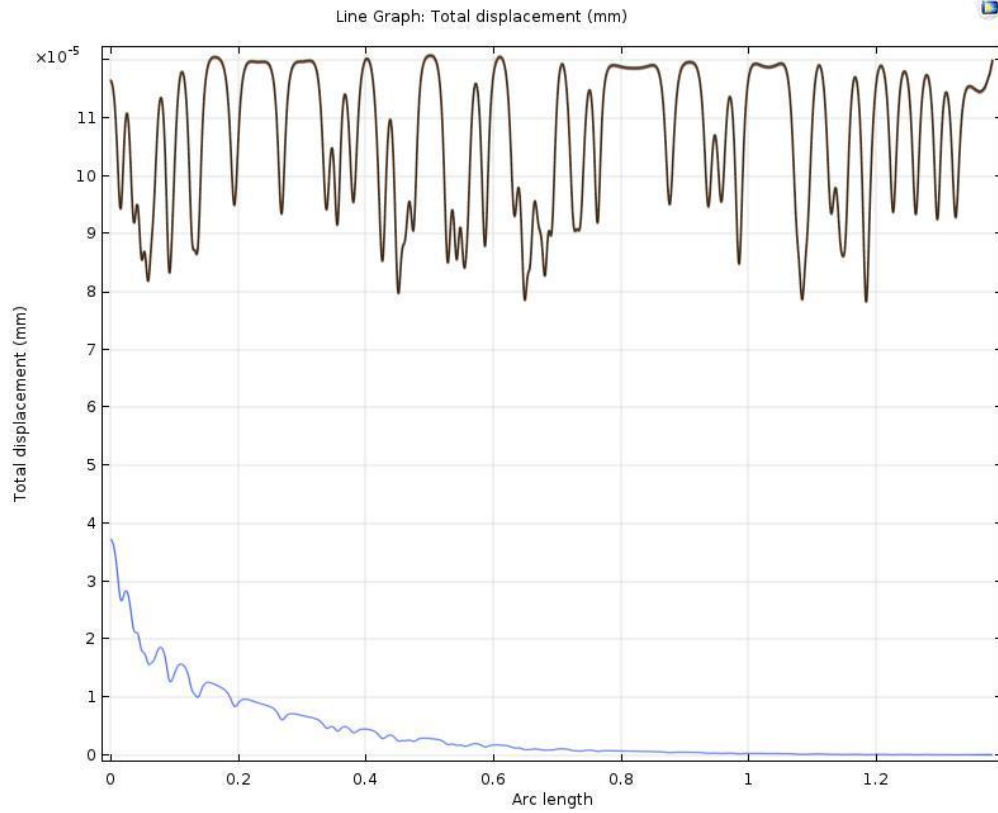
Figure 6. 37. Represents the strain of the up curve for 10% PZT dome shape model.
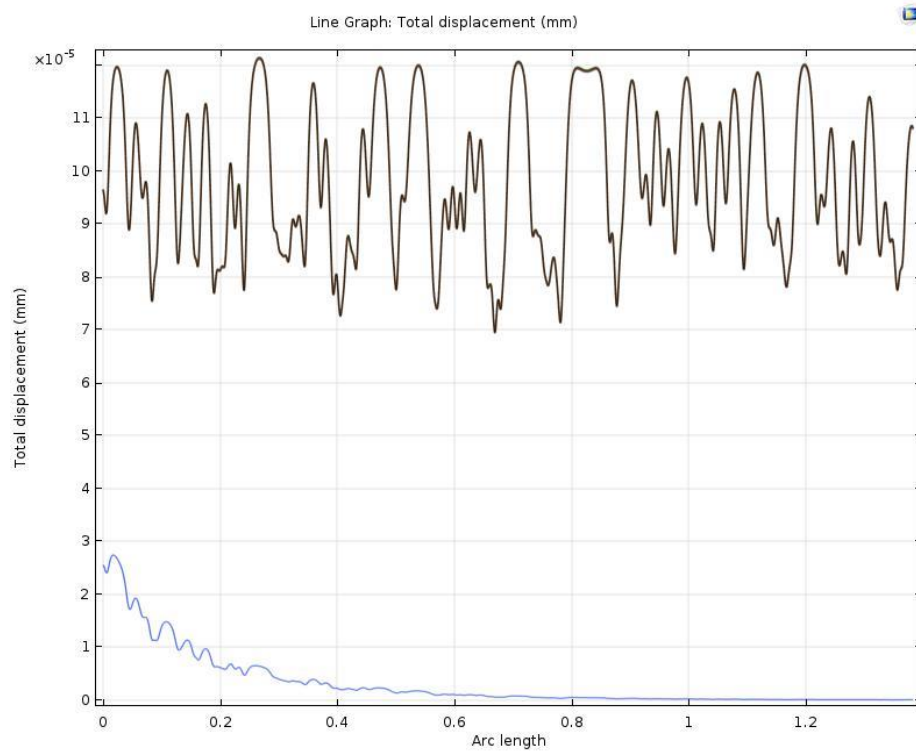
Figure 6. 38. Represents the strain of the up curve for 20% PZT dome shape model.
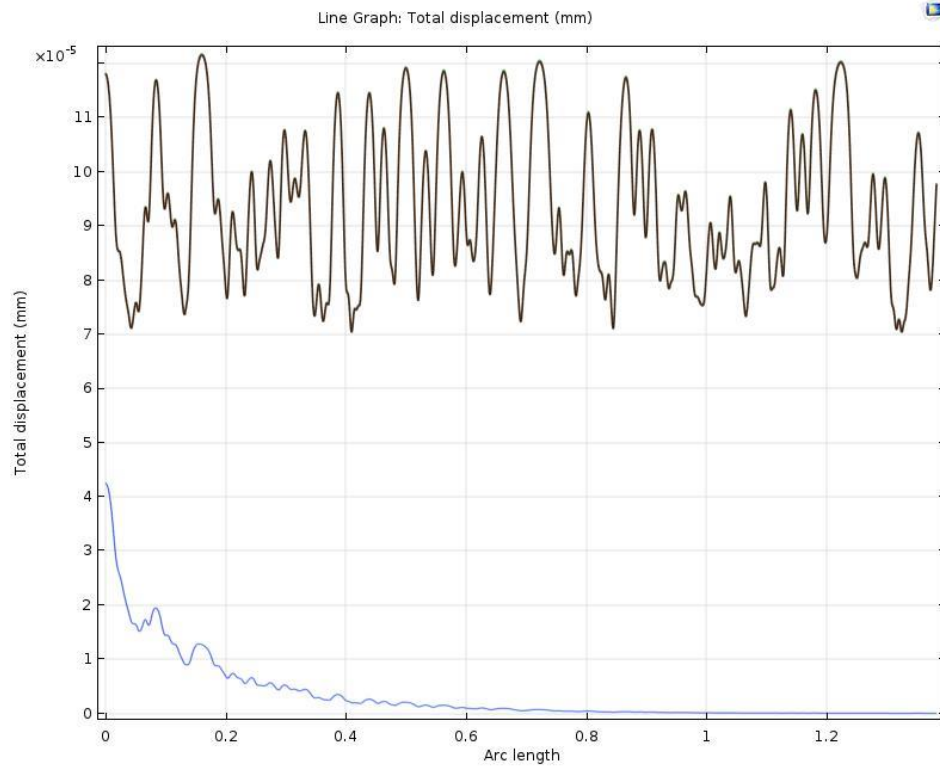
Figure 6. 39. Represents the strain of the up curve for 30% PZT dome shape model.
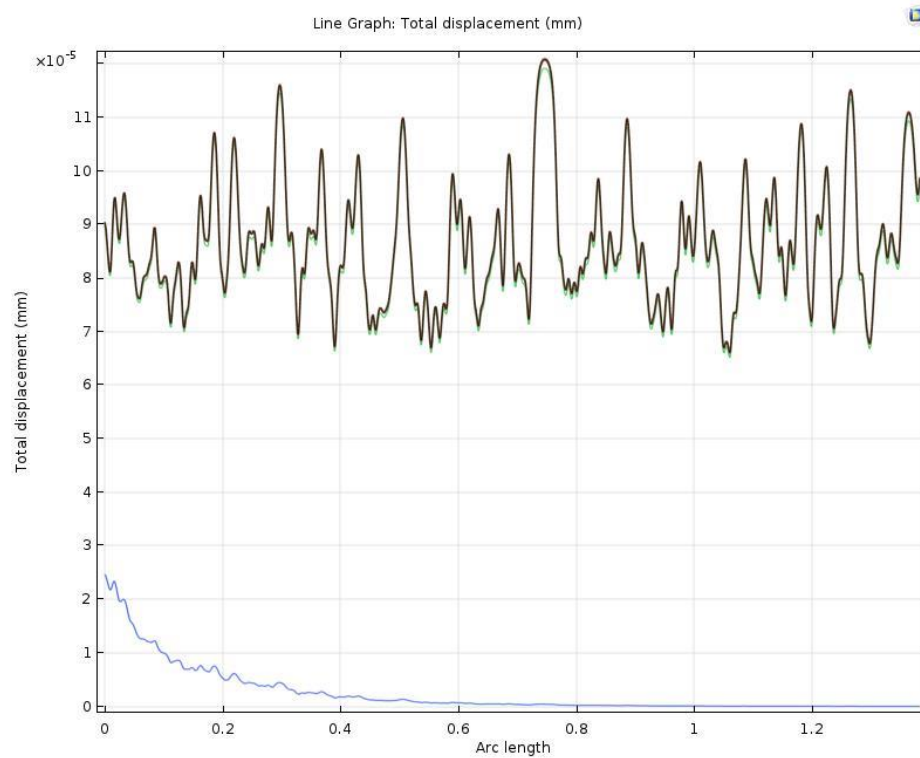
Figure 6. 40. Represents the strain of the up curve for 40% PZT dome shape model.
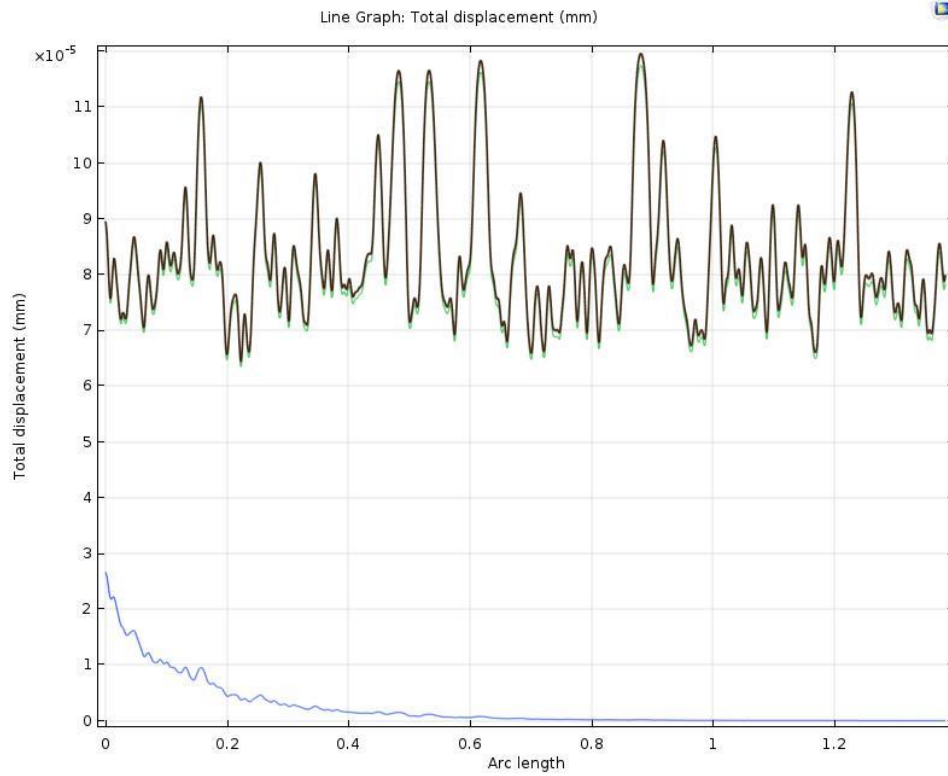
Figure 6. 41. Represents the strain of the up curve for 50% PZT dome shape model.
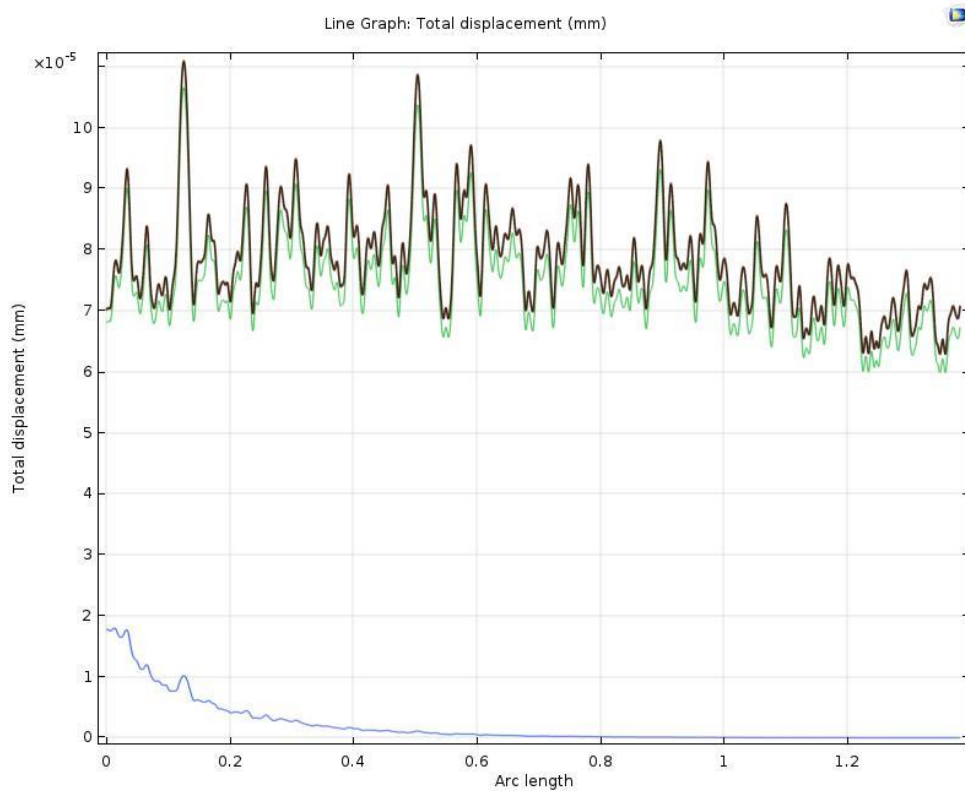
Figure 6. 42. Represents the strain of the up curve for 60% PZT dome shape model.
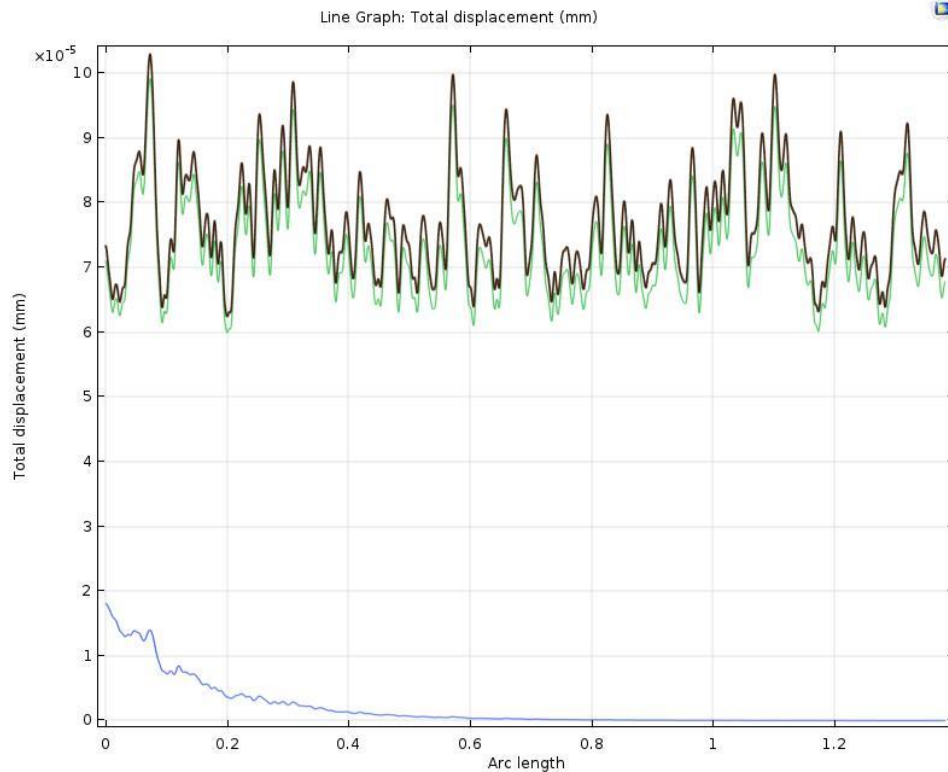
Figure 6. 43. Represents the strain of the up curve for 70% PZT dome shape model.

From the figures, the range of the strain of the up curve for each volume fraction composite models are very similar. It is larger than the strain of the centerline of the unit cell of bulk and planar models, which means dome shape models have more deformation during the heat transfer process under a same applied heat source than bulk and planar models. In this case, the dome shape samples may have a better piezoelectric effect than bulk and planar samples because they can have larger deformation under the same condition. This is the reason the dome shape geometry samples were studied to see if they have a better application to sensors and actuators by using this type of geometry samples.

6.3 Electrical displacement and electric potential generated by each volume fraction PZT model.

In the above two sections in this Chapter, the results for thermal properties and solid mechanics results caused by thermal expansion were discussed. In this section, the results for piezoelectric effect related to solid mechanics will be discussed. First, the electrical displacement will be introduced. Electric displacement (D), also known as electric flux density, is the charge per unit area that would be displaced across a layer of conductor placed across an electric field. It is different from the strain discussed in section 6.2. In section 6.2, the strain is caused by thermal expansion and it describes the deformation of the composites. However, electric displacement describes the displacement of the charge per unit area when an external electric field is applied. In our study, the external electric field is applied in the -Z-direction. In the experimental part, the piezometer was used to measure the piezoelectric strain coefficient (d_{33}). In order to get the piezoelectric strain coefficient with each volume fraction, the boundary load and electrical displacement were kept with the same value for all volume fraction PZT models on the up curve, which boundary load is 0.25N. The boundary load is in -Z-direction. As the numerical results need to be compared with experimental data, the same conditions of boundary load and electric displacement need to be set up in our Comosl models. However, a problem is that the electrical displacement cannot be measured in the experimental work. But it can be calculated according to equation 2.13 ($S_{33} = d_{33} . E_3$), where S_{33} is the electrical displacement in Z-direction, d_{33} is piezoelectric strain coefficient and E_3 is the applied external electric field in Z-direction.

Since the piezoelectric strain coefficient of pure PZT-5A can be checked from the material library in Comsol, which is 584pc/N, and the applied external electric field is 0.2kV in dome shape models. Thus, the value of electrical displacement can be calculated as 1.168×10^{-7}m for pure PZT dome shape model. This same value was kept for all volume fraction PZT models which is the same as experimental work.

Once the value of the boundary load and electrical displacement was got for all the models, the next step is to find out the electric potential (voltage) generated by the direct piezoelectric effect. In experimental work, the dielectric constant was measured at the frequency 110HZ. The same value of frequency was kept in the study in Comsol models. Then the results for electric potential generated by direct piezoelectric effect is listed in Table 6.1:

Table 6. 1: Electric potential generated by direct piezoelectric effect for each volume fraction PZT dome shape model

Volume fraction PZT models	Electric potential(V)
Pure PZT	307.42
10%	46.94
20%	82.969
30%	96.658
40%	85.071
50%	109.22
60%	156.96
70%	149.84

From the table, it shows that pure PZT model gets the largest value of electric

potential. This is because pure PZT model is one-phase material, which has a great piezoelectric effect. Once a boundary load was applied on the sample, it generates a large voltage. The electric potential generally increases with increasing the volume fraction of PZT composite models except 40% and 70% models. The reason for this phenomenon might be caused by the overlap of the PZT particles. Since the script for generating the PZT particles in dome shape models is different in bulk and planar models. The effective area of the PZT particles of these two volume fraction models may be smaller than 30% and 60%. Another difference is that the dimension of PZT particles in unit cell method is range from 5μm to 8 μm in diameter, but in dome shape model, the diameter of the PZT particles is kept at 8μm. In this case, the higher the volume fraction model is, the more overlapped area of PZT particles have. Thus, these two reasons may lead to the smaller electrical potential for these two volume fraction models. Generally, a higher volume fraction of PZT composites may have a better piezoelectric effect. But since the composites are two-phase materials, epoxy may also affect the piezoelectric effect of the composites. From the table, the minimum value of electric potential occurs at 10% PZT composite model, which is 46.94V and largest value of electric potential happens at 60% PZT composite model, which is 156.96V. In this case, it shows that 60% PZT composite model has the best direct piezoelectric effect among these composite models and 10% PZT model has the lowest piezoelectric effect compared to other composite models.

6.4 Capacitance for each volume fraction of PZT model

Capacitance is the ability of a component or circuit to collect and store energy in the form of an electrical charge. In this study, the Maxwell capacitance can be got from the Comsol models. In the results part, right click "Derived Value" and choose "Global Evaluation". Then the expression can be put for Maxwell capacitance, which is "es.C11" into the setting window. Then if click the "Evaluation" button in the setting window, the Maxwell capacitance can be got directly from the model. The capacitances for all volume fraction PZT composite models are listed in Table 6.2:

Table 6. 2: Maxwell capacitance for all volume fraction PZT composite models

Volume fraction PZT models	Maxwell capacitance(F)
Pure PZT	2.0898×10^{-11}
10%	1.5788×10^{-12}
20%	1.5844×10^{-12}
30%	1.8707×10^{-12}
40%	1.9607×10^{-12}
50%	1.9638×10^{-12}
60%	1.9979×10^{-12}
70%	1.9920×10^{-12}

From the table, it shows that the Maxwell capacitance generally increases with increasing the volume fraction of PZT composites from 10% to 70%, except 70% which is a little bit smaller than 60%. The reason lead to this phenomenon was mentioned in section 6.3. From the results, it means that a higher percentage volume fraction PZT

models has better ability to store the energy of electrical charges.

6.5 Curing condition study

In this section, the results for the curing process of epoxy DGEBA will be discussed. As mentioned before in Chapter 3, the degree of cure α will be expressed to describe the ability the epoxy DGEBA absorbs heat as the material cures. The epoxy will have phase change from gel form to sold form during the curing process. Two different curing conditions will be discussed in this section, one is curing on a hot plate at a fixed temperature 75C and the other one is curing in a room temperature 20C in the air. The difference is that the dimension of the model is different from the bulk model, which is much smaller and thinner than the bulk model and it is like a curved beam.

6.5.1 Curing on a hot plate

First, the curing process of epoxy DGEBA on a hot plate at a fixed temperature 75C will be discussed. The reason why the temperature was chosen as 75C is because 75C is the Curie temperature of epoxy DGEBA. Above this temperature, the structure of epoxy DGEBA will be centrosymmetric and it will become stable. However, when the temperature is below this temperature, the structure is non-centrosymmetric and the epoxy is in gel form. In addition, the Curie temperature of PZT particles is much higher than 75C, so if the temperature was fixed at 75C, it cannot only get the phase change of epoxy DGEBA and make the polymer matrix stable so as to keep the PZT particles

inside the matrix, but also it can still keep the piezoelectric and dielectric properties of PZT-5A so that the composites can still possess piezoelectric effect since the Curie temperature of PZT is much higher than 75C. Such properties are mentioned in Chapter 2, Perovskite Structure in Figure 2.16. Two interfaces are used in Comsol model to simulate this process, one is 'Heat transfer in solid" and the other one is "Domain ODEs and DAEs". The governing equations used for this process are mentioned in Chapter 3, equation 3.33 and 3.34 and the material properties used for this model are listed in table 3.8. The result for the degree of curie of the upcurve of the cross-section of pure epoxy DGEBA will be discussed to express the curing process since the bottom curve is set up as a fixed constraint. The result is shown in Figure 6.44 and 6.45:

The value of the degree of cure is from 0 to 1. When it is close to zero, which means the epoxy is not cured and it is the gel form. When the curing process is done, the value of the degree of cure is equal to 1 or very close to 1. From the two figures, it shows that the epoxy DGEBA cured very fast at the beginning and it may take 1 week to be mostly cured, which the value of the degree of cure is close to 0.8. However, it may take very long to be fully cured as it shows from Figure 6.45. In experimental work, it takes about 8-10 hours to be fully cured. It has a great difference between Comsol models and the experimental work. The reason is that the data for the material properties of the epoxy DGEBA was unknown. The thermal material properties used in this model get from the articles found online. There are no instruments in our lab to measure the thermal properties of the epoxy DGEBA used in our experimental work. That might be one of the reasons leads to the big difference. The other reason might be that the epoxy

is fully cured or not was unknown in our experimental work because it cannot be measured. It might take more time to be fully cured. In addition, if the results were compared with the bulk model, it shows that it takes much faster for dome shape model to be fully cured than bulk model because it is much thinner than the bulk model.
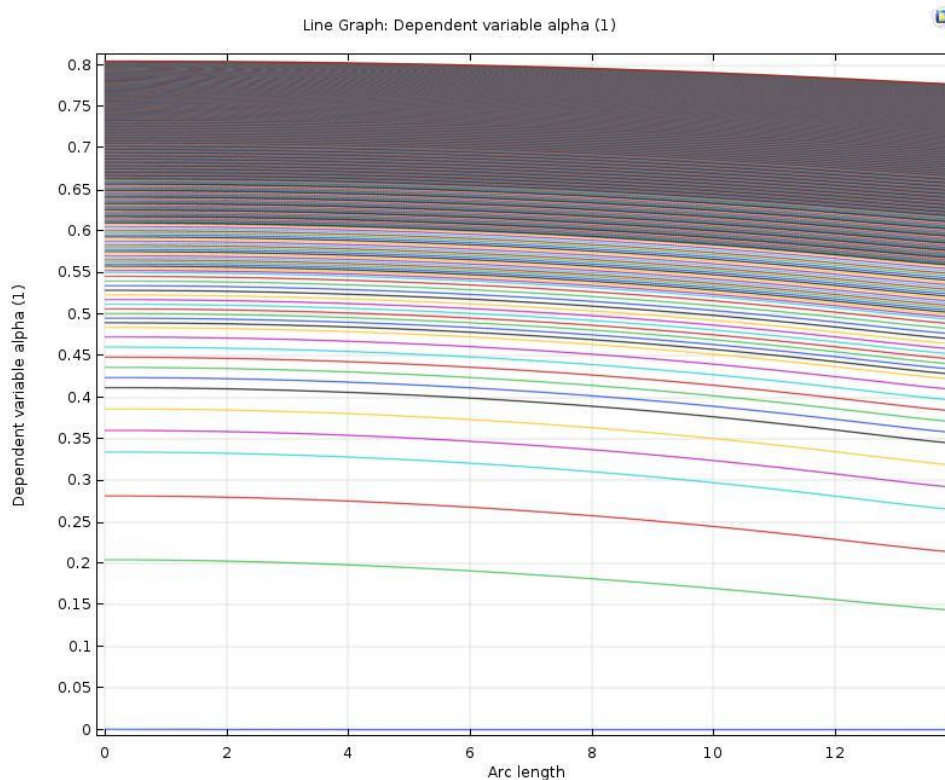
Figure 6. 44. Represents the degree of cure from 0 to 800000s at 75C.
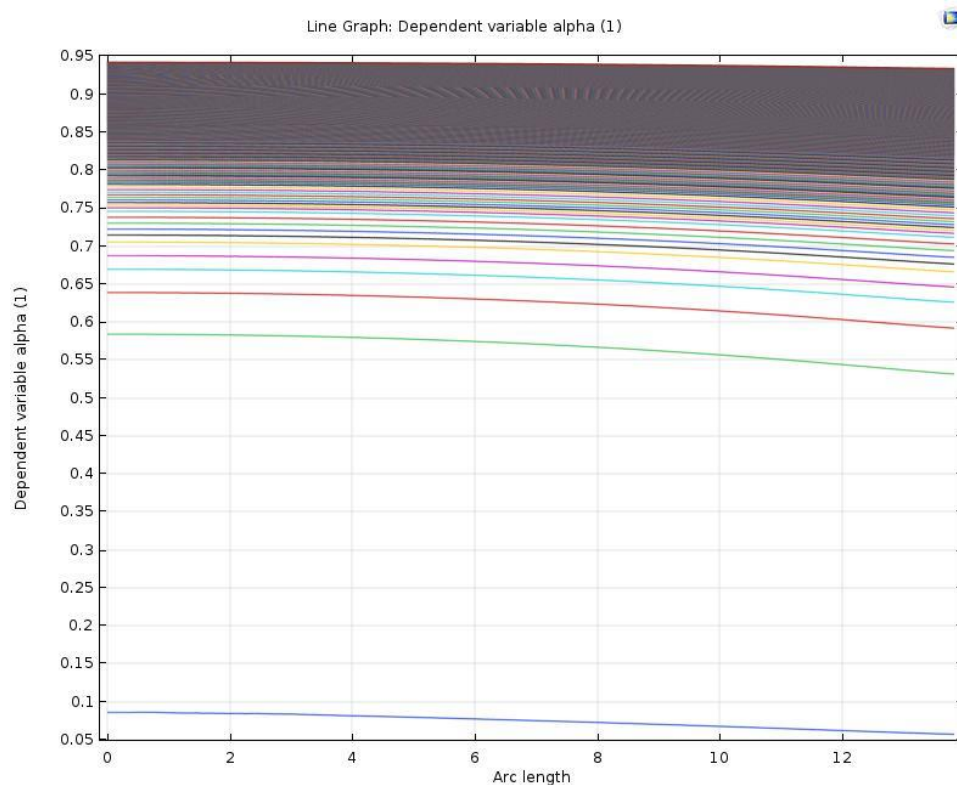
Figure 6. 45. Represents the degree of cure from 0 to 500000mins at 75C.

6.5.2 Curing in room temperature 20C in the air

Next, the curing process of epoxy DGEBA in room temperature 20C in the air will be discussed. Such a process is not affected by the heat transfer process because there is no temperature difference between air and the sample. The difference between this curing condition and the condition discussed in section 6.5.1 will be shown. The result for the degree of cure of the upcurve of the cross-section of pure epoxy DGEBA is given by Figure 6.46:
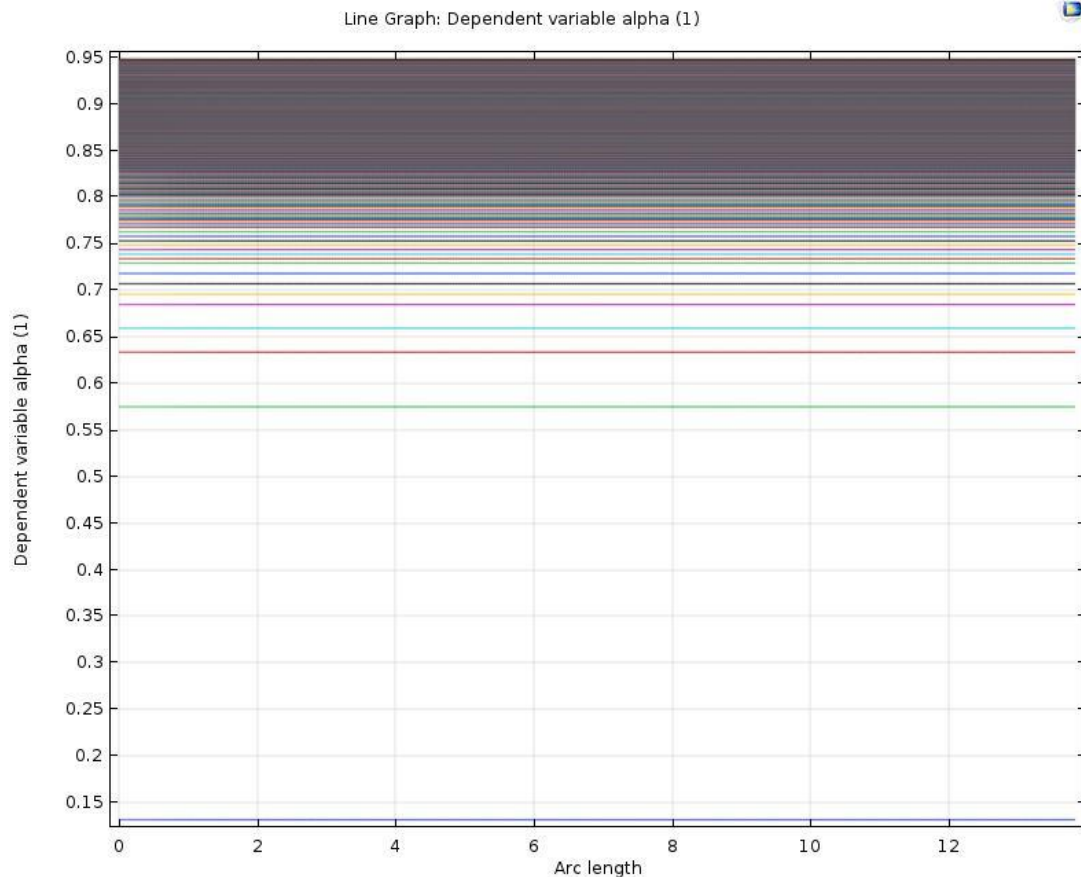
Figure 6. 46. Represents the degree of cure from 0 to 800000hours at 20C.

From the figure, it shows that it takes about 30 days to get the value of the degree of cure about 0.95 which is almost fully cured. However, the same procedure was done in the experimental work. It takes about 3 weeks that the epoxy DGEBA was fully cured in room temperature, which does not have too much difference for dome shape models. The reason that leads to this difference between the experimental work and the simulation result is that the material properties of the epoxy input in the Comsol models have some difference of the epoxy used for the experimental work. But the good news is that the simulation result of the curing process of the epoxy DGEBA for dome shape model at room temperature is similar to experimental work.

6.6 Piezoelectric and dielectric properties of the composites

In this section, the results for piezoelectric and dielectric properties of the composites for each volume fraction PZT model will be discussed. In order to find out one of the hypotheses, as mentioned in Chapter 2. The piezoelectric and dielectric properties of the composites for two different conditions will be discussed. One is considering the boundary conditions of heat convection and surface radiation. The other one is without considering these two boundary conditions. Dielectric constant ε_r and the piezoelectric strain coefficient d_{33} will be calculated to express piezoelectric and dielectric properties. Such two values will be calculated by equation 2.5 and equation 3.31:

$$\varepsilon_r = \frac{Cd}{\varepsilon_0 A} \qquad (2.5)$$

$$d_{33} = \frac{V \varepsilon_r \varepsilon_0 A}{Fd} \qquad (3.31)$$

where C is the Maxwell capacitance, d is the thickness of the sample, A is the area of the surface, ε_0 is the permittivity of free space - a vacuum - is equal to approximately 8.85 x 10^{-12} Farads/meter(F/m), V is the electric potential, F is the fixed boundary load, which is 0.25N. In addition, the simulation results with both experimental results and results calculated by analytical models in this section will be compared as well.

6.6.1 Piezoelectric and dielectric properties of the composites with considering the boundary conditions in "heat transfer" in the solid interface.

First, the results for the dielectric constant and piezoelectric strain coefficient for

the simulation work with considering the boundary conditions for heat convection and surface radiation will be discussed. Four models were done for each volume fraction PZT model and take the average value for dielectric constant and piezoelectric strain coefficient. The results for piezoelectric and dielectric constant are under frequency 110HZ. The results for the dielectric constant are given in Table 5.3:

Table 6. 3: dielectric constant for all volume fraction PZT samples from Comsol models

Volume fraction PZT models	Dielectric constant ε_r(F/m)
Pure PZT	1700
10%	12.733
20%	12.78
30%	15.09
40%	15.81
50%	15.84
60%	16.11
70%	16.01

From the table, the dielectric constant generally increases with increasing the volume fraction of PZT except 70% model. The reason for this phenomenon is mentioned in section 6.4. The capacitance of 70% model is smaller than the capacitance of 60% model which is that the effective area of PZT particles in 70% model might be smaller than 60% model. The largest value of dielectric constant occurs at 60% PZT model, which is 16.11F/m. The smallest value occurs at 10% PZT model, which is 12.733 F/m. The dielectric constant of the dome shape composite models is smaller than the dielectric constant of planar composite models in Chapter 5. The reason is that

the effect of area of PZT particles in each volume fraction dome shape model is less than the real area it should be because some of the PZT particles are overlapped with each other. PZT is the main material which leads to piezoelectric and dielectric properties of the composites. In the ideal case, the dielectric constant of dome shape composite models might be larger than planar composite models because the dome shape model has more deformation than planar models under the same amount of applied force.

The experimental work for the dielectric constant was measured by Wanlin Du, a former Ph.D. student in our lab. Thus, the results for the dielectric constant will be compared with her experimental work[14]. The results are given in Figure 6.47:
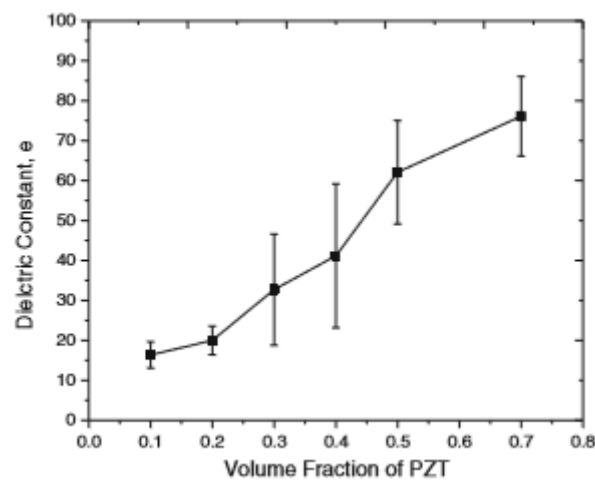
Figure 6. 47. The dielectric constant of the experimental work for dome shape composite models by Wanlin Du[14].

From the figure, it shows that the dielectric constant increases with increasing the volume fraction of PZT. However, they are larger than the simulation data. The reason for this difference is the same for the overlapped PZT particles. Since the effective area of the PZT is lower than the real volume fraction of PZT in real samples. Thus, the dielectric constant for the simulation data is smaller than the experimental results. This

can be proved by lower volume fraction composite models. If both 10% and 20% models were compared with the simulation data, it shows that the results are very similar. This is because, in lower volume fraction composite models, there is only a very small overlapped area for PZT particles. In this case, the effective area for PZT is almost to the real volume fraction of PZT in these two models. That is why the dielectric constant is very similar in lower volume fraction composite models, but the simulation results are lower than experimental results for higher volume fraction models because more and more PZT particles are overlapped with each other in higher volume fraction composite models. The results for dielectric constant of both experimental work and numerical work are given in Figure 6.48:
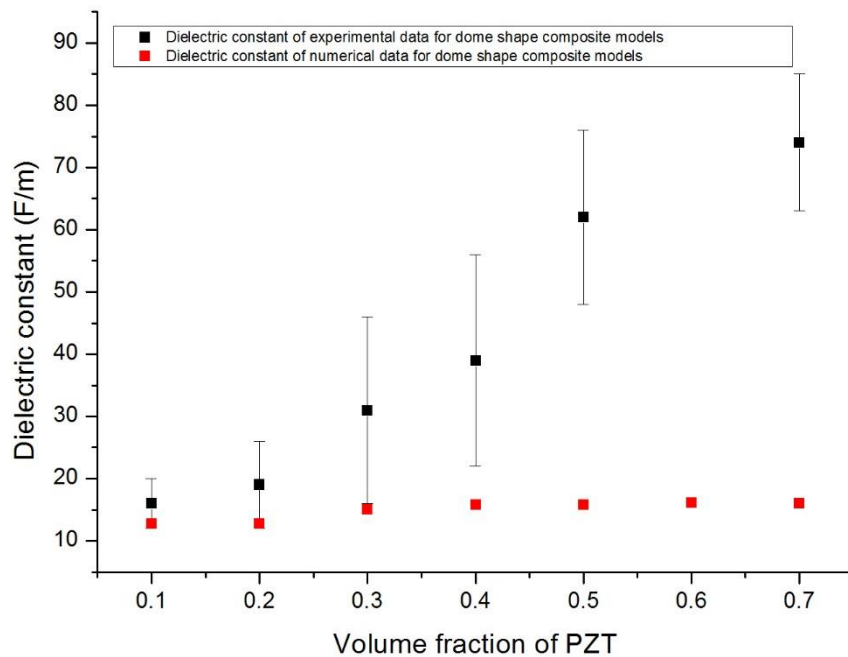
Figure 6. 48. Represents the dielectric constant of both experimental data and numerical data for dome shape composite models.

From the figure, black points represent the experimental work and red points represent the numerical work. For the low volume fraction PZT models, the numerical

data are inside the error bar of the experimental data. But for high volume fraction models, the numerical data are much lower than the experimental data. This is because there is a limitation for the scale method. It is not as good as the unit cell method because the PZT particles in the unit cell method are not overlapped with each other so that the volume fraction of PZT is equal to the real volume fraction of the composite. However, in scale method, the PZT particles are overlapped with each other, especially in high volume fraction PZT models. In this case, the dielectric constant of the high-volume fraction composite models for numerical results are much slower than the experimental work.

Next, the piezoelectric strain coefficient d_{33} will be discussed. This value is calculated by equation 3.31. The voltage V can be got for each volume fraction by the Comsol models. The data for dielectric constant was used by table 6.3. Boundary load F is kept at 0.25N. The results for the piezoelectric strain coefficient are given by Table 6.4:

Table 6. 4: piezoelectric strain coefficient of calculated by simulation work

Volume fraction PZT models	Piezoelectric strain coefficient d_{33} (pC/N)
Pure PZT	584
10%	2.96
20%	5.25
30%	7.23
40%	6.67
50%	8.58

60%	12.54
70%	11.89

From the table, it shows that piezoelectric strain coefficient generally increases with increasing the volume fraction of PZT model except 40% and 70% models which are because that the voltage and the dielectric constant of these two models are lower than 30% and 60% models. The reason is mentioned before. Thus, the minimum result occurs at 10% model which is 2.96pC/N and largest value occurs at 60% model which is 12.54 pC/N. This result shows that higher volume fraction PZT composites generally have a better piezoelectric effect than lower volume fraction composites. This is quite making sense because PZT is the phase material that has the piezoelectric effect. The piezoelectric strain coefficient of dome shape models is larger than the planar models. This means that the dome shape model can have larger deformation than planar model under the same applied load. Thus, the dome shape samples have a better piezoelectric effect than planar samples. The results of the piezoelectric strain coefficient for the dome shape composite models are plot in Figure 6.49:
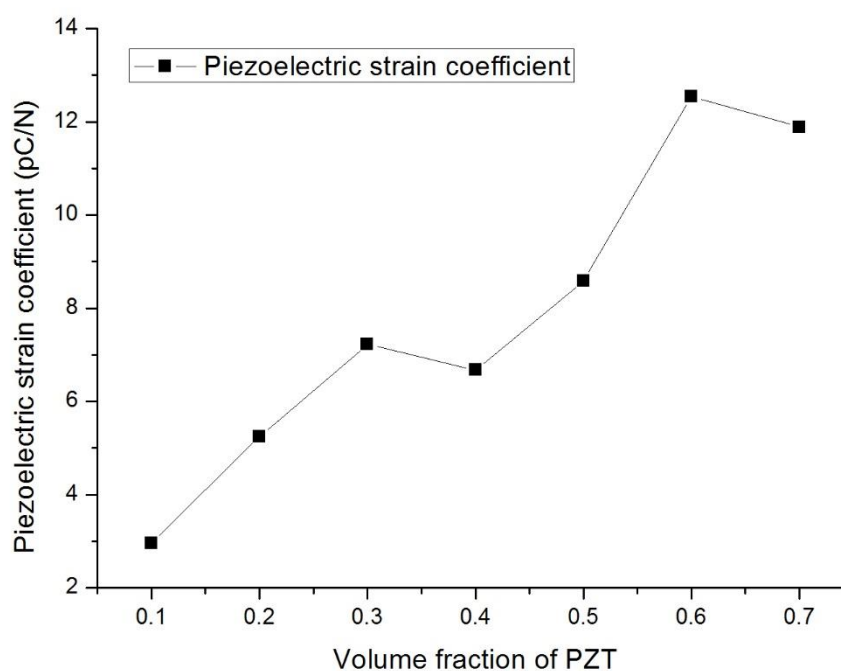
Figure 6. 49. Represents the piezoelectric strain coefficient of the dome shape composite models.

Next, let us compare the simulation result with experimental results. The dome shape composite samples were fabricated by Wanlin Du in our group and the piezoelectric strain coefficient is also measured by her[14]. She fabricated 10%-70% planar samples and she made 4 samples for each volume fraction PZT composite and the results are the averaged results for each volume fraction composites. The results are shown in Figure 6.48:
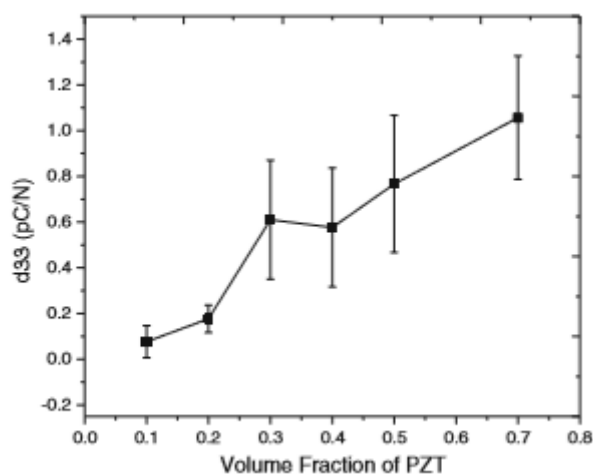
Figure 6. 50. The piezoelectric strain coefficient of the experimental work for dome shape composite models by Wanlin Du[14].

From the figure, the piezoelectric strain coefficient of dome shape composite models of the experimental result generally increases with increasing the volume fraction of PZT except 40% samples, which has the same phenomenon with simulation work. But the simulation results are a little bit larger than experimental results. The reason for this difference is that simulation work is generally ideal models. They do not affect by the environmental conditions, such as room temperature, humidity and so on, or affected by the manual operation, such as the fabrication procedure. Thus, it is making sense that the simulation results are a little bit larger than the experimental results. The good thing is that the simulation results are generally matched with experimental results. This means our models are doing well. In addition, the piezoelectric property for the PZT-epoxy dome shape composites should be better than PZT-epoxy planar sheet composite models because dome shape samples can have much deformation than the planar sheet samples under a same amount of applied force. In my simulation work for those two types of composites, the piezoelectric strain coefficient of the dome shape models is larger than the piezoelectric strain coefficient of the planar sheet models, which means the numerical work is making sense. However, the experimental work is vice versa. I have no idea why this happened. It is possible that the fabrication procedure for those two types of composite samples are different because they were done by different people.

6.6.2 Piezoelectric and dielectric properties of the composites without considering the boundary conditions in "heat transfer" in the solid interface.

In the last section, the results for dielectric constant and piezoelectric strain coefficient was discussed with considering the boundary conditions of heat transfer, such as heat convection and surface radiation. However, in this section, these results without considering such boundary conditions will be discussed so as to see if there are a big difference in the results or not.

In Chapter 4 and 5, it was proved that there is no big difference for both conditions, which means boundary conditions of heat transfer process do not have much influence on piezoelectric and dielectric properties of the composites. For here, it will show that if the same thing will happen in dome shape composites which have different geometry of bulk and planar models.

First, let us see the capacitance of each volume fraction PZT model without considering the boundary conditions of heat transfer. Table 6.5 gives the result for the capacitance of each volume fraction PZT model:

Table 6. 5: Maxwell capacitance without considering boundary conditions od heat transfer

Volume fraction PZT models	Maxwell capacitance(F)
Pure PZT	2.7115×10^{-10}
10%	1.5707×10^{-12}
20%	1.5705×10^{-12}
30%	1.9810×10^{-12}

40%	1.9841×10^{-12}
50%	1.9883×10^{-12}
60%	2.0054×10^{-12}
70%	1.9932×10^{-12}

From the table, it shows that Maxwell capacitance has a big difference with the results for considering the boundary conditions heat transfer. It generally increases with increasing the volume fraction of PZT composite. Compared with the results in table 6.2. The results for capacitance are generally larger than considering the boundary conditions. Since the hot plate is not directly applied to the bottom curve of the dome shape models. Heat conduction is not the main type of the heat transfer process. Heat convection and surface radiation are the main types in this procedure. In this case, it shows that the boundary conditions of heat transfer have a great influence on dome shape models.

Next, let us discuss the results for the voltage generated by the piezoelectric effect without considering the boundary conditions of heat transfer. Table 6.6 gives the results for voltage of all volume fraction models.

Table 6. 6: electric potential generated by the piezoelectric effect without considering boundary conditions of heat transfer

Volume fraction PZT models	Electric potential(V)
Pure PZT	17.292
10%	1.877
20%	3.319
30%	3.866

40%	4.573
50%	5.367
60%	6.278
70%	5.897

From this table, it shows that the electric potential generated by the piezoelectric effect is much smaller than the results in table 6.1 which is the electric potential with considering the boundary conditions of heat transfer. This is because if the other two types of heat transfer ways which are heat convection and surface radiation were not considered. The heat transfer process in the dome shape is very slow because the temperature is transferred mainly through the air around the dome shape model. If the boundary conditions of heat convection and surface radiation were not considered, the deformation of the model is very small because there is only a little heat absorbed by the material. In this case, the voltage caused by the piezoelectric effect is very small. Thus, these two boundary conditions will greatly affect the heat transfer procedure in dome shape models.

Next, let us calculate the dielectric constant and piezoelectric strain coefficient by using the data from table 6.5 and 6.6 to see the difference in the results between these two types of conditions. The results for the dielectric constant and piezoelectric strain coefficient are given by Table 6.7 and 6.8:

Table 6. 7: dielectric constant of all volume fraction models without considering the boundary conditions of heat transfer

Volume fraction PZT models	Dielectric constant ε_r(F/m)
Pure PZT	1700

10%	12.67
20%	12.67
30%	15.98
40%	16.00
50%	16.03
60%	16.17
70%	16.07

Table 6. 8: piezoelectric strain coefficient of all volume fraction models without considering the boundary conditions of heat transfer

Volume fraction PZT models	Piezoelectric strain coefficient d_{33} (pC/N)
Pure PZT	584
10%	0.12
20%	0.21
30%	0.31
40%	0.36
50%	0.43
60%	0.503
70%	0.47

From Table 6.7 and 6.8, it shows that the results for the dielectric constant and piezoelectric strain coefficient are different from the results with boundary conditions of heat transfer. This is because the capacitance and voltage are different from table 6.1 and 6.2. Thus, the boundary conditions of heat transfer have great influence on piezoelectric and dielectric properties for dome shape models, which is different from bulk and planar models. The results for both two types of boundary conditions are given by Figure 6.49 and 6.50:
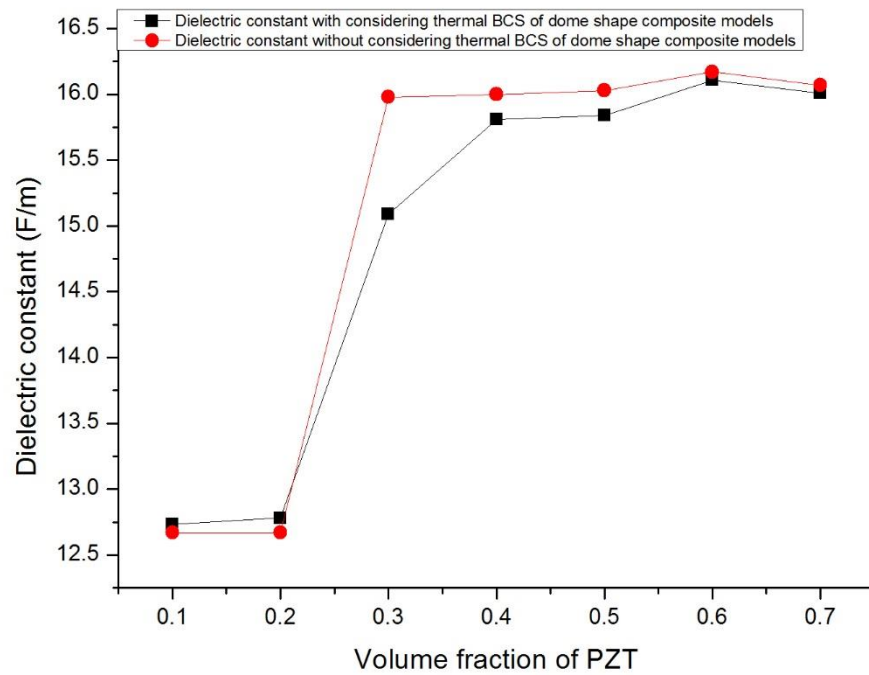
Figure 6. 51. Represents the dielectric constant for both two types of thermal boundary conditions
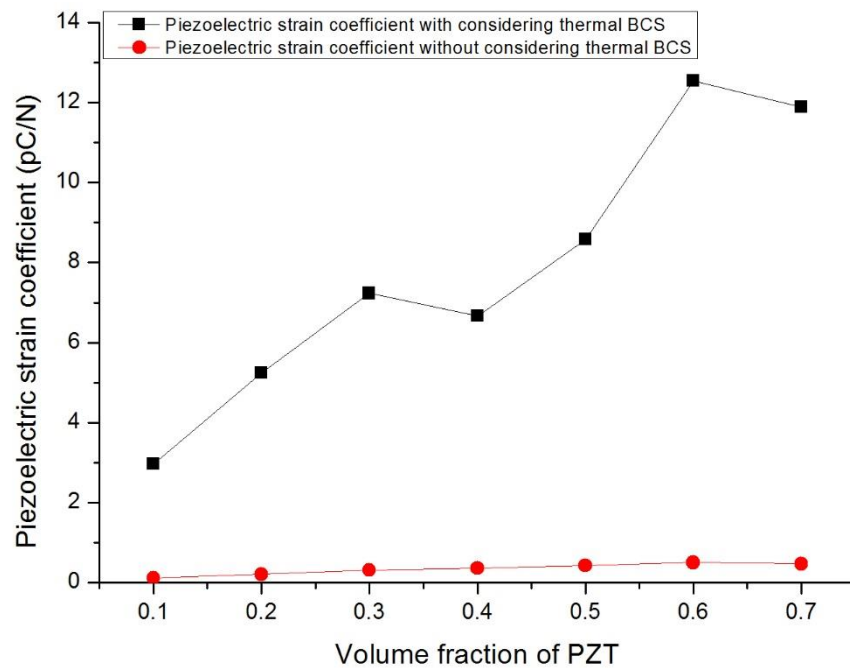
Figure 6. 52. Represents the piezoelectric strain coefficient for both two types of thermal boundary conditions

From the two figure, the thermal boundary conditions have greatly affected the

results for dome shape models. This might because that more heat energy will be absorbed during the heat transfer process if consider the boundary conditions such as heat convection and surface radiation. In this case, the composites will have more deformation and that is why they have better piezoelectric properties than the case that do not consider the boundary conditions.

Chapter 7

Conclusions and Future work

7.1 Conclusions

In this study, piezoelectric 0-3 composites PZT-Epoxy models with PZT's volume fractions 0-0.7 with three different types of geometries: bulk, planar sheet, and dome shape were simulated by Comsol 5.3a and Mat lab 2016a. The simulation work is to find out how will the temperature and the curing process of epoxy DGEBA affect the piezoelectric and dielectric properties of the composites if a fixed temperature 75C was applied on the bottom side of the composites. In addition, the simulation results of the piezoelectric strain coefficient and dielectric constant will be compared with the experimental results so as to see if these data make sense or not. The bulk and planar sheet composite models were made by the 2D module which the cross-section of these two types of composites was simulated as the geometry in the Comsol models. However, the 2D axial-symmetry module was used to generate the dome shape models. The Mat lab script was written to generate the geometry of the unit cell method used in bulk and planar sheet composite models by the Comsol Mat lab Live link. The "Record Model Method" was used in the scaled method to generate the geometry of the dome shape models by writing a Java script in Comsol. Several Multiphysics was used to generate these composite models. They are "Solid Mechanics", 'Heat Transfer in Solid", "Electrostatics", "Laminar flow", "Level set" and "Domain ODEs and DAEs". Different boundary conditions were added to each interface. The piezoelectric and dielectric

properties were considered for both considering the boundary conditions of heat convection and surface radiation and without considering them so as to see if there are some difference under these two conditions. In this study, a lot of results were got from these models. Some of the results were caused by the heat transfer process and thermal expansion of the composites, such as temperature distribution, stress and strain, and curing process at a fixed temperature 75C. The curing process in room temperature was also done as well. Some results were got from the piezoelectric effect, such as capacitance and electrical potential generated by applying the same amount of boundary load 0.25N. In addition, the piezoelectric strain coefficient d_{33} and the dielectric constant ε_r were calculated by using the results of capacitance and voltage got from the Comsol models and the dimension of the models.

The temperature of all the three types of composite models can reach the same value of temperature applied at the bottom side of the model, which is 75C. This is because the dimension for both unit cell method and scaled method for the geometries of these three different shape models were very tiny so that it seems no heat loss during the heat transfer process. However, in the real case, there is some heat loss in the experimental work for bulk samples that the temperature cannot reach to 75C at the top side because the thickness of the bulk samples is much larger than planar sheet samples and dome shape samples. But it has the same results for planar sheet samples and dome shape models because their real dimension for thickness is very small and the direction of the heat transfer process is the same with the thickness of the models.

For bulk models, the largest stress happened at 70% bulk composite models and

the largest strain occurred at 50% bulk composite models. For planar sheet models, the largest stress happened at 60% composite models and the largest strain occurred at 10% composite models. For the dome shape models, the range of the stress and strain for both the bottom curve and the upcurve are very similar. For the bottom curve, the largest stress happened at 30% composite models and the strain for all composite models is kept at zero because it was set up as the fixed constraint. For the upcurve, the largest stress also happened at 30% composite models and the largest strain occurred at 10% composite models. In addition, the strain caused by thermal expansion in dome shape models was larger than the strain generated in planar sheet models, which means dome shape model has more deformation than planar sheet model under the same heat source.

The external electric field applied for all three types of models is 0.2kV/mm. The electric potential generated by the direct piezoelectric effect for all three types of models is generally increasing with increasing the volume fraction of PZT except for a few volume fraction models. The largest electric potential for bulk composite models occurred in 70% PZT model, which is 118.72V. The largest electric potential for planar sheet composite models also occurred in 70% PZT model, which is 31.567V. And the largest electric potential for dome shape composite models also occurred in 60% PZT model, which is 156.96V. As the result shows, the voltage generated in dome shape models is larger than in planar models under the same amount of boundary load 0.25N, which means dome shape models have a better piezoelectric effect than planar sheet models. The largest value for capacitance for each type of model is 1.1056×10^{-11}F for the bulk model which occurred in 70% composite model, 6.9367×10^{-12}F for planar

sheet model which also occurred in 70% composite model and 1.9979×10^{-12}F for dome shape model which occurred in 60% composite model.

Two types of curing process were done in this study. One is curing on a hot plate which is at a fixed temperature 75C and the other one is curing in the room temperature which is 20C. Compared the two curing conditions, it takes much more time for the material to be fully cured at room temperature for all three types of models which means that higher temperature will make the material to be cured much faster than low temperature. In this study, the Curie temperature for epoxy DGEBA is 75C. At this temperature, the material will have a phase change from the gel form to the solid form because of the cross-linking of the chemical group of the epoxy occurred in the material. It was found that the curing time for the simulation model is longer than the curing time in the experimental work. It might be the reason that the material properties of the epoxy DGEBA used in Comsol models are not the same with the material used in the experimental work, or the experimental work might be affected by the temperature change in the environment because the room temperature was not set up at a fixed temperature when this process was done. The epoxy was used as the matrix to hold the PZT particles inside because PZT is very brittle. However, if the epoxy was not fully cured, it is impossible for the composites to have the piezoelectric effect because the material is in gel form that the boundary load cannot be applied to them. Thus, the curing process of the epoxy is very important for the composite. It will improve piezoelectric and dielectric properties of the composites when the epoxy is fully cured because large boundary load can be applied to it so as to generate the larger voltage. In

addition, most of the PZT particles will accumulate at the top side of the samples during the curing process which means the third hypothesis mentioned in Chapter 1 was proved.

Lastly, the piezoelectric and dielectric properties of all three types of composite models were generally increasing with increasing the volume fraction of PZT. The largest value for dielectric constant and piezoelectric strain coefficient for bulk models is 89.23 F/m and 26.25pC/N which occurred at 70% composite model. The largest value for dielectric constant and piezoelectric strain coefficient for bulk models is 89.23F/m and 26.25pC/N which occurred at 70% composite model. The largest value for dielectric constant and piezoelectric strain coefficient for planar models is 30.86F/m and 2.41pC/N which also occurred at 70% composite model. The largest value for dielectric constant and piezoelectric strain coefficient for planar models is 16.11F/m and 12.54pC/N which occurred at 60% composite model. As the result shows, dome shape composite models have a better piezoelectric effect than planar sheet composite models. This is the reason that the dome shape models were studied. All these simulation data were compared with the experimental data for all three types of samples. The good thing is that the simulation data are generally matched with the experimental data. And the simulation data are generally a little bit larger than the experimental data. This is because the simulation models are ideal models. They were not affected by the manual operation, such as fabrication procedure and people's operation errors. This means the simulation work in this study is generally good and make sense.

7.2 Limitations and future work

In this study, even though a lot of work were done, there are still some limitations in this work. First, the geometry of the Comsol models is not like the real dimension of each type. Instead, the unit cell method and the scaled method were used to generate the geometries of all three types. This is because of the limitation of the computer. For the composite models, it is impossible to generate a huge amount of PZT particles for each volume fraction composite models. There is no enough disk and Installed memory (RAM) for regular computers to run these kinds of models. Properly HPC or some supercomputers can generate so many particles and run the models. The second limitation for our study is that the material properties used for the Comsol models are the approximate data found online or from the Comsol library. It might be some difference from the materials used for the experimental work. The limitation leads to this situation is that our lab does not have the instruments to measure the thermal properties and mechanical properties of the materials. Thus, if such instruments will be bought in the future, it is possible to get better data from these models. The third limitation occurred in the curing process. It is impossible for Comsol to simulate the microscopic level for the curing process of epoxy, such as the cross-linking process. Comsol can only simulate the macroscopic level of the curing process, such as the degree of curie and the phase change process of the epoxy. The limitation is that our lab still does not have the instruments, such as DSC and DMTA. Thus, if such types of instruments can be bought or if the materials can be tested by some labs and companies who have these instruments, the curing process in microscopic level can be observed in

the future. In that case, it might be possible to get more detailed information for how will the curing procedure affect the piezoelectric and dielectric properties of the composites. In addition, the phase change process of epoxy DGEBA was not done for planar sheet models and dome shape models. This is because the calculation for this simulation is very large. It might take more than one month to run this type of simulation. This process was tried several times in this study. However, the models were automatically stopped during the simulation for these two types of models because the computer does not have enough disk and RAM to run this type of models. In the future, if supercomputers or HPC can run these types of models, the phase change process can be done for planar sheet models and dome shape models. The fourth limitation is about the PZT particles floating up to the top side of the composite during the curing process of epoxy. This limitation is similar to the third one. The regular computers cannot simulate too much PZT particles in one model floating up during the curing process. That is why only two and three PZT particles were simulated for showing this process. The whole procedure might be simulated in the future if supercomputers can do this calculation or some other types of software can simulate this process for all of PZT particles. The last limitation is about the scaled method used in dome shape models. As there are no related references about the unit cell method for dome shape piezoelectric composite models found online, the unit cell method cannot be used in dome shape models which have curved boundaries for the geometry. Instead, the scaled method was proved working for dome shape composite models. However, it is not as good as the unit cell method. This is because the script for the scaled method is not as good as the

script for the unit cell method. In the unit cell method, it obeys the rules for the periodic boundary condition and the range of the diameter of the PZT particle is from 5μm to 8μm which is the same with the real case. In addition, all the PZT particles are separated in each volume fraction composite models so that the volume fraction of PZT is set up as the exact value for each model. However, the diameter for The PZT particles is kept as 8μm for all models and some of the PZT particles were overlapped with each other so that the volume fraction for each composite model is smaller than the real case. This will affect the piezoelectric and dielectric properties of the composite models. In the real case, the results should be larger than the simulation data got from our dome shape models. Thus, if a better script for "Record Model Method" can be written by some people so as to generate better geometry of the dome shape models or better methods are discovered and proved by some people, the better results will be got from the dome shape composite models.

Appendix 1

Material properties for air

Property	Value	Unit
Relative permittivity	1	[]
Heat capacity at constant pressure	Cp(T[1/K])	J/(kg·K)
Density	Rho(pA[1/Pa], T[1/K])	kg/m^3
Thermal conductivity	K(T[1/K])	W/(m*K)
Relative permeability	1	1
Dynamic viscosity	Eta(T[1/K])	Pa·s
The ratio of specific heats	1.4	1
Electrical conductivity	0	S/m
Speed of sound	cs(T[1/K])	m/s
Refractive index, the real part	1	[]
Refractive index, the imaginary part	0	[]

Appendix 2

Material properties for PZT-5A

Property	Value	Unit
Density	7750	kg/m^3
Thermal conductivity	1.2	W/(m*K)
Heat capacity at constant pressure	330	J/(kg·K)
Coefficient of thermal expansion	0.000004	1/K
Dynamic viscosity	int1(t)	Pa·s
Elastic matrix	{1.20346e+011[Pa], 7.51791e+010[Pa], 1.20346e+011[Pa], 7.50901e+010[Pa], 7.50901e+010[Pa], 1.10867e+011[Pa], 0[Pa], 0[Pa], 0[Pa], 2.10526e+010[Pa], 0[Pa], 0[Pa], 0[Pa], 0[Pa], 2.10526e+010[Pa], 0[Pa], 0[Pa], 0[Pa], 0[Pa], 2.25734e+010[Pa]}	Pa
Coupling matrix	{0[C/m^2], 0[C/m^2], -5.35116[C/m^2], 0[C/m^2], 0[C/m^2], -5.35116[C/m^2], 0[C/m^2], 0[C/m^2], 15.7835[C/m^2], 0[C/m^2], 12.2947[C/m^2], 0[C/m^2], 12.2947[C/m^2], 0[C/m^2],	C/m^2

	0[C/m^2], 0[C/m^2], 0[C/m^2], 0[C/m^2]}	
Relative permittivity	{919.1, 919.1, 826.6}	[]
Young's modulus	50500000000	Pa
Poisson's ratio	0.3	[]
Compliance matrix	{1.64e-011[1/Pa], -5.74e-012[1/Pa], 1.64e-011[1/Pa], -7.22e-012[1/Pa], -7.22e-012[1/Pa], 1.88e-011[1/Pa], 0[1/Pa], 0[1/Pa], 0[1/Pa], 4.75e-011[1/Pa], 0[1/Pa], 0[1/Pa], 0[1/Pa], 0[1/Pa], 4.75e-011[1/Pa], 0[1/Pa], 0[1/Pa], 0[1/Pa], 0[1/Pa], 4.43e-011[1/Pa]}	1/Pa
Coupling matrix	{0[C/N], 0[C/N], -1.71e-010[C/N], 0[C/N], 0[C/N], -1.71e-010[C/N], 0[C/N], 0[C/N], 3.74e-010[C/N], 0[C/N], 5.84e-010[C/N], 0[C/N], 5.84e-010[C/N], 0[C/N], 0[C/N], 0[C/N], 0[C/N], 0[C/N]}	C/N
Relative permittivity	{1730, 1730, 1700}	[]
Loss factor for compliance matrix sE	0	[]
Loss factor for coupling matrix d	{0, 0, 0, 0, 0, 0, 0, 0, 0, 0, 0, 0, 0, 0, 0, 0, 0, 0}	[]
Loss factor for electrical	0	[]

permittivity εT		
Loss factor for elasticity matrix cE	0	[]
Loss factor for coupling matrix e	{0, 0, 0, 0, 0, 0, 0, 0, 0, 0, 0, 0, 0, 0, 0, 0, 0, 0}	[]
Loss factor for electrical permittivity εS	0	[]

Appendix 3

Material properties for partially cured epoxy (all these properties are listed by Comsol library itself)

Property	Value	Unit
Density	rho0(T)	kg/m^3
Thermal conductivity	Tc(T)	W/(m*K)
Heat capacity at constant pressure	Cp0(T)	J/(kg·K)
Relative permittivity	3.7	1
The coefficient of thermal expansion	int2(t)	1/K
Dynamic viscosity	int1(t)	Pa·s
The ratio of specific heats	0.6	1
Young's modulus	E_partially_cured_2(T[1/K])	Pa
Poisson's ratio	0.4	1

Appendix 4

Material properties for fully cured epoxy

Property	Value	Unit
Density	1140	kg/m^3
Heat capacity at constant pressure	345	J/(kg·K)
Thermal conductivity	0.2	W/(m*K)
Ratio of specific heats	0.6	1
Coefficient of thermal expansion	(alpha(T[1/K])[1/K]+(Tempref-293[K])*if(abs(T-Tempref)>1e-3,(alpha(T[1/K])[1/K]-alpha(Tempref[1/K])[1/K])/(T-Tempref),d(alpha(T[1/K])[1/K],T)))/(1+alpha(Tempref[1/K])[1/K]*(Tempref-293[K]))	1/K
Relative permittivity	3.7	1
Tangent coefficient of thermal expansion	0.0000043	1/K
Thermal strain	(dL(T[1/K])-dL (Tempref[1/K]))/ (1+dL (Tempref[1/K]))	1
Isotropic tangent coefficient	0.0000043	1/K

of thermal expansion		
Isotropic thermal strain	(dL(T)-dL (Tempref))/ (1+dL (Tempref))	1
Young's modulus	E_fully_cured_1(T[1/K])	Pa
Poisson's ratio	0.4	1

Appendix 5

Material properties for the hot plate (all these properties are listed by Comsol library itself)

Property	Value	Unit
Thermal conductivity	k_solid_1(T[1/K])	W/(m*K)
Coefficient of thermal expansion	(alpha_solid_1(T[1/K])[1/K]+(Tempref-293[K])*if(abs(T-Tempref)>1e-3,(alpha_solid_1(T[1/K])[1/K]-alpha_solid_1(Tempref[1/K])[1/K])/(T-Tempref),d(alpha_solid_1(T[1/K]),T)[1/K]))/(1+alpha_solid_1(Tempref[1/K])[1/K]*(Tempref-293[K]))	1/K
Heat capacity at constant pressure	C_solid_1(T[1/K])	J/(kg·K)
Density	rho_solid_1(T[1/K])	kg/m^3
Relative permittivity	1	1
Young's modulus	E(T[1/K])	Pa
Poisson's ratio	nu(T[1/K])	1
dL	(dL_solid_1(T[1/K])-dL_solid_1(Tempref[1/K]))/(1+dL_solid_1(Tempref[1/K]))	
CTE	CTE(T[1/K])	1/K
Resistivity	res_solid_1(T[1/K]	Ω.m
Surface	epsilon(T[1/K])	1

emissivity		J/(mol· K)
HC	HC_solid_1(T[1/K])	J/(mol· K)
Electric conductivity	sigma_solid_1(T[1/K])	S/m
nemiss	nemiss_solid_polished_1(T[1/K])	
VP	VP_solid_1(T[1/K])	Pa
Bulk modulus	kappa(T[1/K])	N/m^2
Shear Modulus	mu(T[1/K])	N/m^2

Reference

[1]   B. Dong and Z. Li, "Cement-based piezoelectric ceramic smart composites," *Composites Science and Technology,* vol. 65, no. 9, pp. 1363-1371, 2005.

[2]   Z. J. Li, D. Zhang, and K. R. Wu, "Cement-based 0-3 piezoelectric composites," (in English), *Journal of the American Ceramic Society,* vol. 85, no. 2, pp. 305-313, Feb 2002.

[3]   S. Alessi, E. Caponetti, O. Güven, M. Akbulut, G. Spadaro, and A. Spinella, "Study of the Curing Process of DGEBA Epoxy Resin Through Structural Investigation," *Macromolecular Chemistry and Physics,* vol. 216, no. 5, pp. 538-546, 2015.

[4]   H. Gong, Z. Li, Y. Zhang, and R. Fan, "Piezoelectric and dielectric behavior of 0-3 cement-based composites mixed with carbon black," *Journal of the European Ceramic Society,* vol. 29, no. 10, pp. 2013-2019, 2009.

[5]   S. Huang *et al.*, "Piezoelectric properties of 0-3 PZT/sulfoaluminate cement composites," *Smart Materials and Structures,* vol. 13, no. 2, pp. 270-274, 2004.

[6]   E. K. Akdogan, M. Allahverdi, and A. Safari, "Piezoelectric composites for sensor and actuator applications," (in English), *Ieee Transactions on Ultrasonics Ferroelectrics and Frequency Control,* vol. 52, no. 5, pp. 746-775, May 2005.

[7]   Z. J. Li and B. Q. Dong, "0-3 cement-based piezoelectric ceramic composites," (in English), *Smart Nondestructive Evaluation and Health Monitoring of Structural and Biological Systems Ii,* vol. 5047, pp. 219-230, 2003.

[8]   H. P. Konka, M. A. Wahab, and K. Lian, "Piezoelectric fiber composite transducers for health monitoring in composite structures," *Sensors and Actuators A: Physical,* vol. 194, pp. 84-94, 2013.

[9]   K. Umesh and R. Ganguli, "Composite material and piezoelectric coefficient uncertainty effects on structural health monitoring using feedback control gains as damage indicators," *Structural Health Monitoring: An International Journal,* vol. 10, no. 2, pp. 115-129, 2010.

[10]   G. P. Zhang, J. Cheng, L. Shi, X. Lin, and J. Y. Zhang, "Study on curing kinetics of diallyl-bearing epoxy resin using sulfur as curing agent," (in English), *Thermochimica Acta,* vol. 538, pp. 36-42, Jun 20 2012.

[11]   X.-P. Miao, D.-J. Cheng, Y.-D. Dai, Y. Meng, and X.-Y. Li, "Origin of Modulus Improvement for Epoxide-terminated Hyperbranched Poly(ether sulphone)/DGEBA/TETA Systems," *Chinese Journal of Polymer Science,* vol. 36, no. 8, pp. 991-998, 2018.

[12]   S. Banerjee and K. A. Cook-Chennault, "Influence of Al Particle Size and Lead Zirconate Titanate (PZT) Volume Fraction on the Dielectric Properties of PZT-Epoxy-Aluminum Composites," (in English), *Journal of Engineering Materials and Technology-Transactions of the Asme,* vol. 133, no. 4, Oct 2011.

[13]   S. Banerjee and K. A. Cook-Chennault, "An investigation into the influence of electrically conductive particle size on electromechanical coupling and effective dielectric strain coefficients in three phase composite piezoelectric polymers," (in English), *Composites Part a-Applied Science and Manufacturing,* vol. 43, no. 9, pp. 1612-1619, Sep 2012.

[14]   S. Banerjee, W. Du, L. Wang, and K. A. Cook-Chennault, "Fabrication of dome-shaped PZT-epoxy actuator using modified solvent and spin coating technique," (in English), *Journal of Electroceramics,* vol. 31, no. 1-2, pp. 148-158, Oct 2013.

[15]   S. F. Huang *et al.*, "Piezoelectric properties of 0-3 PZT/sulfoaluminate cement composites," (in

English), *Smart Materials & Structures,* vol. 13, no. 2, pp. 270-274, Apr 2004.

[16]   J. Peng, C. Chao, and H. Tang, "Piezoelectric micromachined ultrasonic transducer based on dome-shaped piezoelectric single layer," (in English), *Microsystem Technologies-Micro-and Nanosystems-Information Storage and Processing Systems,* vol. 16, no. 10, pp. 1771-1775, Oct 2010.

[17]   H. S. Yoon, G. Washington, and A. Danak, "Modeling, optimization, and design of efficient initially curved piezoceramic unimorphs for energy harvesting applications," (in English), *Journal of Intelligent Material Systems and Structures,* vol. 16, no. 10, pp. 877-888, Oct 2005.

[18]   G. H. Feng and E. S. Kim, "Piezoelectrically actuated dome-shaped diaphragm micropump," (in English), *Journal of Microelectromechanical Systems,* vol. 14, no. 2, pp. 192-199, Apr 2005.

[19]   G. H. Feng, C. C. Sharp, Q. F. Zhou, W. Pang, E. S. Kim, and K. K. Shung, "Fabrication of MEMS ZnO dome-shaped-diaphragm transducers for high frequency ultrasonic Imaging," (in English), *2004 IEEE Ultrasonics Symposium, Vols 1-3,* pp. 1950-1953, 2004.

[20]   G. Bonfante *et al.*, "Polarization mechanisms of dielectric materials at a binary liquid interface: impacts on electrowetting actuation," (in English), *Physical Chemistry Chemical Physics,* vol. 19, no. 44, pp. 30139-30146, Nov 28 2017.

[21]   C. T. Dervos, C. D. Paraskevas, P. D. Skafidas, and P. Vassiliou, "A complex permittivity based sensor for the electrical characterization of high-voltage transformer oils," (in English), *Sensors,* vol. 5, no. 4-5, pp. 302-316, Apr-May 2005.

[22]   R. Rianyoi, R. Potong, N. Jaitanong, R. Yimnirun, and A. Chaipanich, "Dielectric, ferroelectric and piezoelectric properties of 0-3 barium titanate–Portland cement composites," *Applied Physics A,* vol. 104, no. 2, pp. 661-666, 2011.

[23]   G. H. Haertling, "Ferroelectric Ceramics: History and Technology," (in English), *Ferroelectricity: The Fundamentals Collection,* pp. 157-178, 2005.

[24]   R. S. Dahiya and O. Akinyele, "Oscillation Theorems of Nth-Order Functional-Differential Equations with Forcing Terms," (in English), *Journal of Mathematical Analysis and Applications,* vol. 109, no. 2, pp. 325-332, 1985.

[25]   V. Jamadar, P. Pingle, and S. Kanase, "Possibility of Harvesting Vibration Energy from Power Producing Devices: A Review," (in English), *2016 International Conference on Automatic Control and Dynamic Optimization Techniques (Icacdot),* pp. 496-503, 2016.

[26]   Y. Kuroiwa *et al.*, "Ferroelectric Materials and Their Applications FOREWORD," (in English), *Japanese Journal of Applied Physics,* vol. 56, no. 10, Oct 2017.

[27]   X. Q. Jin, Y. J. Luo, Y. Lu, L. L. Mang, and D. Z. Sun, "Investigation on aging behavior in ferroelectric materials with perovskite structure," (in English), *Ferroelectrics,* vol. 363, pp. 163-167, 2008.

[28]   S. B. Lang, "Guide to the Literature of Piezoelectricity and Pyroelectricity. 19," (in English), *Ferroelectrics,* vol. 287, pp. 71-72, 2003.

[29]   M. Lethiecq *et al.*, "New low acoustic impedance piezoelectric material for broadband transducer applications," (in English), *2004 Ieee Ultrasonics Symposium, Vols 1-3,* pp. 1153-1156, 2004.

[30]   Y. Takahiro, K. Masako, and S. Norikazu, "Influence of poling conditions on the piezoelectric properties of PZT ceramics," (in English), *Journal of Materials Science-Materials in Electronics,* vol. 11, no. 5, pp. 425-428, Jul 2000.

[31]   D. W. Wang *et al.*, "Mechanical Reinforcement and Piezoelectric Properties of PZT Ceramics

Embedded with Nano-Crystalline," (in English), *Chinese Physics Letters,* vol. 27, no. 4, Apr 2010.

[32]   H. W. Kim *et al.*, "Energy harvesting using a piezoelectric "cymbal" transducer in dynamic environment," (in English), *Japanese Journal of Applied Physics Part 1-Regular Papers Brief Communications & Review Papers,* vol. 43, no. 9a, pp. 6178-6183, Sep 2004.

[33]   G. Yesner, A. Jasim, H. Wang, B. Basily, A. Maher, and A. Safari, "Energy harvesting and evaluation of a novel piezoelectric bridge transducer," (in English), *Sensors and Actuators a-Physical,* vol. 285, pp. 348-354, Jan 1 2019.

[34]   F. S. Ip and C. Ting, "Dielectric properties of low dielectric constant polymeric materials," (in English), *Low-Dielectric Constant Materials - Synthesis and Applications in Microelectronics,* vol. 381, pp. 135-139, 1995.

[35]   M. M. Li, S. F. Huang, S. H. Xie, M. J. Zhou, and X. Cheng, "A study on polarization properties of the carbon black modified 0-3 cement-based piezoelectric composites," (in English), *Advanced Building Materials and Sustainable Architecture, Pts 1-4,* vol. 174-177, pp. 791-794, 2012.

[36]   M. Dietze and M. Es-Souni, "Structural and functional properties of screen-printed PZT-PVDF-TrFE composites," (in English), *Sensors and Actuators a-Physical,* vol. 143, no. 2, pp. 329-334, May 16 2008.

[37]   E. M. McKenna, A. S. Lin, A. R. Mickelson, R. Dinu, and D. Lin, "Comparison of r(33) values for AJ404 films prepared with parallel plate and corona poling," (in English), *Journal of the Optical Society of America B-Optical Physics,* vol. 24, no. 11, pp. 2888-2892, Nov 2007.

[38]   X. F. Chen, Z. Y. Zhou, F. Cao, H. C. Nie, X. L. Dong, and G. S. Wang, "Temperature-Dependent Scaling Behavior of Dynamic Hysteresis in Pb(Zr,Ti)O-3 Ceramics," (in English), *Journal of the American Ceramic Society,* vol. 98, no. 10, pp. 3159-3164, Oct 2015.

[39]   J. A. Lewis, Jr., "The use of thermoplastic impression materials to identify children and young adults," *Pediatr Dent,* vol. 26, no. 6, p. 480, Nov-Dec 2004.

[40]   V. Fombuena, L. Sanchez-Nacher, M. D. Samper, D. Juarez, and R. Balart, "Study of the Properties of Thermoset Materials Derived from Epoxidized Soybean Oil and Protein Fillers," (in English), *Journal of the American Oil Chemists Society,* vol. 90, no. 3, pp. 449-457, Mar 2013.

[41]   H. Y. Cai *et al.*, "Curing kinetics study of epoxy resin/flexible amine toughness systems by dynamic and isothermal DSC," (in English), *Thermochimica Acta,* vol. 473, no. 1-2, pp. 101-105, Jul 10 2008.

[42]   A. Shokuhfar and B. Arab, "The effect of cross linking density on the mechanical properties and structure of the epoxy polymers: molecular dynamics simulation," (in English), *Journal of Molecular Modeling,* vol. 19, no. 9, pp. 3719-3731, Sep 2013.

[43]   J. D. McCoy *et al.*, "Cure mechanisms of diglycidyl ether of bisphenol A (DGEBA) epoxy with diethanolamine," *Polymer,* vol. 105, pp. 243-254, 2016.

[44]   A. Shokuhfar and B. Arab, "The effect of cross linking density on the mechanical properties and structure of the epoxy polymers: molecular dynamics simulation," *J Mol Model,* vol. 19, no. 9, pp. 3719-31, Sep 2013.

[45]   A. Safari, V. F. Janas, and A. Bandyopadhyay, "Development of fine-scale piezoelectric composites for transducers," (in English), *Aiche Journal,* vol. 43, no. 11, pp. 2849-2856, 1997.

[46]   C. J. Dias and D. K. DasGupta, "Inorganic ceramic/polymer ferroelectric composite electrets," (in English), *Ieee Transactions on Dielectrics and Electrical Insulation,* vol. 3, no. 5, pp. 706-734, Oct 1996.

[47]   R. E. Newnham, "Composite Electroceramics," (in English), *Annual Review of Materials Science,*

vol. 16, pp. 47-68, 1986.

[48]   R. E. Newnham, D. P. Skinner, K. A. Klicker, A. S. Bhalla, B. Hardiman, and T. R. Gururaja, "Ferroelectric Ceramic-Plastic Composites for Piezoelectric and Pyroelectric Applications," (in English), *Ferroelectrics,* vol. 27, no. 1-4, pp. 49-55, 1980.

[49]   S. M. Pilgrim and R. E. Newnham, "3-0 - a New Composite Connectivity," (in English), *Ieee Transactions on Ultrasonics Ferroelectrics and Frequency Control,* vol. 33, no. 6, pp. 805-805, Nov 1986.

[50]   S. K. Bhattacharya and R. R. Tummala, "Epoxy nanocomposite capacitors for application as MCM-L compatible integral passives," (in English), *Journal of Electronic Packaging,* vol. 124, no. 1, pp. 1-6, Mar 2002.

[51]   S. Ogitani, S. A. Bidstrup-Allen, and P. A. Kohl, "Factors influencing the permittivity of polymer/ceramic composites for embedded capacitors," (in English), *Ieee Transactions on Advanced Packaging,* vol. 23, no. 2, pp. 313-322, May 2000.

[52]   J. W. Xu, K. S. Moon, C. Tison, and C. P. Wong, "A novel aluminum-filled composite dielectric for embedded passive applications," (in English), *Ieee Transactions on Advanced Packaging,* vol. 29, no. 2, pp. 295-306, May 2006.

[53]   N. H. Afgan, "Fundamental Heat and Mass-Transfer Research in the Development of New Heat-Exchangers Concepts," (in English), *Journal of Enhanced Heat Transfer,* vol. 2, no. 1-2, pp. 1-16, 1995.

[54]   L. L. Li *et al.*, "1-3 piezoelectric composites for high-temperature transducer applications," (in English), *Journal of Physics D-Applied Physics,* vol. 46, no. 16, Apr 24 2013.

[55]   H. J. Lee and D. A. Saravanos, "The effect of temperature dependent material properties on the response of piezoelectric composite materials," (in English), *Journal of Intelligent Material Systems and Structures,* vol. 9, no. 7, pp. 503-508, Jul 1998.

[56]   M. Kang and E. M. Yeatman, "Thermal Energy Harvesting Using Pyroelectric and Piezoelectric Effect," (in English), *16th International Conference on Micro and Nanotechnology for Power Generation and Energy Conversion Applications (Powermems 2016),* vol. 773, 2016.

[57]   C. Maurini, M. Porfiri, and J. Pouget, "Numerical methods for modal analysis of stepped piezoelectric beams," (in English), *Journal of Sound and Vibration,* vol. 298, no. 4-5, pp. 918-933, Dec 22 2006.

[58]   H. Berger, S. Kari, U. Gabbert, R. Rodriguez-Ramos, J. Bravo-Castillero, and R. Guinovart-Diaz, "Calculation of effective coefficients for piezoelectric fiber composites based on a general numerical homogenization technique," (in English), *Composite Structures,* vol. 71, no. 3-4, pp. 397-400, Dec 2005.

[59]   H. E. Pettermann and S. Suresh, "A comprehensive unit cell model: a study of coupled effects in piezoelectric 1-3 composites," (in English), *International Journal of Solids and Structures,* vol. 37, no. 39, pp. 5447-5464, Sep 2000.

[60]   S. Kari, H. Berger, R. Rodriguez-Ramos, and U. Gabbert, "Computational evaluation of effective material properties of composites reinforced by randomly distributed spherical particles," *Composite Structures,* vol. 77, no. 2, pp. 223-231, 2007.

[61]   M. Sakthivel and A. Arockiarajan, "An analytical model for predicting thermo-electro-mechanical response of 1-3 piezoelectric composites," (in English), *Computational Materials Science,* vol. 48, no. 4, pp. 759-767, Jun 2010.

[62]   R. Simpkin, "Derivation of Lichtenecker's Logarithmic Mixture Formula From Maxwell's

Equations," (in English), *Ieee Transactions on Microwave Theory and Techniques,* vol. 58, no. 3, pp. 545-550, Mar 2010.

[63]   V. A. Markel, "Introduction to the Maxwell Garnett approximation: tutorial," *J Opt Soc Am A Opt Image Sci Vis,* vol. 33, no. 7, pp. 1244-56, Jul 1 2016.

[64]   I. S. L. Bhaskar Patham General Motors Global Research and Development, GM Technical Centre India Pvt. Ltd., "COMSOL® Implementation of a viscoelastic model with cure-temperature-time superposition for predicting cure stresses and spring back in a thermoset resin."

[65]   Z. Zeng *et al.*, "A flexible, sandwich structure piezoelectric energy harvester using PIN-PMN-PT/epoxy 2-2 composite flake for wearable application," (in English), *Sensors and Actuators a-Physical,* vol. 265, pp. 62-69, Oct 1 2017.

[66]   Y. B. Yi, L. Berhan, and A. M. Sastry, "Statistical geometry of random fibrous networks, revisited: Waviness, dimensionality, and percolation," (in English), *Journal of Applied Physics,* vol. 96, no. 3, pp. 1318-1327, Aug 1 2004.

[67]   M. Sakthivel and A. Arockiarajan, "An analytical model for predicting thermo-electro-mechanical response of 1–3 piezoelectric composites," *Computational Materials Science,* vol. 48, no. 4, pp. 759-767, 2010.

[68]   M. Rudolph, C. Naumann, and M. Stockmann, "Degree of Cure Definition for an Epoxy Resin Based on Thermal Diffusivity Measurements," *Materials Today: Proceedings,* vol. 3, no. 4, pp. 1144-1149, 2016.

[69]   L. Pardo, J. Mendiola, and C. Alemany, "Theoretical treatment of ferroelectric composites using Monte Carlo calculations," *Journal of Applied Physics,* vol. 64, no. 10, pp. 5092-5097, 1988.

[70]   T. T. Nguyen *et al.*, "Elaboration and dielectric property of modified PZT/epoxy nanocomposites," *Polymer Composites,* vol. 37, no. 2, pp. 455-461, 2016.

[71]   L. Berhan and A. M. Sastry, "Modeling percolation in high-aspect-ratio fiber systems. I. Soft-core versus hard-core models," *Phys Rev E Stat Nonlin Soft Matter Phys,* vol. 75, no. 4 Pt 1, p. 041120, Apr 2007.

[72]   L. Berhan and A. M. Sastry, "Modeling percolation in high-aspect-ratio fiber systems. I. Soft-core versus hard-core models," (in English), *Physical Review E,* vol. 75, no. 4, Apr 2007.

[73]   L. Berhan and A. M. Sastry, "On Modeling Bonds in Fused, Porous Networks: 3D Simulations of Fibrous–Particulate Joints," *Journal of Composite Materials,* vol. 37, no. 8, pp. 715-740, 2016.

[74]   L. Berhan, Y. B. Yi, and A. M. Sastry, "Effect of nanorope waviness on the effective moduli of nanotube sheets," (in English), *Journal of Applied Physics,* vol. 95, no. 9, pp. 5027-5034, May 1 2004.

[75]   W. Zhang, X. Li, and R. Yang, "Blowing-out effect and temperature profile in condensed phase in flame retarding epoxy resins by phosphorus-containing oligomeric silsesquioxane," *Polymers for Advanced Technologies,* vol. 24, no. 11, pp. 951-961, 2013.

[76]   X. Wang, L. Mao, M. Luo, P. Fang, Y. Dai, and K. M. Liew, "Study of fullerene-containing epoxy membranes with tunable ultraviolet light-filtering properties," *Progress in Organic Coatings,* vol. 67, no. 4, pp. 398-404, 2010.

[77]   M. Sitthiracha, P. A. Kilmartin, and N. R. Edmonds, "Novel organic–inorganic hybrid materials based on epoxy-functionalized silanes," *Journal of Sol-Gel Science and Technology,* vol. 76, no. 3, pp. 542-551, 2015.

[78]   M. Sharifi, C. Jang, C. F. Abrams, and G. R. Palmese, "Epoxy Polymer Networks with Improved

Thermal and Mechanical Properties via Controlled Dispersion of Reactive Toughening Agents," *Macromolecules,* vol. 48, no. 20, pp. 7495-7502, 2015.

[79]   E. Serrano, G. Kortaberria, P. Arruti, A. Tercjak, and I. Mondragon, "Molecular dynamics of an epoxy resin modified with an epoxidized poly(styrene–butadiene) linear block copolymer during cure and microphase separation processes," *European Polymer Journal,* vol. 45, no. 4, pp. 1046-1057, 2009.

[80]   S. Naumann, M. Speiser, R. Schowner, E. Giebel, and M. R. Buchmeiser, "Air Stable and Latent Single-Component Curing of Epoxy/Anhydride Resins Catalyzed by Thermally Liberated N-Heterocyclic Carbenes," *Macromolecules,* vol. 47, no. 14, pp. 4548-4556, 2014.

[81]   J. M. Morancho *et al.*, "Thermal curing and photocuring of a DGEBA modified with multiarm star poly(glycidol)-b-poly(ε-caprolactone) polymers of different arm lengths," *Journal of Thermal Analysis and Calorimetry,* vol. 114, no. 1, pp. 409-416, 2013.

[82]   S. Masoumi, B. Arab, and H. Valipour, "A study of thermo-mechanical properties of the cross-linked epoxy: An atomistic simulation," *Polymer,* vol. 70, pp. 351-360, 2015.

[83]   J. Macan, H. Ivanković, M. Ivanković, and H. J. Mencer, "Study of cure kinetics of epoxy-silica organic–inorganic hybrid materials," *Thermochimica Acta,* vol. 414, no. 2, pp. 219-225, 2004.

[84]   M. Hayaty, M. H. Beheshty, and M. Esfandeh, "Isothermal differential scanning calorimetry study of a glass/epoxy prepreg," *Polymers for Advanced Technologies,* vol. 22, no. 6, pp. 1001-1006, 2011.

[85]   A. Alibeigloo, "Thermoelastic analysis of functionally graded carbon nanotube reinforced composite cylindrical panel embedded in piezoelectric sensor and actuator layers," *Composites Part B: Engineering,* vol. 98, pp. 225-243, 2016.

[86]   F. Côté, P. Masson, N. Mrad, and V. Cotoni, "Dynamic and static modelling of piezoelectric composite structures using a thermal analogy with MSC/NASTRAN," *Composite Structures,* vol. 65, no. 3-4, pp. 471-484, 2004.

[87]   C. Li, E. T. Ooi, C. Song, and S. Natarajan, "SBFEM for fracture analysis of piezoelectric composites under thermal load," *International Journal of Solids and Structures,* vol. 52, pp. 114-129, 2015.

[88]   P. Liu, T. Yu, T. Q. Bui, C. Zhang, Y. Xu, and C. W. Lim, "Transient thermal shock fracture analysis of functionally graded piezoelectric materials by the extended finite element method," *International Journal of Solids and Structures,* vol. 51, no. 11-12, pp. 2167-2182, 2014.

[89]   D. Shen *et al.*, "Enhanced thermal conductivity of epoxy composites filled with silicon carbide nanowires," *Sci Rep,* vol. 7, no. 1, p. 2606, Jun 1 2017.

[90]   E. T. Thostenson and T.-W. Chou, "Corrigendum: 'On the elastic properties of carbon nanotube-based composites: modelling and characterization' (2003 J. Phys. D: Appl. Phys. 36 573)," *Journal of Physics D: Applied Physics,* vol. 47, no. 7, p. 079501, 2014.

[91]   D. Zhang, E. Cherkaev, and M. P. Lamoureux, "Stieltjes representation of the 3D Bruggeman effective medium and Padé approximation," *Applied Mathematics and Computation,* vol. 217, no. 17, pp. 7092-7107, 2011.

[92]   F. Xing, B. Dong, and Z. Li, "Impedance spectroscopic studies of cement-based piezoelectric ceramic composites," *Composites Science and Technology,* vol. 68, no. 12, pp. 2456-2460, 2008.

[93]   C. Xin, H. Shifeng, C. Jun, and L. Zongjin, "Piezoelectric, dielectric, and ferroelectric properties of 0–3 ceramic/cement composites," *Journal of Applied Physics,* vol. 101, no. 9, p. 094110, 2007.

[94]   C. Xin, H. Shifeng, C. Jun, X. Ronghua, L. Futian, and L. Lingchao, "Piezoelectric and dielectric properties of piezoelectric ceramic–sulphoaluminate cement composites," *Journal of the European Ceramic Society,* vol. 25, no. 13, pp. 3223-3228, 2005.

[95]   B. Shen, X. Yang, and Z. Li, "A Cement-Based Piezoelectric Sensor for Civil Engineering Structure," *Materials and Structures,* vol. 39, no. 1, pp. 37-42, 2006.

[96]   Y. Lu, Z. Li, and W.-I. Liao, "Damage monitoring of reinforced concrete frames under seismic loading using cement-based piezoelectric sensor," *Materials and Structures,* vol. 44, no. 7, pp. 1273-1285, 2010.

[97]   Z. Li, B. Dong, and D. Zhang, "Influence of polarization on properties of 0–3 cement-based PZT composites," *Cement and Concrete Composites,* vol. 27, no. 1, pp. 27-32, 2005.

[98]   B. Dong, F. Xing, and Z. Li, "The study of poling behavior and modeling of cement-based piezoelectric ceramic composites," *Materials Science and Engineering: A,* vol. 456, no. 1-2, pp. 317-322, 2007.

[99]   T. Chappex and K. L. Scrivener, "The influence of aluminium on the dissolution of amorphous silica and its relation to alkali silica reaction," *Cement and Concrete Research,* vol. 42, no. 12, pp. 1645-1649, 2012.

[100]   S. Bhattacharya, V. K. Sachdev, R. Chatterjee, and R. P. Tandon, "Decisive properties of graphite-filled cement composites for device application," *Applied Physics A,* vol. 92, no. 2, pp. 417-420, 2008.

[101]   D. A. van den Ende, W. A. Groen, and S. van der Zwaag, "The effect of calcining temperature on the properties of 0-3 piezoelectric composites of PZT and a liquid crystalline thermosetting polymer," *Journal of Electroceramics,* vol. 27, no. 1, pp. 13-19, 2010.

[102]   S. N. Kallaev, G. G. Gadzhiev, I. K. Kamilov, Z. M. Omarov, S. A. Sadykov, and L. A. Reznichenko, "Thermal properties of PZT-based ferroelectric ceramics," *Physics of the Solid State,* vol. 48, no. 6, pp. 1169-1170, 2006.

[103]   Z. Ahmad, "Polymer Dielectric Materials," 2012.

[104]   H. Berger *et al.*, "Unit cell models of piezoelectric fiber composites for numerical and analytical calculation of effective properties," *Smart Materials and Structures,* vol. 15, no. 2, pp. 451-458, 2006.

[105]   Q. Dai and K. Ng, "Investigation of electromechanical properties of piezoelectric structural fiber composites with micromechanics analysis and finite element modeling," *Mechanics of Materials,* vol. 53, pp. 29-46, 2012.

[106]   Y. Amini, H. Emdad, and M. Farid, "Finite element modeling of functionally graded piezoelectric harvesters," *Composite Structures,* vol. 129, pp. 165-176, 2015.

[107]   L. Guadagno *et al.*, "Cure behavior and physical properties of epoxy resin-filled with multiwalled carbon nanotubes," *J Nanosci Nanotechnol,* vol. 10, no. 4, pp. 2686-93, Apr 2010.

[108]   Q. Zhang, K. Naito, B. Qi, and Y. Kagawa, "Epoxy nanocomposites based on high temperature pyridinium-modified clays," *J Nanosci Nanotechnol,* vol. 9, no. 1, pp. 209-15, Jan 2009.

[109]   E. Lenglet, A. C. Hladky-Hennion, and J. C. Debus, "Numerical homogenization techniques applied to piezoelectric composites," *J Acoust Soc Am,* vol. 113, no. 2, pp. 826-33, Feb 2003.

[110]   H. R. Wenk and A. Bulakh, "Minerals Their Constitution and Origin Second Edition Preface," (in English), *Minerals: Their Constitution and Origin, 2nd Edition,* pp. Xiii-+, 2016.

[111]   M. Abbasipour, R. Khajavi, A. A. Yousefi, M. E. Yazdanshenas, F. Razaghian, and A. Akbarzadeh, "Improving piezoelectric and pyroelectric properties of electrospun PVDF nanofibers using

nanofillers for energy harvesting application," (in English), *Polymers for Advanced Technologies,* vol. 30, no. 2, pp. 279-291, Feb 2019.

[112]   W. Wang, C. P. Yue, J. F. Gu, J. Z. Du, F. P. Li, and K. Yang, "Status Assessment of Polymeric Materials in Mineral Oil under Electro-thermal Aging by Frequency-domain Dielectric Spectroscopy," (in English), *Ieee Transactions on Dielectrics and Electrical Insulation,* vol. 22, no. 2, pp. 831-841, Apr 2015.

[113]   E. Shin, J. Yoo, G. Yoo, Y. J. Kim, and Y. S. Kim, "Eco-friendly cross-linked polymeric dielectric material based on natural tannic acid," (in English), *Chemical Engineering Journal,* vol. 358, pp. 170-175, Feb 15 2019.

[114]   A. Abdelkefi, Z. M. Yan, and M. R. Hajj, "Modeling and nonlinear analysis of piezoelectric energy harvesting from transverse galloping," (in English), *Smart Materials and Structures,* vol. 22, no. 2, Feb 2013.

[115]   S. Banerjee and K. A. Cook-Chennault, "An Analytical Model for the Effective Dielectric Constant of a 0-3-0 Composite," (in English), *Journal of Engineering Materials and Technology-Transactions of the Asme,* vol. 133, no. 4, Oct 2011.

[116]   S. Banerjee and K. A. Cook-Chennault, "Influence of aluminium inclusions on dielectric properties of three-phase PZT-cement-aluminium composites," (in English), *Advances in Cement Research,* vol. 26, no. 2, pp. 63-76, Aug 2014.

[117]   S. Banerjee, K. A. Cook-Chennault, W. Du, U. Sundar, H. Halim, and A. Tang, "Piezoelectric and dielectric characterization of corona and contact poled PZT-epoxy-MWCNT bulk composites," (in English), *Smart Materials and Structures,* vol. 25, no. 11, Nov 2016.

[118]   S. Banerjee, W. Du, U. Sundar, and K. A. Cook-Chennault, "Piezoelectric and Dielectric Characterization of MWCNT-Based Nanocomposite Flexible Films," (in English), *Journal of Nanomaterials,* 2018.

[119]   K. A. Cook-Chennault and S. Banerjee, "An analytical model for the effective dielectric constant of a 0-3-0 composite," (in English), *Proceedings of the Asme International Mechanical Engineering Congress and Exposition 2010, Vol 12,* pp. 65-70, 2012.

[120]   K. A. Cook-Chennault, D. Cosaboon, D. Eigbe, B. Pitcavage, M. Whitzer, and D. Castley, "Enhanced Output Voltage and Power from Conductive Inclusions in a 0-3-0 Piezoelectric Composite," (in English), *Proceedings of the Asme International Mechanical Engineering Congress and Exposition 2010, Vol 12,* pp. 61-+, 2012.

[121]   H. Y. Gong, Z. J. Li, Y. J. Zhang, and R. H. Fan, "Piezoelectric and dielectric behavior of 0-3 cement-based composites mixed with carbon black," (in English), *Journal of the European Ceramic Society,* vol. 29, no. 10, pp. 2013-2019, Jul 2009.

[122]   S. F. Huang, J. Chang, L. C. Lu, F. T. Liu, Z. M. Ye, and X. Cheng, "Preparation and polarization of 0-3 cement based piezoelectric composites," (in English), *Materials Research Bulletin,* vol. 41, no. 2, pp. 291-297, Feb 2 2006.

[123]   V. A. Markel, "Introduction to the Maxwell Garnett approximation: tutorial," (in English), *Journal of the Optical Society of America a-Optics Image Science and Vision,* vol. 33, no. 7, pp. 1244-1256, Jul 1 2016.

[124]   A. M. Sastry, C. W. Wang, and L. Berhan, "Deformation and failure in stochastic fibrous networks: Scale, dimension and application," (in English), *Probabilistic Methods in Fatigue and Fracture,* vol. 200, pp. 229-250, 2001.

[125]   L. Berhan and A. M. Sastry, "On Modeling bonds in fused, porous networks: 3D simulations of

fibrous-particulate joints," (in English), *Journal of Composite Materials,* vol. 37, no. 8, pp. 715-740, 2003.

[126]   L. Berhan and A. M. Sastry, "Modeling percolation in high-aspect-ratio fiber systems. II. The effect of waviness on the percolation onset," (in English), *Physical Review E,* vol. 75, no. 4, Apr 2007.

[127]   L. Berhan, Y. B. Yi, A. M. Sastry, E. Munoz, M. Selvidge, and R. Baughman, "Mechanical properties of nanotube sheets: Alterations in joint morphology and achievable moduli in manufacturable materials," (in English), *Journal of Applied Physics,* vol. 95, no. 8, pp. 4335-4345, Apr 15 2004.

[128]   C. W. Wang, L. Berhan, and A. M. Sastry, "Structure, mechanics and failure of stochastic fibrous networks: Part I - Microscale considerations," (in English), *Journal of Engineering Materials and Technology-Transactions of the Asme,* vol. 122, no. 4, pp. 450-459, Oct 2000.

[129]   X. Dongyu, C. Xin, S. Banerjee, and H. Shifeng, "Design, fabrication, and properties of 2-2 connectivity cement/polymer based piezoelectric composites with varied piezoelectric phase distribution," *J Appl Phys,* vol. 116, no. 24, p. 244103, Dec 28 2014.

[130]   H. Khanbareh, S. van der Zwaag, and W. A. Groen, "In-situ poling and structurization of piezoelectric particulate composites," *J Intell Mater Syst Struct,* vol. 28, no. 18, pp. 2467-2472, Nov 2017.

[131]   R. Rouffaud, A. C. Hladky-Hennion, and F. Levassort, "A combined genetic algorithm and finite element method for the determination of a practical elasto-electric set for 1-3 piezocomposite phases," *Ultrasonics,* vol. 77, pp. 214-223, May 2017.

[132]   H. Xiao *et al.*, "Design for Highly Piezoelectric and Visible/Near-Infrared Photoresponsive Perovskite Oxides," *Adv Mater,* vol. 31, no. 4, p. e1805802, Jan 2019.

[133]   J. Zaragoza *et al.*, "Experimental Investigation of Mechanical and Thermal Properties of Silica Nanoparticle-Reinforced Poly(acrylamide) Nanocomposite Hydrogels," *PLoS One,* vol. 10, no. 8, p. e0136293, 2015.

[134]   R. Torrico *et al.*, "Structure and properties of epoxy-siloxane-silica nanocomposite coatings for corrosion protection," *J Colloid Interface Sci,* vol. 513, pp. 617-628, Mar 1 2018.

[135]   S.-J. Park, H.-Y. Lee, M. Han, and S.-K. Hong, "Thermal and mechanical interfacial properties of the DGEBA/PMR-15 blend system," *Journal of Colloid and Interface Science,* vol. 270, no. 2, pp. 288-294, 2004.

[136]   F. Jeyranpour, G. Alahyarizadeh, and B. Arab, "Comparative investigation of thermal and mechanical properties of cross-linked epoxy polymers with different curing agents by molecular dynamics simulation," *J Mol Graph Model,* vol. 62, pp. 157-164, Nov 2015.